DAWNING OF NUCLEAR MAGICITY IN N = 32 SEEN THROUGH PRECISION MASS SPECTROMETRY

by

Erich Leistenschneider

A THESIS SUBMITTED IN PARTIAL FULFILLMENT OF THE REQUIREMENTS FOR THE DEGREE OF

Doctor of Philosophy

in

The Faculty of Graduate and Postdoctoral Studies
(Physics)

The University of British Columbia
(Vancouver)

October 2019

The following individuals certify that they have read, and recommend to the Faculty of Graduate and Postdoctoral Studies for acceptance, the dissertation entitled:

Dawning of Nuclear Magicity in N=32 Seen Through Precision Mass Spectrometry

submitted by	**Erich Leistenschneider**	in partial fulfillment of the requirements for
the degree of	Doctor of Philosophy	
in	Physics.	

Examining Committee:

Jens Dilling, Physics and Astronomy
Supervisor

Gordon W. Semenoff, Physics and Astronomy
Supervisory Committee Member

John Behr, Physics and Astronomy
Supervisory Committee Member

Takamasa Momose, Chemistry
University Examiner

Alison Lister, Physics and Astronomy
University Examiner

Kumar S. Sharma, The University of Manitoba
External Examiner

Additional Supervisory Committee Member:

Reiner Kruecken, Physics and Astronomy
Supervisory Committee Member

ABSTRACT

In the early days of nuclear science, physicists were astounded that specific "magic" combinations of neutrons or protons within nuclei seemed to bind together more tightly than other combinations. This phenomenon was related to the formation of shell structures in nuclei. More recently, nuclear shells were observed to emerge or vanish as we inspect nuclei further from stability. The structural evolution of these changing shells has been the object of intense experimental investigation, and their behavior has become a standard ruler to benchmark theoretical predictions.

In this work, we investigated the emergence of shell effects in systems with 32 neutrons ($N = 32$) using mass spectrometry techniques. Evidence for "magicity" was observed in potassium (with 19 protons, or $Z = 19$), calcium ($Z = 20$) and scandium ($Z = 21$), but not in vanadium ($Z = 23$) and higher-Z elements. In between, the picture at titanium ($Z = 22$) was unclear.

We produced neutron-rich isotopes of titanium and vanadium through nuclear reactions at the ISAC facility and measured their atomic masses at the TITAN facility, in the TRIUMF Laboratory in Vancouver. These measurements were performed with the newly commissioned Multiple-Reflection Time-of-Flight Mass Spectrometer at TITAN facility and were substantiated by independent measurements from the Penning trap mass spectrometer. The atomic masses of $^{52-55}$Ti and $^{52-55}$V isotopes were measured with high precision, right at the expected emergence of $N = 32$ shell effects. Our results conclusively establish the existence of weak shell effects in titanium and confirm their absence in vanadium.

Calculations of the $N = 32$ nuclear shell are within reach of the so-called *ab initio* theories. In these, complex atomic nuclei are described theoretically from fundamental principles, by applying principles of Quantum Chromodynamics to many-body quantum methods. Our data were compared with a few state-of-the-art *ab initio* calculations which, despite very successfully describing the $N = 32$ shell effects in Ca and Sc isotopes, overpredict its strength in Ti and erroneously assign V as its point of appearance. We hope the deficiencies revealed by our work will guide the development of the next generation of *ab initio* theories.

LAY SUMMARY

Protons and neutrons inside the atomic nucleus organize themselves in structures that resemble the shells of an onion. Specific combinations of protons or neutrons are known to form closed shells, which grant remarkable stability to the nucleus and leave imprints on its mass and other properties. However, these shells may harden or soften if the number of neutrons is too different from the number of protons.

We observed the ”hardening” of a nuclear shell formed by 32 neutrons by precisely measuring the masses of rare nuclei. We discovered that this shell does not form when the nucleus has 23 protons or more but is weakly present with 22 protons. The extreme imbalance between protons and neutrons required for shell formation makes this case a good test bench for nuclear theories. We tested the predictions of a few modern theories, which slightly differ from our results. We hope our work will guide future theoretical developments.

PREFACE

The material presented in this thesis is the result of the collaborative work involving many people. The TITAN facility at TRIUMF Laboratory has been in operation since 2007. It has been maintained by the TITAN Scientific Collaboration which has members from several Canadian universities and has partners from many international institutions. Many of the techniques and devices employed in this thesis were developed over the years by several members of the collaboration. In the following, I list all the individual contributions relevant to the work presented in this thesis:

- From Summer 2016 to Summer 2019, I lead the working group of the Measurement Penning Trap (MPET) mass spectrometer. I was responsible for its maintenance, operation, preparation for experiments, and upgrades.
- The planning and coordination of the experiment herein described was done by me and M. P. Reiter.
- The preparation and operation of the MPET mass spectrometer before and during the experiment was done by me, R. Steinbrügge and A. A. Kwiatkowski.
- The online commissioning of the Multiple Reflection Time-of-Flight Mass Spectrometer (MR-ToF-MS), as well as its preparation and operation before and during the experiment, was done by M. P. Reiter, S. Ayet San Andrés, C. Hornung, C. Will and A. Finlay.
- The data collection was performed with the support of B. Kootte, C. Babcock, B. R. Barquest, J. Bollig, E. Dunling, L. Graham, R. Klawitter, Y. Lan, D. Lascar, J. E. McKay and S. F. Paul.
- Laser ionization of titanium using the TRILIS ion source was set up by J. Lassen.
- The theoretical calculations were performed by J. D. Holt, P. Navrátil, C. Barbieri, H. Hergert, A. Schwenk, J. Simonis, V. Somà and S. R. Stroberg.
- The analysis of the MPET data was done independently by me and B. Kootte. The analysis of the MR-ToF-MS data was done independently by M. P. Reiter and S. Ayet San Andrés.
- I organized the scientific discussions following the experimental and theoretical results with all the collaborators.

A letter describing the main part of the work, containing the experimental results with titanium isotopes, the theoretical calculations and the discussion of scientific implications, was prepared by me and published in

E. Leistenschneider *et al.*,- *Dawning of the $N = 32$ Shell Closure Seen through Precision Mass Measurements of Neutron-Rich Titanium Isotopes* - Physical Review Letters 120, 062503 (2018).

A second article containing further experimental details and results with vanadium isotopes was published in

M. P. Reiter *et al.,- Quenching of the $N = 32$ neutron shell closure studied via precision mass measurements of neutron-rich vanadium isotopes* - Physical Review C 98, 024310 (2018).

Appendix A describes a proof-of-principle experiment on the Decay and Recapture Ion Trapping technique and subsequent data analysis and simulations. The experiment was performed with R. Klawitter, M. Alanssari, J. C. Bale, B. R. Barquest, U. Chowdhury, A. Finlay, A. T. Gallant, B. Kootte, D. Lascar, K. G. Leach, A. Lennarz, A. J. Mayer, D. Short and A. A. Kwiatkowski. The data analysis was performed by me and R. Klawitter. The simulations presented were performed by me. The content of the appendix will form a future publication.

Appendix B presents the motivation and the design of the cryogenic upgrade to TITAN's Penning trap mass spectrometer. The motivation material presented in the first two sections is my original work and was previously published in

E. Leistenschneider *et al.,- Vacuum requirements for Penning trap mass spectrometry with highly charged ions* - Nuclear Instruments and Methods in Physics Research Section B: Beam Interactions with Materials and Atoms 0168-583X (2019).

The simulations and preliminary concept studies are also my original work. The design of the upgraded system was made by me and M. Good based on the original MPET design by V.L. Ryjkov. Performance tests and assembly of the system were performed together with M. Lykiardopoulou, C. Izzo, R. Steinbrügge, J. L. Tracy Jr., J. E. McKay, D. Fusco and M. Vansteenkiste. The unpublished part of this appendix will also form a future publication.

TABLE OF CONTENTS

LIST OF TABLES

LIST OF FIGURES

ACRONYMS

2N or NN 2-body (or Nucleon-Nucleon) interactions

3N 3-body Nuclear interactions

AME16 Atomic Mass Evaluation - 2016 edition

ARIEL Advanced Rare Isotope Laboratory

BNG Bradbury-Nielsen Gate

CERN European Organization for Nuclear Research

χEFT Chiral Effective Field Theory

ChPT Chiral Perturbation Theory

CPET Cooler Penning Trap

CryoMPET Cryogenic Measurement Penning Trap

CSRe Cooler Storage Ring

DRIT Decay and Recapture Ion Trapping technique

EBIT Electron Beam Ion Trap

EFT Effective Field Theory

FT-ICR Fourier Transform Ion Cyclotron Resonance technique

FWHM Full Width at Half Maximum

GGF self-consistent Gorkov-Green's Function

HCI Highly Charged Ions

HO Harmonic Oscillator

IMS Isochronous Mass Spectrometry

IMSRG In-Medium Similarity Renormalization Group

IPM Independent Particle Model (also known as Non-Interacting Shell Model)

ISAC Isotope Separator and ACcelerator facility

ISOL Isotope Separation On-Line method

ISOLDE Isotope Separator On Line DEtector facility

ITER International Thermonuclear Experimental Reactor

LEBIT Low-Energy Beam and Ion Trap facility

LO Leading Order

MCP Micro-Channel Plates detector

MPET mass Measurement PEnning Trap

MR-IMSRG Multi-Reference In-Medium Similarity Renormalization Group

MR-ToF-MS Multiple-Reflection Time-of-Flight Mass Spectrometer

MRS Mass Range Selector

NCSM No-Core Shell Model

NLO Next-to-Leading Order

NNLO or N^{2}LO Next-to-Next-to-Leading Order

OPEP One-Pion Exchange Potential

PI-ICR Phase-Image Ion Cyclotron Resonance technique

PLT Pulsed Drift Tube

PTMS Penning Trap Mass Spectrometry

QCD Quantum Chromodynamics

QED Quantum Electrodynamics

RF Radio-Frequency

RFQ Radio-Frequency Quadrupole cooler and buncher

RG Renormalization Group

RGA Residual Gas Analyzer

RIB Radioactive Ion Beam

RRR Residual Resistive Ratio

SCI Singly Charged Ions

SMILETRAP Stockholm-Mainz Ion Levitation Trap

SRG Similarity Renormalization Group

TFS Time Focus Shift

TITAN TRIUMF's Ion Trap for Atomic and Nuclear science

ToF-ICR Time-of-Flight Ion Cyclotron Resonance technique

ToF-MS Time-of-Flight Mass Spectrometry

TOFI Time-of-Flight Isochronous spectrometer

TRC Time-Resolved Calibration

TRILIS TRIUMF's Resonance Ionization Laser Ion Source

UHV Ultra-High Vacuum

VS-IMSRG Valence Space In-Medium Similarity Renormalization Group

ACKNOWLEDGEMENTS

In Portuguese, the word we use to express gratitude is *obrigado*. It is cognate to the English *obligated*: it implies recognition but also the establishment of a more profound commitment between the two parts. It is a graceful, warm, and thoughtful way to thank. And with that word, I sway the tone of my next few words.

In the preface, I have formally recognized the academic input of each person involved in the work of this thesis. But it is not enough. It ignores personal nuances and bonds required to forge such work. It disregards the friendship, the leadership, the conflict, the celebration, the anguish, the apprenticeship inherent of any human team. And, more than ever, scientific research is a collective business. We must never fail to acknowledge the importance of healthy teams to the success of Science.

Through those years, our team was led by Jens and Ania. Each at their own style, both advised me through the program — Jens as my academic advisor, Ania as the captain of the group's daily operations. I thank them for the guidance, the inspiration, the trust, and the freedom. Above all, I must acknowledge their will and of other TITAN principal investigators to foster a strong team, a safe learning environment, and a friendly atmosphere.

Aaron and Ania taught me their art of taming ions and performing mass spectrometry with Penning traps. And, with Julia, René, Marilena, James, and Chris, we were able to run the MPET mass spectrometer smoothly through all these years. I also acknowledge Renee, Pascal, Carla, Kyle, Dan, and all those smart and experienced young researchers who shared their expertise on the other ion traps at TITAN. I thank Mel for sharing his wisdom and providing creative solutions to our problems. Working alongside all those brilliant people deeply refined me as a professional.

I thank the companionship of all my group mates, Brian, Stefan, Eli, Ruben, Annika, the Andrews, Brad, Yang, Matt, Leigh, Jeff, Usman, Devin, Ish, Roshani, Abhilash, Killian, Zach, Tobias, Jon, Rio, and everyone mentioned previously. I thank you for all the mundane and scientific discussions, the laughs, the good and bad coffee, the unconditional support, and the joys of being surrounded by you all. I especially thank John, Danny, and Mike for trusting my guidance on their projects. I have learned a lot from our experience.

I also acknowledge TRIUMF and UBC staff and scientists for their support. In particular, I thank Jason, Sonia, and the members of my advisory committee: John, Reiner, and Gordon. They have shared their time, their expertise, taught me lessons, and had a genuine interest in my success. I also thank my colleagues back home, who encouraged me to pursue this program and kept encouraging me at a distance; with special thanks to Alinka, my former supervisor and friend.

I thank the affection shared with Bruno, Mateus, Carol, Acza, and Rogerio. Through these years, we sew our fabrics into one piece, taking caring of each other and fighting against homesickness. And above all, I must thank the love and support of my family, specially Taís and my parents, Mario and Emili.

I must also acknowledge the invisible work of those who invest in Science and advocate for it. This work was partially funded by Brazil's Conselho Nacional de Desenvolvimento Científico e Tecnológico (CNPq) through the Science Without Borders Program (grant $249121/2013-1$).

Obrigado implies the acknowledgment of a moral bond between the two parts. I expect this bond will be translated into the commitment to, wherever our career paths go, support research to our best extents, advocate for Science in our communities, help to build better academia, and foster healthy minds among our peers. But for now, to all of those that made this research possible, please, feel embraced.

1 INTRODUCTION

Physical Sciences' ultimate ambition is to understand nature through the precise language of mathematics. Therefore, increments on the predictive power of theories through enhanced calculation tools and refined models is the fundamental product of physicists' work.

One remarkable example of the outcomes of such endeavor is the theory referred to as Quantum Electrodynamics (QED), the quantum field theory of the electromagnetic force. It is currently known as the most successful theory in the field of physics, providing accurate predictions of humankind's most precise measurements of physical phenomena to date [1, 2, 3].

The outstanding predictive power of QED is a result of earlier developments of electromagnetism and quantum mechanics, but it is not the only result. Nowadays, the modeling of complex molecular processes derived from the very first principles of the same scientific framework is widely and routinely applied in chemistry, molecular and solid-state physics, pharmaceutical sciences, material development and nanotechnology [4, 5, 6].

Nuclear science, the field describing phenomena involving the "strong" force, still does not have the same fortune. After more than one hundred years of studying the atomic nucleus, we are still seeking a theory that explains the behavior of all nuclear matter. Theoretical frameworks derived from fundamental principles, also known as *ab initio* (*i.e.* "from the beginning", in Latin), are already a reality in nuclear sciences. However, they are far from having a similar success as in electromagnetism. If developed, they could have an enormous scientific and technological impact. Not only by enabling the development of reliable models for applications, such as in medical imaging, radiopharmaceuticals, energy generation and radioactive waste management, but also accurate understanding of the behavior of nuclear matter may fill critical missing pieces in our understanding of the origin of elements [7], of the origins of life [8, 9] and of other fundamental subatomic interactions [10].

The story of this thesis is the story of another piece in our ongoing collective quest to paint such an unerring mathematical portrait of the atomic nucleus. I describe our efforts to provide precision mass spectrometry data of very rare isotopes that are of high value to understand particular nuclear structure behaviors. The new data is used to evaluate the performance of a few state-of-the-art nuclear *ab initio* theories. Ultimately, we give guidance on which approaches are best suited to explain the data and where they must be improved.

In this introductory chapter, I start with a short overview of the research on nuclear interactions and how we arrive at the current methods of describing nuclear matter from first principles. Then, I motivate the need for mass spectrometry data and its intimate relationship with the study of the nuclear structure, focusing on the specific behaviors that are relevant to this study. Finally, I conclude the chapter stating our research goals and achievements, and by giving an overview of the structure of the remainder of the thesis.

1.1 A Brief History of the Nuclear Force

In 1911, E. Rutherford and his team impinged a gold foil with alpha particles and observed a tiny fraction of them bouncing back. This observation led to an important interpretation of the structure of an atom: that most of its mass and all of its positive charge is concentrated in a diminute fraction of its volume [11]. This structure located at the core is called the *nucleus* of an atom, and this experiment was considered the birth of nuclear science.

Concurrently, studies in chemistry and on the nature of radioactivity had already shown that several chemical elements would present themselves in different atomic weights [12], always approximately a multiple of the mass of a hydrogen atom. The different mass species of the same chemical element were called different *isotopes*.

By 1920, it had been postulated that the nucleus inside of all isotopes would be formed by combinations of two "fundamental" nuclear particles [13], or *nucleons*. One was the nucleus of the hydrogen atom, called *proton*, which was a positively charged particle that defined the chemical properties of the atom. The other was a neutral counterpart of similar mass: the *neutron*. The discovery of the neutron in 1932 [14] marked the first triumph of this hypothesis and, nowadays, a proton-neutron model [15] of the atomic nucleus forms the basis of nuclear science.

Within such a model, however, the system consisting of protons and neutrons could not be stable based only on electrical forces. Protons would repel each other while the neutrons, transparent to electric fields, would drift away. Another force was needed to describe the interactions among nucleons. It needed to have the following features: be attractive, independent of electric charge, stronger than the electromagnetic force and short ranged, since no influence of it could be felt outside of the nucleus.

One of the first postulations for such *nuclear force* was made by H. Yukawa in 1934 [16]. He proposed that the nuclear potential (V_{Yukawa}) arising from a nucleon had a similar form to the Coulomb electric potential, but it was strictly attractive with an exponential "screening" factor to modulate its range:

$$V_{\text{Yukawa}}(r) = -g^2 \frac{e^{-\mu r}}{r} \quad , \tag{1.1}$$

where r is the distance from the generating particle, g is a coupling constant and μ is a screening factor known as Yukawa mass. The addition of this screening factor implied the existence of a "mediating" particle of mass around 100 MeV/c^2, later discovered by C. Lattes and colleagues [17] and named *pion*.

Subsequent studies, mainly arising from nucleon-nucleon scattering experiments, revealed further details about the properties of the nuclear force and proposed updated versions for the nucleon-nucleon potential [18]. Some of the found remarkable behaviors are the dependence on the intrinsic angular momentum (or *spin*) of the nucleons [19, 20] (e.g. spin-orbit coupling and pairing), the dependence on the spin orientation [21] (tensor nature) and even a slight breaking of the charge independence [22, 23].

The inner mechanisms of the nuclear force were finally unveiled in 1969. A series of electron-proton scattering experiments revealed clear evidence of internal structure in the proton at energies above 1 GeV [24, 25]. The proton lost its status as a fundamental particle, giving way to a *quark* model [26, 27] to explain the structure of protons, neutrons, pions and many other particles that had already been discovered by that time.

The quark model described protons and neutrons as composite particles of three quarks of types *up* (u) and *down* (d): uud for protons and udd for neutrons. The pion, on the other hand, is formed by a ud pair. Within the theory of Quantum Chromodynamics (QCD), those particles are bound together by the action of the so-called *strong interaction*. In very general terms, each quark carries one of three types of *color charge* (hence *chromo*), an analog of the electric charge (which has two types). The interaction between particles of different color charges is mediated by a massless particle called *gluon* [28], which has a similar role as the *photon* in QED.

Over the last decades, significant experimental evidence has shown support of the quark model and QCD theory. Nowadays, they form an essential part of what is now accepted as the *Standard Model* of particle physics [29]. Although the nature of the strong force is still subject to a very active research field, here we are interested in how its inner workings affect the structure of nuclear matter.

After the emergence of QCD, the nuclear force has been interpreted as a residual strong force, similarly as the Van der Waals forces are residual electromagnetic forces acting among neutral molecules. However, a direct derivation of nuclear forces from QCD is complicated since the techniques typically employed in quantum field theory (mainly from perturbation theory) cannot be applied in the energy regime of nuclear phenomena. The description of nuclei from QCD is even harder due to its many-body nature.

In the late 1980's, effective field theories (EFT) started to be applied to QCD in the energy regimes of nuclear physics. In those approaches, approximations are performed to compute only the physical phenomena relevant to the energy scales of the system of interest. The simplification brought by those techniques finally opened the doors for nuclear *ab initio* calculations.

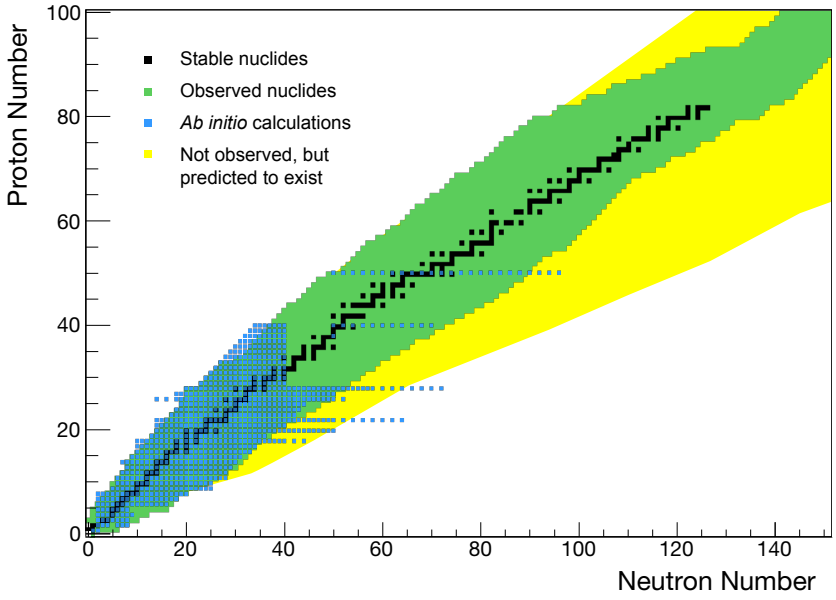

Figure 1.1: Chart of nuclides showing the nuclei observed so far (green, and black for the stables). Nuclei whose properties have been calculated through *ab initio* methods up to 2017 are marked in blue (from [30]). The regions where nuclei are believed to exist within the drip lines are marked in yellow.

Since then, calculation techniques and EFT-based descriptions for nuclear interactions have been evolving. At the current stage, properties from simple and light nuclear systems (up to a few tens of nucleons) are currently well reproduced. Figure 1.1 shows all nuclei whose properties were calculated through those *ab initio* methods up to 2017 [30]. However, those methods are computationally costly; thus the interplay between theory and experiment is crucial to pinpoint key behaviors, select successful approaches and benchmark whether the embedded assumptions and approximations, when performed, are appropriate. As nuclear science advances side-by-side to technological improvements in computing, larger and more complex systems are being tackled [31].

1.2 Atomic Nuclei and Mass Observables

The atomic nucleus is a particular form of nuclear matter. It is a quantum many-body system about which we want to answer questions like: What combinations of protons and neutrons can form a nucleus, and where are the limits? How do protons and neutrons behave collectively? How do the properties of the nuclear force influence those behaviors? Or, can we accurately predict the properties of nuclei that are barely accessible through experiments or even beyond our reach?

To answer those questions, we need to inspect observables[1] of nuclei and study how do they evolve as we look at different nuclear systems. Our body of knowledge revolves around the observations of about 3000 different nuclei (see figure 1.1) [32]. About 300 of them are available on Earth's crust, while the remaining must be produced in specialized facilities. Meanwhile, another few thousands of nuclei are also predicted to exist according to some models, but many of them may never be experimentally accessible.

Among all properties, the atomic mass is perhaps the most fundamental observable. It reflects the net energy content of the system, including not only the mass of all individual constituents but also the effects of the bonding agents acting among them. These effects result in what we call the *binding energy* (E_B). The mass of a neutral atom (m_a) whose nucleus contains N neutrons and Z protons is expressed in this form[2]:

$$m_a(N,Z) \;=\; Z\cdot m_p \;+\; N\cdot m_n + \; Z\cdot m_e \;+\; \frac{E_B(N,Z)}{c^2} \qquad , \tag{1.2}$$

where m_p, m_n and m_e are the masses of the proton, the neutron, and the electron, respectively (c is the speed of light).

The Bethe–Weizsäcker mass formula [33] beautifully illustrates the concept of binding energy. It was one of the earliest attempts to model the effects that contribute to the binding energy and, consequentially, to infer properties of nuclear matter. It is based on a very simple model of the nucleus:

$$E_B(A,Z) \;=\; -a_V A + a_S A^{2/3} + a_C \frac{Z^2}{A^{1/3}} + a_A E_A(A,Z) + a_P E_P(A,Z)\,. \tag{1.3}$$

Here, it is expressed in terms of the atomic (Z) and mass ($A = Z + N$) numbers. The coefficients a_V, a_S, a_C, a_A, a_P are determined through a fit to the available data.

The first term accounts for the bulk effect of the nuclear force and is the only exclusively binding term. It incorporates the same characteristics of the nuclear force that inspired the Yukawa potential: charge independence and short-ranged nature. It assumes that the total binding from nuclear forces will be proportional to the total number of nucleons (A) because each nucleon will only interact through nuclear force with its nearest neighbors. The second term, however, accounts for nucleons at the surface of the nucleus, which have fewer neighbors to interact with. The binding is decreased by a factor proportional to the number of nucleons in the surface ($\approx A^{2/3}$).

These very first two terms make one remarkable assumption about the overall structure of a nucleus: it behaves like a drop of an incompressible fluid, and the terms may be interpreted as volume and surface tension contributions, respectively. Experimentally, it is known that nuclear matter has a constant density of about 0.17 nucleons/fm^3 (called *nuclear saturation density*), which supports this assumption.

1 Observables are physical properties that can be measured, such as mass, spin, radius, etc.

2 The binding energy, as presented in equation 1.2, accounts for both the binding energy of the nucleons to the nucleus and the electrons to the atom, although the latter is much more weakly bound than the former.

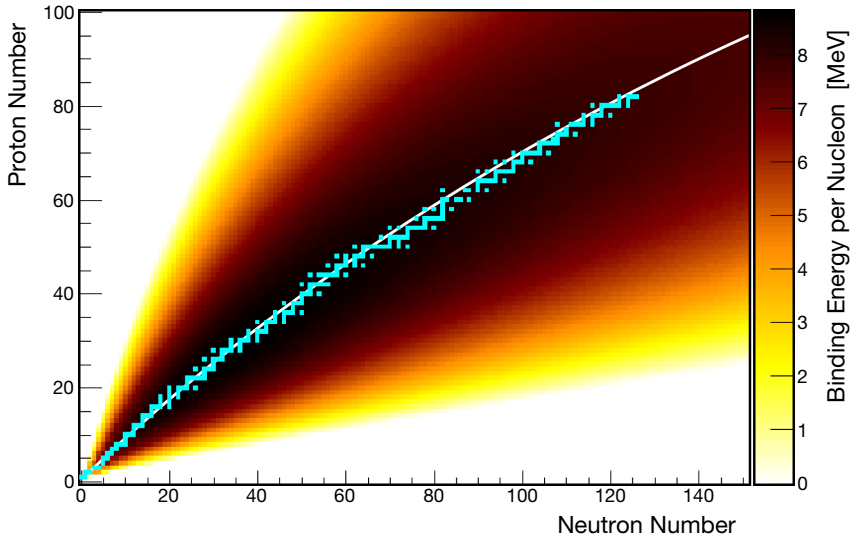

Figure 1.2: Nuclear chart showing the binding energy per nucleon calculated through the Bethe–Weizsäcker formula (eq. 1.3). The white curve connects the predictions for most bound nucleon for every mass number, which has overall good agreement to the actual location of the stable nuclides, marked in light blue.

The third term accounts for the Coulomb repulsion between protons and therefore causes a loss in binding energy. Quantum mechanical effects associated with Pauli's exclusion principle, which states that identical half-integer spin particles cannot occupy the same quantum state, are accounted for in the last two terms (E_A and E_P). Their interpretation and detailed form were modified and adjusted over the decades since their first inception.

The approach of the Bethe–Weizsäcker formula is surprisingly successful given its simplicity. It correctly predicts E_B/A within 0.5 MeV/u for the vast majority of the known nuclides. It reproduces overall trends and bulk properties of nuclear matter such as the quadratic behavior of masses of isobars[3], the overall shape of the stability line[4] (see figure 1.2) and the location of the most bound nucleus in the nuclear chart.

Albeit this liquid drop model brings an enlightening understanding of the nature of nuclear matter, it fails to describe some details. It strictly considers the nucleus as spherical without accounting for possible deformations, neither it is capable of giving any insight into other essential observables, such as nuclear spins and radioactive half-lives. Yet, the most noteworthy limitation of this model is its failure to explain the emergence of *magic numbers*.

Magic numbers are special numbers of nucleons that are common to nuclei with exceptional stability. One way of seeing them is by inspecting the energy necessary

3 A set of isobars is a set of nuclides with the same number of nucleons, also referred to as with same mass number (A).

4 The stability line is a reference line that virtually connects the stable nuclei at the nuclear chart, marked as light blue in figure 1.2.

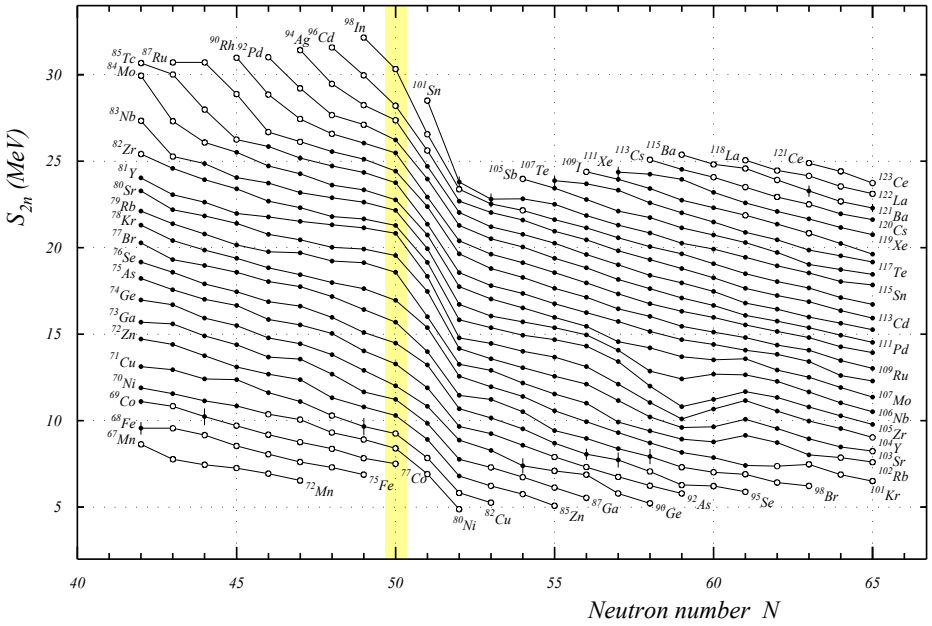

Figure 1.3: The two-neutron separation energies between $N = 42$ and $N = 65$, adapted from [34] (full circles are based on measured data, while open circles include mass extrapolations). The magic number $N = 50$ is evident from a sudden break of the smooth trend for all isotopic chains.

to break nucleus apart in two or more nuclear systems. Here, we look at the two-particle separation energies for neutrons (S_{2n}) or protons (S_{2p}):

$$S_{2n}(N,Z) = m_a(Z,N-2) + 2m_n - m_a(N,Z) \quad \text{and} \tag{1.4}$$

$$S_{2p}(N,Z) = m_a(Z-2,N) + 2m_p - m_a(N,Z) \quad , \tag{1.5}$$

which are simply given by mass differences between atoms. Evidences of magic numbers can also be noticed in several other separation energies, such as one-proton separation energy or one-alpha separation energy, but are clearer and more prominent in S_{2n} and S_{2p}.

An example of how S_{2n} evolves across isotopic chains is shown in figure 1.3. As can be seen, S_{2n} exhibit a general smooth trend, until a sudden decrease is observed right after crossing the $N = 50$ mark, consistently found in all isotopic chains. This means that additional pairs of neutrons to any nucleus with 50 neutrons will be considerably less bound.

Another way of looking at those effects is through the "derivatives" of the two-particle separation energies (Δ_{2n} for neutrons, Δ_{2p} for protons), often called *Empirical Shell Gaps*, through which special patterns are brought into relief:

$$\Delta_{2n}(N,Z) = S_{2n}(N,Z) - S_{2n}(N+2,Z) \quad \text{and} \tag{1.6}$$

$$\Delta_{2p}(N,Z) = S_{2p}(N,Z) - S_{2p}(N,Z+2) \quad . \tag{1.7}$$

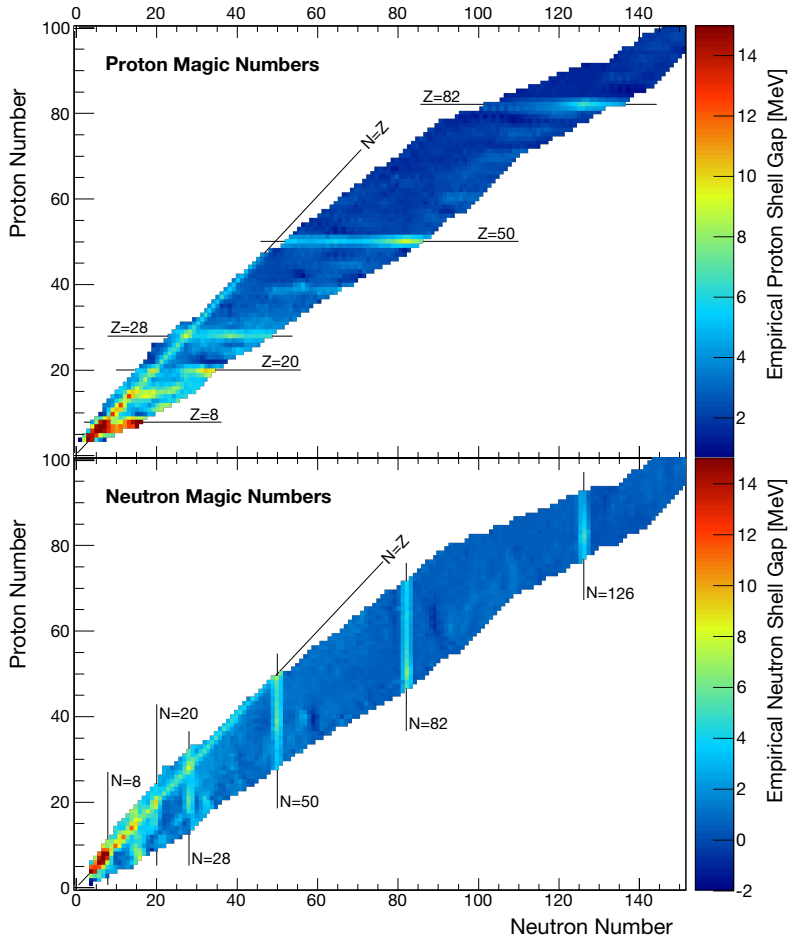

Figure 1.4: Empirical shell gaps across the nuclear chart for protons (top) and neutrons (bottom), calculated from the mass data of [34]. This representation makes the locations of magic numbers evident as a few specific isotonic and isotopic chains get much "brighter" than their neighbors.

Figure 1.4 shows Δ_{2n} and Δ_{2p} for all known nuclei. It makes evident the special patterns occurring at nucleon numbers 8, 20, 28, 50, 82 and 126, for either protons and neutrons.

Nuclei that lie in those magic regions are not only more bound than their neighbors; they also exhibit a collection of other special properties. They are generally more compact nuclei (have smaller charge radii, for example) [37], they tend to offer more resistance to the absorption of nucleons (smaller neutron absorption cross-section, for example) [38] and typically require much higher energy to be promoted to an excited state [36]. Figure 1.5 gives a few examples of the behavior of such observables around the same magic numbers identified previously.

Historically, the term "magic" referred to the lack of plausible explanation (up to mid-1940s) on why particular numbers of protons or neutrons would grant nuclei such unique properties. To understand the origin of such particular behaviors, it is necessary to take a more detailed look at the individual interactions between nucle-

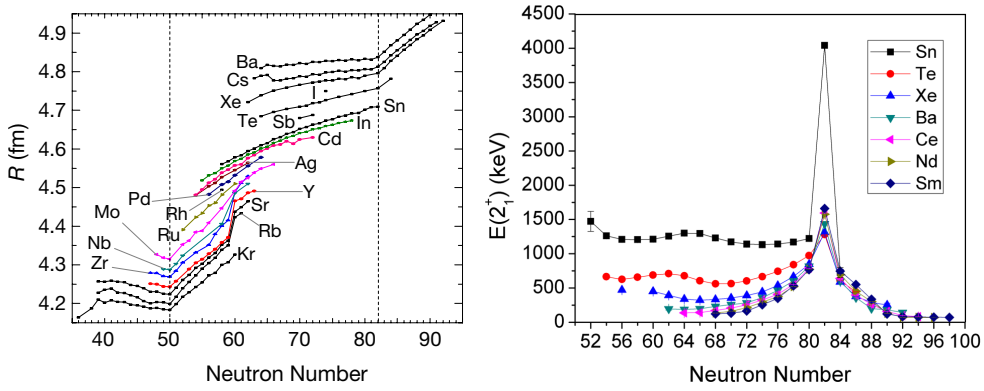

Figure 1.5: Magic properties seen in other nuclear observables: (left) charge radii across isotopic chains of Kr to Ba, "kinks" are seen in $N = 50$ and $N = 82$ (adapted from [35]); and (right) the excitation energy to the first 2^+ state ($E(2_1^+)$) of even-even nuclei for Sn to Sm isotopes (adapted from [36]). A sharp increase is seen at $N = 82$, also Sn isotopes are all proton-magic ($Z = 50$) and exhibit greater overall $E(2_1^+)$. Experimental details can be found in the original references.

ons than what the liquid drop model can provide. For this purpose, several other theoretical approaches have been developed. The earliest was the very successful *Nuclear Shell Model* [39], which is briefly introduced in the next section.

1.3 The Nuclear Shell Model in a Nutshell

Since its initial formulation in the late 1940s [39], the Nuclear Shell Model has been very successful in providing intuitive explanations to complex nuclear structure phenomena. It has proved to be an extremely powerful theoretical tool and is still being employed and further developed. In this section, a simplified version is presented. It is closer to the earlier variants of the model, which is currently called *Independent Particle Model* (IPM) or *Non-Interacting Shell Model*. Introductions to more modern views can be found in [40] and, in more detail, in [41].

The inspiration for the Nuclear Shell Model came from an analogy to the atomic shell model, which provides rules for the structure of electrons in an atom. Like atoms, nuclei are also many-body fermionic systems, which means their constituents must follow the Pauli exclusion principle. Experimentally, atoms of "closed" electron shells share many properties with magic nuclei: compactness, boundness, and inertness, suggesting that magic nuclei may correspond to closed nuclear shells.

The IPM supposes every nucleon is moving independently through the nucleus under a mean-field potential (V) created by the remaining nucleons. The shape of such potential may be, for example, square wells, harmonic oscillators or the so-called Wood-Saxon [42] potential. They will all generate a shell-like structure. However, the correct reproduction of features corresponding to magic numbers could only be achieved by the introduction of a spin-orbit term $\vec{\ell} \cdot \vec{s}$, where $\vec{\ell}$ and $\vec{s}$ are

angular momentum and spin operators, respectively. One example form for this potential is:

$$V(r) = \frac{m}{2}\omega^2 r^2 - V_{oo}\,\vec{\ell}^{\,2} - V_{so}\,\vec{\ell}\cdot\vec{s} \quad , \tag{1.8}$$

where r is the distance from the nucleon to the center of the nucleus, m is the mass of the nucleon, and ω is the harmonic oscillator's frequency. V_{oo} and V_{so} are the potential strengths of their respective terms.

Solving the Schrödinger equation using this potential results in discrete eigenstates that are degenerate with respect to the set of quantum numbers $[n, \ell, j\,]$, where n is a principal quantum number, ℓ is an angular momentum (or orbital) quantum number and j is a total angular momentum number. The latter comes from the spin-orbit interaction and comprises the sum of angular momentum between the nucleon spin and its orbital angular momentum. The degree of degeneracy (or how many particles may occupy the same energy level) is given by $(2j+1)$.

The energy level structure obtained is shown in figure 1.6. Every level is labeled according to the spectroscopic notation: the first number corresponds to n, the following letter indicates the orbital angular momentum (s corresponds to $\ell = 0$, p to $\ell = 1$, d to $\ell = 2$, and so on...), and the last number indicates the total angular momentum j. Indexes π and ν are often added to the spectroscopic notation to differentiate proton shells from neutron shells, respectively.

To get the ground-state configuration of a particular nuclide, one can fill those levels according to the requirements of the Pauli exclusion principle. As one level is "full" (it has the maximum number of nucleons allowed by its degree of degeneracy), it should form a "closed" configuration, a "closed shell".

In some cases the energy separation between some levels is minimal, forming clusters of quasi-degenerate states. However, the gap between a few particular levels happens to be quite large, and they can be associated with magic nuclei. For example, a nucleus with 50 neutrons will have every level up to the $1g_{9/2}$ full. An additional neutron to the system would be placed in a much higher energy level, $1g_{7/2}$, and therefore would be considerably less bound to the "core" nucleus. This neu-

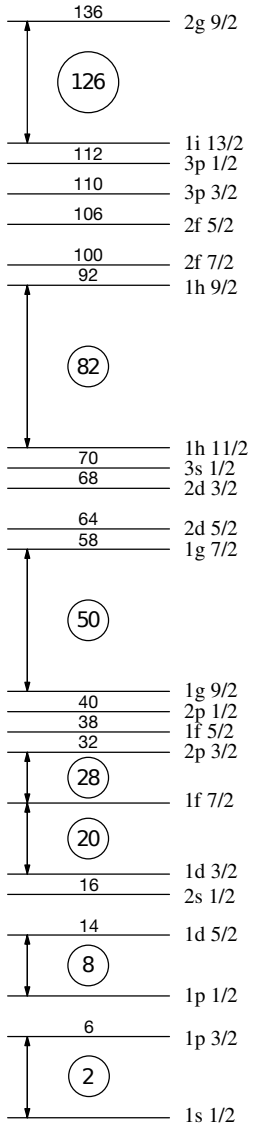

Figure 1.6: Shell structure obtained through the IPM. Each level contains the total number of nucleons occupying the nucleus up to that full level. The vertical arrows mark large energy separations, their occupation number (circled) is associated with magic numbers.

tron would be lying in a "valence shell" (or non-closed shell). This binding energy argument is consistent with the separation energy signatures of magic numbers.

Protons and neutrons fill their shell structures independently. Also, as nuclear forces act in a very similar fashion for both, their level structures are expected to be nearly identical too. As can be seen in figure 1.4, magic numbers are the same for protons and neutrons.

The IPM can correctly predict many nuclear properties of nuclei with configurations near those with closed shells but fails to describe properties far from them. The base assumption of the IPM (that nucleons move through the nucleus nearly independently) may only hold near closed shells.

In modern approaches of the Nuclear Shell Model, nucleons in valence shells are allowed to interact, while nucleons in the core ("inner" levels) remain inert. *Residual interactions*, originating from nuclear forces between nucleons in the valence space, also play a role in the nuclear potential. This *Interacting Shell Model* approach has close ties to development of *ab initio* methods, as presented in chapter 2.

1.4 Not-so-Magic Numbers

At a glance, "magic" properties seem to be sturdy, consistent, and indifferent to the counterpart nucleon number. It seems to make sense since protons and neutrons are distinguishable fermions; therefore, they are expected to have their own internal arrangement rules without affecting each other.

Nevertheless, this picture only holds near stable nuclei. A closer inspection of figure 1.4 reveals interesting effects around the boundaries of the known mass surface. For example, the Δ_{2p} strength of $Z = 82$ slowly fades away as the neutron number decreases. The Δ_{2n} strength of $N = 20$ and $N = 28$ abruptly quenches at low proton numbers. Meanwhile, a weaker but consistent effect seems to emerge at $Z = 40$ as the neutron number increases, and stronger effects appear to be emerging at $N = 16$ and $Z = 14$.

As experiments are able to access increasingly unstable species, we find large deviations from the "canonical" (well established) magic numbers. Some magic numbers seem to vanish, with evidences for that observed at nucleon numbers 8 [43], 20 [44], 28 [45] and 82 [46]. Meanwhile, the appearance of magic-like features is seen at nucleon numbers 14 [47], 16 [48], 32 [49], 34 [50] and 40 [51].

1.4.1 The New Magic Number 32

Particular attention has been given to the emergence of strong magic properties among nuclides with 32 neutrons, on the neutron-rich side of the stability line. The region of interest encompasses nuclei like ^{56}Cr, ^{55}V, ^{54}Ti, ^{53}Sc, ^{52}Ca, ^{51}K and ^{50}Ar. Evidence of magicity starts appearing at ^{56}Cr ($Z = 24$), and it builds up with decreasing proton number. The strength of the effects appears to peak at Ca, which

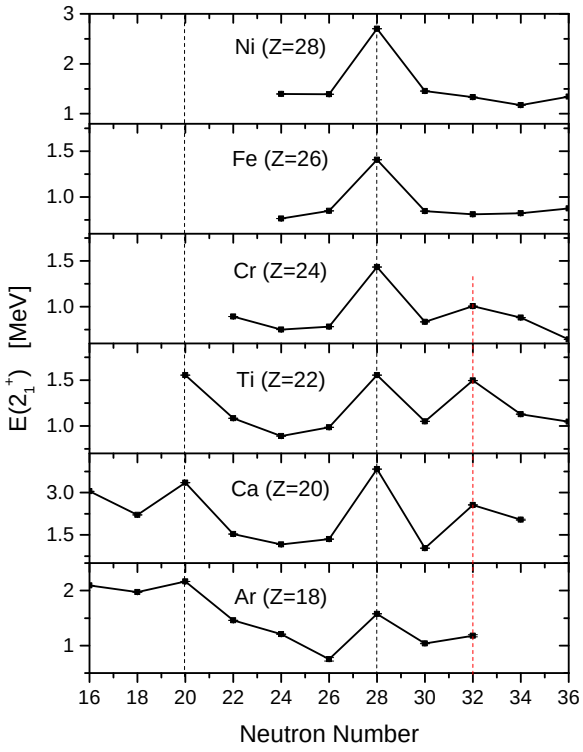

Figure 1.7: Excitation energy to the first 2^+ state of even-even nuclei for Ar to Ni isotopes. Data shows clear enhancement pattern of $E(2_1^+)$ in the canonical magic numbers 20 and 28, and the emergence of similar behavior in $N = 32$ is also seen in $Z \leqslant 24$. Data from [54].

is also proton-magic ($Z = 20$), although very little data exist in this region beyond potassium and argon ($Z < 19$).

The first theoretical [52] and experimental [53] hints that $N = 32$ could be a magic number date back to the early 1980s, with the discovery of a larger than expected first excitation energy of ^{52}Ca. However, just recently experimental facilities were able to perform detailed studies in the region with the increase in isotope production yields.

The current spectroscopic data on first excitation energies $E(2_1^+)$ of even-even nuclei are shown in figure 1.7 for the region of interest. The signatures of magic numbers 20 and 28 are clearly seen as the $E(2_1^+)$ peaks in those neutron numbers. Meanwhile, the data also show a relative, but systematic, increase in $N = 32$ below proton number $Z = 24$, being completely absent otherwise.

Since 2012, mass spectrometry facilities have been able to study this region with high precision. The current mass data indicate behaviour associated with magic signatures at $N = 32$ in the K [55], Ca [56, 49] and Sc [57] isotopic chains. It is evident in the S_{2n} systematics shown in figure 1.8. In contrast, the S_{2n} surface

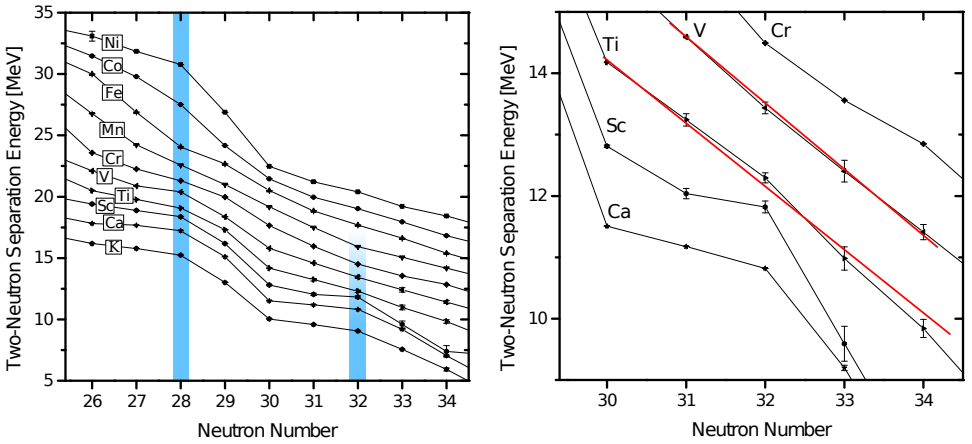

Figure 1.8: S_{2n} surface: left panel provides a broader view in the surroundings of the interest region, showing the presence of magic properties at the canonical $N = 28$ and the appearance of magicity at $N = 32$, both marked in blue; right panel shows a zoomed in view of the $N = 32$ interest region, with linear fits (red) showing the compatibility of smooth trend (absent magicity) in Ti and V chains. The mass data was taken from [34].

is smooth in this region for V and beyond, indicating the absence of magicity, in agreement with spectroscopic data.

However, there are still many missing pieces on our knowledge about the evolution of magic properties in $N = 32$. For instance, the picture at the intermediate Ti chain is unclear; presently available mass data point towards the existence of modest magicity, but the uncertainties are not sufficiently small to reveal detailed information. The data is compatible with the absence of any magic character, as evidenced by the fit shown in the right panel of figure 1.8.

Also, most of the data on Ti and V isotopes in the region comes from low-resolution or indirect mass measurement techniques, and large deviations have been observed in their vicinity after measurements were performed using high-resolution techniques [56, 57, 58, 34]. These issues make this region very appealing to be further studied through mass spectrometry.

Meanwhile, a recent laser spectroscopy measurement of ^{54}Ca revealed its unexpectedly large charge radius [59]. If $N = 32$ is a true magic number in this region, ^{54}Ca ($Z = 20$) is expected to be a doubly-magic nucleus (magic in both neutron and proton numbers), which typically have greatly enhanced closed-shell features[5]. The result of this laser spectroscopy experiment challenges its doubly-magic nature since it is expected to be a more compact nucleus. However, this is the only charge radius measurement in the $N = 32$ isotonic chain so far.

5 See, for example, ^{132}Sn ($N = 82$, $Z = 50$) in right the panel of figure 1.5.

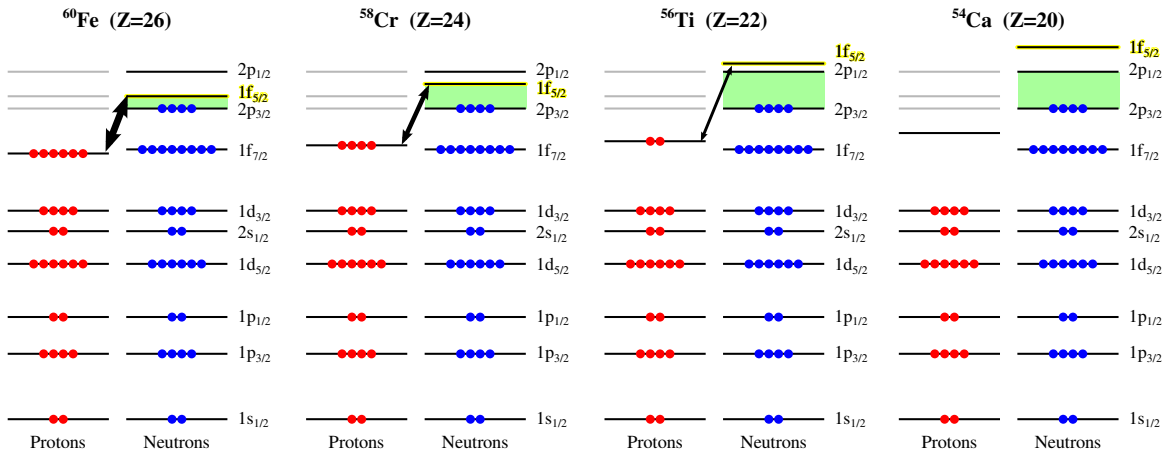

Figure 1.9: Shell evolution of $N = 32$ isotones showing the appearance of magicity at this neutron number as the proton number decreases. The strength of the proton-neutron residual interaction between $\nu 1f_{5/2}$ and $\pi 1f_{7/2}$ orbitals is represented by the thickness of the arrows connecting them. The weakening of this interaction shifts the $\nu 1f_{5/2}$ level and increases the energy gap (in green) from the $\nu 1f_{7/2}$ level.

1.4.2 A Test Bench for Nuclear Theories

Since most of the nuclear models were originally conceived and constrained with data around the stability line, the behaviors that emerge at the extremes of the nuclear chart pose a challenge to nuclear theory. Structural evolution around canonical and non-canonical magic numbers motivated several important updates to nuclear interactions [60, 61, 62, 63].

For example, the magicity in $N = 32$ and $N = 34$ has been investigated in a Shell Model framework (see [50] and references therein). The $N = 32$ is considered as a full valence $\nu 2p_{3/2}$ orbital, which is energetically close to the $\nu 1f_{5/2}$ orbital. This quasi-degeneracy among orbitals prevents the appearance of shell signatures. The emergence of magicity at $Z \leqslant 24$ has been attributed to the weakening of attractive proton-neutron residual interactions between the $\nu 1f_{5/2}$ and $\pi 1f_{7/2}$ orbitals. As $\pi 1f_{7/2}$ empties, the neutrons in $\nu 1f_{5/2}$ become less bound. Due to that, the $\nu 1f_{5/2}$ and $\nu 2p_{1/2}$ orbitals would change their energy order between V and Sc, which has been supported by spectroscopic data [64]. A large energy gap between $\nu 2p_{3/2}$ orbital and the next level would emerge, breaking the local quasi-degeneracy of levels and causing the appearance of magic-like features. A representation of such shell structure evolution is shown in figure 1.9. The mass and spectroscopy data in the region allowed refinements of the proton-neutron residual interactions between those orbitals.

The $N = 32$ region is especially interesting in the context of nuclear *ab initio* theories. Not only due to the interesting emerging phenomena, but also because they occur near the current limit of the reach of these techniques. Although a few *ab initio* methods were able to calculate properties of systems as heavy as $^{100-110}$Sn [65] and ^{132}Sn [66], those lie along magic numbers which permit certain controlled

approximations (see discussion in chapter 2), but may not be applied to all systems in the region[6]. On the other hand, nuclides up to mass $A \approx 50$ are among the heaviest systems that have been accessible and that are well within reach of several *ab initio* theories [30, 68], as can be seen in figure 1.1.

1.5 Scientific Goals

There is a high demand for precision data to further explore the evolution of the magicity in $N = 32$. At first glance, charge radii data on other isotones are required to inspect trends from the anomalous behavior seen in calcium. Also, pushing mass and spectroscopic information further in the low-Z direction, starting from argon, is essential to determine whether the magicity vanishes or persists. Likewise, to finely understand the emergence of such effects at the high-Z frontier, precise experimental determination of the mass surface around titanium is required.

However, except for Ca and K, isotopes of other elements in the $N = 32$ region are not easily produced or experimentally accessible in many facilities (see discussion in chapter 4). Therefore these studies may greatly benefit from the development of high sensitivity experimental techniques and new isotope production methods.

In this study, our team was capable of creating samples of very neutron-rich titanium isotopes for the first time at the TRIUMF laboratory in Vancouver, Canada, and of performing precision mass spectrometry in the $N = 32$ region.

Although identifying shell effects in mass observables can be typically achieved with a precision of hundreds of keV/c^2, titanium is at a transition point where such effects may be very small. Thus, pinpointing detailed magic signatures may require precisions better than 50 keV/c^2. Additionally, the studied isotopes were expected to be produced as rarely as a few per minute, accompanied by large amounts of co-produced contamination.

Fortunately, the studies were possible due to the availability of a novel mass spectrometry technique: the Multiple-Reflection Time-of-Flight Mass Spectrometry (MR-ToF-MS), which had been recently commissioned at TRIUMF's Ion Trap for Atomic and Nuclear science (TITAN) facility [69]. This technology, employed only in a few laboratories so far, is very sensitive and can distinguish isotopes of interest from contamination species while providing enough precision to resolve the ambiguities of the existence of magic effects in titanium.

Masses of titanium isotopes between ^{51}Ti and ^{55}Ti were successfully measured with the MR-ToF-MS. The technique was also used to determine vanadium masses between ^{51}V and ^{55}V that were also present in the sample. The results confirm the existence of mild shell effects in titanium and their absence in vanadium, narrowing down the exact emergence of magicity of $N = 32$ from mass observables.

As this was the first time the MR-ToF-MS technique was employed at TRIUMF, we confirmed these results by performing the same mass measurements independently

6 For example, attempts to perform calculations of properties of ^{125,127,129}Cd did not succeed [67]

at a well established mass spectrometer: TITAN's Mass measurement PEnning Trap (MPET). Although the MPET is a more precise mass spectrometer, its sensitivity is reduced, and its tolerance to contaminants in the sample is more restrictive. Therefore, only the masses of $^{51-53}$Ti were measured. Nevertheless, measurements performed with both spectrometers agreed very well and allowed us to benchmark the MR-ToF-MS technique.

With a more complete picture of the evolution of magicity of $N = 32$ in hand, we challenged four state-of-the-art nuclear *ab initio* theories. Overall, all tested theories perform well reproducing the mass surface in this region, but our work reveals a few systematic deficiencies, such as an overprediction of the Δ_{2n}. This new set of data may help in guiding the development of the next generation of *ab initio* theories and nuclear forces.

In the next chapter, I will give a more in-depth overview of nuclear *ab initio* methods, focusing on the theories that were tested against our data. An overview of mass spectrometry is given in chapter 3, with emphasis on the two mass spectrometry methods used. In chapter 4, I will present the experimental procedure employed, from the production and manipulation of the isotopes to the measurement procedures. The results of the studies with each mass spectrometer are presented in chapter 5, while their comparison and interpretation, as well as the updated picture on the evolution of shell effects in $N = 32$ and its comparison with the *ab initio* theories are presented in chapter 6. Finally, my conclusions and outlook are given in chapter 7.

2 | *AB INITIO* NUCLEAR THEORY

Ab initio is a Latin expression for "from the beginning". In physics, it is used to designate theoretical approaches that describe phenomena "from the ground up", based solely on the most fundamental principles. It differs from phenomenology, whose goal is to describe phenomena as accurately as possible without necessarily having ties to fundamental grounds.

In nuclear physics, the Liquid Drop Model and the Independent Particle Model (presented in chapter 1) are good examples of phenomenological models. In both cases, a model for the nucleus is made from a set of hypotheses about the behavior of nuclear matter, and parameters of the model are adjusted to fit experimental properties. The nucleus is treated in a "mean-field" approach, where the whole dynamics inside the nucleus is averaged and simplified.

Phenomenological models are very useful providing intuitive explanations for complex phenomena, and they can be very accurate within the data range that is used to fit them. However, one has very little control over the limits of validity of these models. Typically their results significantly diverge in regions where data is scarce and cannot provide enough constraints. There is no means to control or to estimate their accuracy passing these regions.

Thereon lies the strength of nuclear *ab initio* approaches. Ideally, if one can build up atomic nuclei from QCD without parameters fitted to experimental nuclear quantities, properties of any nucleus could be accurately calculated or predicted independently of the nuclear data available.

Instead of a mean-field treatment, *ab initio* theories study nuclei microscopically. They account for the contribution of every constituent and their interactions. Ideally, these constituents and their interactions should be handled on the most fundamental quark-gluon level. However, as mentioned earlier, QCD is non-perturbative in the energy ranges of nuclear physics, and only a few simple nuclear physics problems have been tackled at that level (for example, [70]).

Therefore, modern-day nuclear microscopic methods still build nuclei from the nucleon-meson level. The interactions employed, however, are built keeping their ties to QCD through an Effective Field Theory (EFT). Truncations and approximations are often necessary, but the theoretical framework offers means to control and estimate their impact on accuracy. Although they are not directly derived from QCD, we still refer to such theoretical treatments as *ab initio*. This chapter is dedicated to providing an overview of how they are constructed and how they can benefit from experimental input.

2.1 Construction of a Microscopic Nuclear Theory

A generic microscopic description of a nucleus allows one to compute the interactions among nucleons considering them as the fundamental constituents of the many-body system. It searches for the solution of the A-body Schrödinger equation:

$$\left(\sum_{i}^{A} \frac{{p_i}^2}{2m} + V\right) \Psi = \varepsilon \Psi \quad , \tag{2.1}$$

where p is the momentum operator, m is the nucleon mass, Ψ is the many-body wave function, V is the nuclear potential and ε is the eigenenergy associated with Ψ. The eigenvalues ε are the objects of interest here since they are connected to the mass of the system, but other nuclear observables may also be extracted from Ψ.

The nuclear potential V has to reflect all the interactions among participating nucleons, including the strong interaction and the Coulomb interaction for protons[7]. It may be constructed using phenomenological approaches or, as has become common recently, using an effective field theory of the QCD.

Generically, the potential may be written as

$$V = \sum_{i<j}^{A} V_{i,j}^{2N} + \sum_{i<j<k}^{A} V_{i,j,k}^{3N} + \sum_{i<j<k<l}^{A} V_{i,j,k,l}^{4N} + ... + V_{i,j...}^{AN} \quad , \tag{2.2}$$

which explicits the different n-body components of the potential. In most approaches nowadays, this potential is truncated to include up to 3-body (3N) forces. A brief introduction to how nuclear interactions are built is given in section 2.3.

It is worth noting that 1-body potentials, like the one presented in equation 1.8, are not included. In phenomenological approaches, such potentials are often used to describe a "mean-field": a simplified potential that represents the average of the interactions with the other particles in the system. This approach diverges from the *ab initio* philosophy.

We also require a method to construct the many-body wave functions and to solve the many-body system correspondingly. For simplicity, many-body states are typically constructed as a product of the single-particle states ϕ_i (characterized by position, spin and isospin, here only the position vector $\mathbf{r}_i$ is shown for brevity):

$$\Psi(\mathbf{r}_1, \mathbf{r}_2 ... \mathbf{r}_A) = \phi_1(\mathbf{r}_1)\, \phi_2(\mathbf{r}_2)\, \phi_3(\mathbf{r}_3) ... \phi_A(\mathbf{r}_A) = \prod_{i=1}^{A} \phi_i(\mathbf{r}_i) \quad , \tag{2.3}$$

7 The weak interaction is typically neglected as it is irrelevant for the nuclear structure phenomena investigated here. Naturally, the gravitational interaction is also neglected given its much smaller coupling than the other interactions.

but it needs to be antisymmetrized since nucleons are indistinguishable fermions. The antisymmetrized product state can be written in the form of a Slater determinant:

$$\Psi(\mathbf{r}_1, \mathbf{r}_2 ... \mathbf{r}_A) = \mathcal{A}\left[\prod_{i=1}^{A} \phi_i(\mathbf{r}_i)\right] \tag{2.4}$$

$$= \frac{1}{\sqrt{A!}} \begin{vmatrix} \phi_1(\mathbf{r}_1) & \phi_1(\mathbf{r}_2) & \cdots & \phi_1(\mathbf{r}_A) \\ \phi_2(\mathbf{r}_1) & \phi_2(\mathbf{r}_2) & \cdots & \phi_2(\mathbf{r}_A) \\ \vdots & \vdots & \ddots & \vdots \\ \phi_A(\mathbf{r}_1) & \phi_A(\mathbf{r}_2) & \cdots & \phi_A(\mathbf{r}_A) \end{vmatrix} . \tag{2.5}$$

Solving the many-body equation is no simple task. Since interactions among all nucleons and all possible configurations need to be considered, the size of model spaces required grows very quickly (factorially, in some techniques) as the size of the system grows. Hence, methods need to incorporate effective ways to reduce the size of the model space and to perform adequate approximations, without diverging from the *ab initio* philosophy. General concepts on many-body quantum methods and some of their associated strategies are presented in section 2.2.

The interplay between *ab initio* theories and experiments is crucial to test the methods employed both on developing the interactions and solving the many-body equation. A few recent examples that illustrate the importance of these tests are presented in section 2.4, as well as the specific interactions and methods that were put under scrutiny in this work.

2.2 Many-Body Quantum Methods

Many methods were developed to solve the many-body Schrödinger equation (2.1) for systems in several regions of the nuclear chart. The Coupled-Cluster methods [71], the No-Core Shell Model [72], the Green's Function Monte Carlo [73], and the Hyperspherical Harmonics method [74] are a few examples of such techniques.

Some are very simple to understand. For example, the No-Core Shell Model (NCSM) [72] can be understood as an extension of the Interacting Shell Model, presented briefly in section 1.3. The valence space, where nucleons are allowed to interact, is extended to all orbitals, eliminating the roles of an inert core and the mean-field potential. The solution can be found simply through a matrix diagonalization and is numerically exact.

However, the NCSM is only computationally feasible with very light systems. The calculation of systems as simple as ^{16}O already reaches the limit of modern machines. This is evident in figure 2.1, where the current limit of present-day supercomputers is compared to the matrix dimensionality required to compute a few light nuclei through NCSM. Although undesirable, approaches that aim at the construction of heavier systems must employ controlled approximations. Some

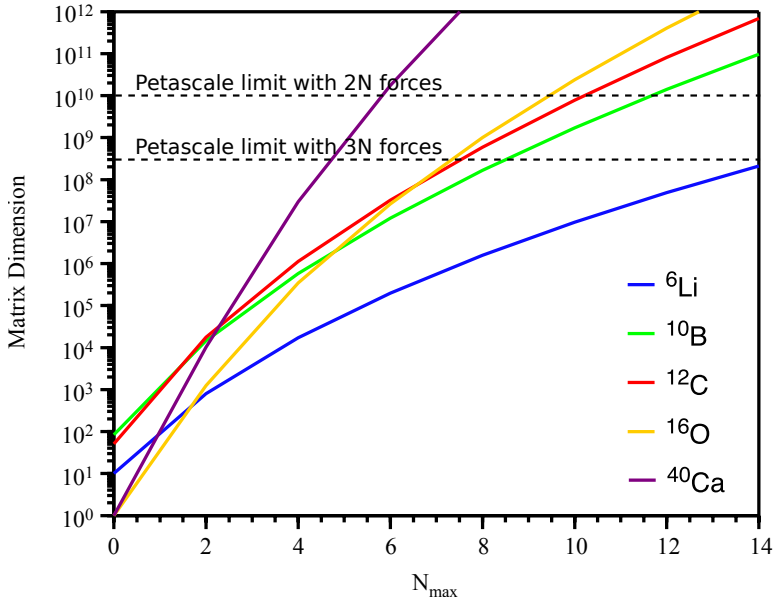

Figure 2.1: Matrix dimensionality required for the computation of a few $N = Z$ nuclei using the NCSM method as a function of the model space size parameter N_{max}. For comparison, the calculation of ^{16}O is expected to require $N_{max} = 10$ to get converged results. Dashed lines show the computing limits of Petascale machines if 2N and 3N forces are included. Figure adapted from [72].

strategies involve resorting to known nuclear properties (such as magic numbers) to truncate the model space or applying transformations to reduce computational costs.

Next, in this section, we explore two general concepts and procedures that are commonly shared among modern techniques, mainly among those employed in this work. They provide a perspective on common challenges and opportunities for improvement, but they are far from providing a comprehensive overview of the state-of-the-art spectrum of these methods.

2.2.1 Harmonic Oscillator Basis

The many-body states of the nuclear system need to be constructed using an appropriate choice of basis. Single-particle states are typically formulated in a harmonic oscillator (HO) basis [75]. Calculations are performed at a fixed oscillator frequency ω, while the model space must be of a finite number of major shells N_{max}. This implies a model space truncation with cut-off energy of $(N_{max} + 3/2)\hbar\omega$.

HO basis is preferred due to its properties that facilitate certain calculations and its straightforward correspondence to the Nuclear Shell Model [75]. Nevertheless, the use of other bases can be advantageous for specific methods (see [76] and [77], for example).

Despite its benefits, working on HO basis requires that the nuclear interactions, typically formulated in momentum space, get transformed to HO basis. One side

effect is the need for a large HO model space (large N_{max}) to accommodate the high-momentum contributions of the interaction (see sec. 2.3.3). Furthermore, the calculations must be performed at different N_{max} and ω to ensure convergence of calculations and independence of results regarding model space parameters. Ultimately, it greatly contributes to the method's computational costs [75].

2.2.2 Reference States and Valence Space

In the medium mass region ($40 \lesssim A \lesssim 100$), calculations can only be carried out in exceptional circumstances. Properties of closed-shell nuclei, such as their spherical symmetry, can be explored to improve their computability by greatly simplifying the Hamiltonians [71]. For example, if only nuclei of spin zero are considered, the parts of the Hamiltonian associated with the dynamics of higher spin states can be neglected.

Naturally, those simplifications make the range of calculations very limited: only ground states of even-even closed-shell nuclei and a few particular excited states are accessible. To extend calculations to open-shell neighbors, the closed-shell Slater determinant can be used as a reference state upon where other states will be built.

In this context, the language of second quantization is very convenient: creation ($\alpha_i^\dagger$) and annihilation (α_i) operators are introduced to add or remove, respectively, a single-particle state ϕ_i from the many-body system in an antisymmetrized way. Hence, a Slater determinant can be written as a string of creation operators acting on a vacuum state Ψ_0 (defined as $\alpha_i \Psi_0 = 0$ for any i):

$$\Psi(\mathbf{r}_1, \mathbf{r}_2 ... \mathbf{r}_A) \;=\; \alpha_1^\dagger \, \alpha_2^\dagger \, ... \, \alpha_A^\dagger \; \Psi_0 \quad . \tag{2.6}$$

Alternatively, an existing A-body Slater determinant may be used as a reference state, so arbitrary Slater determinants may be built from it though particle-hole excitations, applying a series of creation-annihilation operators.

Reference states are used in many different ways to simplify calculations. Relative matrix elements are easier and more efficient to compute than absolute ones. In some methods, the model space can be truncated to a few HO shells around the outermost shells, creating a valence space in a similar prescription as in the Interacting Shell Model. With reduced degrees of freedom, the diagonalization is computationally easier, and many more properties are accessible. An illustrative example of this procedure can be found in figure 2.2.

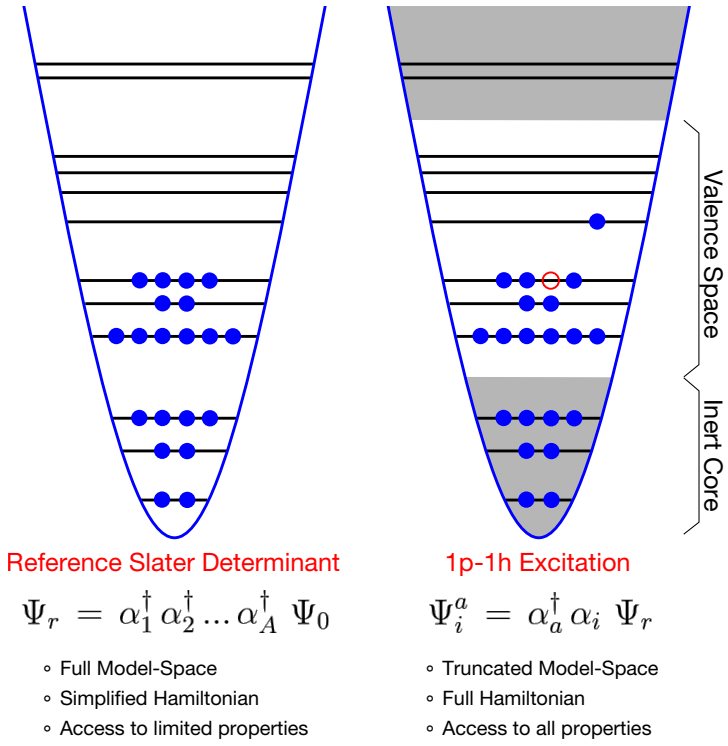

Figure 2.2: Depiction of the construction of a closed-shell reference state from the vacuum using full model space (left). Then, an excited state can be built from the reference using one particle-hole excitation in a truncated model space (right).

2.3 Nuclear Interactions

2.3.1 Nuclear Forces from Phenomenological Approaches

The development of phenomenological potentials dates back to the post-Yukawa era, and they have been heavily employed in nuclear physics. For example, they are used in structure calculations using the Interacting Shell Model (for example in [41]) and in the prediction of scattering cross sections in nucleus-nucleus collisions (as in [78]).

Although phenomenological potentials were inspired by QCD, they are not constructed from it. Their development was historically guided by fitting basic properties of nuclear force between two nucleons (2N), with an underlying *ansatz* regarding multi-meson mediation[8]. Experimental input to nucleon-nucleon and meson-nucleon interactions is relatively straightforward to be obtained from scattering experiments. One example of such potentials is the AV18 [79] (see figure 2.3). It included 18 terms to account for all the clearly disentangled nuclear properties (e.g., spin-orbit, tensor, spin-spin, etc.).

Later on, the refinements of precision potentials lead to the need to include three-nucleon (3N) components [73]. Differently from 2N components, the properties and

8 Besides the pion, some potentials also include other mesons, such as the ρ, ω and σ mesons. They influence shorter ranges in the potential due to their heavier masses.

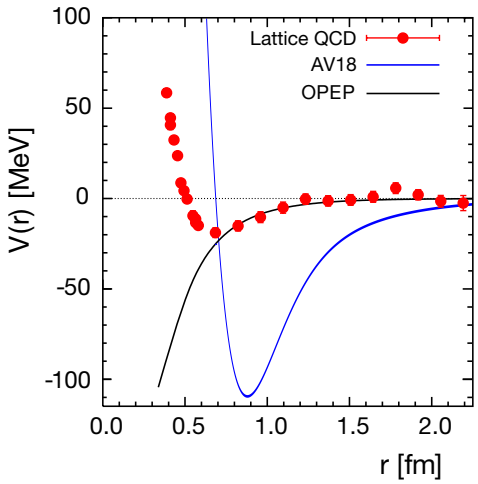

Figure 2.3: The $^1S_0$ central component of the nucleon-nucleon potential derived from Lattice QCD [70] and from the AV18 phenomenological potential [79]. The one-pion exchange potential (OPEP), based on Yukawa's theory, is shown for comparison.

underlying effects of 3N interactions are not intuitive and are hardly disentangled from experimental data. Even today, the conditions for the emergence of attractive or repulsive characters in 3N forces are unclear [80]. This lead to a nearly-blind search for the form of higher order components of phenomenological potentials, weakening their already fading connection to QCD.

Moreover, since the construction of phenomenological forces is based on an *ansatz* of the inner workings of nuclear interactions, the quantification and the control of the accuracy of the theories is difficult. Such limitations have motivated many groups to search for a more consistent route to construct interactions based on QCD.

2.3.2 Nuclear Forces from Chiral Effective Field Theory

Direct construction of atomic nuclei from QCD should naturally include higher order effects. As mentioned, however, QCD is practically intractable in the low-energy regimes of nuclear physics due to the non-linear nature of the strong force. Studies using Lattice QCD, a well-established non-perturbative approach to solve QCD systems, were able to derive simple nucleon-nucleon potentials [70] (see figure 2.3, for example). However, higher-order interactions built through similar techniques are still not on the horizon [81].

Recently, the description of nuclear forces has enormously advanced using Chiral Effective Field Theory (χEFT), about which a complete description can be found in [82]. In an EFT, a low energy approximation is made by freezing out a few degrees of freedom while working up to a certain energy scale, ignoring the structures that may emerge at higher energies. χEFT explores the spontaneous breakdown of the chiral symmetries of QCD to identify the energy scale in which the effective degrees of freedom of nuclear systems become pions and nucleons rather than quarks

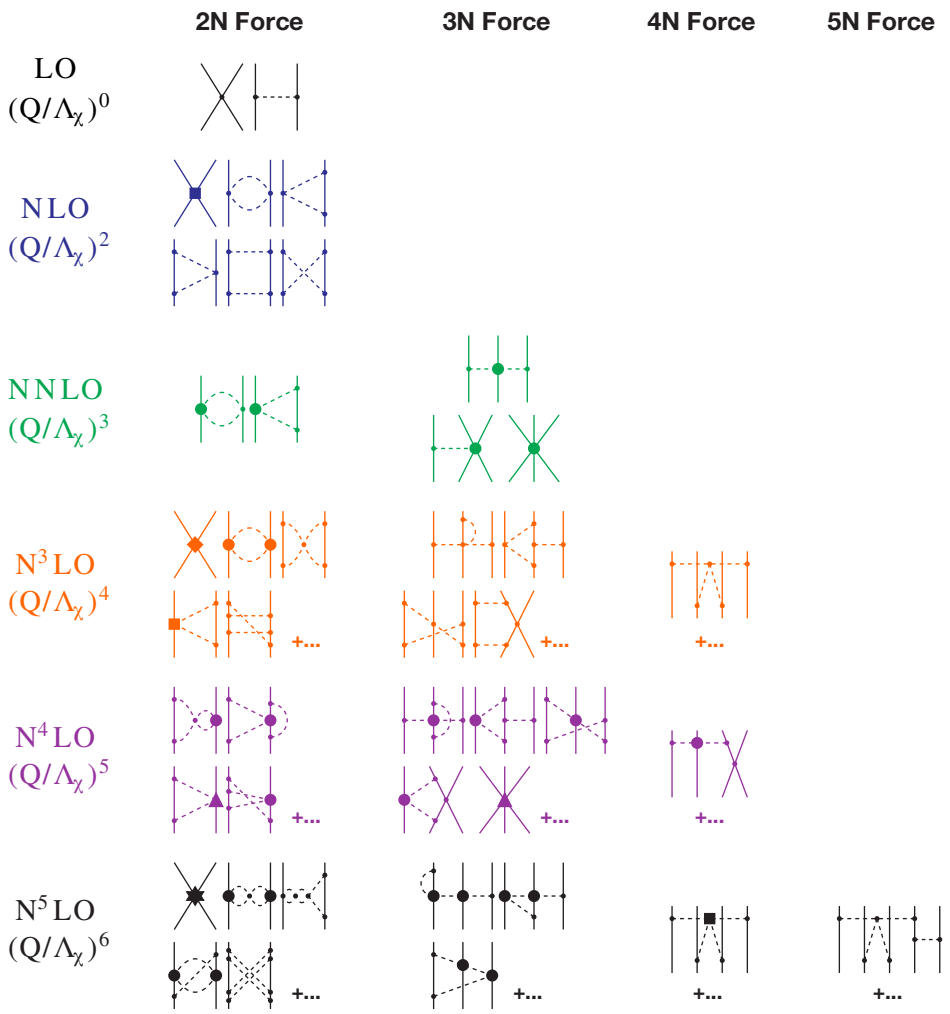

Figure 2.4: Feynman diagram representation of terms in chiral expansion of nuclear forces, classified by their order hierarchy and N-body components. Solid lines represent nucleon propagators while dashed lines represent pion propagators. Reproduced from [82].

and gluons. Chiral symmetry is approximately valid in regimes of high momenta comparatively to the masses of u and d quarks. The energy scale of χEFT (Λ_χ) is usually chosen to be near the nucleon mass scale ($\lessapprox 1$ GeV), so the degrees of freedom associated with their excitations are explicitly frozen.

Then, within the chiral scale, such forces can be constructed at the nucleon-pion level instead of the quark-gluon level. The resulting effective Lagrangian, that conserves properties of the QCD Lagrangian, is expanded in momentum powers of (Q/Λ_χ) and can be treated perturbatively with Chiral Perturbation Theory (ChPT) [82]. Figure 2.4 shows the Feynman diagrams that represent terms in this expansion.

As can be seen, in the leading order (LO), the interaction includes a one-pion exchange term, resembling the early Yukawa-like approaches. In the next-to-leading order (NLO) more complex terms, that involve two-pion exchange, start to appear.

At the next-to-next-to-leading order (NNLO or N^2LO), terms involving three nucleons naturally emerge, giving rise to 3N forces.

As higher orders are included, their contributions have been shown theoretically to diminish. Thus, this order hierarchization allows one to control the errors generated in the truncations, which are proportional to the next order left out. Nowadays, all terms involving 2N interactions were calculated up to N^5LO, while 3N interactions were evaluated up to N^4LO and 4N were only evaluated at N^3LO [82].

Although χEFT is expected to fail beyond its cut-off scale Λ_χ, nuclear forces do not vanish within the chiral limit. Important features above Λ_χ, such as Δ resonances, play relevant roles in shaping the nuclear potential at very short ranges. The properties beyond this scale are typically computed as "contact" terms (in figure 2.4, vertices where nucleon propagators meet, without coupling to a pion propagator) and are present in all orders.

Coupling constants in 2N forces are typically deduced from nucleon-nucleon and pion-nucleon scattering data. Meanwhile, contact terms and 3N coupling constants are fitted to match observables of a few light nuclear systems, such as ^{2}H, ^{3}H, ^{3}He and ^{4}He. The number of coupling constants increases as higher orders are included; therefore, the ambiguities generated may counter-act the purported increase on theoretical accuracy.

The χEFT approach is considered to be more robust than phenomenological approaches. Although χEFT-derived potentials are not purely derived from first principles, the experimental input comes only from very simple nuclear systems, and the results could, in principle, be applied to the whole chart of nuclides. Moreover, χEFT permits consistent derivation of many-body forces, allows control of theoretical accuracies and establishes an adequate connection to QCD.

Still, their increasing complexity must also be compatible with limitations stemming from computing. Strategies to derive those potentials and facilitate their use in many-body calculations form a currently very active area of research.

2.3.3 Interaction Softening

One common trait of nucleon-nucleon potentials is the presence of the "hard core", where it becomes strongly repulsive at very short distances. See, for example, the features present at $r < 1$ fm at the realistic potentials in figure 2.3. Its effect is a strong coupling between low and high momentum modes, and can be seen as non-zero off-diagonal elements in the momentum-space matrix. In turn, calculations require a large model space which, once again, complicates their computation.

Modern methods employ Renormalization Group (RG) techniques to "soften" the hard core of the nuclear potentials. In the class of techniques referred to as Similarity Renormalization Group (SRG) [83], series of unitary transformations are applied to the chiral Hamiltonian to drive its matrix elements to a diagonal band within a regulator λ, which act as a cut-off criterion for the off-diagonal matrix elements. The transformations adapt the interaction to a truncated model space

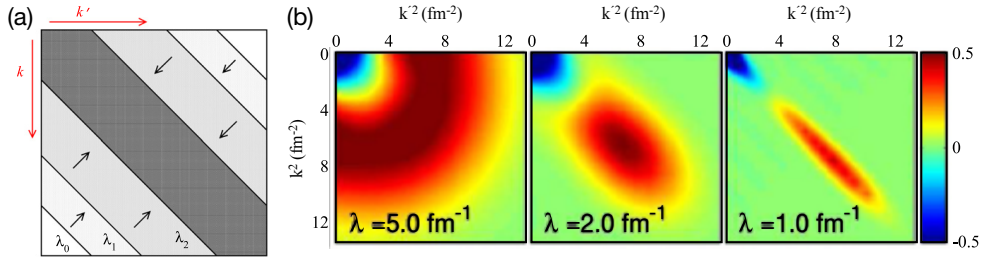

Figure 2.5: SRG evolution aims to drive off-diagonal matrix elements in momentum space towards a diagonal band within a regulator λ, as represented in the schematic illustration shown in (a). An example is given in (b): the momentum-space matrix elements of a chiral N^{3}LO 2N potential in the ^{0}S$_1$ channel is SRG-evolved between $\lambda = 5.0$ and 1.0 fm^{-1} (in natural units system). Figures adapted from [83] and [72], respectively.

while preserving the physical properties contained in the original Hamiltonian. A schematic representation of such SRG evolution and one example are shown in figure 2.5.

Other RG approaches also exist, such as the $V_{\text{low k}}$ that imposes a sharp cut-off regulator Λ directly onto momentum space[9]. Thus the choice of a suitable method may depend on the forces and the many-body method. In any case, RG-evolved χEFT potentials applied to many-body methods dramatically improve their computability [84].

2.4 Tests of *Ab Initio* Theories

In recent years impressive progress has been achieved towards the description of nuclei from first principles. Advances in algorithms, computer performance, and understanding of nuclear forces have generated a sudden jump in the number of nuclei that can be calculated through those techniques [68].

Nuclear potentials, however, are not observables. In principle, there can exist infinitely many nuclear potential constructions with nearly identical performance, and as many ways to derive them using the techniques described. Similarly, a collection of many-body quantum methods is also available in the market, each covering a specific range in masses and properties that they are able to calculate.

The challenge in this field is to narrow down successful approaches against quality, performance, computability, and accuracy. Ideally, one benchmarks the various approaches against well established experimental data. The highest sensitivity to differentiate methods is often found at extreme regions of the nuclear chart, where some behaviors are particularly enhanced.

One example can be found in figure 2.6. Several theoretical approaches describing ground state binding energies of oxygen isotopes are compared. The top two panels show different approaches regarding the interaction applied to the many-body

9 Note that the cut-off regulators λ and Λ differ from the χEFT scale Λ_χ.

methods. In panel *(a)*, two phenomenological interactions are employed. As they are fit to reproduce the known mass surface, they have a remarkable agreement to data closer to stability. As they are used to describe regions where data is scarce, their accuracy is reduced. In panel *(b)*, three χEFT-derived forces are presented: one that includes only a 2N component and two that also include different 3N forces. Their accuracy does not depend on data, but their results are sensitive to the force prescription. It highlights the importance of 3N effects for the appropriate nuclear structure description at extremes of proton-neutron imbalance [85].

The two bottom panels in figure 2.6 compare different many-body quantum methods. Panel *(c)* shows methods that employ valence space truncations. There, it can be seen that there is a high variability regarding the method. This does not happen to methods that employ the full model space, shown at panel *(d)*, which are very consistent with each other and compatible with data. Oxygen is proton-magic, and its isotopes are relatively light systems; thus, large scale approaches are feasible. It worths noting, however, that many of the methods cannot access all isotopes in this chain.

As previously mentioned, the identification of shell effects at $N = 32$ has also become an important test bench of such *ab initio* theories. This region lies close to the high mass boundary of current techniques. One of such tests is presented in figure 2.7, where the S_{2n} data of neutron-rich Ca isotopes are shown. At the time, this was the first evidence of shell effects at $N = 32$ seen in mass observables [56, 49].

Among the confronted theories, there is a wide variation of many-body methods and χEFT force prescriptions, although all include 3N interactions. Hence, the disparities among results may be interpreted as an overall "error" of the current stage of the body of techniques. There is, however, a consistency in correctly predicting the existence of the observed shell effects.

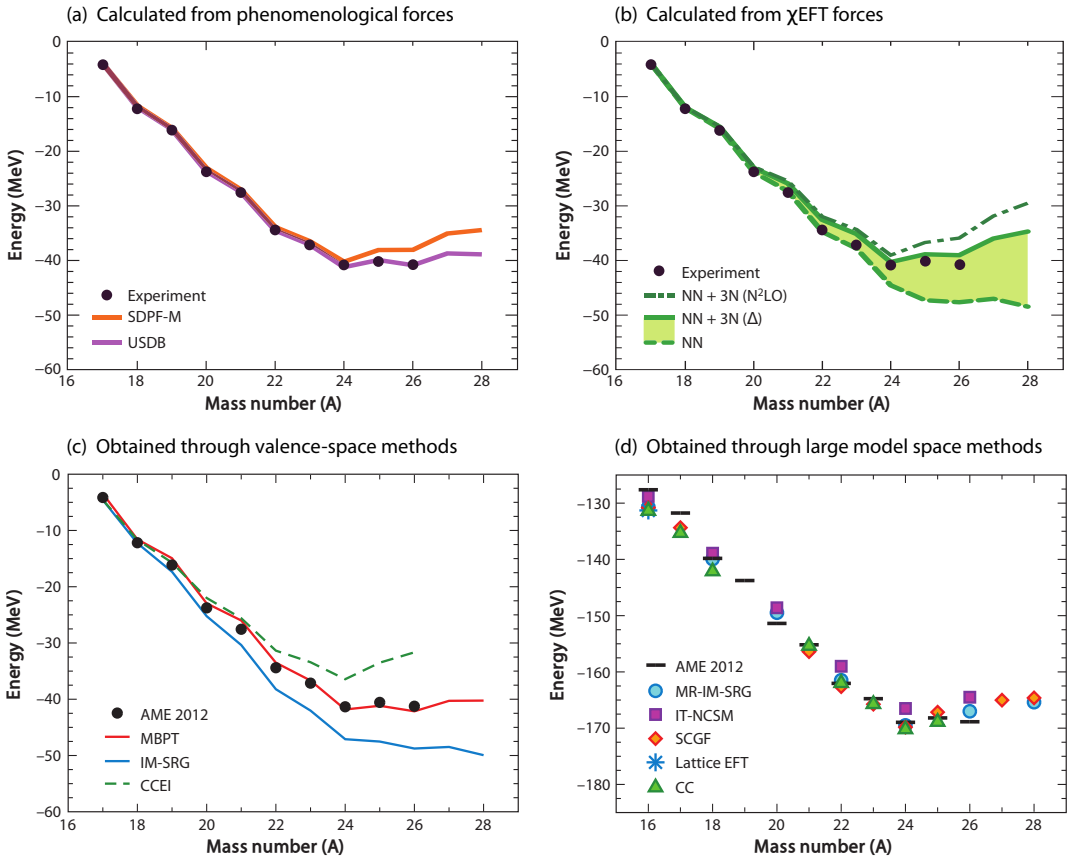

Figure 2.6: Comparisons of *ab initio* nuclear theories on the description of ground state binding energies in the oxygen isotope chain between ^{16}O and ^{26}O. Panel (a) compares results using two phenomenological forces, while panel (b) compares forces derived from χEFT. Many-body quantum methods, with truncated and full model spaces, are compared in panels (c) and (d), respectively. Panels (a), (b) and (c) show the energies relative to ^{16}O, used as reference nucleus; panel (d) shows absolute energies. Adapted from [85], where further details on methods and forces can be found.

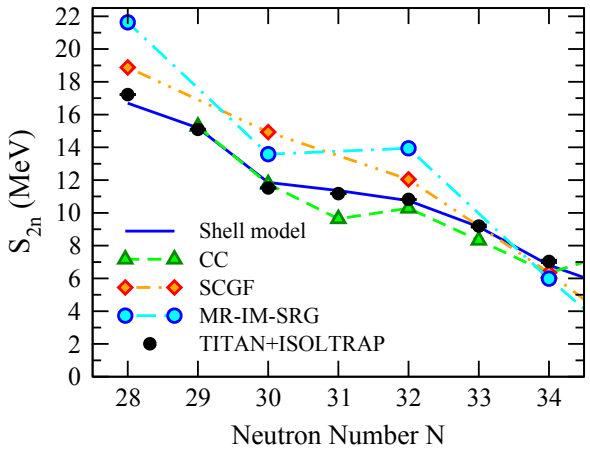

Figure 2.7: Two-neutron separation energy of neutron-rich Ca isotopes, comparing experimental data to theories that include 3N forces. Reproduced from [40] from the works of [56] and [49].

2.4.1 Tested Forces and Methods

In this work, we compared our data to state-of-the-art *ab initio* nuclear structure calculations. All are based on successful nuclear interactions and many-body methods from recent literature.

All calculations were performed with 2N and 3N interactions derived from χEFT, with parameters adjusted typically to light nuclear systems as the only input. The used interactions were the following:

1.8/2.0(EM): this interaction [86, 87, 88] combines an N^{3}LO 2N potential from [89], evolved by SRG techniques with $\lambda = 1.8$ fm^{-1}, with a N^{2}LO 3N force with momentum cut-off of 2.0 fm^{-1}.

N^{2}LO$_{\text{sat}}$: in this interaction [90], 2N and 3N terms are fitted simultaneously to properties of $A = 2, 3, 4$ nuclei as well as to heavier selected systems up to ^{24}O to finely adjust nuclear density saturation[10].

NN+3N(lnl): this interaction is a variant of the NN+3N(400) interaction [91]. It applies regulators to both local and non-local (LNL) 3N forces[11] and, subsequently, refits 3N parameters to $A = 2, 3, 4$ nuclei under a constraint that the contact interactions remain repulsive.

Complementary, two classes of many-body methods were employed:

IMSRG: the In-Medium Similarity Renormalization Group method imports concepts of the SRG methods to efficiently solve the many-body equation, decoupling correlations between the reference state and its particle-hole excitations. Two extensions of this method that allow the computation of open-shell nuclei were applied: the Multi-Reference (MR-) IMSRG [92, 93, 94] and the Valence Space (VS-) IMSRG [95, 96, 97, 98].

GGF: the self-consistent Gorkov-Green's Function method [99, 100, 101, 102] uses Green's functions to describe particle-hole excitations in the many-body system and calculates energy states through sum rules. Its "self-consistency" resides in iteratively feeding results back to input of calculations until convergence [103], making the use of a reference state unnecessary. The Gorkov formalism allows the computation of open-shell nuclei.

In all cases, the many-body calculations were performed in a HO basis of 14 major shells, with 3N interactions restricted to basis states with $e_1 + e_2 + e_3 \leq e_{3\text{max}} = 16$, where $e = 2n + l$.

The calculations were performed by our collaborators at the Jülich Supercomputing Center (JURECA) in Germany, the Très Grand Centre de Calcul du CEA in France, the Institute for Cyber-Enabled Research of Michigan State University in the U.S.A. and the DiRAC Complexity system in the United Kingdom.

10 As discussed in sec. 1.2, nuclear matter saturates at a constant density of about 0.17 nucleons/fm^3.

11 Non-local forces are those that do not depend only on the relative position of the bodies but also depend on other parameters, such as their relative momentum, for example. They pose additional computational challenges and may also be treated using similar techniques as presented in subsection 2.3.3.

3 PRINCIPLES OF MASS SPECTROMETRY

Since the birth of mass spectrometry in the early 20th century [12], a wide variety of techniques have been developed. When applied to nuclear sciences, two classes of mass measurement approaches exist: the direct and the indirect methods.

Indirect or "calorimetric" methods consists in obtaining the mass of a particle by analyzing the energy balance of an associated decay or reaction. The binding energy (thus the mass, see eq. 1.2) is calculated by comparing masses of initial and final systems and their energy differences. Some of those methods achieve very high precision, providing relative uncertainties better than 10^{-8}. For example, neutron capture reactions have provided mass values with relative mass uncertainties in the level of 10^{-10} [104, 34]. However, the kinematic reconstruction may be challenging in some situations, as in three-body decays or in cases that involve multi-level de-excitations, for example. Consequently, indirect methods are prone to large systematic deviations [34].

Direct methods, on the other hand, measure motional properties of the particle to obtain its mass directly. They observe the evolution in time of quantities such as frequency, displacement or momentum of the particle through a well-controlled region in space.

In most direct techniques, particles are charged and move through tunable electromagnetic fields. The motion of a classical non-relativistic charged particle in a region of electric field **E** and magnetic field **B** is governed by the Lorentz force (**F**):

$$\mathbf{F}(\mathbf{r}, \mathbf{v}, t) \;=\; m\,\frac{d\mathbf{v}}{dt} \;=\; q\,e\,\left[\mathbf{E}(\mathbf{r}, t) + \mathbf{v} \times \mathbf{B}(\mathbf{r}, t)\right] \quad , \tag{3.1}$$

where m is the particle's mass, **r** and **v** are the particle's position and velocity vectors, respectively, t is time, q is an dimensionless integer representing the charge state of the particle and e is the elementary charge. In this case, mass spectrometers measure the mass-over-charge ratio (m/q) of the particle. Thus the charge (or the charge state) must be known in order to determine the mass.

Among the associated variables, time (and time-related quantities, like frequency) is the one that can be most accurately accessed. The measurement of time intervals and frequencies is done by simply counting the number of cycles of a frequency standard, like an atomic clock. This procedure is immune to many sources of errors and is limited to the accuracy of the employed clock. This source of error is orders of magnitude smaller than the ones relevant for nuclear structure investigations [105, 106].

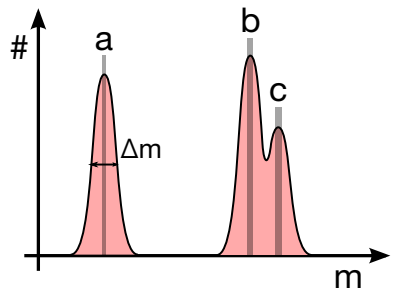

Figure 3.1: A mass spectrum: species *a* is well resolved, while *b* and *c* are overlapping. The gray bands represent the precision δm of the mass centroids, and the mass spread Δm is shown by the arrows only for species *a*.

However, other variables are required to calculate the mass, such as field strength, displacement, speed or energy, which cannot be determined to such level of precision. For this reason, atomic mass measurements are typically done relatively to a reference mass. The same measurement procedure is repeated with a calibrant particle, whose mass is known at similar or better precision than the targeted precision of the experiment. The calibrant probes the same fields and regions of the experimental setup as the particle of interest. Ultimately, these variables can be canceled out in the data analysis.

The challenge then is to keep the other variables under sufficient control. Stability of the electromagnetic fields throughout the measurement, mainly to ensure that calibrant and particle of interest experience the same conditions, is a key requirement for accuracy of those mass spectrometry techniques. Control over initial conditions of the particles is also crucial to assure reproducibility and to narrow the spread of final results. In recent decades, advances in ion sample preparation and stabilization of power supplies enable some direct techniques to greatly improve their relative mass precision, some reaching well beyond the 10^{-9} level (1 part-per-billion) [107].

Besides the mass precision (δm), two other important parameters to characterize a mass spectrometer are its *resolution* (or *resolving power*, R_m) and its *mass range*. They are related to the performance of the device when dealing with admixtures in the sample. The mass range is the interval of masses a spectrometer can analyze in a single measurement procedure. Meanwhile, the resolving power quantifies the capability to distinguish species of different masses (or mass-over-charge ratios), and is associated to the statistical dispersion (or spread, Δm) of the mass measurements[12]:

$$R_m = \frac{m}{\Delta m} \quad . \tag{3.2}$$

These concepts are illustrated in figure 3.1. It shows the resulting spectrum of a mass measurement, where three species were measured. One species is well

12 The definition of the spread Δm varies according to the measurement technique. For example, in the case of ToF-ICR technique (see sec. 3.2) it is the resonance width, while in TOF-MS and related techniques (see sec. 3.3) it is typically the Full Width at Half Maximum (FWHM) of a fully resolved mass peak.

separated from the others, whether the two others are not resolved among each other. This means the mass difference between the two unresolved species is smaller than the spread of the measurements.

Usually, the relative mass precision ($\delta m/m$) and resolving power (R_m) are related by

$$\frac{\delta m}{m} = \frac{C}{R_m \sqrt{N}} \quad , \tag{3.3}$$

where N is the number of measurements registered, which gives the statistical weight to the precision, and C is a factor dependent on the technique. However, unresolved species may considerably deviate from this relation or impact the accuracy of the measurement. In nuclear science, it is desirable that the employed mass spectrometer is able to resolve between isobars, which typically requires a resolving power above 10^5.

Furthermore, modern-day experiments in the field of nuclear physics routinely must fulfill tougher requirements. As rarer isotopes are probed, techniques need to be faster for shorter lifetimes, more sensitive for lower sample yields and larger contamination levels, and still sufficiently precise for scientific interest. Sample preparation, from the creation of isotopes to their transport to mass analyzers, must also be fast and efficient. To put this in perspective, ^{56}Ti has a half-life of 0.200(5) s [108]. Although it is the most unstable among the cases of interest, even ^{55}Ti and ^{54}Ti have half-lives around one second. The complete procedure, from creation to measurement, must accommodate this timescale.

These requirements are typically fulfilled in some mass spectrometry techniques based on *ion trapping*. Ion traps employ electromagnetic fields to confine an ion isolated from the external environment. The motion of the ion is contained in a small volume with well-controlled electromagnetic fields, which is key to high accuracy.

In this experiment, we employed two direct mass spectrometry techniques based on ion trapping. One is the Penning Trap Mass Spectrometry (PTMS), which is considered the most precise and reliable technique to date. The principles of PTMS are detailed in section 3.2. The other is the Multiple Reflection Time-of-Flight Mass Spectrometry (MR-ToF-MS), which is considered an emerging and promising technology. The principles of MR-ToF-MS are described in section 3.3. As in equation 3.1, the presented techniques are described in a classical non-relativistic framework. This approach is accurate in most situations except in a few special cases. The possible errors emerging from performing this approximation are discussed case-by-case in chapter 5 in the context of this experiment.

It is also worth noting that we must follow international standards while reporting spectroscopic data. This is briefly discussed in section 3.1.

3.1 International Standards and the Atomic Mass Evaluation

The body of experimental data on atomic masses is reviewed by the Atomic Mass Evaluation group. The group compiles all reported measurements from all different methods (direct or indirect), performs a global fit taking into account all mass relationships between different nuclides and provides recommended values for the masses of every known isotope. In this work, we use the mass values of the 2016 edition of the Atomic Mass Evaluation (AME16) [34].

The group also provides guidelines for the standards to be followed while reporting mass spectroscopic data, which can also be found in [34]. The ones that are pertinent to this work are presented in the following:

- For consistency, atomic masses are always published in their neutral form (meaning with all electrons included) in the atomic ground state, even if the measurement was done using an ionized state. Therefore, results must be adjusted accordingly.
- As all atomic mass measurements are relative measurements, the employed reference species must be provided.
- The ^{12}C atom serves as a standard to which all masses are connected to: the 12^{th} part of its mass defines the *unified atomic mass unit* (u) [34]. Alternatively, atomic masses (m_a) may also be expressed in *electron-Volts/c^2* (eV/c^2) when shown in more compact forms such as binding energy (see definition in eq. 1.2) or mass excess (ME):

$$ME(A,Z) \;=\; m_a(A,Z) - A\,m_u \quad , \tag{3.4}$$

where $m_u = 1\ \text{u} = 9.314940954(57)\,10^8\ \text{eV}/c^2$ [34]. Throughout this thesis, the mass excess format is preferred since it displays masses in the most compact form.

3.2 Penning Trap Mass Spectrometry

A Penning trap is a type of ion trap that employs only static electromagnetic fields to confine ions. It was conceived in the late 1950s [109] and granted its inventor, Hans Georg Dehmelt[13], a share of the Nobel prize in Physics of 1989. In this section, I will explain the principles of a Penning trap and how the motion of a charged particle confined in such a device can be understood, manipulated, measured and, ultimately, employed in measuring the mass of the particle.

In PTMS, the mass measurement of an ion or any charged particle occurs inside an homogeneous magnetic field. The ion (of mass m and charge qe) revolves about the magnetic field (of strength B) in a circular and periodic motion called *cyclotron motion*, whose frequency (ν_c) is given by:

$$\nu_c = \frac{1}{2\pi}\frac{qe}{m}B \quad . \tag{3.5}$$

The measurement of ν_c is central to PTMS. As can be seen, ν_c is inversely proportional to the mass, q is typically easily determined and B can be calibrated by doing a measurement of $\nu_{c,ref}$ using a well-known reference ion. The atomic mass (m_a) of the species of interest can be obtained from the atomic mass ($m_{a,ref}$) of the reference ion in charge state q_{ref} and the ratio (R_ν) between their cyclotron frequencies:

$$R_\nu = \frac{\nu_{c,ref}}{\nu_c} = \frac{m_a - q\,m_e}{m_{a,ref} - q_{ref}\,m_e}\frac{q_{ref}}{q} \quad , \tag{3.6}$$

where m_e is the mass of the electron[14]. The advantage of this relative measurement is that the absolute knowledge of the magnetic field strength is not required as it cancels out in the equation.

The measurement of the cyclotron frequencies is not simple. First of all, the ions must not probe inhomogeneities of the magnetic field; otherwise, it will hamper the measurement of ν_c. Therefore, they need to be confined in a well-controlled volume. Such confinement of the ions is done by the magnetic field itself and by an additional weak electrostatic field, which completes the Penning trap setup.

Next, I present how the ion can be confined using static electromagnetic fields and how such fields impact the motion of ions inside the trap. Ultimately, the knowledge of how charged particles move inside the Penning trap and how these motions can be manipulated enable us to formulate techniques to measure the cyclotron frequency.

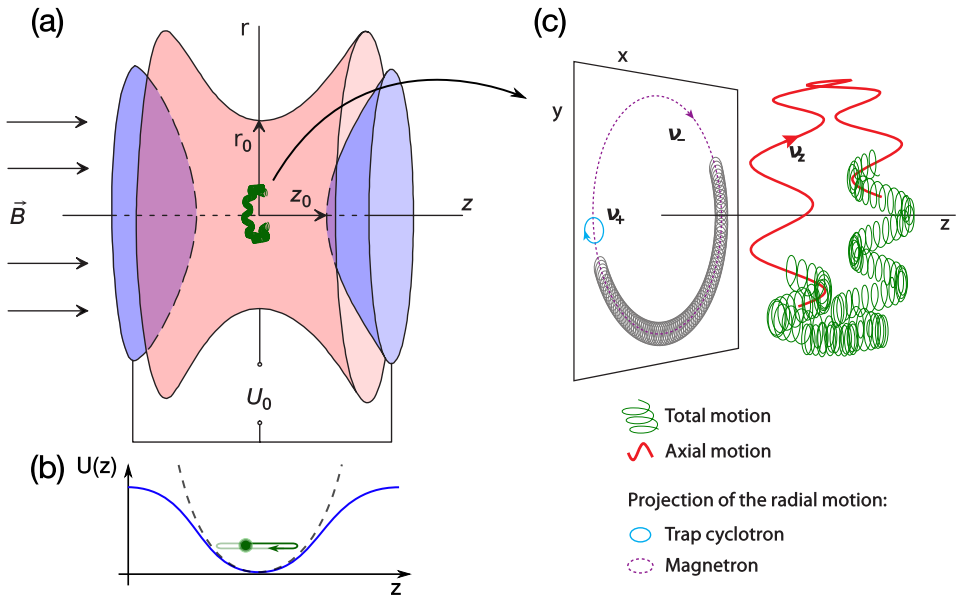

Figure 3.2: In a hyperbolic Penning trap (a), ions are confined in the "radial" plane by the action of a magnetic field. Three main electrodes generate an electrostatic field: a central ring (red) and two end caps (blue). The resulting potential well (b) confines the ion in the axial direction. Within such fields, the final ion motion (c) is quite complex (green trajectories) and can be broken down in three independent eigenmotions (details in text). Panel (c) adapted from [107].

3.2.1 Confinement and Ion Motion in a Penning Trap

The cyclotron motion is confined to an orbit contained in a plane (xy) perpendicular to the magnetic field's direction. It does not provide confinement along this direction, called *axial* (z) direction.

To provide confinement in this axial direction, an electrostatic field is superimposed to the magnetic field, creating a trapping potential well. A natural choice for the shape of this potential U is a quadrupole, since it generates harmonic oscillatory motion:

$$U(r,z) = \frac{U_0}{4\,d_0^2}\left(2z^2 - r^2\right) \quad . \tag{3.7}$$

Here we chose cylindrical coordinates: r is the distance to the z axis ($r = \sqrt{x^2+y^2}$). The parameters U_0 and d_0 describe the magnitude of the potential and depend on the shape of the electrodes that generate it. One common choice of electrode geometry is a pair of finite hyperboloids of revolution as illustrated in panel *(a)* of figure 3.2. In this case, the surface of the electrodes are equipotentials of eq. 3.7, and the parameters are easily interpreted: U_0 is the potential difference between the central ("ring") and the outermost ("end caps") electrodes, and d_0 is a characteristic trap

13 Dehmelt named his invention after Frans Michel Penning, whose work on vacuum gauges inspired the ion trap [109].

14 Note that eq. 3.6 assumes negligible the electron binding energies.

dimension determined by $d_0 = \sqrt{z_0^2/2 + r_0^2/4}$. Parameters z_0 and r_0 are distances from the center of the trap to each of the electrodes (see fig. 3.2).

Real electrodes, however, cannot be perfect equipotentials of eq. 3.7. Their surfaces are finite, and apertures are necessary to introduce and remove ions from the trap volume. For this reason, additional correction electrodes are added to the assembly to approximate the true equipotential performance. The system is tuned to have a potential as harmonic as possible in the region where ions are trapped (see panel *(b)* of fig. 3.2 - some tuning strategies can be found in [110]). Once this is achieved, ions in the trap will undergo a harmonic oscillatory motion along the axial direction with frequency (ν_z):

$$\nu_z = \frac{1}{2\pi}\sqrt{\frac{qe}{m}\frac{U_0}{d_0^2}} \quad . \tag{3.8}$$

The motion most often used in mass spectrometry is the one perpendicular to the axial direction, called *radial* motion[15]. In a Penning trap, the magnetic field is not the only driver of motion in this direction since an electrostatic field is superimposed to it. According to Laplace's equation ($\nabla^2 U = 0$), there cannot be a global minimum in the electrostatic potential, and a saddle point should exist in the center of the trap. Therefore, the confining field in the axial direction implies the existence of a deconfining electrostatic field in the radial direction too.

This deconfining radial field disturbs the "true" cyclotron motion and creates an $\mathbf{E} \times \mathbf{B}$ drift, which is called *magnetron* motion. It precesses about the magnetic field axis and the center of the trap with a magnetron frequency ν_-. The frequency of the cyclotron motion is then reduced by ν_- and is therefore called *reduced cyclotron* frequency[16], denoted by ν_+. The frequencies of the two radial motions are given by:

$$\nu_\pm = \frac{\nu_c}{2} \pm \frac{\nu_c}{2}\sqrt{1 - 2\left(\frac{\nu_z}{\nu_c}\right)^2} \quad . \tag{3.9}$$

This relationship also provides the confinement condition for a Penning trap: $\nu_z < \nu_c/\sqrt{2}$, which in terms of the fields translates to

$$\frac{U_0}{B^2} < \left(\frac{qe}{m}\right)\frac{d_0^2}{2} \quad . \tag{3.10}$$

If this condition is not met, the radial deconfinement promoted by the electrostatic field outweighs the confinement of the magnetic field and the ion escapes radially. Therefore, the electrostatic field in Penning traps are typically much weaker than the magnetic field.

The total motion of the ion in the trap becomes quite complex, as exemplified on panel *(c)* of figure 3.2. Ultimately, it can be decomposed into three independent motions (or *eigenmotions*): axial, magnetron and modified cyclotron, whose

15 Radial motion is named as such despite the fact it occurs both in the radial and azimuthal directions.
16 Also known as *modified cyclotron* or *trap cyclotron* frequency.

characteristic *eigenfrequencies* follow this hierarchy: $\nu_c > \nu_+ \gg \nu_z \gg \nu_-$. In a typical Penning trap for ions, ν_c (and ν_+) are on the order of MHz, ν_z of tens or few hundreds of kHz and ν_- of a few kHz. The eigenfrequencies obey the following identities:

$$\nu_c^2 = \nu_z^2 + \nu_+^2 + \nu_-^2 \quad , \tag{3.11}$$

$$\nu_z^2 = 2\,\nu_+\,\nu_- \quad , \tag{3.12}$$

$$\nu_c = \nu_+ + \nu_- \quad . \tag{3.13}$$

Finally, as we verified earlier, mass spectrometry requires the measurement of the true cyclotron frequency. Identities in equations 3.11 and 3.13 relate eigenfrequencies to the true cyclotron frequency, but equation 3.13 demands only the measurement of the frequencies of radial eigenmotions. These identities also make PTMS very robust.

In the next sections, angular frequencies ($\omega_i = 2\pi\nu_i$) are used instead of ordinary frequencies for compactness.

3.2.2 Manipulation of Ion Motion in a Penning Trap

Manipulating or exciting eigenmotion modes of an ion in a Penning trap is fundamental to the measurement principle of ω_c. Most frequency measurement techniques in Penning traps involve preparing the ion in one pure eigenmotion, damp other modes, or resonantly give energy to a mode. While specific measurement techniques are discussed in the following subsection, some associated ion manipulation techniques are discussed here.

Manipulating the ion motion means altering the total energy it carries and how the energy is distributed among its eigenmodes. The total energy (E_i, summing kinetic and potential energies) stored in each eigenmotion will be a function of the amplitudes r_i of each motion [111]:

$$E_z = \frac{m}{2}\, r_z^2\, \omega_z^2 \quad , \tag{3.14}$$

$$E_+ = \frac{m}{2}\, r_+^2 \left(\omega_+^2 - \omega_+\omega_-\right) \quad , \tag{3.15}$$

$$E_- = \frac{m}{2}\, r_-^2 \left(\omega_-^2 - \omega_+\omega_-\right) \quad . \tag{3.16}$$

In the radial motion, the average kinetic energy $\left\langle E_{r,kin}\right\rangle$ is given by

$$\left\langle E_{r,kin}\right\rangle = \frac{m}{2} \left(r_+^2\omega_+^2 + r_-^2\omega_-^2\right) \quad . \tag{3.17}$$

The amplitudes of the radial motions (r_+, r_-) are the radius of each trajectory (see fig. 3.3). Note that, given the hierarchy of eigenfrequencies, the reduced cyclotron motion dominates in energy contribution.

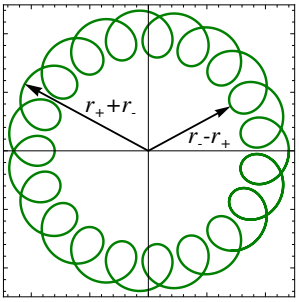

Figure 3.3: Example of trajectory of the ion in a Penning trap, projected in the radial plane.

Enhancing or reducing the total energy of the system can be done by changing the orbits of the eigenmotions. An ion in a pure magnetron motion ($r_+ = 0$, $r_- > 0$) will store much less mechanical energy than an ion in a pure reduced cyclotron orbit ($r_+ > 0$, $r_- = 0$), for example.

The orbit can be changed by applying an external time-varying driving field to the ion to transfer energy to its eigenmotions. Radial motions can be manipulated using azimuthally varying fields. To introduce such fields, a trap electrode (normally the central ring) can be split in two or four ways (see fig. 3.4). An additional radio-frequency (RF) signal is fed to each segment of the electrode, superimposed to the trapping bias. Such RF signal (of angular frequency ω_{RF} and amplitude $U_{RF,0}$, varying in time t) can be of the form

$$U_{RF}(t) = U_{RF,0}\cos(\omega_{RF}\,t + \phi_{RF}) \quad . \tag{3.18}$$

The phase ϕ_{RF} of the signal is applied differently in each electrode depending on the desired field configuration, adjusted to their purposes. Here we briefly discuss two common excitation modes: *dipole excitations* and *quadrupole excitations* of radial motions, but analogue procedures also exist involving the axial motion. A more formal and complete description of such procedures can be found in [112].

Dipole Excitations

Dipole excitations are commonly used in ion preparation in Penning traps. It simply alters the amplitude of the desired eigenmotion. The phase ϕ_{RF} is applied with 180° difference between two parts of the segmented electrode (such as in *(b)* of fig. 3.4), and a dipole field $U_{RF,d}$ is generated in the center of the trap:

$$U_{RF,d}(t,x,y) = \frac{U_{RF,0}}{r_0}\cos(\omega_{RF}\,t + \phi_{RF})\;y \quad , \tag{3.19}$$

where r_0 is the distance between the center of the trap and the segmented ring electrode.

If ω_{RF} matches ω_- or ω_+, this field will resonantly drive the amplitude of the corresponding radial eigenmotion of the ion. Depending on the relative phase $\Delta\phi$ between the driving field and the ion's motion, it may initially damp this motion

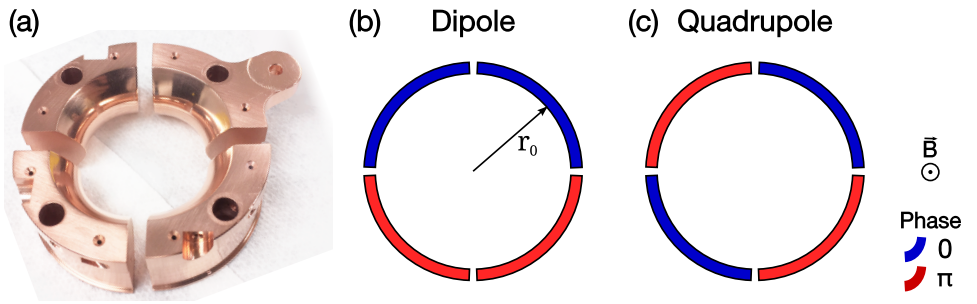

Figure 3.4: (a) An example of a four-way radially segmented ring electrode (disassembled) to drive RF excitations in the radial motion. On top of their trapping bias, each electrode is subject to a signal in the form of eq. 3.18, whose phase ϕ_{RF} is either 0 (blue) or π (red) depending on the desired type of field. Examples of configurations to create dipole (b) and quadrupole (c) fields are given.

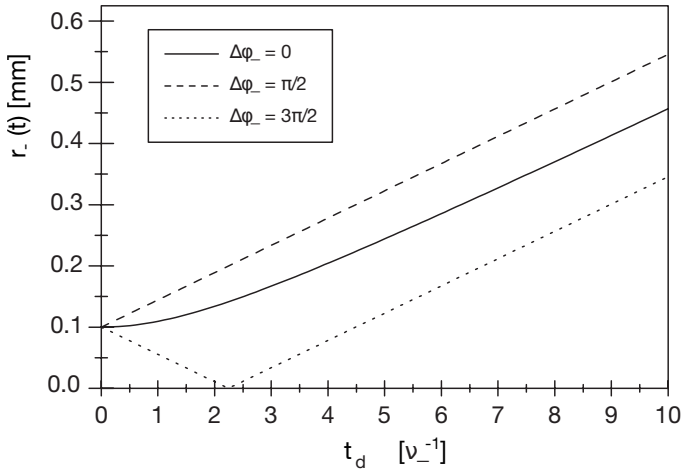

Figure 3.5: Evolution of magnetron radius as a function of the duration of the dipole excitation for three values of the phase difference between the ion's magnetron motion and the RF field. Although this example is constructed for the magnetron motion, it also applies to the reduced cyclotron motion. Figure adapted from [111].

or excite it, as can be seen in figure 3.5. After enough dipole excitation time t_d, the orbit radius will inevitably be incremented independently of $\Delta\phi$.

Dipole excitations are very useful in PTMS. They may be applied in preparing the ion into a very specific orbit or a pure eigenmotion, by exciting one and damping the remaining. One of its most common uses, however, is in the *dipole cleaning* technique [112, 113], which removes contaminant ions from the trap volume. Dipole excitations of the reduced cyclotron motion can be used to drive a known intruder to such a high orbit that it lands on the surface of an electrode, effectively removing it from the trap. Since ω_+ is as mass-dependent as ω_c, a dipole field is tuned to be only in resonance with contaminant ions, leaving ions of interest unaffected.

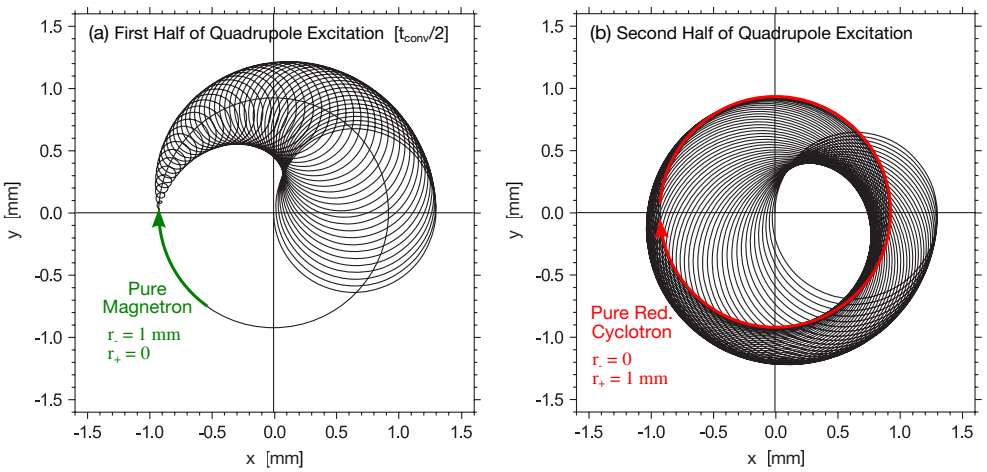

Figure 3.6: One full conversion of a pure magnetron motion (green) in a pure reduced cyclotron motion (red) through a quadruple excitation in the resonance condition $\omega_{RF} = (\omega_+ + \omega_-)$. The ion trajectory through the procedure is divided in two halves for clarity: (a) for the first half and (b) for the second. Figure adapted from [111].

Quadrupole Excitations

In quadrupole excitations, the RF field couples two eigenmotions and, thus, connects two eigenfrequencies. Its most common use is to convert a pure magnetron motion into a pure cyclotron motion through the frequency $\omega_+ + \omega_-$, which directly accesses ω_c in one single procedure.

The field is generated by applying the signal of eq. 3.18 with 180° phase shifts on sets of electrode segments perpendicular to each other, as shown in *(c)* of figure 3.4. The resulting field is described by a quadrupole:

$$U_{RF,q}(t,x,y) = 2\frac{U_{RF,0}}{r_0^2}\cos(\omega_{RF}\,t + \phi_{RF})\;x\,y \quad . \tag{3.20}$$

If the resonant condition $\omega_{RF} = (\omega_+ + \omega_-)$ is met, a full conversion between r_+ and r_- can be obtained. This conversion is illustrated in figure 3.6 in which an initially pure magnetron motion is converted to a pure reduced cyclotron. The process is periodic, and an example of such evolution is shown in figure 3.7. Full conversions are obtained at excitation times t_{RF} that are multiple of the conversion time t_{conv}:

$$t_{conv} = 4\pi\frac{r_0^2}{U_{RF,0}}B \quad , \tag{3.21}$$

which is dependent on the magnetic field strength B and on the amplitude of the RF field, but not dependent on the mass of the particle. One important property can be seen: the product $t_{conv}\cdot U_{RF,0}$ is a constant of the trap system, which greatly facilitates tuning and parameter scaling when different t_{RF} are desired.

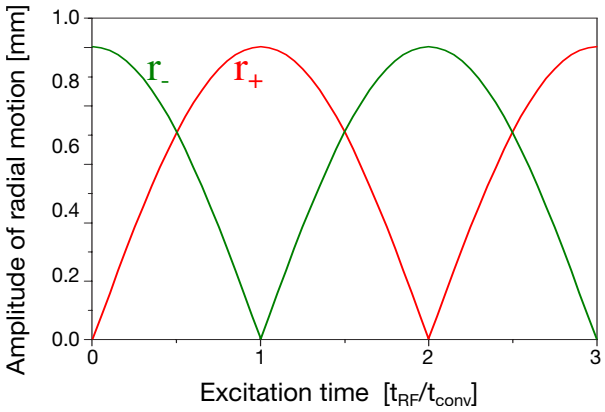

Figure 3.7: Interconversion of magnetron (green) and red. cyclotron (red) motions as a quadrupole excitation is applied indefinitely. Full conversions occur periodically at multiples of t_{conv}. Figure adapted from [111].

Quadrupole excitations are the preferred process of measurement of ω_c in PTMS. It allows the measurement to be done in one single step instead of measuring ω_+ and ω_- independently.

3.2.3 Frequency Measurement Techniques in Penning traps

There are three techniques to measure characteristic frequencies of ions in a Penning trap. All methods employ the manipulation techniques described above to enhance their signals. Here is a brief description of them:

FT-ICR: in the Fourier Transform Ion Cyclotron Resonance technique [114], the signal that the ions induce in the trap electrodes is amplified by low-noise cryogenic electronics, and a Fourier analysis of the signal generates a frequency spectrum.

PI-ICR: in the Phase-Image Ion Cyclotron Resonance technique [115], the ion's radial position in the trap is measured by its careful extraction onto a position-sensitive detector. Positions measured at different times enable the reconstruction of the phase evolution and, consequently, the frequency of the motion.

ToF-ICR: the Time-of-Flight Ion Cyclotron Resonance technique [116] consists of applying an RF excitation and subsequent ejecting of the ion from the trap towards a detector. The time-of-flight from the trap to the detector is measured. In the case when the resonance condition is met, the gain in kinetic energy will be translated into a shorter flight time to the detector. The procedure is repeated using a different ω_{RF}. The scan over the frequency range reveals the cyclotron frequency of the ion motion.

In this work, we employed the ToF-ICR technique. The complete ToF-ICR procedure to measure ω_c using quadrupole excitations is described in the following.

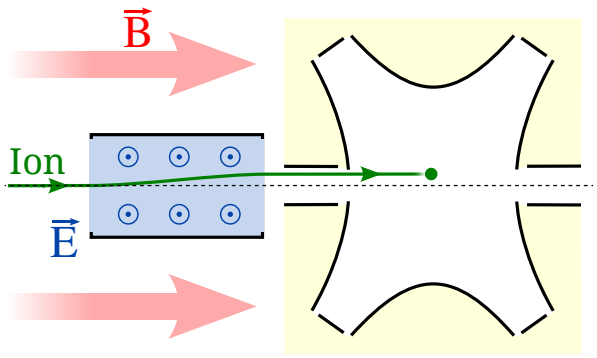

Figure 3.8: Off-axis ion injection in a Penning trap using a Lorentz Steerer (blue).

ToF-ICR: Initial Magnetron Motion

The first step in ToF-ICR for the measurement of ω_c is to prepare the sampled ion in a pure magnetron motion. The ion is normally injected in the center of the trap[17], where $r_+ = r_- = 0$. Then, a dipole excitation prepares the ion at a magnetron orbit (at TITAN, $r_- \approx 1$ mm). Since ω_- has a weak mass dependence, it may be previously measured with a calibrant ion of known mass and easily calculated for the ion of interest.

Alternatively, a technique called *Lorentz steering* [117] is used for fast ion preparation into a pure magnetron motion. A pair of electrostatic steerer plates is put right before the entrance of the trap, well inside the strong magnetic field. The $\mathbf{E} \times \mathbf{B}$ drift drives the ion off-axis prior to its injection into the trap and results in an initial magnetron motion (see fig. 3.8).

This procedure allows one to skip the dipole excitation step, which typically takes a few tens of milliseconds. However, it is also known to induce a small reduced cyclotron motion [117], which is undesirable. Therefore, Lorentz steering is typically only used for mass measurements of very short-lived species (half-life $\lesssim 100$ ms), when long ion preparation times cannot be afforded.

ToF-ICR: Quadrupole Excitation

With the ion in a pure magnetron motion, a conversion to a pure reduced cyclotron is done through quadrupolar excitation. The RF excitation frequency is scanned through many measurement cycles. The detuning frequency ($\Delta\omega_{RF}$) is defined as:

$$\Delta\omega_{RF} = \omega_{RF} - \omega_c \quad . \tag{3.22}$$

Naturally, the conversion is maximal when $\Delta\omega_{RF} = 0$. Since $\omega_+ \gg \omega_-$, the ion's radial kinetic energy is also maximum (see eq. 3.17), so it can be employed as a "gauge" of achieving resonant conditions.

If $\Delta\omega_{RF} \neq 0$, the complete conversion cannot occur. However, some incomplete conversion may still occur if the detuning is sufficiently small. This can be seen in

17 Tuning procedures to achieve that are described in section 4.2.4.

figure 3.9, where the radial kinetic energy of the ion after the quadrupole excitation is shown in function of the detuning frequency.

The width of this frequency window ($\Delta\nu$) is an approximate measure of the full width at half maximum (FWHM) of the conversion line shape as a function of $\Delta\omega_{RF}$ (see panel *(b)* of fig. 3.9). It depends on the conversion time (t_{conv}):

$$\Delta\nu \approx \frac{0.8}{t_{conv}} \quad , \tag{3.23}$$

which implies that a "sharper" (*i.e.* more precise and better resolving) measurement of ω_c can occur with a longer measurement time.

In fact, the conversion line shape is very similar to the Fourier transform of the excitation signal, which is a sine wave modulated by a square pulse of duration t_{RF} (see fig. 3.9). As $t_{RF} \to \infty$, the signal tends to a pure sine wave, whose Fourier transform is a delta function.

Alternatively, a different excitation scheme, invented by Norman Ramsey (Nobel Prize 1989), may be used to reduce $\Delta\nu$ using the same measurement time. It consists of splitting the RF signal in multiple shorter pulses, separated by a time of excitation-free evolution [118, 119].

In a two-pulse Ramsey scheme, as depicted in panel *(a)* of figure 3.10, an initial quadrupole excitation pulse of duration t_{on} is applied to achieve 50% conversion. Then, both radial eigenmotions are allowed to evolve freely for a time t_{off}, creating a phase difference between them. Finally, another quadrupole excitation pulse of duration t_{on} completes the conversion to pure reduced cyclotron motion. The total procedure time is $t_{RF} = 2\,t_{on} + t_{off}$, although the conversion occurs for a duration $t_{conv} = 2\,t_{on}$. The amplitude of the signal must be adjusted according to eq. 3.21.

Using this scheme, the conversion is still maximal at the resonance condition $\omega_{RF} = \omega_c$, but it creates multiple fringes that spread across a large detuning range[18] (see *(b)* of fig. 3.10). This is an effect of the phase interference created as a result of the excitation-free evolution. The big advantage of this scheme is that the central fringe is narrower than the line width obtained using the standard scheme at the same t_{RF}. The Ramsey excitation improves the precision of the measurement by a factor 2 or 3.

One drawback of the Ramsey excitation scheme is the need to perform an initial measurement using a standard quadrupole scheme. Since many fringes may generate conversion levels very close to 100%, even at large $\Delta\omega_{RF}$, the position of the central fringe must be unambiguously identified for accurate frequency measurement.

18 Equation 3.23 is still valid, but for Ramsey excitations $t_{conv} < t_{RF}$, hence the worse overall resolving power.

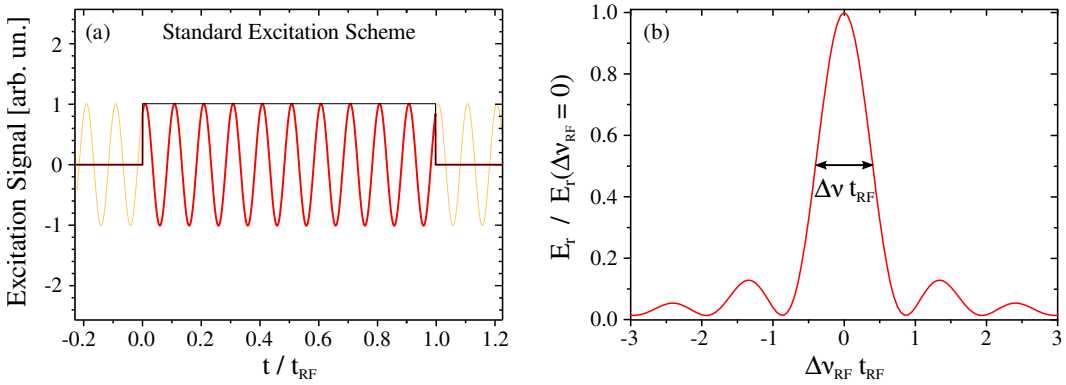

Figure 3.9: (a) The RF signal (red) in a standard quadrupole excitation can be seen as the superposition of a sine wave (yellow) and a square pulse of duration t_{RF} (black). (b) The degree of conversion achieved can be measured by the kinetic energy of the radial motion, which is maximal when $\omega_{RF} = \omega_c$.

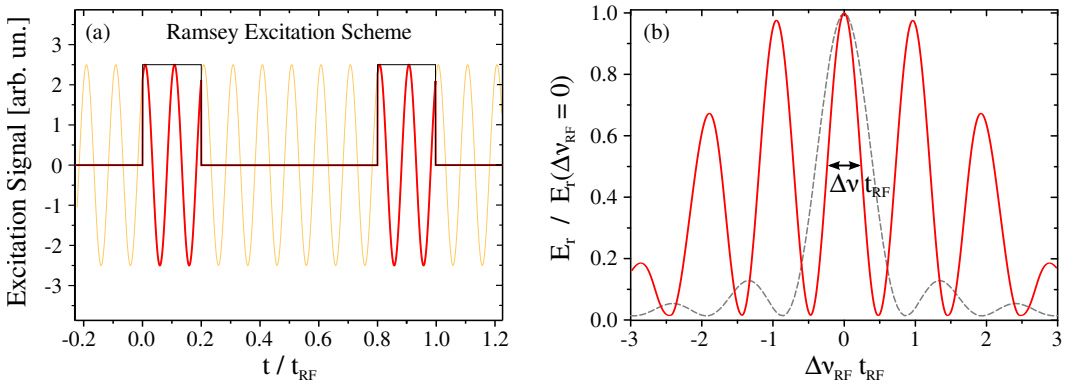

Figure 3.10: (a) The RF signal (red) in a two-pulse Ramsey quadrupole excitation is the superposition of a sine wave (yellow) and two square pulses of duration t_{on} separated by an interval of duration t_{off} (black). (b) The kinetic energy of the radial motion (red) is also maximal when $\omega_{RF} = \omega_c$. However, multiple fringes are seen and the line width in the central fringe is sharper than in the standard scheme (dashed gray), which improves the precision of the measurement.

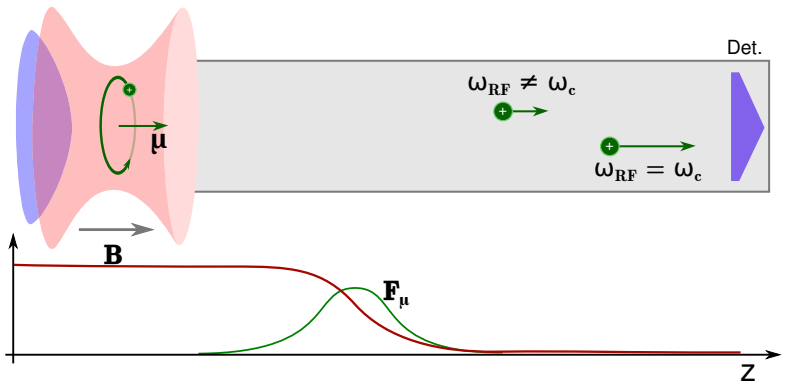

Figure 3.11: Illustrated example on the ion's time-of-flight dependency on the energy of the radial motion in the trap. The radial energy is converted into axial energy as the ion passes through the gradient of the magnetic field; an ion with larger radial energy (by means of an excitation for example) will arrive sooner at the detector. The bottom graph shows the axial map of the magnetic field strength (red) and the magnitude of the force (green, see eq. 3.25) along the path to the detector.

ToF-ICR: Extraction and Detection

In this last step, the "gauge" of achieving resonant condition (ion's radial kinetic energy) is translated to a detectable signal. After the quadrupole excitation, the ion is extracted from the trap by lowering the potential of one end cap electrode. It flies towards a detector, and the time between the trap opening and the detector registering a hit is measured. The ion flies faster towards the detector if $\omega_{RF} = \omega_c$, as explained below.

The ion in the trap, with its radial motion about the magnetic field (of strength B), generates a magnetic dipole whose momentum ($\boldsymbol{\mu}$) is dependent on its radial kinetic energy ($E_{r,kin}$):

$$\boldsymbol{\mu} = -\frac{E_{r,kin}}{B}\,\hat{\mathbf{z}} \quad , \tag{3.24}$$

which should be also a function of the applied excitation frequency ω_{RF}.

The detector lies outside the magnet. Therefore, the ion must pass through a region of a gradient magnetic field. Here, it is subject to a force ($\mathbf{F}_\mu$):

$$\mathbf{F}_\mu = \nabla(\boldsymbol{\mu} \cdot \mathbf{B}) \quad . \tag{3.25}$$

The ion's radial energy is converted to the axial direction and boosts the ion's velocity towards the detector. The time-of-flight from the trap to the detector, passing through the electric potential $U_z(z)$ and the magnetic field strength $B_z(z)$ mapped the axial direction, is then given by:

$$tof(\omega_{RF}) = \int_{z_t}^{z_d} \sqrt{\frac{m}{2\left[E_z(z_t) - qe \cdot U_z(z) + \mu(\omega_{RF}) \cdot B_z(z)\right]}}\, dz \quad , \tag{3.26}$$

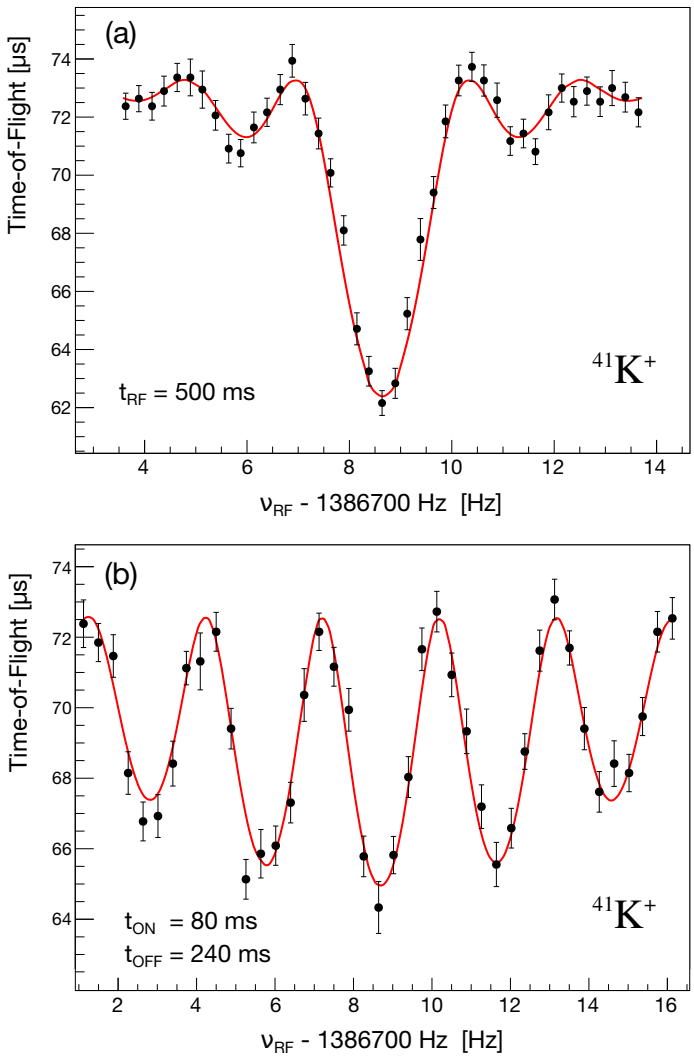

Figure 3.12: Two ToF-ICR measurements of the cyclotron frequency of $^{41}K^+$, measured at TITAN facility: (a) with standard quadrupole excitation for 500 ms and (b) with Ramsey quadrupole excitation for 400 ms ($t_{on} - t_{off} - t_{on} = 80 - 240 - 80$ ms). Red curves are analytical fits to the data based on eq. 3.26.

where z_t and z_d are the positions in the axial direction of the center of the trap and the detector, respectively. $E_z(z_t)$ is the initial kinetic energy of the ion. Since the kinetic energy is boosted by the conversion, the time-of-flight is considerably shorter (see figure 3.11).

Examples of typical ToF-ICR resonances where ν_c is measured are shown in figure 3.12, using both standard and Ramsey excitation schemes. Note the resemblance between the line shapes and the corresponding radial kinetic energy profile seen in figures 3.9 and 3.10.

3.2.4 Practical Considerations of the ToF-ICR Technique

The ToF-ICR technique is a reliable technique that is extensively employed in mass spectrometry. The technique routinely achieves relative mass precisions as low as a few parts per billion and enabled the measurement of nuclides as short-lived as ^{11}Li, with a half-life of only 8.8 ms [120]. However, it does have limitations regarding more challenging experiments in nuclear sciences, as explained next.

Although it is a very precise technique, its resolving power is proportionally worse than in other techniques. In equation 3.3, $C_{\text{ToF-ICR}}$ is on the order of unity, while in the MR-ToF-MS it can be over an order of magnitude larger. The resolution in ToF-ICR is essentially given by $\nu_c/\Delta\nu$, which according to eqs. 3.23 and 3.5 is

$$R_m^{\text{ToF-ICR}} \approx 0.2\,\frac{qe\,B}{m}\,t_{conv} \quad . \tag{3.27}$$

Therefore, it has a hard limit bound by the measurement time and cannot be further improved using better preparation techniques, as most mass spectrometry techniques do. It is considerably worse in the Ramsey excitation case, which sacrifices resolution for large gains in precision, as panel *(b)* of figure 3.12 illustrates.

Isotopes of interest are often co-produced with many other isotopes that may be present in the sample. In a ToF-ICR measurement, such contaminant species may overlap with the species of interest due to the reduced resolution. In addition to that, the sensitivity of the technique is reduced in the presence of contaminants. Clear resonances are typically obtained with a contaminant-to-interest ratio better than 1:5, otherwise the ions of interest would be hardly distinguishable from the background. The dipole cleaning technique can successfully remove contaminant species at ratios of about 1:200. However, it is not infrequent that contaminant species are million times more abundant than the species of interest.

For the same reason, it is rare that the species of interest and the calibrant can be measured in the same frequency spectrum, which is called *internal calibration*. Instead, it requires measurements of ν_c and $\nu_{c,ref}$ to be done in separate measurements. This procedure demands extra caution regarding time-dependent fluctuations in the setup and may lead to additional systematic errors.

ToF-ICR is also a *scanning* technique. It is based on a search for a matching condition, which requires the measurement of many ions to trace a clear baseline. In the measurement shown in panel *(a)* of figure 3.12, about 75% of investigated ions were not in resonant condition, but are necessary to identify the position of the resonance accurately. A typical measurement requires at least a few hundred ions to be successful. It is a concerning factor when dealing with species that are produced in minimal amounts. Moreover, although the mass range can be of almost arbitrary length, it is very costly to perform broad frequency scans. In practice, the mass range of ToF-ICR is very narrow, surrounding only closely lying species.

Next, another mass spectrometry technique is presented. Although not as precise as PTMS, it addresses many of the issues presented here and enables one to extend mass measurements to rarer species.

3.3 Multiple Reflection Time-of-Flight Mass Spectrometry

Time-of-Flight Mass Spectrometers (ToF-MS) also makes up a class of instruments of widespread use in many fields [121], such as nuclear science and analytical chemistry. It is based on the time separation between two particles, distinct in mass, while traveling the same distance L, starting together at same kinetic energy E_{kin}. The time-of-flight (tof) for each particle (of mass m) is given by

$$tof \;=\; L\sqrt{\frac{m}{2\,E_{kin}}} \quad , \tag{3.28}$$

thus the time separation between particles with masses m_1 and m_2 is proportional to $L(\sqrt{m_1}-\sqrt{m_2})$.

In such devices ionized particles are sent, in bunches[19], through an accelerating potential U_a, which defines the initial kinetic energy. The ions enter a field-free region where they drift towards a detector. In such case, as $E_{kin} = qe\,U_a$ (where qe is the charge of the ion), the time separation between different particles arriving at the detector scales with $L(\sqrt{m_1/q_1}-\sqrt{m_2/q_2})$.

Similarly to PTMS, the atomic mass (m_a) of the species of interest can be obtained from the atomic mass of a reference ion ($m_{a,ref}$) and the ratio R_{tof} between their time-of-flights:

$$R_{tof} \;=\; \frac{tof}{tof_{ref}} \;=\; \sqrt{\frac{m_a - q\,m_e}{m_{a,ref} - q_{ref}\,m_e}\,\frac{q_{ref}}{q}} \quad , \tag{3.29}$$

where q and q_{ref} are the charge states of the ion of interest and the reference ion, respectively; and m_e is the mass of the electron.

In experiments, the true time-of-flight through the drift region is systematically shifted from the measured time-of-flight (t_{meas}) by a constant time offset (t_0):

$$tof \;=\; t_{meas} - t_0 \quad . \tag{3.30}$$

The nature of this offset is mostly from ion's flight outside the drift region, such as during the acceleration stage, but has also contributions from the detectors and the electronic processing of the signal. The overall offset is typically a constant in the experiment and needs to be evaluated.

Measurements in ToF-MS are fast compared to PTMS. Cycle times can be on the order of a tens of μs, permitting high measurement cycle frequency. Large ion samples can be distributed over many cycles, so systematic errors from ion-ion interaction are reduced. Moreover, ToF-MS is a *non-scanning*[20] technique with a wide mass range, which allows the analysis of complex admixtures in the sample

19 The bunching feature is necessary to correlate in time a detected event to the start of the flight.

20 A scanning technique, as defined in sec. 3.2.4, is based on a search for a matching condition, like the frequency in ToF-ICR.

in a single measurement. Advanced ToF-MS spectrometers can reach relative mass precisions of a few parts-per-million (10^{-6}) and resolutions of 10^4.

The resolving power (R_m) of such technique depends on the initial energy spread and initial spatial spread of the ions, which translates to a measured time-of-flight dispersion Δt in the detected spectrum:

$$R_m^{\text{TOF-MS}} = \frac{tof}{2\,\Delta t} \quad . \tag{3.31}$$

The overall effect of Δt diminishes as the time-of-flight increases. Therefore the resolution of such technique greatly benefits from an extended flight path. Yet, there are clear practical limitations that prevent the drift region from being expanded to arbitrary lengths. One elegant way of circumventing this is to recycle the flight path, circulating the ions through the same analyzer multiple times.

This is the concept behind the Multiple-Reflection Time-of-Flight Mass Spectrometer (MR-ToF-MS) [122, 123]. The field-free drift region is placed between a pair of electrostatic mirrors. The ion sample is reflected back for as many passes through the analyzer region as desired, effectively making the device in a spectrometer with tunable length. Flight paths on the order of kilometers are achievable using a compact system of about a meter long.

Next, the concept of the MR-ToF-MS and its operation as a mass spectrometer are explained in detail in subsections 3.3.1 and 3.3.2.

3.3.1 Concept of the MR-ToF-MS

A typical MR-ToF-MS setup includes an ion preparation device, a mass analyzer, and a fast-timing detector. The preparation device is required to appropriately inject ions in the mass analyzer. As already mentioned, the ion bunches' initial dispersions in energy and position should be as low as possible for a greater resolution [123]. In many MR-ToF-MS devices a dedicated preparation ion trap, with capabilities of cooling and bunching ion samples, is placed right before the entrance of the analyzer. Further details on ion preparation are given in sec. 4.2.4.

The mass analyzer of an MR-ToF-MS is composed of a drift section between two electrostatic reflectors. A typical electrode structure concept is shown in figure 3.13. During the measurement procedure, the electric potential in the mirrors exceeds the kinetic energy of the ions. Therefore the ions are confined inside the device, moving back and forth between mirrors. The outermost electrodes can be switched to lower potential to allow ion bunches to be injected and extracted through apertures placed in the end electrodes. After the ions fly a certain number of turns inside the analyzer, they are extracted to the detector. The time-of-flight through the whole procedure, from the moment the ions are injected in the analyzer to when they hit the detector, is registered.

In the mass analyzer, the drift section is a field-free region where the ions fly at a constant speed. It is specially designed to minimize electric field penetrations that

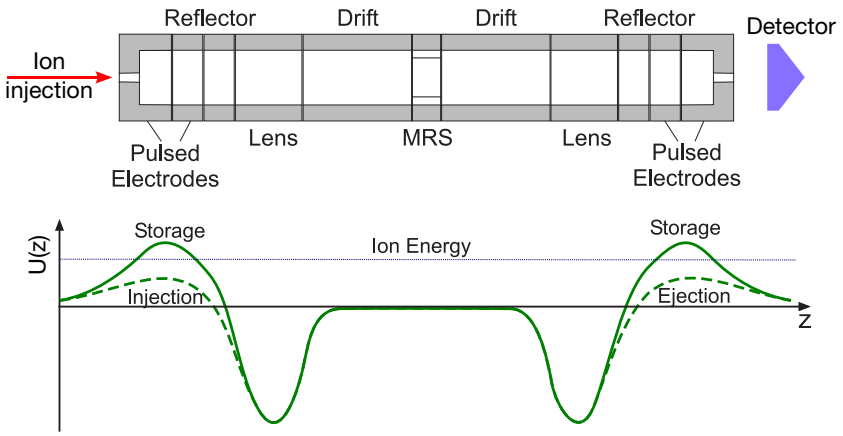

Figure 3.13: Scheme of the electrode structure of a typical MR-ToF-MS mass analyzer (top) and the correspondent generated electrostatic potential along the axis of the spectrometer (bottom). Adapted from [124].

could interfere in the ion's trajectory. Optionally, some systems include a *mass range selector* in the middle of the drift region to aid in the selection of a specific mass range [123]. More details are given in sec. 3.3.2.

The design of the mirrors is a critical step to the appropriate working of the mass spectrometer. They are usually a stack of a few electrodes that shape the electric field of the mirror. The mirrors must be gridless; otherwise, the multiple passes of an ion bunch through the grids would lead to scattering and changes in the ion energy and trajectory, and considerably reduce the efficiency of the device. A gridless design requires extra care in the construction of the mirrors to minimize aberrations, *i.e.* imperfections on the shape of the mirror potential that cause an imperfect reflection.

Most importantly, the mirrors must be tuned to ensure two properties: confinement and *isochronicity*, described next.

Confinement

In order to extend ion flight paths to long lengths (typically hundreds of meters or kilometers), ions need to have stable orbits inside the device. Per design, the axial confinement is provided by the potential well created by the mirrors. However, ion bunches also expand radially. As the flight path grows, this expansion may cause severe ion losses due to collisions with electrodes.

To account for such expansion, one electrode in each mirror also works as an electrostatic device called *Einzel lens* [125] to refocus the ion trajectories in every turn. An Einzel lens, as in fig. 3.14, creates a small region of fast acceleration and deceleration, which changes the ion velocity in the radial direction. Parallel ion beam trajectories should converge in a focal point after the lens. The position of the focal point is tunable according to the potential difference (U_{EL}) between the lens' electrodes and is independent of the ion's mass [126].

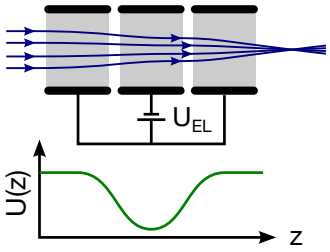

Figure 3.14: Parallel ion trajectories are focused as they pass through an Einzel lens. Below, the electrostatic potential in the axis of the lens is shown.

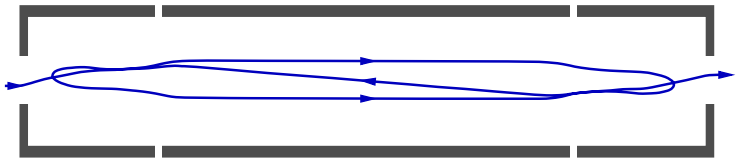

Figure 3.15: Example of a simulated trajectory of an ion being injected, making one full turn in the analyzer and being ejected. Adapted from [129].

In the MR-ToF-MS analyzer, the Einzel lenses in the mirrors can be identified in fig. 3.13 as the two deep potential wells. With appropriate tuning of the lens' potential, radial ion confinement is achievable. Hence, both axial and radial confinement are provided by the mirrors, and trajectories inside the analyzer can be made stable with adequate tuning. One example of such a stable orbit is given in figure 3.15.

Consequentially, the MR-ToF-MS can be considered as a form of electrostatic ion trap. The achievable storing time, however, is typically short compared to most ion traps. The current generation of MR-ToF-MS can confine ions for tens of milliseconds. Meanwhile Penning traps can store a sample for several seconds, or even months in a few devices [127]. Although this remains to be further investigated, losses in MR-ToF-MS are generally attributed to ion interactions with the background gas, and transverse expansion of the beam due to optical aberrations [124, 128, 123].

Isochronicity

Isochronicity is the property that time-of-flight differences in any ToF-MS system only depend on the ion's mass-over-charge ratio, independent of their initial positions, incident angles and energies. Only then eq. 3.29 can be true. Yet, time spreads regarding initial conditions are unavoidable, although they can be minimized.

Ultimately, it is required that the timing detector is positioned in a *time focus* of the analyzer. The concept of time focus is illustrated in an example in figure 3.16. Ions that start their flights at different positions and energies are subject to slightly different works by the accelerating potential. Ions initially closer to the drift section enter it with lower speed than ions initially further; eventually, trajectories cross the same plane at the same time. Such accelerating potentials can be tuned to generate a time focus in a specific point of the setup.

The field gradients of the mirrors are tuned so that faster ions fly further inside the mirror and, thus, take more time to turn. The right balance between the time spent in the analyzer and the time spent in the mirror yields a time focus for every turn. Consequentially isochronous orbits are obtained in the analyzer.

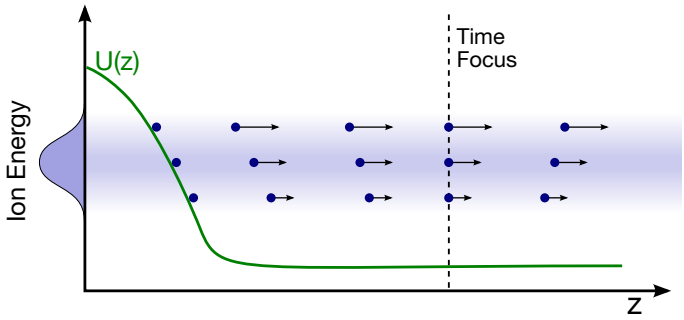

Figure 3.16: The energy and position spread of the ions (with same m/q), under an accelerating potential $U(z)$, causes differences in speed and path length in the drift section. This effect cancels out in the "time focus" position, where ions simultaneously arrive. Changing the shape of $U(z)$ shifts the position of the time focus.

The tuning of the reflectors is done for an ion bunch with specific energy distribution. If one parameter is changed, the system loses its overall isochronicity. Therefore, the stability of the overall system is important, which includes temperature stability, mechanical stability, and stability of power supplies.

Also, a finite number of mirror electrodes means that the "ideal" reflecting potential is truncated up to some order. It generates optical aberrations that affect ion orbit and, thus, the isochronicity of the system. This is illustrated in figure 3.17, which shows the time-of-flight of several simulated particles (with a Gaussian energy distribution) after one isochronous turn in an analyzer. The effect of aberrations due to the truncated potential is seen in the tails of the energy distribution. On the other hand, adding more mirror electrodes increases the degrees of freedom of the system, which makes it harder to tune and more prone to instabilities. An optimal configuration balances aberration effects and ease of tuning and operation.

3.3.2 Operation as a Mass Spectrometer

The isochronous operation of the mass analyzer turns the MR-ToF-MS into a fast and versatile high-resolution mass separator. However, challenges appear when the system is used to reach the highest possible resolving power.

In ToF-MS techniques, the final mass resolution depends on the time spread Δt_0 acquired by initial conditions. MR-ToF-MS systems minimize the influence of initial conditions by extending the flight path to a large number of turns N_a inside a mass analyzer. However, as seen in fig. 3.17, the isochronicity is not perfect, and a small time-of-flight error Δt_a is added at each turn. The resolving power in such system is then [124]

$$R_m^{\text{MR-ToF-MS}} = \frac{t_0 + t_a\, N_a}{2\,\sqrt{(\Delta t_0)^2 + (\Delta t_a\, N_a)^2}} \quad , \tag{3.32}$$

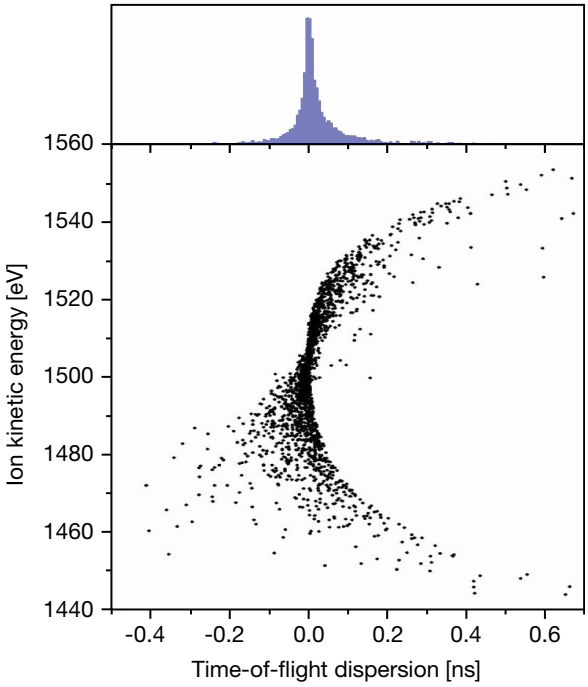

Figure 3.17: Simulated time-energy relation of an ion cloud through one turn in a mass analyzer. All particles departed simultaneously from the middle plane of the analyzer with an energy spread of 22.5 eV around 1.5 keV. The top panel shows the histogram of the simulated events projected in the time axis. The non-isochronous patterns seen in the scattered events are created by the time-of-flight aberrations. Adapted from [129].

where t_a is the time-of-flight through a single turn in the analyzer. As the number of turns increases, the resolution reaches saturation:

$$\lim_{N_a \to \infty} (R_m^{\text{MR-ToF-MS}}) = \frac{t_a}{2\,\Delta t_a} \quad , \tag{3.33}$$

which can be orders of magnitude larger than a standard ToF-MS system.

In figure 3.18, a sample time-of-flight spectrum is shown, which was taken near the saturation resolving power of the used spectrometer. The achieved resolution exceeded $2 \cdot 10^5$ and enabled clear separation of the isobar doublet $^{40}Ar^+$ and $^{40}K^+$.

Naturally, Δt_a can be reduced with careful design and construction of the analyzer: aberrations and field penetrations need to be minimized; pieces need to be precisely machined and aligned; good vacuum need to be reached; materials with low thermal expansion coefficients need to be selected in order to minimize lengths fluctuations due to thermal expansion; power supplies need to be stable, and the electronics for signal processing need to have their noise minimized.

However, a few operational strategies and techniques considerably improve the resolution and the mass spectrometry capabilities of the MR-ToF-MS. Some of those, which are employed at the TITAN MR-ToF-MS system, are discussed next.

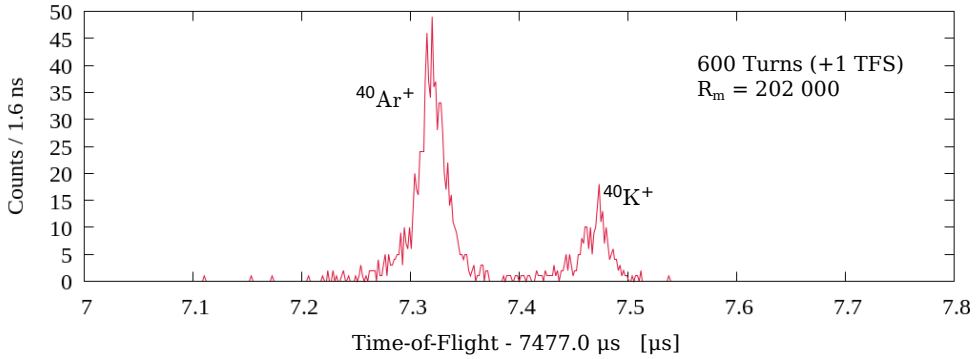

Figure 3.18: A time-of-flight spectrum from a sample containing $^{40}Ar^{+}$ and $^{40}K^{+}$ analyzed at TITAN's MR-ToF-MS using 600 isochronous turns. Reproduced from [130].

Time Focus Matching

As mentioned, a typical mass measurement cycle in an MR-ToF-MS consists of the injection of ions from a preparation device followed by an arbitrary number of isochronous turns inside the analyzer. Subsequent extraction of ions to a timing detector follows. However, the time focus at the isochronous turns is tuned for a specific flight path that does not comprise of the injection and extraction procedures. In such cases, the ideal time focus lies outside the analyzer.

This can be corrected: the time focus matching from injection and extraction is done by *time focus shift* (TFS) reflections [131]. In those cases, one mirror potential is temporarily switched to a different potential shape than the isochronous one. A "harder" potential (steeper derivative) brings the time focus closer, while a "softer" drives it further away. The switch to (or from) a TFS configuration is done when ions are in the other mirror to minimize the influence of ringing and switching noises.

In figure 3.19, one operation scheme is shown. It includes one TFS in the first turn to drive the time focus to the center of the drift region, and another TFS in the last turn to shift the time focus to the detector. In fact, many operations schemes are possible as long as the time focus remains at the detector. Studies reported that the same resolving power was obtained with 3 times fewer turns with the use of TFS turns [131].

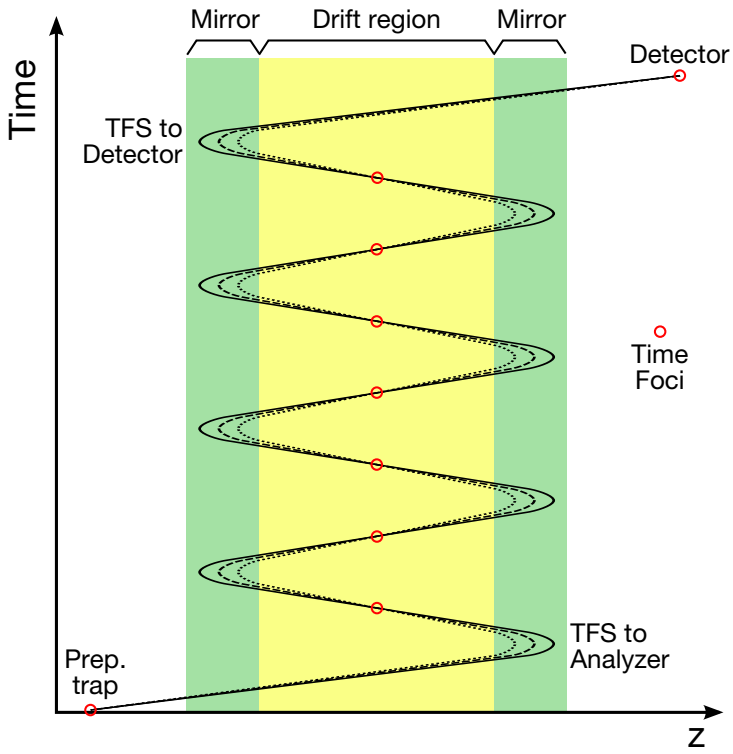

Figure 3.19: Example of a measurement cycle in an MR-ToF-MS. Ions (black trajectories) are injected into the analyzer, where they performed four isochronous turns before getting extracted to a detector. Two time focus shift reflections are performed to focus-match the injection and extraction of ions. Note that more energetic ions (solid line) have a larger amplitude, entering further inside the mirrors; yet, trajectories inside the analyzer are isochronous.

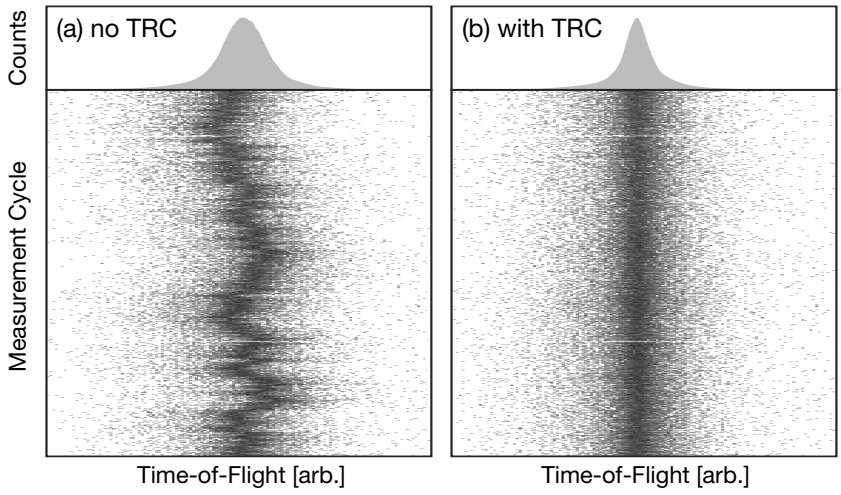

Figure 3.20: Time-of-flight histograms over many measurement cycles of the same sample, measured at the TITAN MR-ToF-MS. On top are the integrated histogram of all measurement cycles. In (a), the raw spectra shows large time fluctuations. In (b), a time-resolved calibration was applied to the same data, and the resolution was improved in 75%. The sample was analyzed for 20 minutes.

Temporal Fluctuations

A typical mass spectrometry measurement for one isotope may range in time from a few minutes to an hour, depending on the desired precision and the available yield of the ion of interest. The longer the measurements take, the more the system is prone to instabilities of power supplies or thermal swings that may alter the overall length of the analyzer. Such temporal variations slightly change the time-of-flight of ions and cause broadening of the peaks.

Such effect can be seen in panel *(a)* of figure 3.20: ion samples from the same source were repeatedly measured for 20 minutes, and the position of its time-of-flight peak significantly varies in time.

To first order, fluctuations affect all ions proportionally to their $\sqrt{m/q}$, keeping the isochronicity of the system. Using this fact, a *time resolved calibration* (TRC) can be applied to correct the spectrum for time-dependent drifts, as a post-measurement procedure [132].

In this procedure, the data is partitioned in time, and one intense peak in the spectrum is taken as a reference (as an internal calibrant). Every time partition is shifted in time-of-flight so that the centroid of the reference peak coincides with its centroid in the first partition. The result can be seen in panel *(b)* of figure 3.20, and may significantly improve the resolving power.

This procedure requires that an intense and well-resolved peak is present in the sample. If such species are not present, one artificially introduces an ion to the sample, preferentially with the same mass number as the species of interest, from an external ion source. Such a procedure is described in [133].

Mass Range Selector

A limitation of the MR-ToF-MS technique is an ambiguous mass range: ions with different masses may undergo a very different number of turns in the analyzer, but may appear very closely, or even overlapping, in the spectrum. This problem is illustrated in panel *(a)* of figure 3.21.

The "unambiguous" mass range can be defined as the mass range that contains only species that went through the same number of turns (N_a). It can be characterized by the ratio between the maximum and minimum m/q:

$$\frac{(m/q)_{max}}{(m/q)_{min}} < \left(\frac{N_a + 1}{N_a}\right)^2 \quad . \tag{3.34}$$

As the number of turns increase, the unambiguous mass range shrinks and the spectrum is more likely to have mixed-turn species.

In principle, it is possible to disentangle mixed-turn spectra by taking multiple spectra at different numbers of turns. However, an elegant solution to this is to include a *mass range selector* (MRS) [134, 123, 135] in the middle of the mass analyzer. It consists of a pair of deflecting electrodes with fast-switching capabilities. An RF signal is applied to one of the electrodes, momentarily switching the MRS from

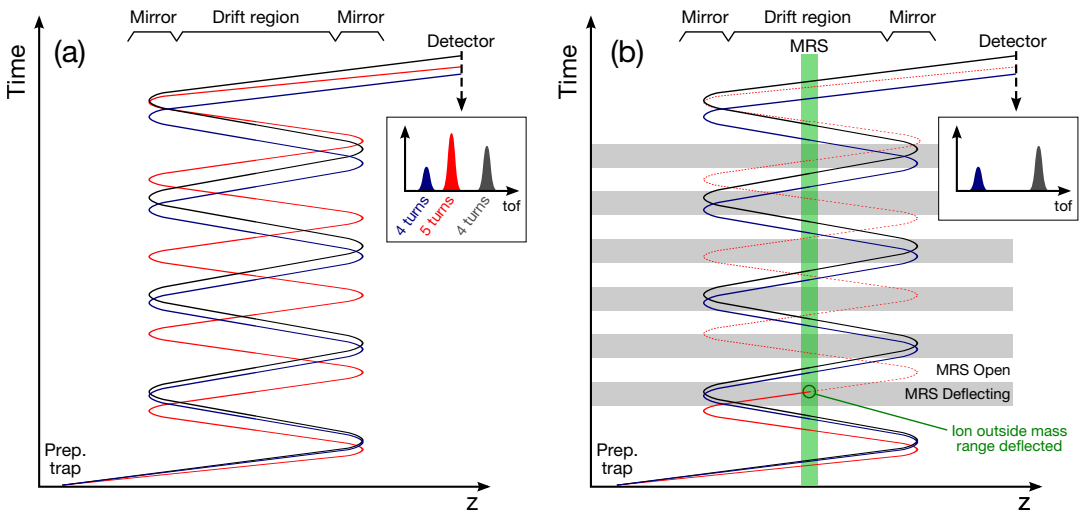

Figure 3.21: (a) The ambiguous mass range of MR-ToF-MS illustrated: a sample containing three different species are analyzer by an MR-ToF-MS, one (red) is considerably lighter and undergo more turns than the other two. In the spectrum (insert) it appears like an intermediate mass between the other two species. (b) A solution to this is to have a mass range selector tuned to only allow species within a certain mass range, deflecting the unwanted species and making the spectrum unambiguous. The green band shows the spatial dimensions of the MRS in the analyzer, while grey bands show the times when the MRS is deflecting.

an open state (through which ions pass unaffected) to a deflecting state, where a transverse electric field drives ions well out of their isochronous orbit, effectively removing them from the analyzer. The frequency of the signal is tuned to the revolution frequency of a specific desired mass range inside the analyzer, and ions within the range always pass through the MRS while it is in the open state.

The principle of the MRS is illustrated in panel *(b)* of figure 3.21. It must be noted that the design of the MRS must take into account minimal fringe fields in the analyzer section, and only low noise electronics should be employed.

3.3.3 Practical Considerations of the MR-ToF-MS Technique

MR-ToF-MS is an emerging technology in nuclear sciences. Its use in nuclear science was first proposed less than two decades ago [136]. The current generation of such spectrometers is able to achieve resolutions of 10^5 and relative mass precisions of 10^{-7} [123] which, combined with the advantages of a typical ToF-MS spectrometer, makes it a very competitive tool for nuclear sciences. Due to its performance, such systems are now in use or planned in every major radioactive ion beam facility [137].

As mentioned, MR-ToF-MS are fast and non-scanning spectrometers. A typical measurement cycle analyzes all species contained in the sample with single ion sensitivity and may only take a few milliseconds. If compared to the typical cycle of hundreds of milliseconds of the ToF-ICR PTMS technique, its performance is

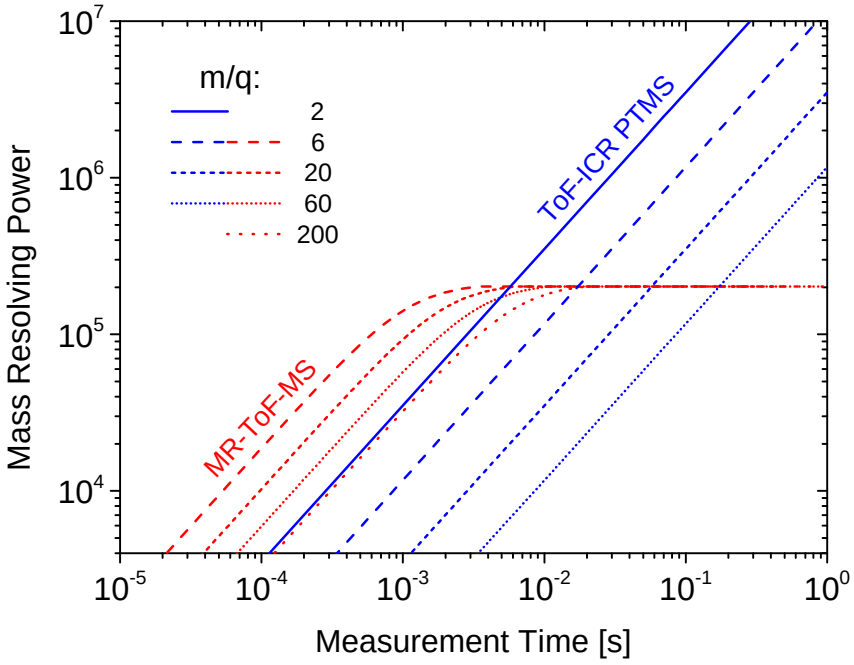

Figure 3.22: Performance of two mass spectrometry techniques (for several m/q) regarding their resolution as a function of their measurement times: MR-ToF-MS in red and ToF-ICR PTMS in blue. Values are based on the two spectrometers of TITAN facility (see sec. 4.2). It worth noting that ToF-ICR PTMS typically yields over one order of magnitude larger precision than MR-ToF-MS for the same resolving power and accumulated statistics.

very appealing for measuring very unstable and rare species. In figure 3.22 the mass resolution of the two techniques is compared as a function of the time scale of their measurements.

Because of its advantages, MR-ToF-MS systems have also been used for other applications in rare ion beam facilities. They have been employed as a high-resolution mass separator to deliver isobarically clean samples to other experiments [49] and as a beam diagnosis tool [138], which is also done in this work. The broadband operation and high sensitivity enable quick identification and quantification of unknown ion samples, which in turn allows fine-tuning of parameters involved in ion sample production and transport.

4 EXPERIMENTAL OVERVIEW

The experiment at the core of this thesis was performed at TRIUMF's Ion Trap for Atomic and Nuclear science (TITAN) facility [69]. Both PTMS and MR-TOF-MS systems were employed. TITAN's Penning trap mass spectrometer, the Measurement Penning Trap (MPET), has been in operation for over a decade. It is a very well established spectrometer for the mass measurement of radioisotopes and holds the World record for the fastest PTMS measurement [120]. TITAN's MR-ToF-MS was installed at the facility in April 2017. The results described here are from the inaugural experiment of the device; therefore, parallel and independent measurements of the same samples were performed using the two spectrometers. In this way, the results of the MR-ToF-MS could be compared with the results of the MPET spectrometer.

The TITAN facility itself is located at the Isotope Separator and ACcelerator (ISAC) [139] facility of TRIUMF laboratory in Vancouver, Canada. In the following section, an overview of the ISAC facility and its equipment employed in this experiment is presented. The TITAN facility is introduced in detail in section 4.2. Finally, the experimental procedure is outlined in section 4.3.

4.1 ISAC Facility and Isotope Production

ISAC uses the well established Isotope Separation On-Line (ISOL) method [139, 140] to produce Radioactive Ion Beams (RIBs). The RIBs are produced through nuclear reactions induced by a highly energetic (typically between 50 MeV to 1.5 GeV) driver beam on a thick target, inside which the reaction products stop. The target is coupled to an ion source, and the ionized isotopes are formed into a beam and sent through a mass separator. The selected isotope beam is then available for experiments.

The ISAC RIB production facility is depicted in figure 4.1. The main stages of the ISOL technique - production, ionization, and separation - are described in the following in the context of this experiment.

Production of Radioisotopes

The neutron-rich titanium isotopes were produced in an ISAC target made of natural tantalum impinged by a 480 MeV proton beam at 40 μA. The driver beam was provided by TRIUMF's main accelerator, an 18-meter cyclotron that can deliver proton beams up to 520 MeV.

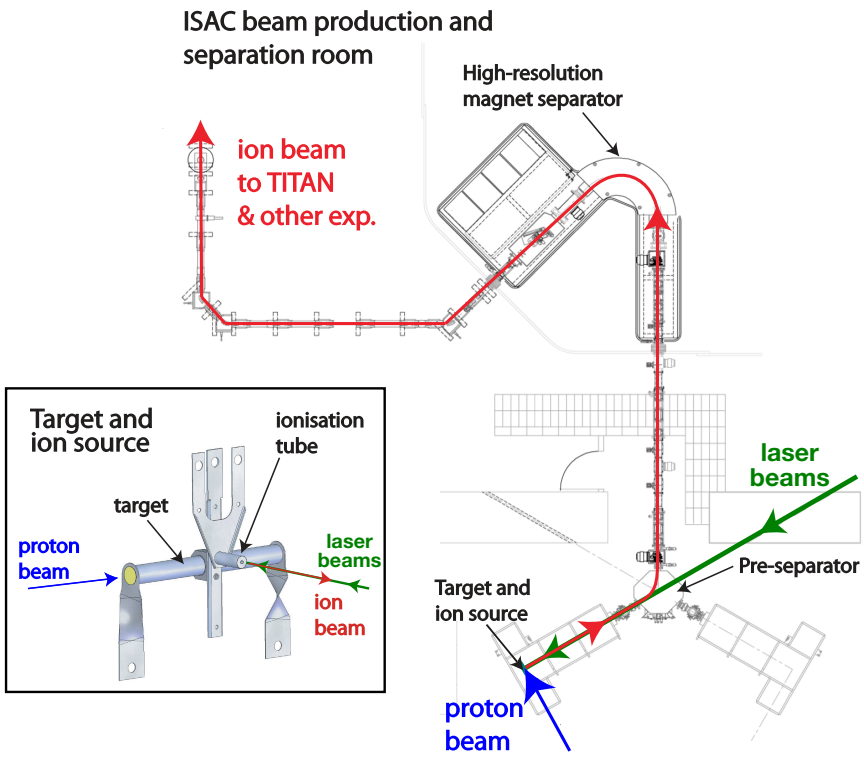

Figure 4.1: The RIB production facility at ISAC receives a high-energy proton beam (blue) from TRIUMF's main cyclotron and produces radioisotopes in a hot thick target, whose module is depicted in the inset. Ions are produced, in the case of this experiment, through resonant photo-ionization by shining lasers (green) onto the target module. An ion beam (red) is created, sent through a mass separator and delivered to experiments. Figure adapted from [141].

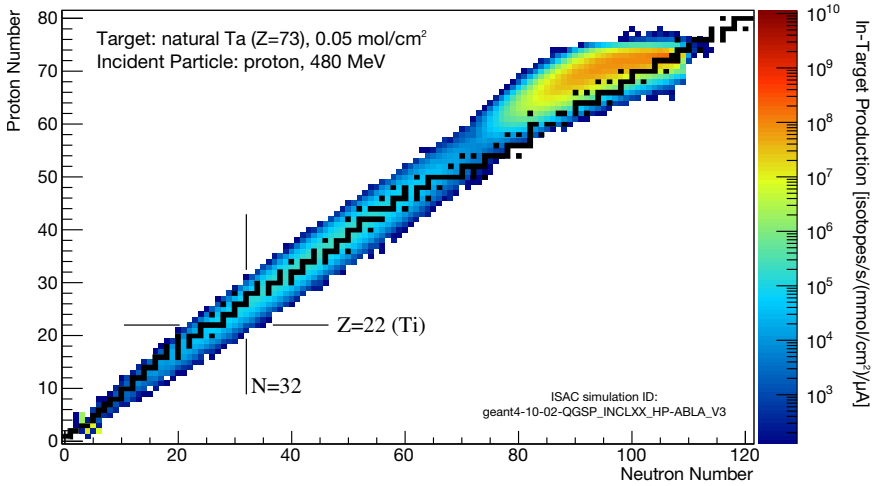

Figure 4.2: Simulated normalized production yields of radioisotopes using a tantalum ISAC target, obtained through the ISAC Yield Database [142]. Both stable isotopes (in black) and the region of interest (titanium isotopes around $N = 32$) are marked for reference.

The protons induce nuclear reactions in the target. Tantalum nuclei undergo spallation and fragmentation reactions, and the product particles stop inside the target medium. In this process, a large number of isotopes are produced [143]. Figure 4.2 shows simulated radioisotope production under the conditions of the experiment, highlighting the region of interest in this experiment.

Release and Ionization

In the ISOL technique, to form an ion beam, the isotopes of interest need to be released from the target and reach an ion source. The release process requires isotopes to diffuse out to the surface of the target material, undergo desorption and effuse out of the target container towards the ion source.

ISOL targets are heated to high temperatures ($T \approx 2000\,^{\circ}\mathrm{C}$) to enhance the release processes. However, chemical and physical processes that influence the release efficiency, such as diffusibility, volatility, and decay half-life, affect the availability of certain beams [140, 144]. As a consequence, for example, the production of ion beams of refractory metals and reactive elements, such as iron and boron, is currently very challenging [145].

After the release, the isotopes are formed into an ion beam by an ion source. The most common and simple ionization process found in ISOL facilities is surface ionization. In many cases, the produced ion beam will have surface ionized components (unless the source is specially designed to suppress them, such as in [146]). The surface ionization efficiency (ε_{ion}) strongly depends on the temperature (T) and on the species' first ionization potential (E_i):

$$\varepsilon_{ion} \propto \left[1 + \mathrm{e}^{-(W-E_i)/k_B T}\right]^{-1} , \tag{4.1}$$

where W is the work function of the surface material and k_B is the Boltzmann constant.

For example, alkali species, whose ionization potential is typically below 5 eV, are very easy to be surface ionized. Titanium, however, has a relatively high ionization potential ($\sim$ 6.8 eV, see fig. 10 of [147]). Moreover, its target release properties are such that it was even included among particularly difficult (or almost impossible) ISOL beams [145]. Therefore, a different technique was employed to efficiently ionize titanium atoms released from the target: the resonant laser ionization [148].

The technique photo-ionizes atoms by using high-power lasers that resonantly promote atomic transitions. In a multi-step process, a valence electron is excited to a high-lying energy level and then detached from the atom by another transition (via an auto-ionizing state, for example) [148]. This method is element selective, and most atoms that reach the laser interaction region are successfully ionized, making it extremely powerful for rare isotope research.

At ISAC, the TRIUMF's Resonance Ionization Laser Ion Source (TRILIS) [149] was employed in the ionization of titanium isotopes, using a two-step laser ionization

scheme [150]. The two laser beams were merged into the ionization region of the target module.

Mass Separation and Delivery to Experiments

After ionization, the ions were formed into a continuum beam from the target. The target and ion source modules were biased at 20 kV, which electrostatically accelerated ions as they leave the modules. The beam was sent through a two-stage dipole magnet separator that includes a pre-separator and a high-resolution magnet separator [151]. This setup has a mass resolution of about $R_m = 2000$ (see eq. 3.2), which is enough to select the desired mass number but does not allow to entirely separate isobars. The ion beam was transported through electrostatic optics in a high vacuum environment and delivered to the TITAN facility.

4.2 The TITAN Facility

The TITAN facility is an ion trap system developed to perform mass spectrometry of rare and short-lived isotopes [152]. It has been in operation since 2007, with the commissioning of its Penning trap mass spectrometer [120, 153]. It distinguishes itself from other facilities by its ability to employ fast measurement cycles and by its capability of increasing the charge state of the analyzed ions. Its diverse combination of ion traps, coupled to the intense isotope production sources available at ISAC, makes TITAN a unique facility in the world.

The TITAN facility is depicted in figure 4.3, highlighting the main components. The two mentioned mass spectrometers are described in detail in sections 4.2.2 and 4.2.3. The following devices are also central to the operation of TITAN experiments:

RFQ: the ion beam delivered from ISAC is accumulated in a Radio-Frequency Quadrupole cooler and buncher (RFQ) [154]. The RFQ is a preparation ion trap filled with He gas for beam cooling. The RFQ delivers bunched beam with a small energy spread to the other ion traps at TITAN. Further details on this device are presented in sec. 4.2.1.

Stable Ion Source: the RFQ can also receive stable beams from a surface ionization alkali source, typically employed for tuning and optimizing the system and as a source of calibrant ions. For both applications, it is desired to use ions with a mass close to the species of interest, $A = 50 - 56$ in this case. A source containing natural potassium and rubidium was installed, so ion species of ^{39}K, ^{41}K, ^{85}Rb and ^{87}Rb were available.

EBIT: an Electron Beam Ion Trap (EBIT) is typically used as an ion charge breeder, further ionizing ions through electron impact ionization [155]. Employing ions at high charge states is known to boost precision and resolving power in the ToF-ICR technique (see eq. 3.27) [156]. However, it requires additional ion preparation time, which can be prohibitive for very short-lived species, and

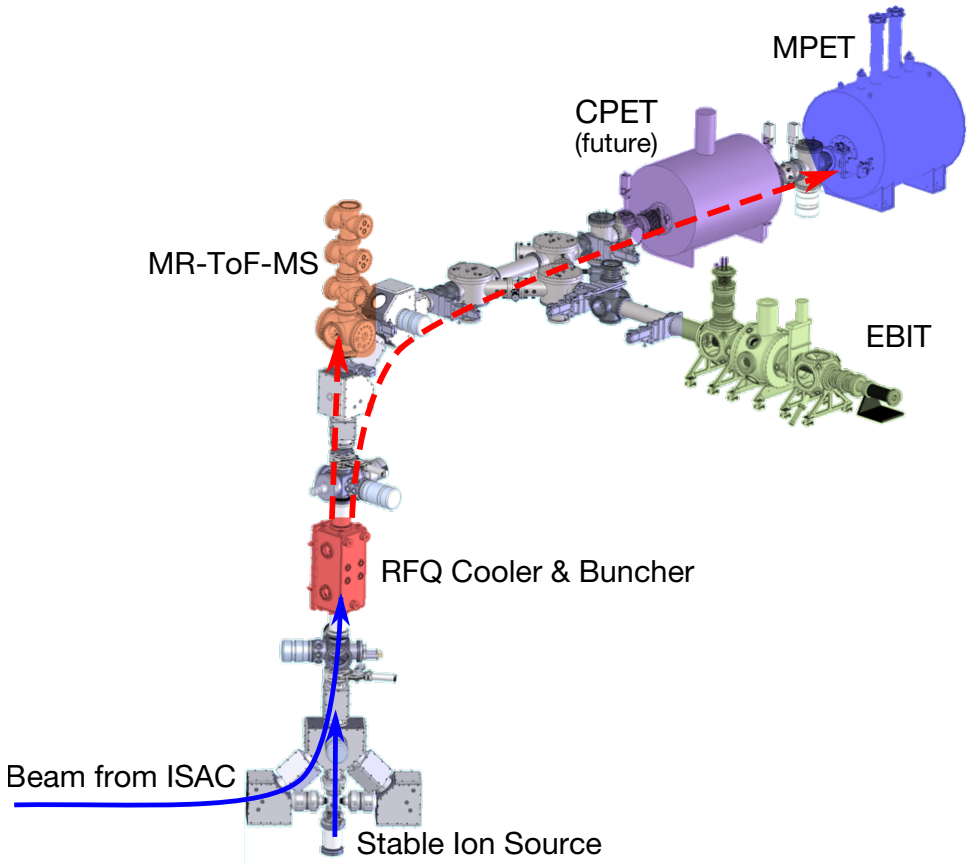

Figure 4.3: Schematic overview of the TITAN facility, depicting its ion traps and the beam transport paths employed in this experiment. Continuous ion beams (blue lines) are received from ISAC or TITAN's stable ion source in the RFQ cooler and buncher. The RFQ delivers cold ion bunches (red dashes) to other traps. In this experiment, ion bunches were independently sent to the MR-ToF-MS and to the MPET.

may reduce the quality of resonances. A Cooler Penning Trap (CPET), designed to provide further cooling of highly charged ions from EBIT, is being prepared to be installed in the TITAN beamline in the near future [157].

With the installation of the MR-ToF-MS, it is essential to compare the two spectrometers accurately. Therefore, it is desirable that both spectrometers measure the same ions in similar conditions to avoid systematic effects. The titanium ions were measured in a singly charged state ($q = 1$) in both spectrometers. The EBIT was bypassed in this experiment.

All TITAN ion traps are connected by about 12 meters of ion transport beam lines kept under ultra-high vacuum (UHV) conditions ($\approx 10^{-8}$ Pa). The transport of ions between devices is done by electrostatic ion optical devices such as Einzel lenses, correction steerers, benders and quadrupoles. The transport and optimization of ion beams through TITAN is described in section 4.2.4.

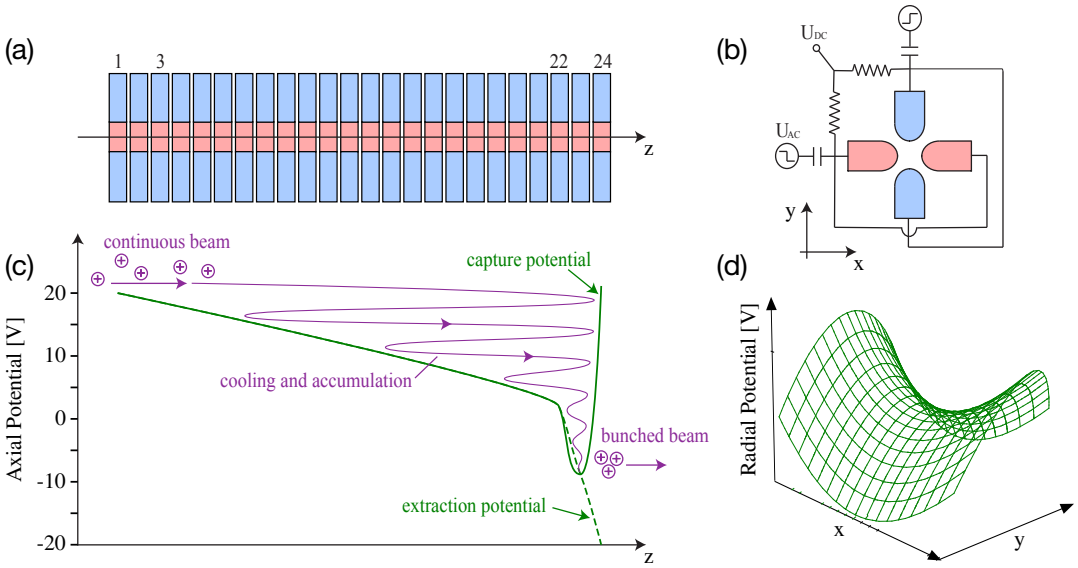

Figure 4.4: The electrode structure of the TITAN RFQ viewed from the (a) axial and (b) radial orientations, the color code indicates the phases of the RF applied to the rods and panel (b) also features a simplified electronic scheme used to bias each electrode with RF and DC voltages. (c) The electrical potential in the axial direction, as used in this experiment, is shaped to guide the ion as it cools towards a potential well by the extraction end. (d) In the radial direction, the alternating saddle potential created between the rods keeps ions confined. Adapted from [154].

4.2.1 Preparation of Ion Beams with the TITAN RFQ

The ISAC facility delivers continuum ion beams to TITAN at a kinetic energy of typically 20 keV. The radioisotope production process introduces energy spreads of a few tens of eV. Such conditions are not favorable for precision experiments in ion traps. In ion traps, ions are brought to a quasi-rest state, with a low energy spread. Moreover, it is desirable to delivered ions in bunches for optimized capture into a trap.

The TITAN RFQ provides the interface between ISAC and TITAN [154]. It is a gas-filled *Paul trap* (introduced below) that is used to accumulate the delivered ions for a certain period, reduce their energy and energy spread, and send them to the subsequent traps in bunches.

The overall structure of the RFQ is shown in figure 4.4. It is mainly composed of four parallel rods of 70 cm length, and each rod is segmented into 24 electrodes. It is contained in a chamber filled with high-purity He gas at a pressure of ≈ 1 Pa. Differential pumping apertures on each side allow ion injection and extraction between the gas-filled chamber and the UHV environments of ISAC and TITAN.

In the following, the principle of trapping, cooling, and bunching of the RFQ are explained.

Trapping

As in any ion trapping device, ions must be confined in three dimensions. In a linear Paul trap such as the TITAN RFQ, the confinement in one of the directions (axial) is given by an electrostatic potential well as in Penning traps. Such configuration can be generated by segmenting the rods, here into 24 electrodes. The very first 22 electrodes generate a slowly-varying drag field that guides ions towards one end of the RFQ. The last few electrodes create a deeper potential well where ions are accumulated as they cool down. This is illustrated in panel *(c)* of figure 4.4.

A dynamic electric field generates the confinement in the radial (or transverse) direction. In each rod, an RF signal is superimposed on the static field that generates the axial potential. The signal is applied with 180° phase shifts on sets of rods perpendicular to each other, as shown in *(b)* of figure 4.4. The resulting field is described by a time-varying quadrupole. The potential surface at a given time is described by a saddle, as in panel *(d)* of figure 4.4. It is metastable. With the correct tuning of the frequency and amplitude of the signal to the m/q of the trapped species, an average confinement is created. Further details can be found in [154].

Cooling

As mentioned, the incoming beam needs to be decelerated from 20 keV to quasi-rest, with minimal energy spread. The bulk of the deceleration is done by floating the RFQ on a high-voltage platform with bias slightly below the beam energy. The beam is injected into the RFQ with a few tens of eV, just enough to surpass the entrance potential barrier.

The rest of the energy is dissipated by collisions with the helium buffer gas inside the RFQ. Multiple collisions occur until the ions are in thermal equilibrium with the gas. After thermalization, the energy distribution is Boltzmann-like with a spread of a few tens of meV. The complete cooling process takes a few milliseconds [154].

Helium is an appropriate choice of a buffer gas[21]. It is a light gas, so it efficiently absorbs momentum from almost any (heavier) incoming beam. Also, He is chemically inert, with a high ionization energy of 24 eV. This is essential to prevent the injected ion from changing its ionization state by electron exchange with the gas particles. This is further facilitated by high purity. Small amounts of contamination in the buffer gas may significantly reduce the efficiency of the device.

Bunching

After a few milliseconds of continuous beam injection and cooling, the ions are accumulated in the potential well. This bunch is then ready to be sent to the other ion traps at TITAN. This is done by switching the last few electrodes to an open trap configuration, as shown in panel *(c)* of figure 4.4 (dashed green curve). The bunch is released to the TITAN system and can be transported to the other devices.

21 Occasionally, different buffer gases may be more suitable to cool the incoming beam. For example, with lighter species ($A < 12$), H_2 has shown to increase the efficiency by a factor 2 compared to He.

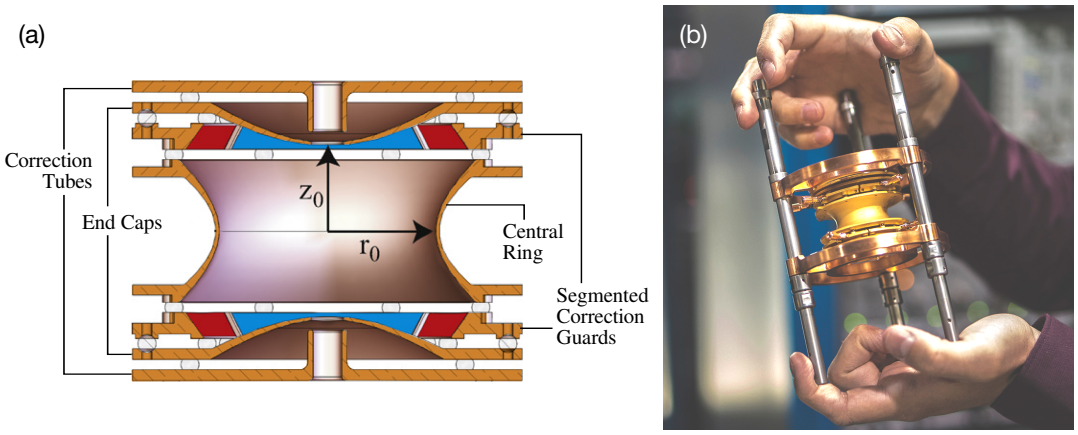

Figure 4.5: (a) Schematic of the MPET electrode structure. On the guard electrodes, the blue-red color code express the opposite phases of quadrupolar excitation. Figure adapted from [110]. (b) Photography of the MPET assembly for scale, courtesy of Stuart Shepherd.

4.2.2 The Measurement Penning Trap

The TITAN MPET is a Penning trap mass spectrometer designed to provide fast measurements of short-lived species, and it is the only in the world to be able to perform mass spectrometry of unstable highly-charged ions. It currently employs the ToF-ICR method and can provide mass precision and accuracy as good as one part-per-billion [110, 158]. The characteristics of the MPET mass spectrometer are described below.

Electrode configuration: the MPET uses a hyperbolic Penning trap system such as described in chapter 3. A schematic of its electrode structure is available in figure 4.5 and its characteristic dimensions are presented in table 4.1. The central ring electrode and the end caps are shaped as surfaces of two hyperboloids of revolution. Besides them, additional electrodes are included to correct the potential for truncations of those surfaces: "tube" electrodes are added after the end caps to compensate for the 4 mm apertures used to inject and extract ions, "guard" electrodes are added between ring and caps to provide higher order field corrections. The trap "depth" of MPET, defined as the potential difference between the ring and end caps, is typically of 35.75 V. The electrode compensation procedure to shape the adequate trapping potential is described in [110].

Table 4.1: Characteristic dimensions of the MPET, according to eq. 3.7.

r_0	15.000 mm
z_0	11.785 mm
d_0	11.210 mm

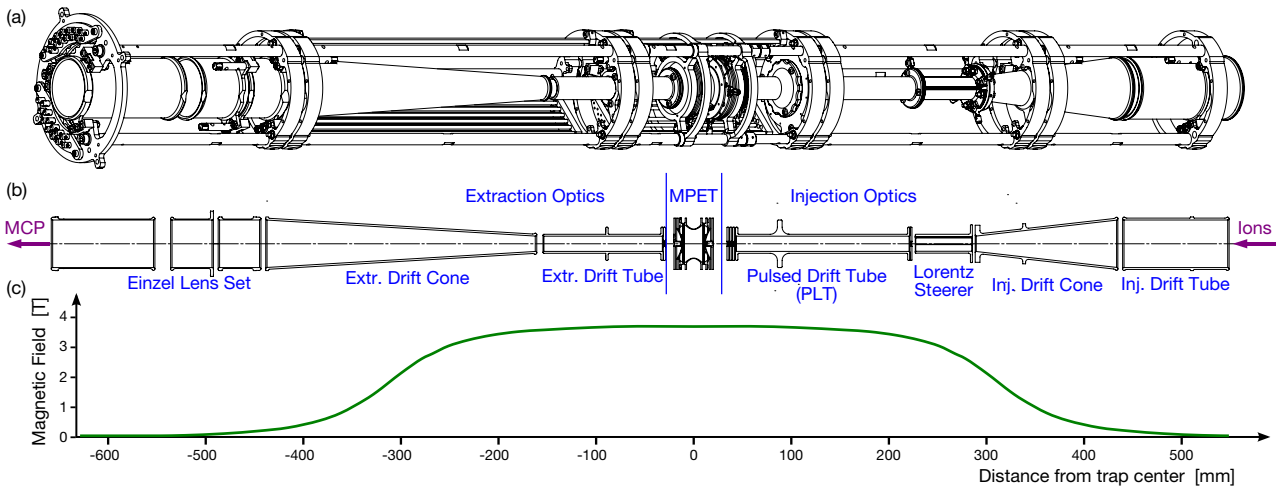

Figure 4.6: (a) Drawing of the MPET setup enclosed inside the magnet bore, showing the trap, its injection and extraction systems and the support and wiring structures. (b) The electrode setup of MPET and its associated ion optics. (c) Map of the axial magnetic field strength across the position inside the bore.

Magnetic field: the trap configuration sits in a 3.7 T magnetic field generated by a superconducting solenoid (see fig. 4.6). The used magnet performs stably over time, which reduces systematic uncertainties. The MPET magnetic field decays at a relative rate on the order of 10^{-11} per hour.

RF excitations: the RF signal for ion manipulations is applied to the guard electrodes, which are appropriately segmented (see fig. 4.5.a).

Fast ion preparation: MPET is one of the few PTMS systems to employ Lorentz steerers in ion preparation into an initial magnetron orbit [117] (see fig. 4.6). As explained in section 3.2, this technique allows for rapid magnetron radius preparation of the sample and achieves a high level of reproducibility. The use of Lorentz steering enabled, for example, the measurement of ^{11}Li at MPET, with a half-life of 8.75(14) ms [120].

Detector: the ToF-ICR method requires detection with single-ion sensitivity. For this purpose, a Micro-Channel Plates (MCP) [159] detector was installed about one meter downstream of the trap ejection. The efficiency of MCP detectors typically ranges between 40% to 60%, depending on the ion's velocity, charge state, age and conditioning of the detector.

The sources of systematic deviations in mass measurements due to the construction of MPET, such as imperfections of trapping electrodes, field misalignments, instabilities of the trapping potential and magnetic field and anharmonicities of the trapping potential, were evaluated. Combined, they yield deviations on the order of $2 \cdot 10^{-10}$ per unit of m/q [110]. However, other systematic sources such as ion-ion interactions and relativistic effects should be evaluated on a case-by-case basis.

MPET sits in a UHV environment at a pressure on the order of 10^{-7} Pa, which enables mass measurements of ions at high charge states up to $q \approx 18$. The experiment

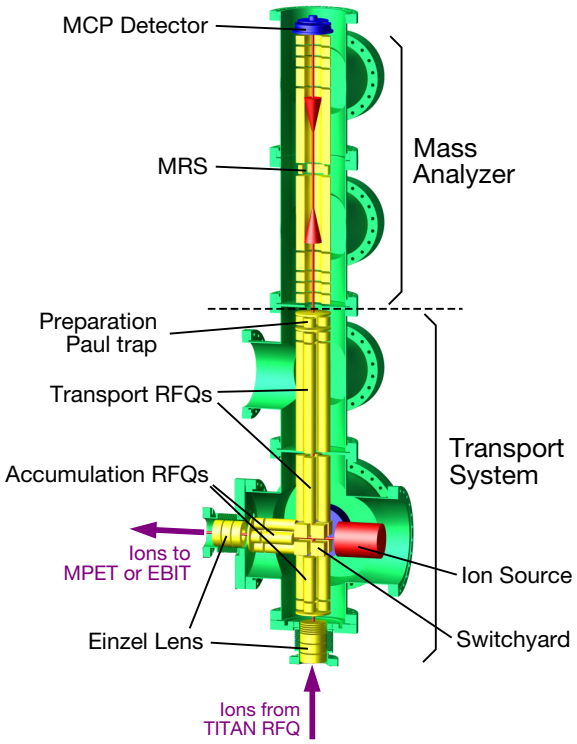

Figure 4.7: Scheme of the TITAN MR-ToF-MS, highlighting its main components. Figure adapted from [160].

described here is the last one performed with this trap configuration after a decade of operation. A new Penning trap system that will replace MPET is under commissioning. The new system, described in appendix B, has an improved cryogenic vacuum system to be able to access charge states well beyond +20 and is being prepared to enable the PI-ICR technique [115] of cyclotron frequency measurement (briefly described in section 3.2.3).

4.2.3 The TITAN MR-ToF-MS Spectrometer

The TITAN MR-ToF-MS system [160] was installed and commissioned at TITAN facility in April 2017 [130]. It was developed by the IONAS group at the University of Gießen [161, 123] based on the established concept of the MR-ToF-MS installed downstream of the fragment separator at the GSI laboratory [124] in Darmstadt, Germany. It can provide mass values with 10^{-7} relative precision with great ion sensitivity. In addition, the system is able to tolerate contaminant ions with rates up to 10^6 times higher than the rate of ions of interest. Hence, it acts as a complementary mass spectrometer to MPET.

Besides being a research station itself, the TITAN MR-ToF-MS was also designed to serve as a high-resolution mass separator to couple to other traps at TITAN. With a mass resolution beyond $2 \cdot 10^5$, overall efficiency on the order of 50% and capacity

to hold more than 10^4 ions per cycle, the TITAN MR-ToF-MS is capable of performing sample purification up to the isobar level. Therefore, beyond its operation as a mass spectrometer, its setup is also able to separate specific isobars from a highly contaminated sample in the mass analyzer, recapture only the desired species, and send ions back to the TITAN facility to be used in other experiments. This section focuses on the operation of the TITAN MR-ToF-MS as a mass spectrometer.

The MR-ToF-MS was designed to be a stand-alone system. It has its own internal ion source and ion preparation apparatus to allow independence with the rest of TITAN beamline. It enables its tuning and operation simultaneously with other TITAN systems without conflicts. The MR-ToF-MS system is schematically depicted in figure 4.7. It can be divided into two sectors: the ion transport system and the mass analyzer, described next.

Transport System

As a stand-alone system, the TITAN MR-ToF-MS has its own ion preparation setup. Ions are received from the TITAN RFQ and accumulated, cooled and bunched before their injection into the mass analyzer. The preparation and transport system allows the TITAN MR-ToF-MS flexibility. Beyond the aforementioned advantage of independent tuning from the rest of the TITAN system, the MR-ToF-MS can keep its own measurement cycle independent of the rest of the TITAN setup.

The transport system is schematically depicted in figure 4.7. All transport components are based on RF quadrupole optics in a He buffer gas environment, using the same concept of the TITAN RFQ[22]. Ions are efficiently transported through the system at low kinetic energy, on the order of a few eV. The main components are briefly described in the following, while a more complete description can be found in [162].

Accumulation RFQs: the interface between TITAN and its MR-ToF-MS is done through a pair of RFQs. One receives ions from the TITAN RFQ while the other sends isobarically clean beams towards MPET or EBIT. The latter is done after a separation cycle in the mass analyzer.

RFQ Switchyard: the RFQ switchyard is a cube-shaped RF optics device with 6 RFQs overlapping on its center. It is capable of receiving and transmitting ions at any side. It may receive ions from multiple sides and merge them into one single output. Technical aspects of the switchyard are discussed in [163, 162].

Internal Ion Source: the MR-ToF-MS has a surface ionization source to provide alkali ions. It is employed for offline tuning of the system and to provide calibrant ions for online measurement when convenient. The ion source streams ions into one of the inputs of the switchyard, which can merge it with the sample coming from TITAN RFQ.

22 One important technical difference between the TITAN RFQ and the RFQs in the MR-ToF-MS is the generation of the potential gradient that guides ions from one side to the other. They are created by resistive plastic rods, which provides a much smoother gradient than the discrete segmentation of the rods.

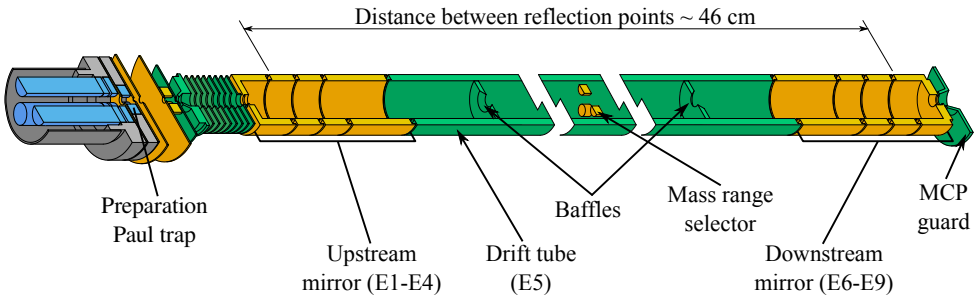

Figure 4.8: Electrode structure of the mass analyzer of the TITAN MR-ToF-MS, including the preparation Paul trap upstream. Figure adapted from [162].

Transfer RFQ: this RFQ connects the switchyard to the preparation Paul trap at the entrance of the analyzer. It can work in both directions, bringing ions to the analyzer or returning purified samples from the analyzer to the switchyard.

Preparation Paul trap: prior to their injection into the analyzer, ions are further cooled in a Paul trap. It provides well-defined starting conditions of the ion sample, so ions enter the analyzer with a small time spread.

Additional to the main RF optics, electrostatic optic elements are included through the transport system for steering and focusing of ions. Similarly to the TITAN RFQ, it is also filled with high-purity He gas at a pressure on the order of $\approx$ 1 Pa. Differential pumping apertures separate the transport system from the $\approx 10^{-5}$ Pa environment of the mass analyzer.

Mass Analyzer

The mass analyzer of the TITAN MR-ToF-MS is a scaled version of the mass analyzer of the MR-ToF-MS at GSI [160]. Its electrode structure is depicted in picture 4.8. Ions fly roughly one meter each turn with a kinetic energy of about 1.3 keV. The central drift region is grounded, while the mirrors can be switched to load or eject ions, or to perform TFS turns (see section 3.3).

The analyzer is symmetric, having identical Einzel lensing mirrors in both ends. The mirrors have a four-electrode design, which is a compromise between tolerable aberrations and ease of tuning and stability. The electric potential generated at the mass analyzer during isochronous reflections is also similar to the one depicted in figure 3.13. The existing aberrations introduced by the mirrors allow symmetric peak shapes, with roughly identical tails in both sides. This is advantageous during data analysis, reducing potential systematic errors.

A mass range selector (MRS) system, as described in sec. 3.3.2, is installed at the center of the drift region, and its performance is characterized in [135]. A pair of baffles are mounted in the analyzer to block the particles deflected by the MRS and to limit the field penetration between mirrors.

As in the MPET, the time-of-flight detector placed after the analyzer is an MCP detector.

4.2.4 Transport and Optimization of Ion Beams

ISAC delivers ion beams typically at a kinetic energy of 20 keV. Such energies allow beam transport through long and complex paths with high efficiency. To simulate similar conditions of beam entering the TITAN RFQ, the TITAN ion source for stable isotopes is also biased at 20 kV.

The beam is decelerated and cooled at the TITAN RFQ, which is biased slightly below 20 kV to allow for ions to enter. As ions are bunched out of the RFQ, they are accelerated again. The next unit is a pulsed drift tube (PB5). The PB5 has its bias pulsed down while ions are flying through it. This allows one to adjust the transport energy through the TITAN beamline.

The ion transport energy through TITAN is typically a few keV, which allows efficient beam transport without the need for advanced high-voltage instrumentation. The beam transport to the MPET and the MR-ToF-MS are sketched in figure 4.9.

At the MR-ToF-MS, the transport system is biased to 1.3 keV and ions are decelerated and transported at a few eV. Then, they are accelerated back to 1.3 keV when entering the analyzer. The use of its own independent transport system and high-stability power supplies makes the beam properties and the tune of MR-ToF-MS very stable and independent of the tune of the TITAN RFQ.

The beam is sent to the MPET with 2.2 keV transport energy. Before entering the trap, the beam is decelerated and pulsed down by another pulsed drift tube (PLT). The energy is regulated so that ions enter the trap and reach its center at quasi-rest, when the trap is closed. The long flight path to the trap makes the transport to MPET very sensitive to instabilities in power supplies. One volt fluctuation in the biases of RFQ or PB5 ($\sim$ 0.005%) alters considerably the properties of the ion captured. Therefore, beam energies (biases of PB5 and PLT) and the capture timing are finely tuned to yield the ToF-ICR resonance with the best quality and ion transport efficiency, and those must be readjusted once or twice daily to account for potential drifts. The procedure for optimizing injection, mainly regarding beam energy and timing, is discussed in [141].

The beam is guided through the TITAN beam line using electrostatic optical devices. Benders, pairs of parallel plates to which a potential difference is applied, are used to steer the beam path, either to transfer the beam to a different section of the beamline or to perform a small correction. In addition, the beam focus is adjusted by Einzel lenses (already explained in ch. 3, see fig. 3.14) and electrostatic quadrupoles. The map of the TITAN beam line showing its optical devices between the RFQ and the MR-ToF-MS and the MPET is shown in figure 4.10.

Since the MR-ToF-MS is closer to the TITAN RFQ and has its own preparation system, tuning the beam transport to it is relatively straightforward. The transport to the MPET, however, requires the optimization of a few tens of parameters, and this may be a very complex procedure. Recently, an algorithm was implemented to perform the optimization of beam transport once an initial tune is found.

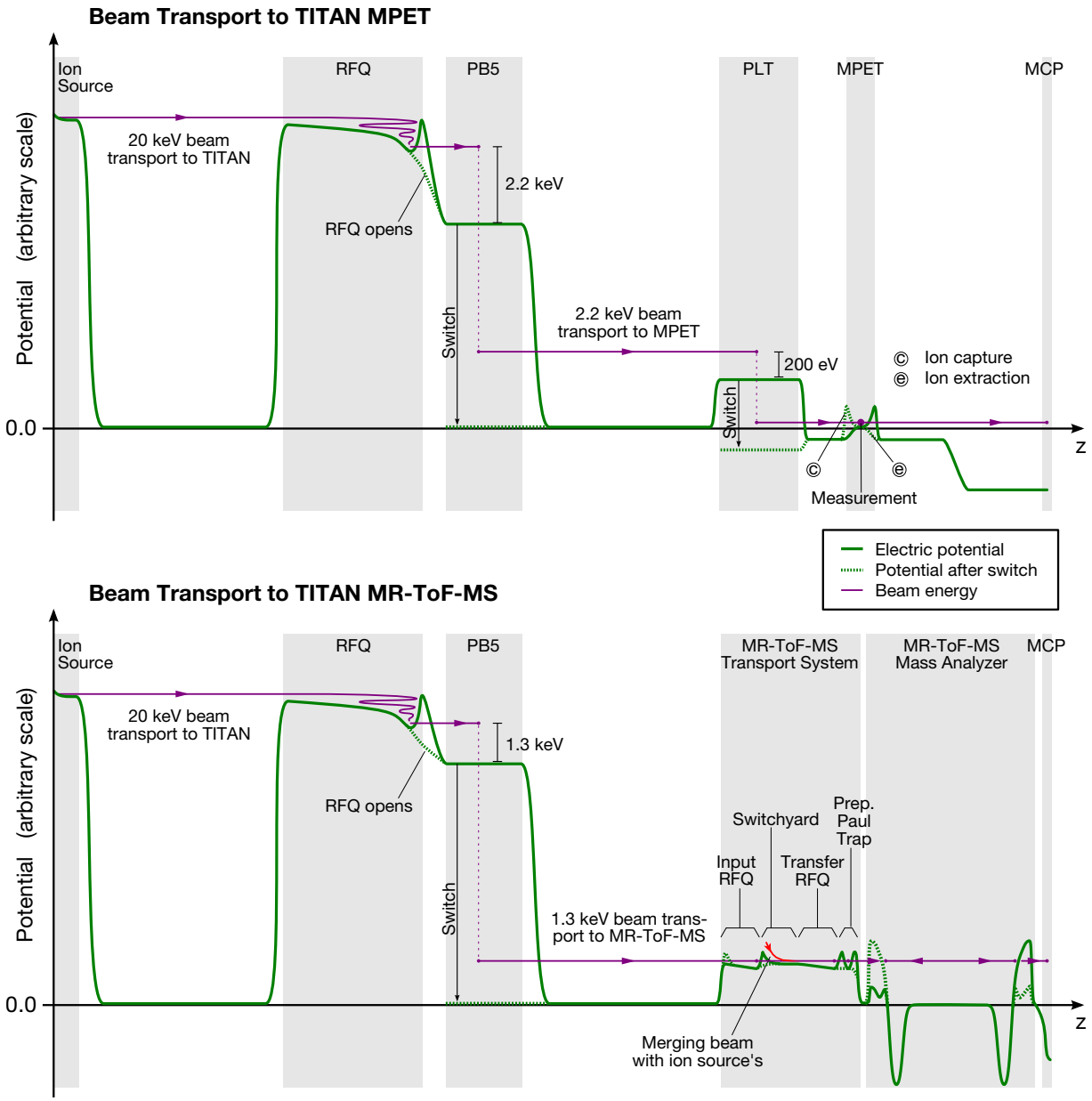

Figure 4.9: Sketch of the electric potential and total beam energy along the beam transport path to send ions from the used ion source (either TITAN's or ISAC's) to the MPET (top) and the MR-ToF-MS (bottom). The contributions to the electric potential generated by electrostatic optic elements are not shown. Shaded regions represent the placement of specific equipment. Distances and energies are not to scale.

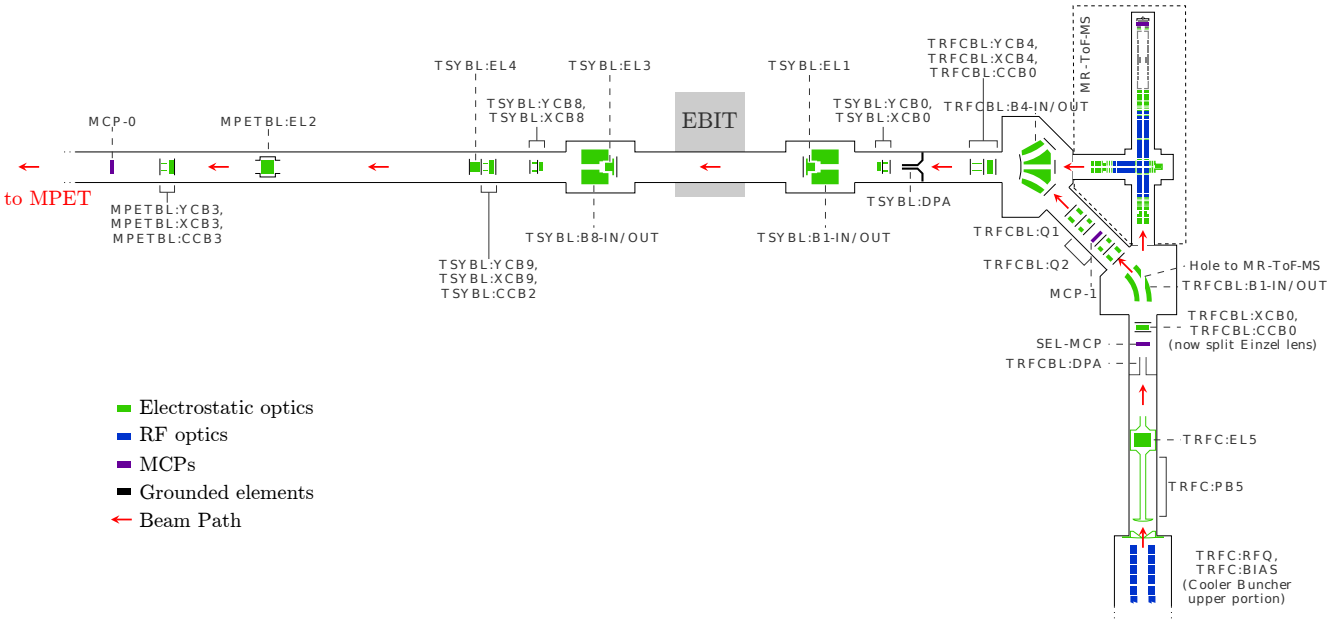

Figure 4.10: Optics map of TITAN beamline to transfer beam from the RFQ to the MR-ToF-MS or the MPET. The beam line towards EBIT is not shown. Figure adapted from [130].

The optimizer is a genetic-type algorithm that searches for the optimal value of a given criterion. Generically, the criteria combine transport efficiency (number of ion counts per cycle), ToF-ICR resonance quality and proximity of the converged parameters to the ones found by theory[23]. For each element in the beamline, the optimizer searches for the value that optimizes the criteria. Then it moves to the next element in the list and keeps performing this procedure until convergence.

In figure 4.11, an example of such optimization is shown. Initially, a reasonable ion count (black line) is observed, but a large injection steering (red line) is present. This means that the incoming beam is not being injected in a straight path and, thus, the quality of its injection is non-optimal. Injection steering can be measured by the time-of-flight effect when the Lorenz steerers are off. Time-of-flight effect is defined by by $ToF_{eff} = [tof(0) - tof(\omega_{RF})]/tof(\omega_0)$ (see eq. 3.26) and is an indirect measurement of initial magnetron radius. Ideally, with the Lorenz steerers off, ion should be injected in the center and $ToF_{eff} = 0$. After about 80 iterations, the steering was removed and the transmission improved by 40%. The whole procedure ran for about 12 hours without human interference.

Typically, beam transport optimization is done using stable ions from the TITAN ion source. Once optimal settings are found, it is only necessary to scale the timings for the m/q of the isotopes of interest from the time values obtained for the stable ions. Ion optical devices are kept constant.

23 For example, an ideal transmission tune would not require correction benders to be used. Therefore the optimizer shall search for a configuration in which such elements are performing minimal steering.

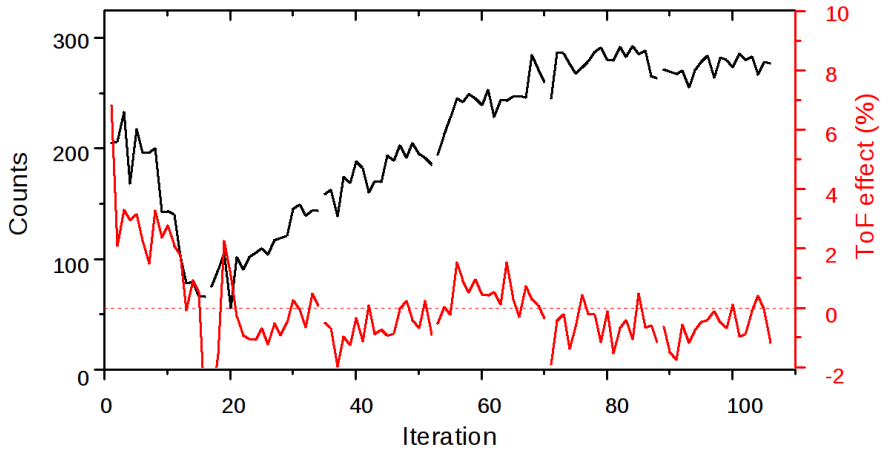

Figure 4.11: An example of automatic optimization of beam transport to MPET. The algorithm scanned a parameter space of 16 optical elements to remove an initial injection steering, seen on its effects on the the time-of-flight effect (red line), and improve the count-rate (black line).

4.3 Experimental Procedure

The experimental procedure for the presented studies was divided into two phases for each ion beam received from ISAC. Firstly, the beam was sent to the MR-ToF-MS for a preliminary characterization and optimization, taking advantage of the fast diagnosing capabilities of the spectrometer. Then, a mass measurement was performed with the MR-ToF-MS and, subsequently, sent to the MPET also for a mass measurement whenever available isotope yields allowed. The two phases, of characterization and measurement, are described next.

4.3.1 Initial Beam Assessment with the MR-ToF-MS

Each beam delivered was initially characterized at the MR-ToF-MS. A typical spectrum obtained is shown in figure 4.12, through which the beam composition can be assessed. In a preliminary analysis, the peaks in the spectra were fitted and their masses calculated through a previous calibration using ions from the stable ion source. The preliminary masses were compared to the values reported in the literature [34], and each peak was assigned.

Besides Ti, the delivered beam typically contained surface-ionized V, Cr, Mn, and other lesser produced isobars. The identification of the titanium species was confirmed by blocking one of the laser ionization transitions in the TRILIS ion source. In this way, only surface-ionized species were transmitted, and a reduction in the Ti yields could be observed. This can be seen in figure 4.12.

In some mass numbers, a few peaks present in the spectra could not be identified. Although they are probably from ionized molecular species, little effort was taken

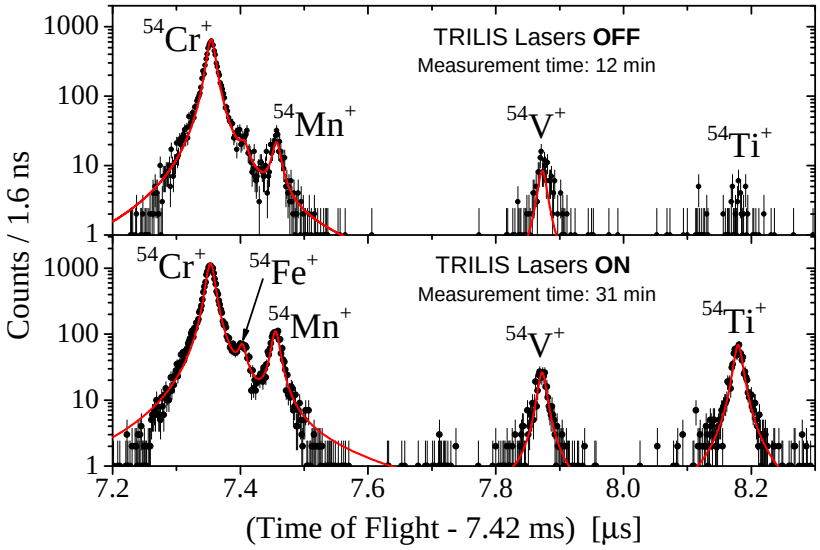

Figure 4.12: This typical MR-ToF-MS spectrum shows how the identification of titanium peaks was confirmed by blocking one of the TRILIS lasers. Then, only surface ionized species were delivered to TITAN, causing a reduction only in Ti yields. Red curves are fits to the data. Figure published first in [164].

to identify them. Since they are not overlapping with peaks of species of interest, they were considered not to influence the relevant measurements.

The fast measurement provided by the MR-ToF-MS allowed, for the first time, the fine optimization of the ISAC Mass Separator for the species of interest. Although the resolution of the mass separator is not high enough to fully separate most isobars, it can favor the transmission of certain species over others within that range.

Guided by the MR-ToF-MS, the ratio between titanium species over contaminant species was optimized by changing the parameters of the ISAC mass separator [138]. The impact of such a procedure can be seen in figure 4.13. This is particularly useful for very exotic species, where beams are typically highly contaminated by stable isobars but also share a significant mass difference with them.

4.3.2 Mass Measurement Procedure: MR-ToF-MS

During the online studies, the first mass measurement at every mass number was done at the MR-ToF-MS. All were done with 512 isochronous turns plus one TFS turn inside the analyzer for the ions of interest. The total length of the measurement cycle was $\approx$ 20 ms. 13 ms of those were spent on cooling and preparation in the transport system.

In the analyzer, the ions spent between 7.2 ms to 7.6 ms (depending on their mass number) before being sent to the MCP. Peaks in the time-of-flight spectra had a width of about 17 ns, yielding a mass resolving power of $R_m \approx 220\,000$. For

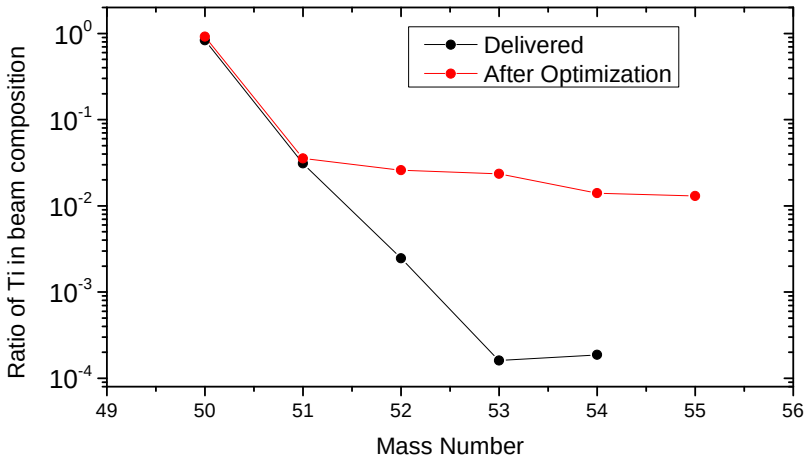

Figure 4.13: Ratio of titanium isotopes present in the beam delivered from ISAC before (black) and after (red) optimization of the ISAC Mass Separator aided by the TITAN MR-ToF-MS. As can be seen, up to two orders of magnitude in interest-to-contaminant ratio was recovered from this procedure in the most exotic cases. In the $A = 55$ case, no ^{55}Ti could be seen initially. Figure first published in [138].

isotopes of each mass number, data were taken until at least a few hundreds of counts were acquired at the corresponding titanium peak.

Chromium ions, mostly stable or close to stability, were widely present and were identified as appropriate calibrants for all spectra except of mass numbers $A = 51$ and 56, in which ^{51}V and ^{56}Fe were chosen as calibrants. The atomic masses of these calibrants would also be measured with the MPET for an independent verification (see sec. 4.3.3).

Measurements were performed with less than one ion per cycle on average. This is well below the threshold where ion-ion interactions inside the analyzer start causing a relevant systematic effect. The MRS was used to deflect any particle outside the desired mass window.

A few supporting measurements were also taken. One lower statistics spectrum was acquired with the MRS switched off in order to allow calibrant ions with a different mass number to reach the detector. Thus $^{39}K^+$ and $^{41}K^+$ from MR-TOF-MS's internal ion source could be measured simultaneously to the radioactive ion beam and could be used to validate the mass accuracy. Moreover, a single turn spectrum using $^{39}K^+$ and $^{41}K^+$ was acquired to calibrate time offsets in the electronics and acquisition system.

The total data taking time with the MR-ToF-MS was 12 hours, excluding preparation and characterization times. Results of the measurements with the MR-ToF-MS, as well as the data analysis procedure, are presented in section 5.1.

4.3.3 Mass Measurement Procedure: MPET

Following the mass measurement at MR-ToF-MS, the beam was sent directly from the TITAN RFQ to the MPET. Mass measurements of both the titanium isotopes and of the chosen MR-ToF-MS calibrants were performed whenever possible.

Although the MPET has a Lorentz steerer, the half-lives of the species of interest were well above 100 ms, and ion preparation through dipole excitation was possible. Therefore, ions were injected into the center of the trap, one ion per bunch on average, and prepared in a pure initial magnetron motion (of radius ≈ 1.5 mm) by dipole excitation. Subsequently, the major contaminant ions, previously identified through the MR-ToF-MS spectra, were removed through dipole excitation of their reduced cyclotron motion. The total ion preparation time in the MPET was between 60 ms and 70 ms.

After preparation, the ions were subjected to the ToF-ICR measurement of the cyclotron frequency of the interest ions. A two-pulse Ramsey excitation scheme (see sec. 3.2.3) was employed for measurements of all ions with $A \leq 53$ while a standard scheme was used for $A = 54$. Total ToF-ICR excitation times ranged from 100 to 250 ms, depending on the species.

Every ν_c measurement of the ions of interest was interleaved by a $\nu_{c,ref}$ measurement of a reference $^{39}K^+$ ion from TITAN's ion source, to calibrate the magnetic field and to account for other possible time-dependent variations during the measurement. Measurements of ν_c of $^{85}Rb^+$ ion, also obtained from TITAN's ion source, were also interleaved to study potential systematic mass-dependent shifts.

Complementary, systematic mass-dependent shifts were studied in more detail in dedicated mass measurements of stable species before and after the experiment. Measurements of $^{41}K^+$ and $^{85}Rb^+$ were performed in the same conditions of the online measurements, also using $^{39}K^+$ as reference ion.

The total measurement time with the MPET was of 14 hours, excluding preparation times. Results of the measurements with the MPET, as well as the data analysis procedure, are presented in section 5.2.

5 MEASUREMENTS AND DATA ANALYSIS

In this chapter, I present the characteristics of the data acquired during the experiment (described in sec. 4.3) and the analysis procedure employed to obtain the mass values of the studied nuclides. Section 5.1 presents the data pertaining to the MR-ToF-MS, while section 5.2 discusses the data acquired with the MPET. Finally, a brief discussion on the assignment of the nuclear state of the measured species is presented in section 5.3.

5.1 Mass Measurements with the MR-TOF-MS

A sample MR-ToF-MS spectrum of each mass number is shown in figure 5.1. In each spectrum, a calibrant was chosen among the identified species (see sec. 4.3.1 for a description of the identification procedure). The criteria for calibrant choice were species whose mass was known in literature [34] with a precision better than what the MR-ToF-MS can provide (mass uncertainty $\lesssim$ 1 keV), preferably with at least 1000 counts in a non-overlapping peak. The characteristics of the spectra acquired at each mass number are described next.

A = 51: for this mass number, measurements with the MR-ToF-MS cannot contribute to improve the mass precision of the isotopes of interest, since they are reported to sub-keV/c^2 levels in the literature [34]. The measurements were performed to validate the accuracy of the technique employed. The MR-TOF-MS acquired time-of-flight spectra for about half an hour, and peaks of $^{51}Ti^+$, $^{51}V^+$ and $^{51}Cr^+$ were identified, as well as 10 counts compatible with $^{51}Sc^+$. The peak corresponding to $^{51}Cr^+$ was found overlapping with the much more intense $^{51}V^+$ peak. Although the masses of both species are known to sub-keV/c^2 levels [34], the position of the $^{51}V^+$ peak is much less affected by its overlap with the $^{51}Cr^+$ peak due to its much higher intensity. Therefore, $^{51}V^+$ was chosen as a suitable calibrant for the spectrum.

A = 52: as in the $A = 51$ case, the MR-ToF-MS measurements in this mass number also served to validate the technique. Data were acquired for about one hour. $^{52}Cr^+$, stable and whose mass is known to 0.34 keV/c^2 precision [34], was the most intense component of the beam, making it a suitable calibrant. $^{52}Ti^+$ was also largely present, while a few tens of events corresponding to $^{52}V^+$ and $^{52}Mn^+$ were registered.

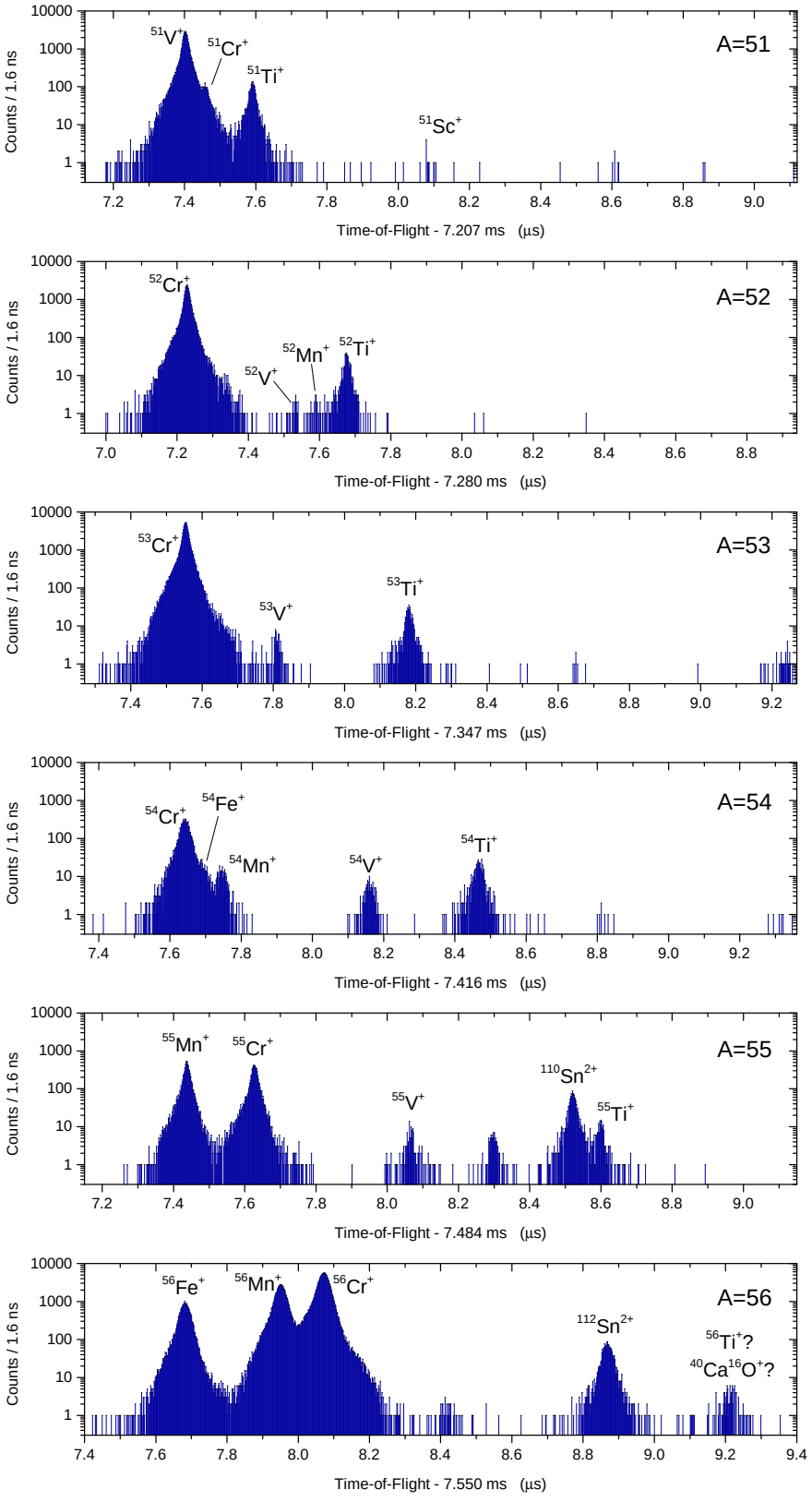

Figure 5.1: A sample MR-ToF-MS spectrum is shown for each of the measured radioactive beams delivered from ISAC (with TRILIS lasers on). Identified peaks are marked. For further details of each measurement, see text.

A = 53: this was the first mass number where the MR-ToF-MS could provide improvements on literature, since the mass of $^{53}Ti^{+}$ is reported to have an uncertainty of 100 keV/c^2 [34]. Data were acquired for about one and a half hours. $^{53}Cr^{+}$ was the most intense peak and taken as calibrant. $^{53}Ti^{+}$ and $^{53}V^{+}$ were also present in the spectra.

A = 54: as the probed titanium isotopes become more neutron-rich, their yields significantly decrease, and the measurements require more time to gather enough statistics. The measurements on this mass number required about 2.5 hours, and $^{54}Ti^{+}$ was a minor component of the beam. $^{54}Cr^{+}$ was the dominant component and chosen as calibrant. $^{54}Mn^{+}$, $^{54}V^{+}$ and $^{54}Fe^{+}$ were also present.

A = 55: the MR-ToF-MS acquired data for about 2 hours in this mass number. $^{55}Mn^{+}$ and $^{55}Cr^{+}$ were the dominant species, and the chromium isotope was chosen as calibrant. $^{55}Ti^{+}$ and $^{55}V^{+}$ appear in the spectra but represent together less than 2% of the counts. The doubly-charged $^{110}Sn^{2+}$ also appeared in large quantities in the spectra. Since it has the same m/q of the interest species, its behavior under the influence of electrostatic ion optics is identical. Therefore, once it is produced in the ISAC target and doubly-ionized in the ion source, it will be present in the sample.

A = 56: the beam at this mass number was composed by $^{56}Fe^{+}$, $^{56}Mn^{+}$, $^{56}Cr^{+}$ and $^{112}Sn^{2+}$ However, after 4 hours of data acquisition, it is uncertain whether $^{56}Ti^{+}$ was present. The observed peak may correspond to ionized $^{40}Ca^{16}O^{+}$, a common molecule that may be released from the ISAC target. A complete discussion about this issue is given in sec. 5.1.5. $^{56}V^{+}$ was not found in the beam. $^{56}Fe^{+}$ was chosen as a suitable calibrant for the spectra on this mass number.

5.1.1 Data Analysis

The data analysis procedure for the MR-ToF-MS spectra followed very similar guidelines as for the MR-ToF-MS system at GSI, presented in [132], but adapted to the specifications of the TITAN system.

First, all time-of-flight spectra were corrected for temperature drifts and instabilities in the power supplies by using a time-resolved calibration (see sec. 3.3.2) with respect to the calibrant peak.

To obtain the time-of-flight of each species, their peaks in the spectra must be fit to an appropriate peak function. The shape of the peaks is a function that reflects several processes, such as ion optical parameters of the mass analyzer (see fig. 3.17) and ion-gas collisions [129, 165]. In some MR-ToF-MS systems, time-of-flight peaks can be Gaussian-like or present large asymmetric tails (see for example [55]). Nevertheless, the peak shape is identical for all isobars in the same spectrum, since they go through the same processes.

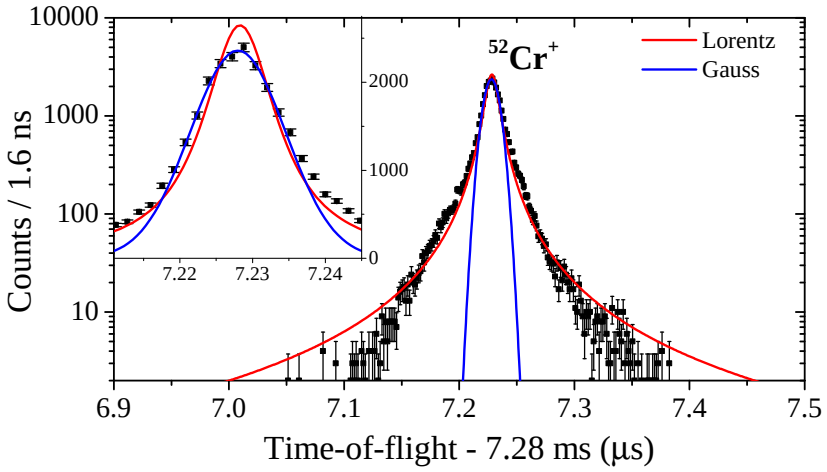

Figure 5.2: Fits of a $^{52}Cr^{+}$ time-of-flight peak with Gaussian (blue) and Lorentzian (red) peak shapes. The vertical axis is in logarithmic scale to evidence the shape of the tails. The insert contains the same information, but it has its vertical axis in linear scale to evidence the centroid.

Several approaches exist in the literature on how to obtain the corresponding peak shape. Some authors obtain a peak shape from computer simulations of the ion optics of their device (such as in [165]); while others perform one high-statistics measurement of a single-species sample and fit the data to a complex function with many degrees of freedom (as done in [166]).

The TITAN MR-ToF-MS has the advantage of generating symmetric peaks, which simplifies this analysis. This is a feature of the optical aberrations of the mirrors and, ultimately, of how they are tuned. We opt to fit the data to two standard spectral line shapes: Gaussian (f_{Gauss}) and Lorentzian ($f_{Lorentz}$), whose functions are:

$$f_{Gauss}(t) = Y\, e^{-\frac{1}{2}[(t-t_c)/\sigma]^2} \qquad \text{and} \tag{5.1}$$

$$f_{Lorentz}(t) = Y\, \frac{\sigma}{(t-t_c)^2 + \frac{\sigma^2}{4}} \quad . \tag{5.2}$$

In both cases, Y, t_c and σ are free parameters of the fit. Y is the height of the peak, related to the number of counts measured; t_c is the centroid, from where the species' time-of-flight is obtained; and σ is a parameter related to the width of the peak.

A sample peak fit with each of the functions is shown in figure 5.2. The Gaussian peak shape reproduces very well the data around the centroid, but not the tails of the peak. Meanwhile, the Lorentzian reproduces the tails well but has a reduced performance around the centroid.

We performed an independent analysis using both peak shapes. All peaks in every spectrum were fitted by a Least-Square method [167] using a multi-peak fitting routine, which accounts for overlapping peaks. Parameters Y and t_c were adjusted for every peak, the width parameter σ was fitted under the constraint that it was the same to every peak in the spectrum ($\sigma \approx 17$ ns). Doubly-charged peaks had

slightly larger widths[24] and were excluded from the analysis. The fits using the two peak shapes resulted in values for t_c with a relative difference within $< 5 \cdot 10^{-8}$ and compatible uncertainties. The final t_c (and respective uncertainties) for each peak was obtained through an unweighted average of the two values.

The time-of-flight of every species was calibrated in m/q using (see eq. 3.29):

$$m/q = \mathcal{C}\,(t_c - t_0)^2 \quad , \tag{5.3}$$

where $\mathcal{C}$ is a calibration factor and t_0 is an offset that mostly comes from delays in the electronic signal processing, which is nearly constant for a given experiment. The calibration factor $\mathcal{C}$ was obtained by the atomic mass ($m_{a,ref}$ - taken from [34]), charge state (q_{ref}) and measured time-of-flight ($t_{c,ref}$) of the calibrant ion:

$$\mathcal{C} = \frac{m_{a,ref} - q_{ref}\, m_e}{q_{ref}\,(t_{c,ref} - t_0)^2} \quad , \tag{5.4}$$

where m_e is the mass of the electron. The offset t_0 was measured from a single turn spectrum containing $^{39}K^+$ and $^{41}K^+$ ions and evaluated in $t_0 = 111(4)$ ns.

The obtained ionic masses were converted to atomic form (see ch. 3). In all cases, ions of interest and calibrant ions were in a singly charged state ($q = 1$); therefore, atomic mass calculations account for one electron removed. Electron binding energies (on the order of a few eV [168]) are negligible for the studied cases.

Contributions to the statistical errors came from the peak fits and the calibration. The evaluation of systematic errors is discussed in the following.

5.1.2 Evaluation of Systematic Errors

Systematic contributions to uncertainties in MR-ToF-MS can come from many sources, such as effects from voltage fluctuations during ejection of the ions from the analyzer, from the time-resolved calibration procedure, from ion-ion interaction during the flight, from the use of the mass-range selector, or from the presence of overlapping peaks when applicable [132, 164].

The upper limit of systematic errors of the TITAN MR-ToF-MS was evaluated to contribute up to $3 \cdot 10^{-7}$ to the relative mass uncertainty [135]. It was determined from offline accuracy measurements performed before and after the experiment with $^{39}K^+$ and $^{41}K^+$ ions. This can also be verified by comparing the online mass measurements to well known mass values in the Atomic Mass Evaluation of 2016 (AME16) [34]. We inspected the relative atomic mass differences (Δm) between the

24 Although it remains to be further investigated, peaks of doubly-charged species may have larger width due to differences in the ion preparation step, before entering the analyzer.

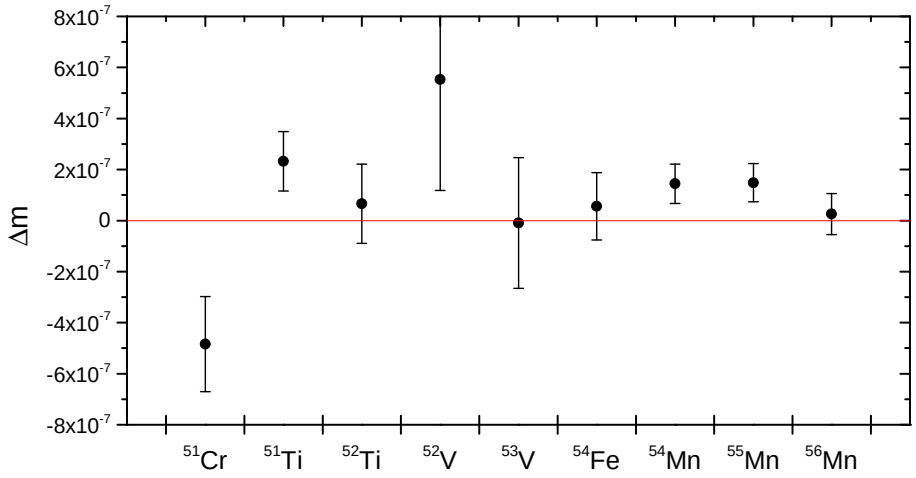

Figure 5.3: Relative atomic mass differences (eq. 5.5) between the values measured by the MR-ToF-MS and the mass values in the AME16 [34]. Only species with well known masses in the literature are shown. Error bars represent the statistical error from the MR-ToF-MS measurement only.

values obtained by the MR-ToF-MS ($m_a(\text{MR-ToF-MS})$) and the mass values recommended by the AME16 ($m_a(\text{AME16})$):

$$\Delta m = \frac{m_a(\text{MR-ToF-MS}) - m_a(\text{AME16})}{m_a(\text{AME16})} \quad . \tag{5.5}$$

Figure 5.3 shows Δm for the 9 species whose mass uncertainty reported in the literature was smaller than the obtained with the MR-ToF-MS. On average, the MR-ToF-MS mass values leaned towards the heavier side of the AME16 values by about one part in ten million, compatible with the offline measurements [135]. This is not true for ^{51}Cr only, which was affected by a more intense overlapping species (see fig. 5.1). Finally, a systematic contribution of $3 \cdot 10^{-7}$ was added to the relative mass uncertainty of every species.

5.1.3 Relativistic Corrections

It is also important to consider relativistic effects during the measurement. In high-precision measurements, a small relativistic effect may be introduced by the spectrometer when operated at sufficiently high kinetic energies. In chapter 3, the principles of the MR-ToF-MS were presented using a classical non-relativistic formalism. In the following, the error in approximating the problem with non-relativistic physics is quantified.

An MR-ToF-MS measures the time (t) passed as the particle travels a fixed distance (L), or equivalently, its speed ($v = L/t$). At fixed kinetic energy (E_{kin}), the speed of the particle in the appropriate relativistic description is given by

$$v = c\sqrt{1 - \left(\frac{mc^2}{E_{kin} + mc^2}\right)^2} \quad , \tag{5.6}$$

where m is the mass of the particle and c is the speed of light. The non-relativistic limit is taken when $E_{kin} \ll mc^2$, so the expression can be approximated by a Taylor expansion around $E_{kin}/(mc^2) = 0$ as

$$v = c\sqrt{2\left(\frac{E_{kin}}{mc^2}\right)} - \frac{3c}{\sqrt{8}}\left(\frac{E_{kin}}{mc^2}\right)^{3/2} + \dots \tag{5.7}$$

The first term in the right-hand side is the non-relativistic expression, and the second can be used to estimate the error in approximating the problem within a non-relativistic framework. The relative error (δv) in velocity by calculating it using the classical expression (v_{cl}) is then given by

$$\delta v = \frac{v - v_{cl}}{v_{cl}} \approx \frac{3}{4}\left(\frac{E_{kin}}{mc^2}\right) \quad . \tag{5.8}$$

For the values of this experiment ($E_{kin} = 1.3$ keV, $m \approx 50$ u), the relative error is on the order of $\delta v = 2 \cdot 10^{-8}$. Since the fight path is fixed, the relative error in velocity directly translates into the relative error in time-of-flight, which is much smaller than the resolution of our equipment. It is then justifiable to neglect relativistic corrections.

5.1.4 Final Mass Values

The mass values obtained with the MR-ToF-MS are shown in table 5.1 as mass excesses (ME - see eq. 3.4). The errors presented show both statistic and systematic contributions. The mass differences ($\Delta M_{\text{Cal-IoI}}$) between calibrants and ions of interest measured by the MR-ToF-MS are also shown to allow the independent reconstruction of the mass relationship between the pair of isobars. In total, the masses of 14 isotopes were measured.

5.1.5 The case of ^{56}Ti

In the $A = 56$ spectrum, a total of 264 counts were registered in a peak compatible with previous mass measurements of ^{56}Ti. However, the measurement with TRILIS lasers off showed too little reduction of the count rate. While most isotopes showed a reduction between 80% to 90%, the peak corresponding to ^{56}Ti reduced by only 25(15)% (see fig. 5.4).

Table 5.1: Mass excesses (ME) and half-lives of the isotopes measured by the TITAN MR-ToF-MS. Half-life data were taken from [108]. The mass difference ($\Delta M_{\text{Cal-IoI}}$) between the pair of isobars measured by the MR-ToF-MS are also shown to allow the reconstruction of their mass relationship.

Species	Half-life [s]	**Reference**	$\Delta M_{\text{Cal-IoI}}$ [keV/c^2]	ME [keV/c^2]
^{51}Cr	$2.3934(1) \cdot 10^6$	^{51}V	$-729\,(17)$	$-51474\ (8.8)_{\text{stat}}\,(14)_{\text{sys}}$
^{51}Ti	345.6(6)	^{51}V	$-2482\,(16)$	$-49722\ (5.5)_{\text{stat}}\,(14)_{\text{sys}}$
^{52}V	224.6(3)	^{52}Cr	$-4002\,(25)$	$-51417\ (21)_{\text{stat}}\,(14)_{\text{sys}}$
^{52}Ti	102(6)	^{52}Cr	$-5953\,(17)$	$-49466\ (7.5)_{\text{stat}}\,(14)_{\text{sys}}$
^{53}V	92.6(8)	^{53}Cr	$-3436\,(20)$	$-51851\ (13)_{\text{stat}}\,(15)_{\text{sys}}$
^{53}Ti	32.7(9)	^{53}Cr	$-8410\,(18)$	$-46877\ (9.6)_{\text{stat}}\,(15)_{\text{sys}}$
^{54}Fe	(stable)	^{54}Cr	$-683\,(16)$	$-56252\ (6.6)_{\text{stat}}\,(15)_{\text{sys}}$
^{54}Mn	$2.697(2) \cdot 10^7$	^{54}Cr	$-1384\,(15)$	$-55550\ (3.9)_{\text{stat}}\,(15)_{\text{sys}}$
^{54}V	49.8(5)	^{54}Cr	$-7031\,(17)$	$-49904\ (6.7)_{\text{stat}}\,(15)_{\text{sys}}$
^{54}Ti	2.1(1.0)	^{54}Cr	$-11191\,(16)$	$-45744\ (4.7)_{\text{stat}}\,(15)_{\text{sys}}$
^{55}Mn	(stable)	^{55}Cr	$+2594\,(15)$	$-57704\ (3.8)_{\text{stat}}\,(15)_{\text{sys}}$
^{55}V	6.54(15)	^{55}Cr	$-5985\,(27)$	$-49125\ (22)_{\text{stat}}\,(15)_{\text{sys}}$
^{55}Ti	1.3(1)	^{55}Cr	$-13277\,(29)$	$-41832\ (24)_{\text{stat}}\,(15)_{\text{sys}}$
^{56}Mn	$9.2840(4) \cdot 10^3$	^{56}Fe	$-3697\,(16)$	$-56910\ (4.2)_{\text{stat}}\,(16)_{\text{sys}}$

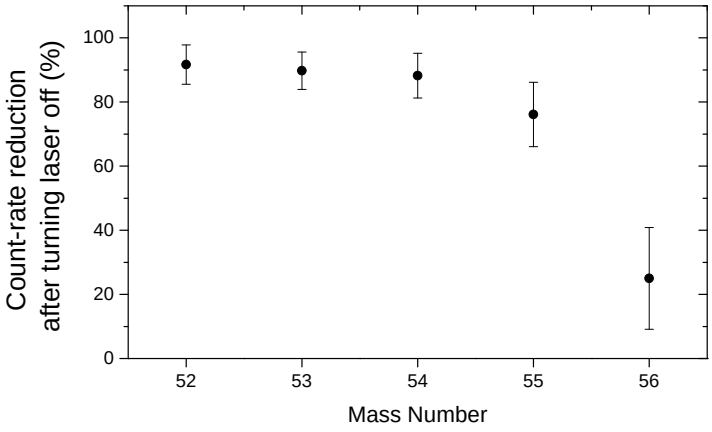

Figure 5.4: Reduction in count-rate of titanium observed after turning TRILIS laser off. Most isotopes show a reduction between $80 - 90$ %.

Moreover, the peak is also compatible in mass with the ionized molecule of ^{40}Ca^{16}O$^+$. It is unclear whether the observed peak is purely ^{56}Ti or an admixture of the isotope of interest and the contaminant molecule. Therefore, the identification of the isotope of interest was inconclusive in this case.

5.2 Mass Measurements with the MPET

Measurements with the Penning trap targeted the titanium isotopes and the species used as calibrant of the MR-ToF-MS. A sample ToF-ICR resonance obtained for each species of interest is shown in figure 5.5.

As mentioned in sec. 4.3.3, $^{39}K^{+}$ was the reference ion for all measurements and measurements of $^{85}Rb^{+}$ were also taken to evaluate the accuracy of the procedure. Two-pulse Ramsey excitation schemes were preferred as they yield higher precision, but only if the species of interest were expected to be well resolved from the other isobars present in the sample.

The characteristics of the measurements performed at each mass number are described in the following.

A = 51: the masses of the species of interest (^{51}Ti and ^{51}V) are already known with high precision [34]. Thus, measurements were performed to validate further the accuracy of the procedure. Ramsey resonances with $t_{on} = 40$ ms and $t_{off} = 120$ ms (see sec. 3.2.3) were employed, preceded by a dipole excitation of the magnetron motion for 50 ms and a dipole cleaning for 20 ms. The cleaning procedure was set to remove ^{51}V when ^{51}Ti was being measured and vice-versa. In total 5 ToF-ICR resonances were acquired for each species, taking about 5 minutes each. The complete measurement took about one hour.

A = 52: the species of interest for this mass number are ^{52}Ti and ^{52}Cr. The characteristics of the cycle remained unchanged from the previous mass number. 5 ToF-ICR resonances were acquired for ^{52}Cr, taking about 5 minutes each; 4 resonances were measured for ^{52}Ti, taking about 50 minutes each. The measurements in this mass number took about 6 hours in total.

A = 53: in this mass number, the yield of titanium in the beam decreased considerably compared to the previous masses. To compensate for the lower rates, a few adjustments were made to keep the same precision of the measurement. The Ramsey excitation time was increased to $t_{on} = 50$ ms and $t_{off} = 150$ ms and the magnetron preparation time was reduced to 45 ms. 3 ToF-ICR resonances were acquired for ^{53}Ti, taking about one and a half hours each; 4 resonances were measured for ^{53}Cr, taking about 10 minutes each. The measurements took about 6 hours in total.

A = 54: as can be seen in the MR-ToF-spectrum (fig. 5.1), many isobars were more abundant than ^{54}Ti, such as ^{54}Cr, ^{54}Fe and ^{54}Mn. The dipole cleaning of all contaminant species became challenging, and obtaining a ToF-ICR resonance of ^{54}Ti was not possible. The measurement focused only on the calibrant of the MR-ToF-MS spectrum ^{54}Cr. The isobars ^{54}Fe and ^{54}Mn are also very close in mass to ^{54}Cr, so a standard ToF-ICR resonance ($t_{RF} = 100$ ms) was preferred over Ramsey. In total 5 ToF-ICR resonances were acquired, which took about 5 minutes each. The procedure took about one hour.

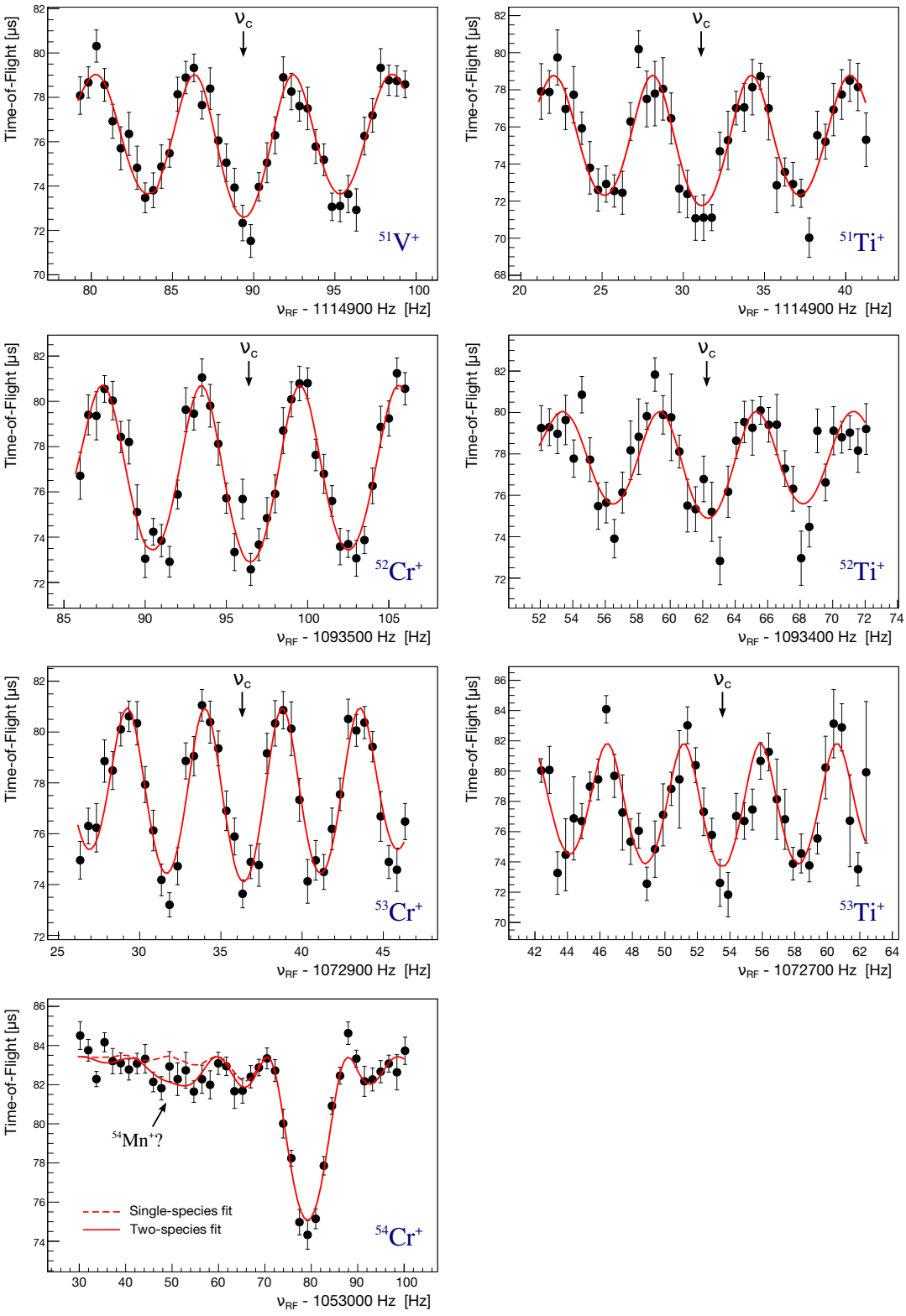

Figure 5.5: A sample ToF-ICR resonance is shown for each of the species measured with the MPET in this campaign. Red curves are analytical fits to the data and, in the case of Ramsey resonances, the center fringe is indicated by the arrow and labelled ν_c. For further details of each measurement, see text.

At masses $A = 55$ and $A = 56$, the ratio of species of interest over contaminants was even worse than in the $A = 54$ case. Therefore, MPET measurements in those masses were not attempted.

5.2.1 Data Analysis

As discussed in sec. 3.2, obtaining the atomic masses from the ToF-ICR method requires obtaining the ratio (R_ν) between cyclotron frequencies of the reference ion and the ion of interest (see eq. 3.6). Thus it requires the fitting of the ToF-ICR resonances to obtain the cyclotron frequencies.

First, a preliminary selection was performed to the ToF-ICR resonance data. Each time-of-flight event was accepted if two criteria were met:

1. Its measurement cycle had a maximum of two ions detected. This is to minimize effects from ion-ion interactions that may result in shifts from the true cyclotron frequency [169].
2. The events were inside a time-of-flight window predetermined by its m/q. For example, for $^{54}Cr^{+}$ this window was between 63 μs and 91 μs. Events registered outside this window are considered dark counts. They can be triggered, for example, by cosmic rays passing through the detector or by decays of radioactive ions deposited in the MCP detector.

After the data cuts, all ToF-ICR resonances were fit to a function in the form of eq. 3.26 to obtain the cyclotron frequency ν_c of the ion of interest. The fits are shown in fig. 5.5 (red curves). However, the measurements were not done simultaneously and the magnetic field may have varied over the course of the procedure. Therefore, the cyclotron frequency of the reference ion is interpolated to the mid-time of the measurement of the ion of interest. This is depicted at figure 5.6. The cyclotron frequency ratio was obtained with the interpolated $\tilde{\nu}_{c,ref}$:

$$R_\nu = \frac{\tilde{\nu}_{c,ref}}{\nu_c} \quad . \tag{5.9}$$

A weighted average was performed with all measurements of R_ν of the same ion of interest, and its atomic mass (m_a) was calculated through

$$m_a \;=\; R_\nu \left(m_{a,ref} - q_{ref}\, m_e \right) \frac{q}{q_{ref}} \;+\; q\, m_e \quad , \tag{5.10}$$

where $m_{a,ref}$ is the atomic mass of the reference ion ^{39}K, taken from [34], and m_e is the mass of the electron. The charge states q and q_{ref} of the ions of interest and reference, respectively, were both $+1$. Note that this formula does not account for electron binding energies to the atom. In the cases tackled in this experiment, the electron binding energies are on the order of a few eV [168], which are negligible compared to the precision achieved in the measurements.

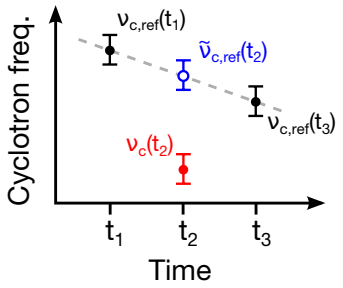

Figure 5.6: A linear interpolation of the reference measurements (black) is done to determine the reference cyclotron frequency (blue) at the time of the measurement of the ion of interest (red).

The statistical uncertainties come from the fit and the frequency interpolation. Systematic errors are discussed in the following.

5.2.2 Evaluation of Systematic Errors

Common sources of systematic errors are well studied in Penning traps [170, 110]. They come from the construction of the trap, such as imperfections of trapping electrodes and field misalignments, from instabilities of the trapping potential and magnetic field and from ion-ion or ion-atom interactions.

The effect of ion-ion interactions was minimized in this experiment due to the data selection, as explained in the previous section. In a previous analysis, the sources of systematic deviations in MPET related to its construction and field stability were evaluated to $2 \cdot 10^{-10}$ per unit of m/q [110]. This yields deviations on the order of 10^{-8} in relative mass uncertainty for this experiment.

The magnitude of the systematic deviations in this experiment was evaluated using the measurements of ^{85}Rb taken during the experiment and the measurements of ^{85}Rb and ^{41}K performed before and after it. In total, 90 mass measurements of ^{41}K were done and 107 of ^{85}Rb, all using ^{39}K as a reference ion. Since they were measured many more times than the ions with masses between $A = 51$ and 54, their higher precision provides a better determination of systematic deviations.

In a similar way as done for the MR-ToF-MS, we inspected the relative atomic mass differences (Δm) between the values obtained by the MPET ($m_a(\mathrm{MPET})$) and the mass values recommended by the AME16 ($m_a(\mathrm{AME16})$):

$$\Delta m = \frac{m_a(\mathrm{MPET}) - m_a(\mathrm{AME16})}{m_a(\mathrm{AME16})} \quad . \tag{5.11}$$

Figure 5.3 shows Δm for ^{85}Rb and ^{41}K. Measurements for some species of interest were also included, given that their mass uncertainty reported in the literature [34] was smaller than the obtained with the MPET. A mass-dependent systematic trend is observed. It was evaluated in $6.5 \cdot 10^{-10}$ per m/q. This is larger than obtained

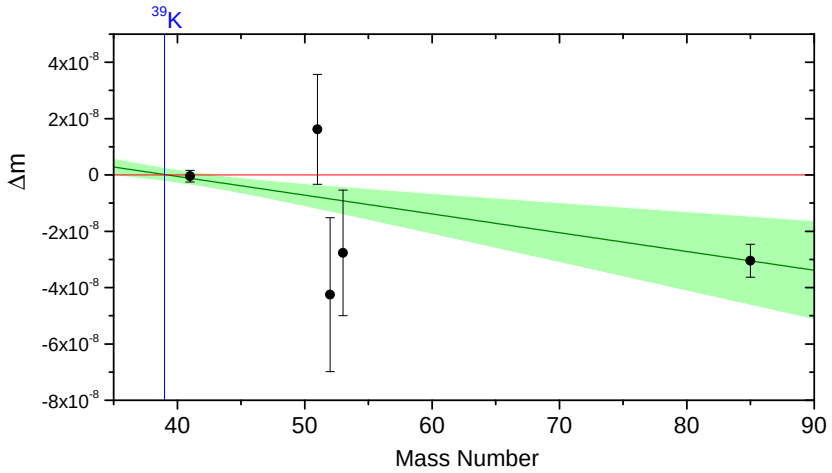

Figure 5.7: Relative atomic mass differences (eq. 5.11) between the values measured by the MPET and the mass values in the AME16 [34]. Only species with well known masses in the literature were considered. Error bars represent the statistical error from the MPET measurement. The green line is a linear fit to the data (light green region represents a 95% confidence band) to get the systematic trend from the reference mass (^{39}K, marked in blue).

by [110], but on the same order of magnitude. The systematic contribution to the relative mass uncertainty was evaluated in $< 1.5 \cdot 10^{-8}$ among the masses of interest.

It is worth noting that this analysis significantly differs from the one performed for the MR-ToF-MS, shown in figure 5.3. In the MR-ToF-MS case, all ions of interest were calibrated using an isobaric reference ion. Therefore, mass-dependent systematic effects are expected to be negligible. In the case of the measurements done with MPET, the reference particle (^{39}K) is several mass units away from the masses of interest. For this reason, mass-dependent systematic effects are expected to play a more relevant role.

5.2.3 Relativistic Corrections

Differently than the MR-ToF-MS case (sec. 5.1.3), relativistic corrections in Penning traps are more frequently needed since they are more precise. In the MPET, relativistic shifts were observed when measuring light ions such as $^{6}Li^{+}$ [158].

The cyclotron frequency (ν_c) in the relativistic formulation is simply

$$\nu_c = \frac{1}{2\pi}\frac{qe\,B}{\gamma\,m} \quad , \tag{5.12}$$

where qe and m are the charge and mass of the particle, B the magnetic field strength and γ is the Lorentz factor. The relative error in the mass (δm) in approximating the cyclotron frequency using the classical expression ($\gamma = 1$) can be estimated by

$$\delta m = \frac{m - m_{cl}}{m_{cl}} = \frac{1}{\gamma} - 1 = \sqrt{1 - \left(\frac{v}{c}\right)^2} - 1 \quad , \tag{5.13}$$

where m_{cl} is the mass obtained from the classical approximation, v is the ion motion's tangential velocity and c is the speed of light. The velocity v can be estimated by $v \approx 2\pi\, r\, \nu_c$, where r is the radius of the radial motion of the ion in the trap.

Considering $r = 1.5$ mm, δm for $^{39}K^+$ ($\nu_c \approx 1.45$ MHz) is on the order of $1 \cdot 10^{-9}$. Meanwhile, δm for the heaviest species measured in this experiment, $^{85}Rb^+$ ($\nu_c \approx$ 0.66 MHz), is on the order of $2 \cdot 10^{-10}$. Since these values are much smaller than the precision and accuracy of this experiment, relativistic effects were considered negligible.

5.2.4 Final Mass Values

The frequency ratios and mass values obtained with the MPET are shown in table 5.1, masses are presented as mass excesses (ME - see eq. 3.4). The errors presented show both statistic and systematic contributions to the final mass value. In total, the masses of 7 species were measured.

Table 5.2: Frequency ratios (R_ν), atomic mass excesses (ME) and half-lives of the species measured by the TITAN MPET. Half-life data were taken from [108].

Species	Half-life [s]	**Reference**	R_ν †	ME [keV/c^2]
^{51}V	(stable)	^{39}K	1.307476380 (50)	$-52203.5\ (1.2)_{stat}\ (0.65)_{sys}$
^{51}Ti	345.6(6)	^{39}K	1.307544491 (58)	$-49731.5\ (1.5)_{stat}\ (0.65)_{sys}$
^{52}Cr	(stable)	^{39}K	1.333052991 (55)	$-55421.3\ (1.3)_{stat}\ (0.70)_{sys}$
^{52}Ti	102(6)	^{39}K	1.333216716 (83)	$-49479.1\ (2.3)_{stat}\ (0.70)_{sys}$
^{53}Cr	(stable)	^{39}K	1.358721924 (52)	$-55288.4\ (1.1)_{stat}\ (0.75)_{sys}$
^{53}Ti	32.7(9)	^{39}K	1.358953560 (80)	$-46881.4\ (2.2)_{stat}\ (0.75)_{sys}$
^{54}Cr	(stable)	^{39}K	1.384341984 (130)	$-56929.3\ (3.8)_{stat}\ (0.81)_{sys}$

† The cyclotron frequency ratios are relative to the measured ionic species.

5.3 Low-Lying Isomers and Ground-State Assignment

Isomers are long-lived excited nuclear states. They may be co-produced with the ground-state configurations and may live long enough to be delivered and participate in the experimental procedure. They play a relevant role in several studies of nuclear structure. However, in the case of this experiment, the scientific interest lies in the ground-state configurations only. Therefore, the impact of the presence of isomeric states in the sample must be considered.

With the achieved resolving power of 220 000, the MR-ToF-MS would be able to resolve isomeric states with excitation energies above $\sim$ 250 keV. In the case of the MPET, the resolving power depends on the excitation time and on the excitation

scheme employed, as discussed in section 3.2 (see eq. 3.23). In this experiment, the MPET would be able to resolve isomeric states with minimum excitation energies between 150 keV and 500 keV, depending on the case.

The presence of unresolved low-lying isomers in the sample may cause several undesired effects. For example, they can cause a broadening of the MR-ToF-MS peak [132] or of the ToF-ICR resonance [171], which may also lead to a systematic shift in the position of the peak's or resonance's centroid. On some occasions, isomeric states may be much more abundant in the sample than the ground state [67, 172], which may lead to incorrect assignment of the state of the observed species.

However, no broadening was observed in any of the acquired data sets. Moreover, this particular region of the nuclear chart has little known or reported isomers [54]. Among the nuclides of interest, the only known isomer is a 5^+ state of ^{54}V, which has excitation energy of $108(1)$ keV and half-life of $0.9(5)$ μs [54]. It does not live long enough to take part in the experiments and influence our results, since the ion preparation state takes tens of ms.

Given the lack of evidence of isomeric states in the data, the systematic absence of known low-lying and long-lived isomers in the region, and the good agreement between our data and the ground-state properties reported in the literature (as discussed in the following chapter), all the measured nuclides of interest were assigned to be in their ground-state configuration.

6 DISCUSSION

The impact and the implications of our measurements are discussed in this chapter. First, in section 6.1, the performance of the MR-ToF-MS is compared to the MPET. In section 6.2, the measurements are compared with the existing measurements reported in the literature. With the new data, the mass surface in the isotopic chains of Ti and V is updated, and its implications on the evolution of the $N = 32$ shell closure are discussed in sec. 6.3. Finally, in sec. 6.4, the predictions of the *ab initio* theories presented in chapter 2 are tested against the data.

6.1 Comparison Between Spectrometers

In order to provide further validation of MR-ToF-MS measurements, the differences $\Delta M_{\text{Cal-IoI}}$ between atomic masses (m_a) of ions of interest and their MR-ToF-MS calibrants were evaluated for both spectrometers:

$$\Delta M_{\text{Cal-IoI}} = m_a(\text{MR-ToF-MS calibrant}) - m_a(\text{Ion of Interest}) \quad . \tag{6.1}$$

This is a more robust form of comparison than comparing directly mass values. It is essentially insensitive to choices of calibration and to mass-dependent systematic effects. In table 6.1 and figure 6.1, this quantity is presented using values from the MPET, the MR-ToF-MS and the AME16.

Table 6.1: Mass differences $\Delta M_{\text{Cal-IoI}}$ (in keV/c^2) between atomic masses of Ti isotopes and their MR-ToF-MS calibrants, using MPET, MR-ToF-MS and AME16 [34] values.

Species	MPET	MR-ToF-MS	AME16
^{51}V - ^{51}Ti	−2472.0 (2.8)	−2482 (16)	−2471.01 (64)
^{52}Cr - ^{52}Ti	−5942.2 (3.7)	−5953 (17)	−5949 (7)
^{53}Cr - ^{53}Ti	−8407.0 (3.5)	−8410 (18)	−8456 (100)
^{54}Cr - ^{54}Ti		−11191 (16)	−11313 (82)
^{55}Cr - ^{55}Ti		−13277 (29)	−13440 (160)

The three cases that were measured by both spectrometers (^{51}V-^{51}Ti, ^{52}Cr-^{52}Ti and ^{53}Cr-^{53}Ti) confirm the agreement between the two techniques. Figure 6.1 also illustrates well the strengths and weaknesses of each technique. The MR-ToF-MS has higher sensitivity and could measure isotopes with lower production rate, while the MPET could provide one order of magnitude better precision in the current

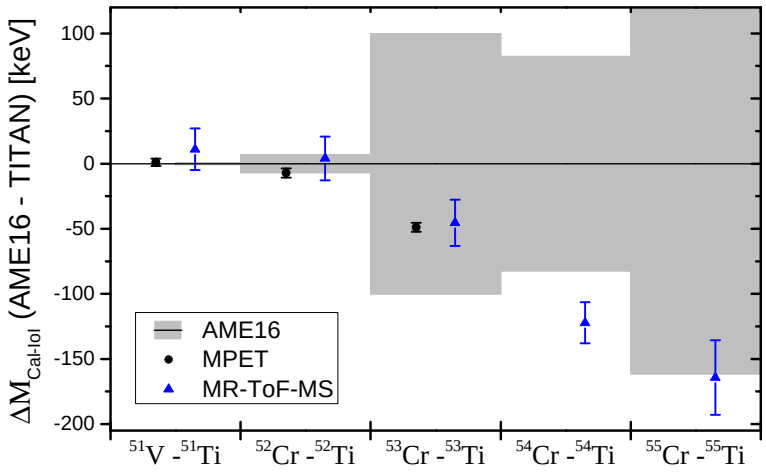

Figure 6.1: The comparison between mass differences $\Delta M_{\text{Cal-IoI}}$ (between Ti isotopes and their respective MR-ToF-MS calibrant) measured by both spectrometers show the agreement between them. Here, $\Delta M_{\text{Cal-Ti}}$ is plotted against the AME16 values for a cleaner comparison. Grey bands represent the uncertainties of the AME16.

configuration of both systems. The results of both spectrometers were also in good agreement (within one sigma) with the values in the literature, which is discussed further in the next section.

6.2 Comparison with Previous Measurements

The agreement between the two spectrometers is essential to assess the reliability of our resulting mass values, particularly in the case of the newly commissioned MR-ToF-MS system. It is also essential that the results are compared with the measurements previously reported in literature, especially with well-measured cases. In this section, a compilation of all the measurements of each isotope measured in this campaign is presented. In all cases, the results of both TITAN spectrometers are generally in good agreement with past measurements and within $1.5\,\sigma$ against the AME16 recommended values.

6.2.1 Titanium Isotopes

^{51}Ti: In ^{51}Ti, shown in fig. 6.2, all previous measurements are indirect. AME16 includes two early measurements from the β-decay of ^{51}Ti [173, 174] and four reaction-based measurements: three one-neutron transfer reactions [175, 176] and a neutron capture reaction [177]. The two most recent reaction experiments [176, 177] provided measurements with precision on the order of one keV. The two TITAN measurements agree within 1σ with the AME16.

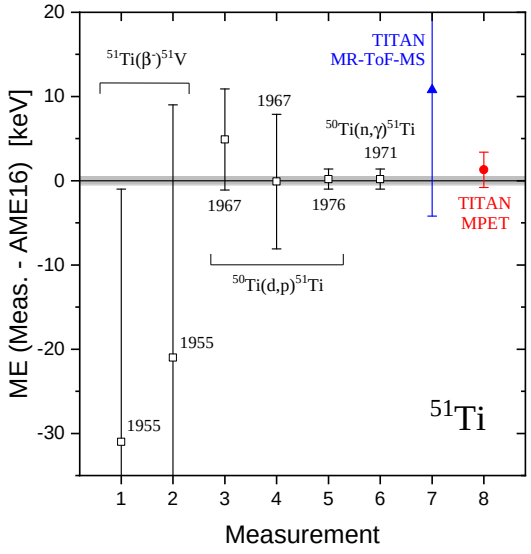

Figure 6.2: Difference between AME16 value [34] and all individual mass measurements of ^{51}Ti [173, 174, 175, 176, 177, 164]. Open symbols are indirect measurements and the gray band shows the error of the AME16 value.

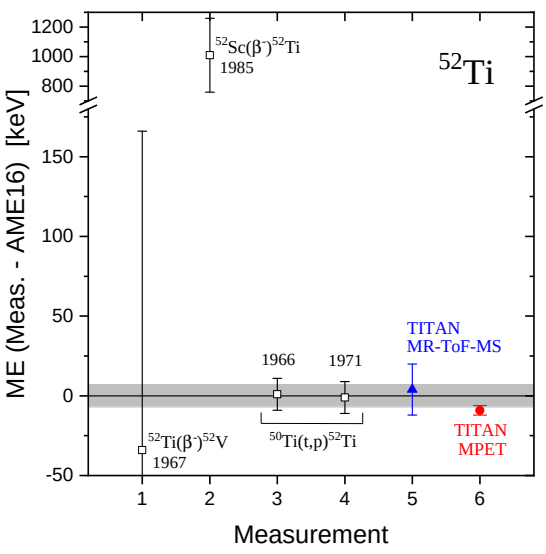

Figure 6.3: Difference between AME16 value [34] and all individual mass measurements of ^{52}Ti [178, 53, 179, 180, 164]. Open symbols are indirect measurements and the gray band shows the error of the AME16 value.

^{52}Ti: All previous measurements of the mass of ^{52}Ti are indirect, as can be seen in fig. 6.3. Two measurements were obtained through the β-decays of ^{52}Ti [178] and of ^{52}Sc [53]. The latter significantly disagrees with all other measurements. The lowest uncertainties were provided by two measurements of the ^{50}Ti(t,p)^{52}Ti reaction [179, 180]. The two TITAN measurements agree within 1σ with the AME16.

^{53}Ti: Only one measurement of the mass of ^{53}Ti is reported in literature, coming from the analysis of its β-decay [181]. As typical for this type of measurement, its uncertainty is large (100 keV). The two TITAN measurements are easily in agreement, as seen in figure 6.4.

^{54}Ti and ^{55}Ti: the knowledge of the masses of the ^{54}Ti and ^{55}Ti isotopes was obtained by the same experiments. The only indirect information comes from an experiment dedicated to studying the β-decays of these isotopes [182]. The remaining data come from direct measurements, mostly from three ToF-MS experiments performed at the Time-of-Flight Isochronous (TOFI) spectrometer in Los Alamos [183, 184, 185]. Additionally, an Isochronous Mass Spectrometry (IMS) measurement of ^{54}Ti was recently performed at the experimental Cooler Storage Ring (CSRe) in Lanzhou [57]. Overall, TITAN MR-ToF-MS values are systematically lighter than the previous measurements, but still in good agreement with them. As shown in figures 6.5 and 6.6, MR-ToF-MS values are within 1σ against most measurements, being barely over 1σ only against a few TOFI results.

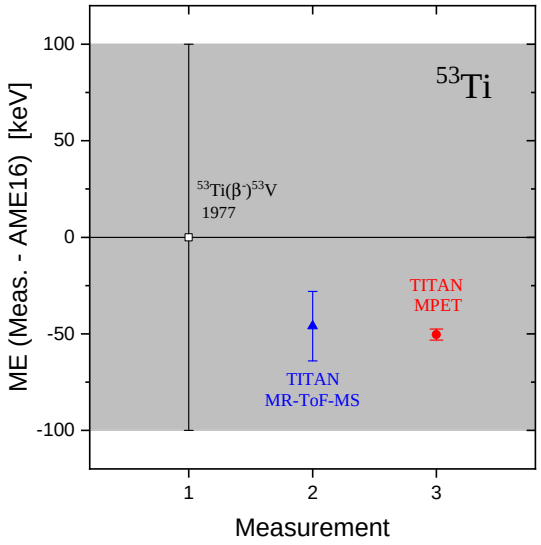

Figure 6.4: Difference between AME16 value [34] and TITAN mass measurements of ^{53}Ti [164]. The AME16 value is based on a single indirect measurement [181] and the gray band shows its error.

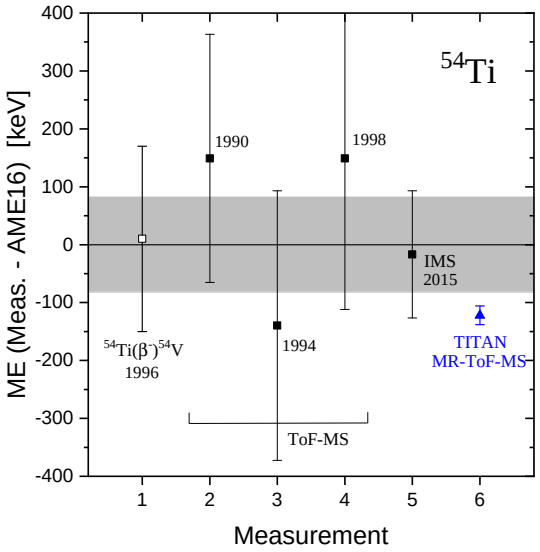

Figure 6.5: Difference between AME16 value [34] and all individual mass measurements of ^{54}Ti [182, 183, 184, 185, 57, 164]. The open symbol is an indirect measurement and the gray band shows the error of the AME16 value.

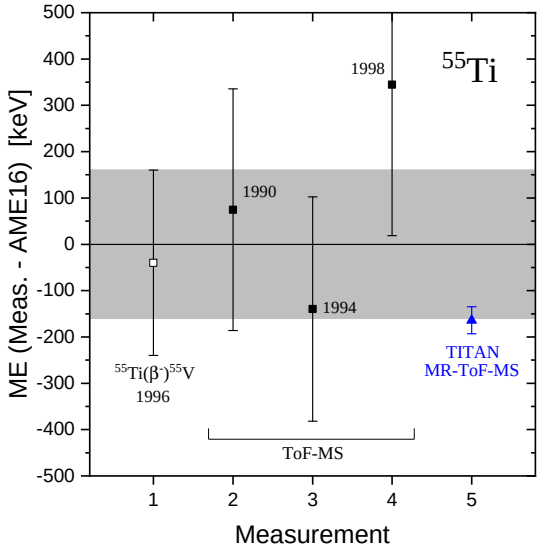

Figure 6.6: Difference between AME16 value [34] and all individual mass measurements of ^{55}Ti [182, 183, 184, 185, 164]. The open symbol is an indirect measurement and the gray band shows the error of the AME16 value.

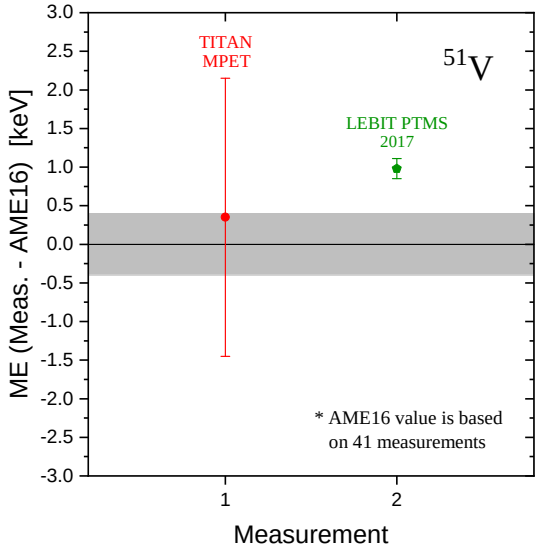

Figure 6.7: Difference between AME16 value [34] and the recent mass measurements of ^{51}V [164, 186]. The AME16 value is based on 41 different measurements (not shown) and the gray band shows its error.

6.2.2 Vanadium Isotopes

^{51}V: the mass of ^{51}V is very well determined in the literature, with 41 direct and indirect measurements included in the AME16 evaluation [34]. They contribute to an uncertainty below 0.5 keV of this quantity. Also, recent results from the LEBIT PTMS system at Michigan State University provided updated mass values for Cr and V isotopes near stability [186] but are not included in the AME16. The LEBIT value for ^{51}V has an uncertainty of only 0.13 keV, but is about 2.5σ from the AME16 value. Nevertheless, the results of the TITAN MPET agree with both, as shown in fig. 6.7.

^{52}V: the mass of ^{52}V is also well measured, with 11 measurements included in the AME16 [34]. However, they are all from indirect techniques. The TITAN MR-ToF-MS measurement is the first to assess this quantity directly. It is 1σ from the AME16, as shown in fig. 6.8.

^{53}V: similarly to ^{52}V, all previous measurements of the mass of ^{53}V are indirect, as can be seen in fig. 6.9. Two measurements were obtained through the β-decays of ^{53}V [187] and of ^{53}Ti [181]. The remaining data were obtained through nuclear reactions: one from the ^{51}V(t,p)^{53}V reaction [188] and another from the ^{54}Cr(d,^{3}He)^{53}V reaction [189], which provides the lowest uncertainty. The TITAN MR-ToF-MS measurement is in good agreement with all measurements, except with the one obtained through the β-decay of ^{53}V.

^{54}V: in the literature, three indirect measurements were reported for the mass of ^{54}V, as shown in fig. 6.10. Two are from β-decays: of ^{54}V [190] and of the parent ^{54}Ti [182]. The lowest uncertainty is provided by a ^{54}Cr(t,^{3}He)^{54}V reaction experiment [191]. The TITAN MR-ToF-MS measurement agrees with all of them.

^{55}V: Only one measurement of the mass of ^{55}V is reported in the literature. It comes from the analysis of its β-decay [192] and has a large uncertainty ($\sim$ 100 keV). The TITAN MR-ToF-MS measurement is in good agreement with it, as seen in figure 6.11.

6.2.3 Other Isotopes

The other isotopes measured in this campaign are all well studied and documented in literature, with a few tens of different measurements reported for each. Since there is a high degree of reproducibility and small uncertainties among those previous measurements, they provide a great test to our data.

In figure 6.12, mass measurements of chromium isotopes $^{52-54}$Cr performed with the MPET are compared to AME16 values. In total, the AME16 congregates 33 measurements of ^{52}Cr, 28 of ^{53}Cr and 38 of ^{54}Cr [34]. Results from the LEBIT PTMS spectrometer [186] published after the AME16 evaluation provided better precision and are also shown. The TITAN MPET measurements are in good agreement with all presented values.

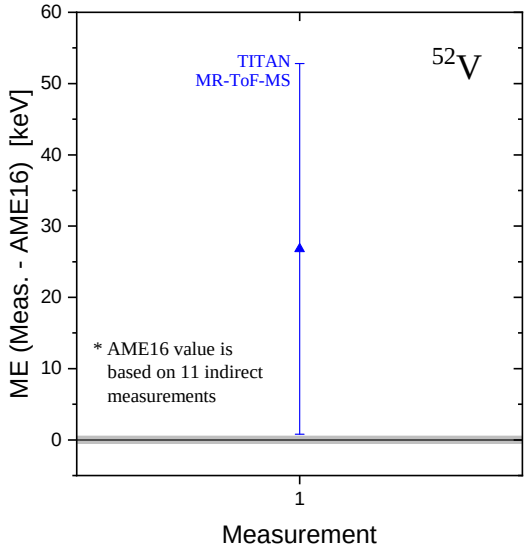

Figure 6.8: Difference between AME16 value [34] and the recent first direct mass measurement of ^{52}V [193]. The AME16 value is based on 11 different indirect measurements (not shown) and the gray band shows its error.

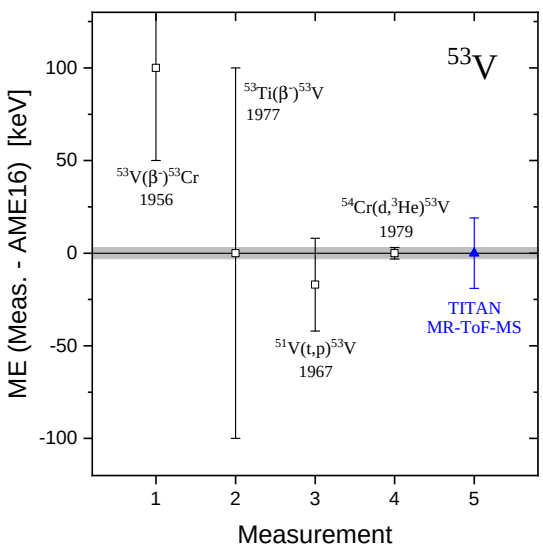

Figure 6.9: Difference between AME16 value [34] and all individual mass measurements of ^{53}V [187, 181, 188, 189, 193]. Open symbols are indirect measurements and the gray band shows the error of the AME16 value.

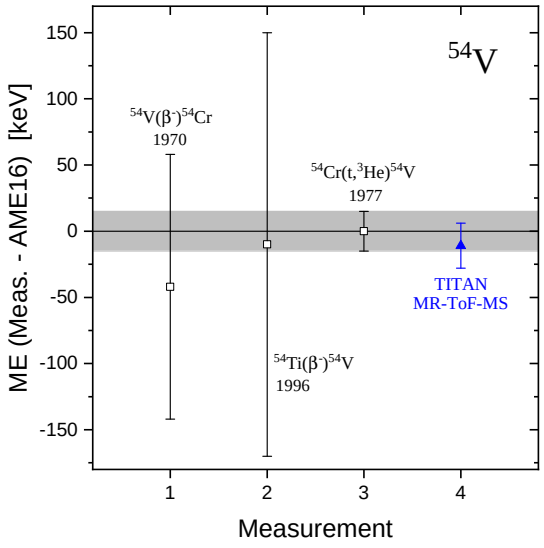

Figure 6.10: Difference between AME16 value [34] and all individual mass measurements of ^{54}V [190, 182, 191, 193]. Open symbols are indirect measurements and the gray band shows the error of the AME16 value.

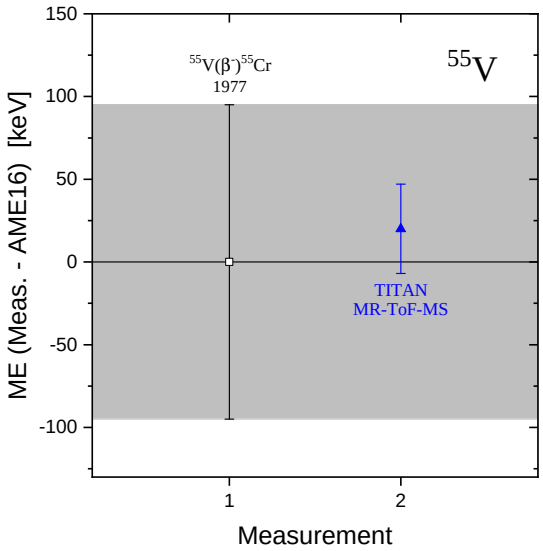

Figure 6.11: Difference between AME16 value [34] and TITAN mass measurements of ^{55}V [193]. The AME16 value is based on a single indirect measurement [192] and the gray band shows its error.

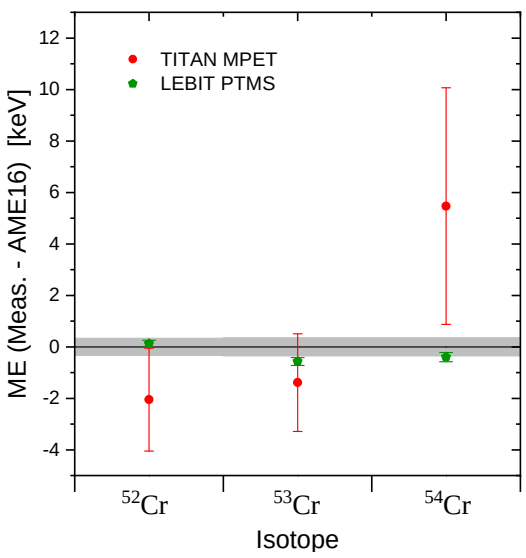

Figure 6.12: Difference between AME16 value [34] and the recent PTMS mass measurements of $^{52-54}$Cr [164, 186]. The gray band shows the errors of the AME16 values.

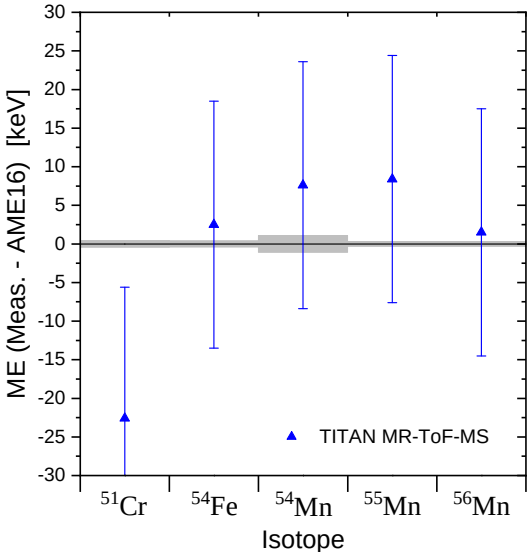

Figure 6.13: Difference between AME16 value [34] and the recent MR-ToF-MS mass measurements of ^{51}Cr, ^{54}Fe, ^{54}Mn, ^{55}Mn and ^{56}Mn. The gray band shows the errors of the AME16 values.

The measurements performed with the MR-ToF-MS are in good agreement with the AME16. The comparison is shown in figure 6.13 for ^{51}Cr, ^{54}Fe, ^{54}Mn, ^{55}Mn and ^{56}Mn. The body of knowledge involves 13 measurements of ^{51}Cr, 49 of ^{54}Fe, 39 of ^{55}Mn and 9 of ^{56}Mn [34]. In the case of ^{54}Mn, 13 indirect measurements are reported. However, none is reported from direct techniques, making the one done at the MR-ToF-MS the first for this isotope.

6.3 Updated Isotopic Chains and Evolution of the N=32 Shell Closure

Given the good agreement between the results of our spectrometers and with the literature, the masses of the measured isotopes were updated by taking the weighted average of all measurements of each of them. In table 6.2, the weighted average of the measurements of the two TITAN spectrometers are shown. As can be seen, the combined TITAN values are dominated by MPET measurements where available, since it provided lower uncertainties than MR-TOF-MS. Also in table 6.2 the weighted average between TITAN measurements and the values recommended by AME16 are shown. With TITAN data, the mass uncertainties were considerably reduced in 6 of the isotopes: of $^{52-55}$Ti and ^{54,55}V.

The new measurements bring the structure of the nuclear mass landscape around $N = 32$ of the Ti and V isotopic chains to the scale of a few tens of keV. Since there were no deviations from the literature, the data did not change the shape of the mass

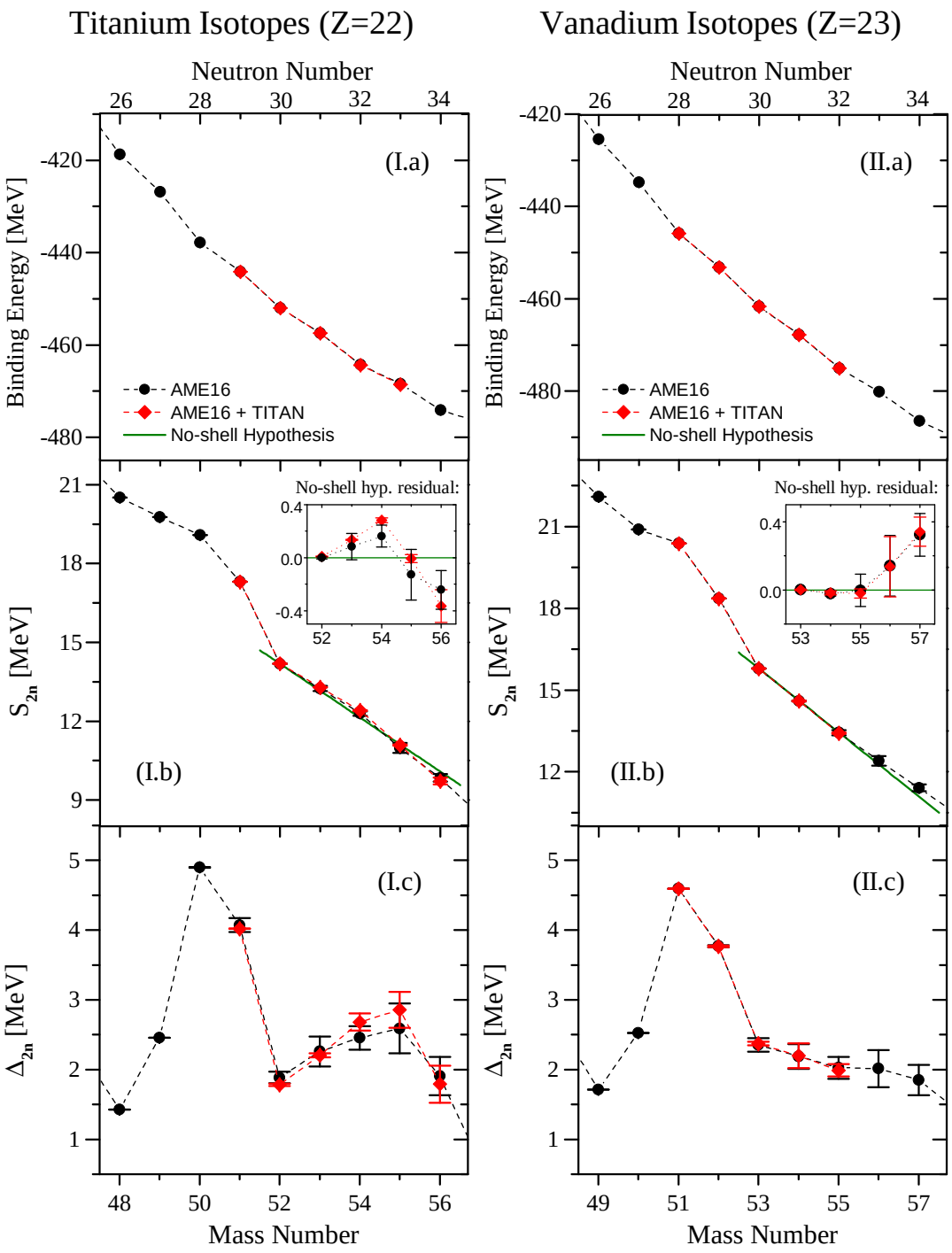

Figure 6.14: The mass landscape around titanium *(I)* and vanadium *(II)* isotopes is shown from three perspectives: *(a)* absolute masses (shown in binding energy format), *(b)* its first "derivative" as two-neutron separation energies (S_{2n}), and *(c)* its second "derivative" as empirical neutron-shell gaps (Δ_{2n}). Data prior to this experiment are shown in black, while updated data are shown in red. The no-shell hypothesis on $N = 32$ is presented in the *(b)* panels as smooth linear fits to S_{2n} AME16 data between $^{52-56}$Ti and $^{53-57}$V, and their residuals are shown in the inserts.

Table 6.2: Mass excesses (in keV/c^2) of Ti and V isotopes recommended by AME16 and measured with the TITAN MR-ToF-MS and the TITAN MPET. Weighted averages of combined TITAN measurements and of all values are presented. Neighboring isotopes are also shown for reference. TITAN measurements performed in other isotopic chains did not provide significant improvements to the existing mass uncertainties, so they were omitted.

Species	AME16	MR-ToF-MS	MPET	TITAN (combined)	**AME16 + TITAN**
^{49}Ti	−48563.79 (11)				−48563.79 (11)
^{50}Ti	−51431.66 (12)				−51431.66 (12)
^{51}Ti	−49732.84 (51)	−49722 (15)	−49731.5 (2.1)	−49731.3 (2.1)	−49732.75 (49)
^{52}Ti	−49470 (7)	−49466 (16)	−49479.1 (3.0)	−49478.7 (3.0)	−49477.3 (2.8)
^{53}Ti	−46831 (100)	−46877 (18)	−46881.4 (2.9)	−46881.3 (2.9)	−46881.2 (2.9)
^{54}Ti	−45622 (82)	−45744 (16)		−45744 (16)	−45740 (15)
^{55}Ti	−41668 (162)	−41832 (29)		−41832 (29)	−41827 (29)
^{56}Ti	−39320 (121)				−39320 (121)
^{57}Ti	−33916 (256)				−33916 (256)
^{49}V	−47961.93 (83)				−47961.93 (83)
^{50}V	−49224.01 (41)				−49224.01 (41)
^{51}V	−52203.84 (40)		−52203.5 (1.8)	−52203.5 (1.8)	−52203.83 (39)
^{52}V	−51443.77 (42)	−51417 (26)		−51417 (26)	−51443.76 (42)
^{53}V	−51851 (3)	−51851 (19)		−51851 (19)	−51851 (3)
^{54}V	−49893 (15)	−49904 (17)		−49904 (17)	−49898 (11)
^{55}V	−49145 (95)	−49125 (27)		−49125 (27)	−49126 (26)
^{56}V	−46155 (177)				−46155 (177)
^{57}V	−44413 (80)				−44413 (80)

surface in the region. However, the refined precision solved ambiguities regarding the existence of particular shell effects. The remaining of this section explores this in detail.

The impact of the measurements can be seen in figure 6.14, which presents the binding energies (E_B) and their "derivatives": the two-neutron separation energies (S_{2n}) and the empirical neutron-shell gaps (Δ_{2n}). These quantities were defined in chapter 1 in equations 1.2, 1.4 and 1.6, respectively. For convenience, they are reproduced here:

$$\begin{aligned} E_B(N,Z) &= \left[m_a(N,Z) - Z\cdot m_p - N\cdot m_n - Z\cdot m_e\right] c^2 \quad , \\ S_{2n}(N,Z) &= \left[m_a(Z,N-2) + 2m_n - m_a(N,Z)\right] c^2 \qquad \text{and} \\ \Delta_{2n}(N,Z) &= S_{2n}(N,Z) - S_{2n}(N+2,Z) \quad ; \end{aligned}$$

where Z and N are the atomic and neutron numbers, m_a, m_p, m_n and m_e are the masses of the atom, the proton, the neutron and the electron, respectively, and c is the speed of light.

In figure 6.14, the canonical $N = 28$ shell closure is easily recognized through the sharp features at S_{2n} and Δ_{2n} around ^{50}Ti and ^{51}V. In the S_{2n}, it can be recognized by a downwards "kink". In the Δ_{2n}, it is evidenced by a peak arising from the baseline, which in the region is around 2 MeV. A search for these signatures in $N = 32$ was

performed among titanium isotopes (described in sec. 6.3.1) and vanadium isotopes (shown in sec. 6.3.2).

As pointed out in section 1.2, these signatures must be consistent across several isotopic chains to characterize a shell closure. Therefore the evolution of shell effects in $N = 32$ is also analyzed across the neighboring isotopic chains in sec. 6.3.3.

6.3.1 Signatures of N=32 Shell Effects in Titanium

Although less pronounced, similar features seen at $N = 28$ are also present around ^{54}Ti. They possibly correspond to the effects of a shell closure in $N = 32$. To explore these effects in the S_{2n} surface with more precision, the hypothesis of absence of any shell effect (No-Shell Hypothesis) was analyzed. This hypothesis assumes a smooth and linear behavior of S_{2n} around $N = 32$, with no observed discontinuities or kinks.

To test this hypothesis, a linear function was fit to the S_{2n} data between ^{52}Ti and ^{56}Ti. The result is shown as the green line in panel *(I.b)* of figure 6.14, and the residual of the fit is shown in the insert of the same panel. Using only data from AME16, the fit produces[25] a χ^2_{red} of 1.94. This result is not statistically significant to rule out any interpretation. With the inclusion of the data from this experiment, the fit produces a χ^2_{red} of 51.13. Therefore, the No-Shell Hypothesis is completely ruled out by the new mass measurements. Then, with the observation of a downwards "kink" in S_{2n}, the data presented here conclusively establish the existence of signatures of shell effects at $N = 32$ in the Ti chain.

The empirical neutron-shell gap at ^{54}Ti (panel *(I.c)* of figure 6.14) has changed from 2.45(17) MeV to 2.70(12) MeV, with the mass of ^{56}Ti now the largest source of uncertainty. The new measurements also better define the peak at $N = 32$ rising from the ~ 2 MeV baseline, confirming the signature of shell effect seen at S_{2n}.

However, the shell features observed in titanium are very weak and well below normally expected for shell closures. A comparison with the traits seen at $N = 28$ in figure 6.14 illustrates this discrepancy. The existence of a special pattern at titanium can be identified by looking at the systematics with the nearby elements, which is done in sec. 6.3.3.

6.3.2 Signatures of N=32 Shell Effects in Vanadium

The signatures of a shell closure in $N = 32$ are entirely absent in vanadium. This was evident from the previous measurements and confirmed by the addition of the new measurements with higher precision.

In the Δ_{2n} data (panel *(II.c)* of fig. 6.14), there is clearly no peak or raise above the baseline seen in ^{55}Ti. In the S_{2n} data (panel *(II.b)* of the same figure), a smooth trend is seen between ^{53}Ti and ^{57}Ti.

25 χ^2_{red} is the χ^2 divided by the number of degrees of freedom of the fitting procedure.

A similar analysis of a No-shell Hypothesis reveals it to be incompatible with the S_{2n} data. It reveals a subtle upwards "kink" at ^{55}Ti, which does not characterize a shell effect. Possible interpretations for this effect are discussed in the following.

6.3.3 Evolution of the N=32 Shell Closure

It is important to analyse the features seen in titanium and in vanadium in the context of the neighboring nuclides. In figures 6.15 and 6.16, the S_{2n} and Δ_{2n} data are shown between K ($Z = 19$) and Cr ($Z = 24$) isotopic chains around $N = 32$. The same shell signatures seen in Ti are reproduced, with more intensity, towards lower Z. It is evident that titanium is at a transition point between V and Cr, which shows no sign of a $N = 32$ shell closure, and the strong closure seen in Sc, Ca, and K.

Towards higher Z, starting from vanadium, different phenomena occur. The S_{2n} surface subtly bends upwards, systematically through many isotopic chains. This behavior is commonly associated with the emergence of nuclear shape deformation [194, 195]. V, Cr, and Mn are located in a mid-shell region between $Z = 20$ and $Z = 28$, where the effects of deformation are more likely to occur. Moreover, as was mentioned in sec. 1.4.2, there is spectroscopic evidence that there is an energy level ordering change between Sc and V [64]. Nevertheless, it is possible to affirm that vanadium is also a transition point where a particular systematic behavior starts to occur towards higher Z. However, it requires a more in-depth analysis to state anything about the nature of this behavior.

To better inspect the evolution of the $N = 32$ shell closure, figure 6.17 shows the empirical neutron-shell gap across the $N = 32$ isotonic chain and compares it to the data across the canonical $N = 28$ chain. Overall, $\Delta_{2n}(N = 32)$ mirrors the behavior of $\Delta_{2n}(N = 28)$, being systematically lower by about 2 MeV. It suggests that the mechanism that governs the evolution of the $N = 28$ shell might be the same governing the evolution of the emerging $N = 32$ shell. This hypothesis could be explored in future shell model studies.

Figure 6.17 also includes Δ_{2n} data across the $N = 30$ isotonic chain. Since shell features are not recognized in this neutron number, this data can be used as an estimation of the Δ_{2n} baseline. It is interesting to point out the crossing between $\Delta_{2n}(N = 32)$ and $\Delta_{2n}(N = 30)$ occurring amid Ti ($Z = 22$) and V ($Z = 23$), revealing the point of emergence of shell signatures in $N = 32$ among mass observables.

The trends in Δ_{2n} also reveal how abrupt the onset of magicity in $N = 32$ is. It starts from weak effects in titanium to its peak in scandium. However, peaks in the shell gap usually occur in doubly-magic nuclei, as illustrated by the $N = 28$ case shown in 6.17. It is expected that the peak of $\Delta_{2n}(N = 32)$ occurs in ^{52}Ca, which should be extra bound due to the closure of the proton shell in $Z = 20$. After the mass measurements described here, the only isotopic chain not studied with high-resolution mass spectrometry techniques is of scandium. Therefore, new mass measurements between ^{51}Sc and ^{55}Sc are required to confirm the evolution of magicity in $N = 32$.

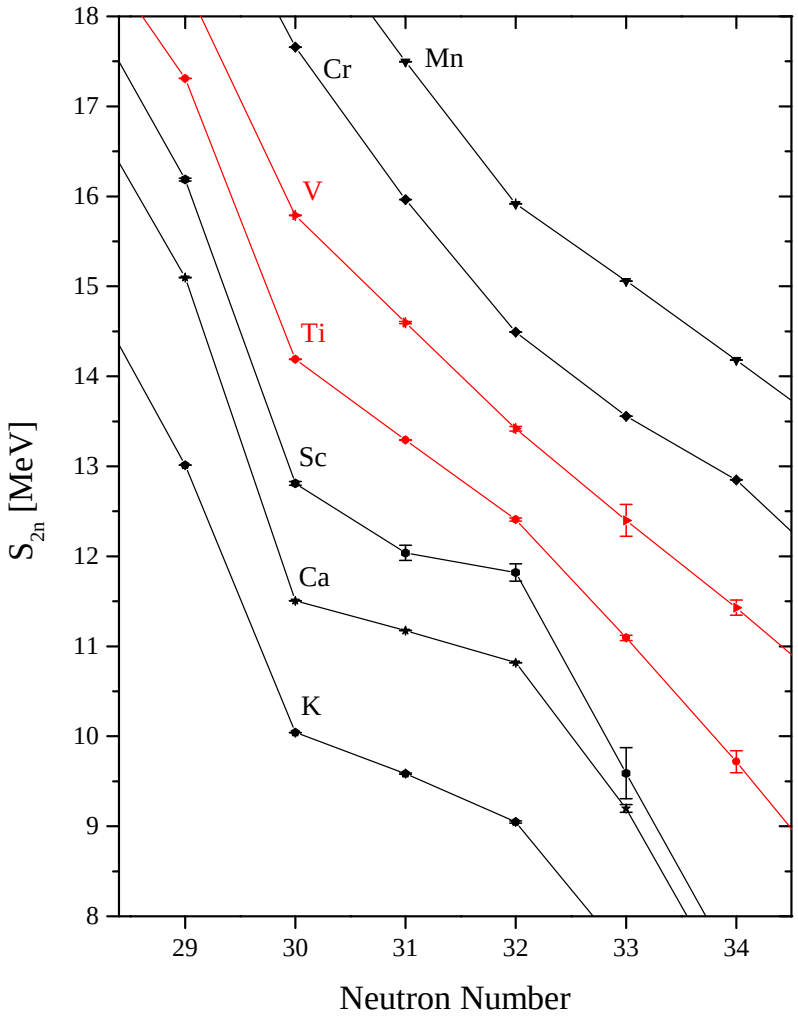

Figure 6.15: The two-neutron separation energies between K ($Z = 19$) and Mn ($Z = 25$) isotopic chains around $N = 32$. Data is taken from the AME16 [34], chains updated with TITAN data are shown in red.

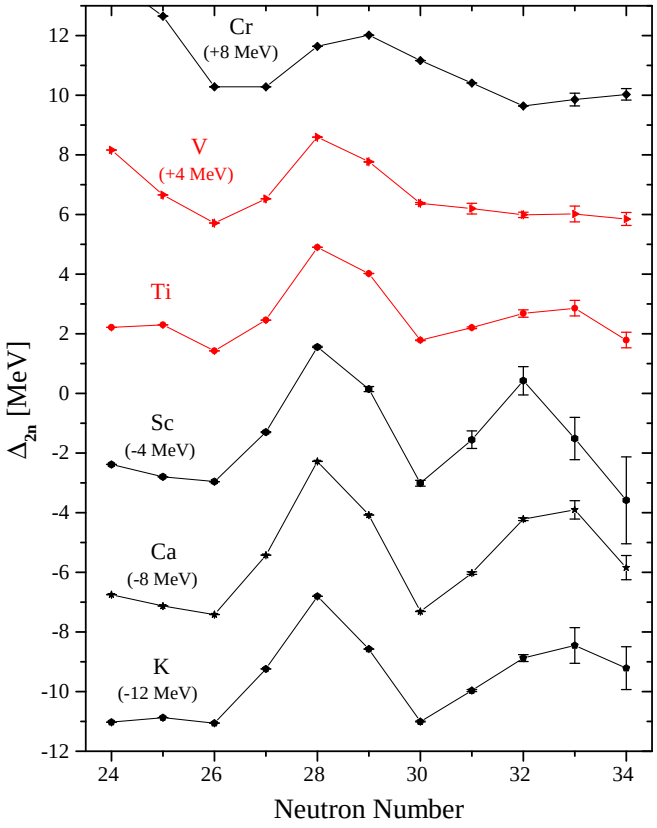

Figure 6.16: Empirical neutron-shell gaps between K ($Z = 19$) and Cr ($Z = 24$) isotopic chains showing the effect of the $N = 28$ shell and the rise of shell effects in $N = 32$. Data is taken from the AME16 [34], chains updated with TITAN data are shown in red. Each isotopic chain was shifted by a multiple of 4 MeV for clarity.

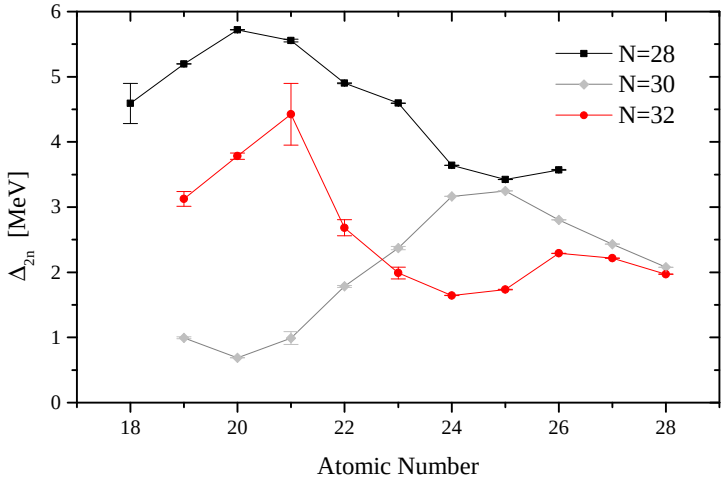

Figure 6.17: Empirical neutron-shell gaps across isotonic chains of $N = 28$ (black) and $N = 32$ (red), where shell effects have been recognized, and of $N = 30$ (gray) where no shell effects exist and serve as a reference line. The crossing between $N = 30$ and $N = 32$ Δ_{2n} data in Ti ($Z = 22$) and V ($Z = 23$) reveals the point of emergence of shell signatures in $N = 32$ among mass observables.

6.4 Tests of *Ab Initio* Theories

The clearer picture of the evolution of the $N = 32$ shell allows us to investigate how well our knowledge of nuclear forces and many-body methods describes the observed behaviors. The mass data in the $N = 32$ region was compared to state-of-the-art *ab initio* nuclear structure calculations. The tested methods and interactions were described in sec. 2.4.

In particular, the Multi-Reference In-Medium Similarity Renormalization Group (MR-IMSRG) [92, 93, 94], the Valence-Space (VS-) IMSRG [95, 96, 97, 98], and the self-consistent Gorkov-Green's Function (GGF) [99, 100, 101, 102] approaches were applied. All calculations were performed with interactions based on the chiral effective field theory: 1.8/2.0(EM) [86, 88], the N^2LO_{sat} [90] and the NN+3N(lnl) interactions. They all included two- (NN) and three-nucleon (3N) interactions with parameters adjusted typically to the lightest systems ($A = 2, 3, 4$) as the only input[26] [85, 196, 197].

To get an overall picture of the current stage of techniques, four large-scale calculations were performed using different permutations among the available methods and interactions. IMSRG-based methods employed two different interactions: the 1.8/2.0(EM) interaction was used in a VS-IMSRG calculation, and the N^2LO_{sat} was used in an MR-IMSRG calculation. The GGF method was also employed in calculations with two different interactions: N^2LO_{sat} and NN+3N(lnl) interactions. The N^2LO_{sat} interaction was employed in calculations using the GGF method and MR-IMSRG method. In this way, the breadth of the variations seen among the results can be interpreted as an overall "error" of the employed techniques.

All calculations were performed for all Ti isotopes in the region of interest. One exception is the calculation performed with the MR-IMSRG method, which can only provide results for even-mass titanium isotopes. Additionally, since the VS-IMSRG can access all nuclei in this region, the calculations employing the 1.8/2.0(EM) + VS-IMSRG combination were extended to neighboring isotopes as well. Some of the VS-IMSRG calculations had already been published for the Cr [195], Sc [198] and Ca [88] chains. Calculations employing the NN+3N(lnl) + GGF combination were also available for odd-mass scandium isotopes.

6.4.1 Results

The results of the calculations are compared to experimental mass data for Ti and V in figure 6.18. All approaches predicted signatures of shell closures at $N = 28$ and $N = 32$, although the strengths of the neutron-shell gaps in the magic numbers are systematically overpredicted in all cases.

Calculations with the N^2LO_{sat} interaction typically performs well for radii and charge distributions in this mass range [59], but here are found to be the least ac-

26 Exception given to the N^2LO_{sat} interaction that also uses selected heavier systems to adjust the nuclear saturation density, as explained in sec. 2.4.

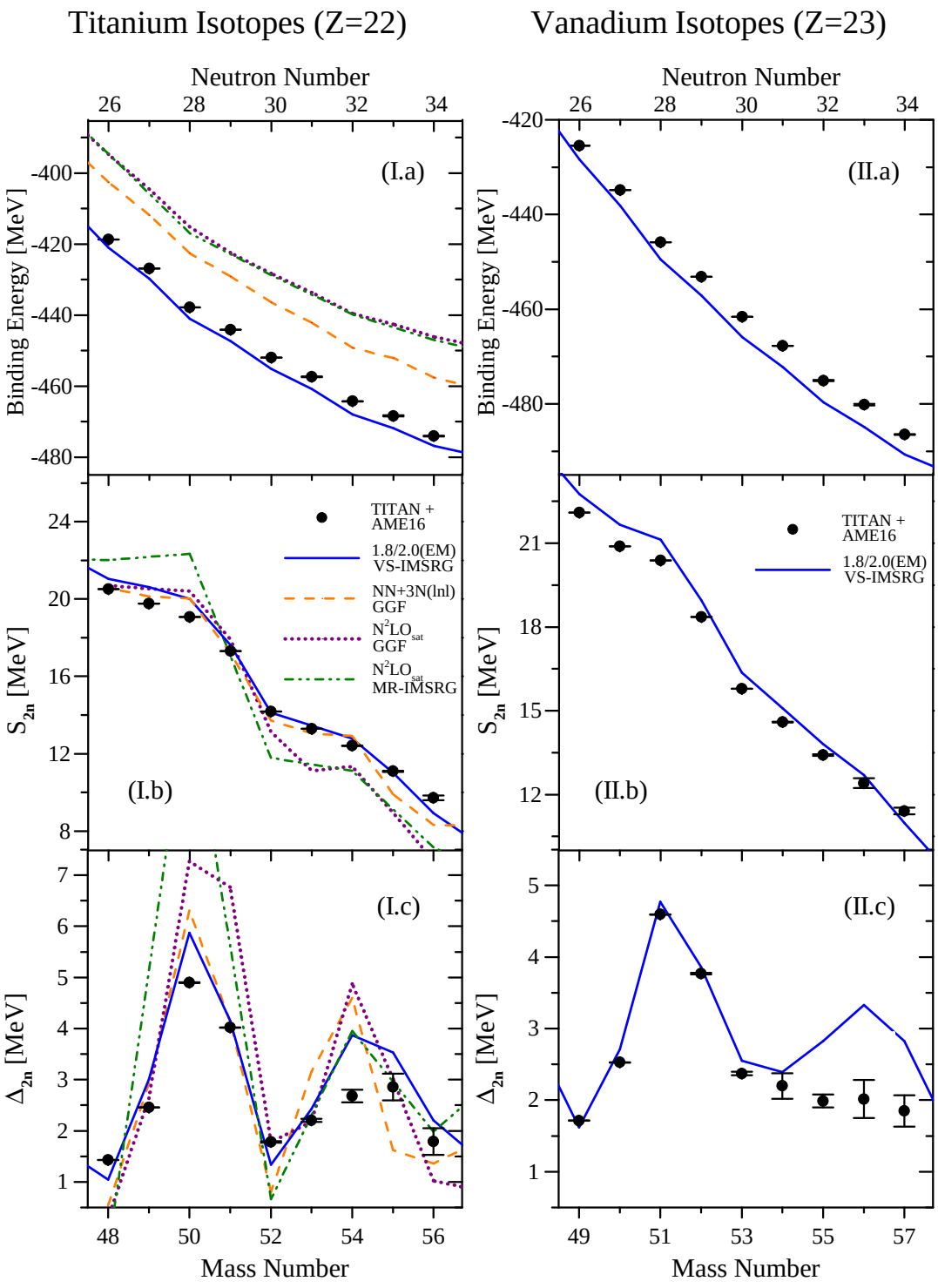

Figure 6.18: Results of *ab initio* calculations (lines) are compared to experimental values (points) of the mass landscape around titanium *(I)* and vanadium *(II)* isotopes. Mass observables are shown from three perspectives: *(a)* binding energy, *(b)* two-neutron separation energies (S_{2n}), and *(c)* empirical neutron-shell gaps (Δ_{2n}). Experimental data combines measurements incorporated in AME16 and this TITAN experiment.

curate in describing mass observables. They predict underbound titanium isotopes by about 30 MeV, independently of the many-body method employed. Also, this interaction highly overpredicts the strength of the neutron-shell gaps both at $N = 28$ and $N = 32$, compared to the other studied interactions.

The calculations with the 1.8/2.0(EM) interaction provide the best description of the Ti data. Masses are overbound by only ≈ 3.0 MeV, and the neutron shell gaps are the closest to the experimentally observed values. In the vanadium chain it had similar performance; however, it wrongly predicted the existence of shell effects in $N = 32$.

The results with the NN+3N(lnl) interaction are also in good agreement with data, but titanium isotopes are underbound by about 20 MeV. Truncation schemes currently employed in GGF calculations are known to result in less total binding energy (typically $10 - 15$ MeV for mid-mass nuclei) compared to more advanced truncation schemes [199]. This would bring NN+3N(lnl) in better agreement with the experimental binding energies.

Results of Δ_{2n} calculations for all isotopic chains between Ca ($Z = 19$) and Cr ($Z = 24$) with the 1.8/2.0(EM) + VS-IMSRG combination are shown in figure 6.19. Calculations with the NN+3N(lnl) + GGF combination are also included for Ti and Sc chains. The calculations provide an excellent description of neutron shell evolution at $N = 28$ and of the $N = 32$ where it is strong, in Ca and Sc. Also, while there is a general overprediction of the neutron shell gap at $N = 32$, the trends from $N = 28$ to $N = 32$ are mostly reproduced. In contrast, calculated shell gaps in titanium rise too steeply from $N = 30$ to $N = 32$ compared to experiment and even predict modest shell effects in the vanadium chain. This indicates that the $N = 32$ closure is predicted to arise too early towards Ca.

The evolution of Δ_{2n} across isotonic chains is shown in figure 6.20 with results from the 1.8/2.0(EM) + VS-IMSRG calculation. The comparison with experimental data makes evident the overestimation of shell gaps by the theoretical calculation. Both in the $N = 28$ and the $N = 32$ shells, titanium ($Z = 22$) is the isotone with largest overprediction of Δ_{2n}. While the origin of this discrepancy is not completely clear, it is known that signatures of shell closures, such as first excited 2^+ energies and shell gaps, are often modestly overestimated by the VS-IMSRG [88]. This systematic overprediction might also explain the early rising of shell effects in vanadium.

As also seen in experimental data, the 1.8/2.0(EM) + VS-IMSRG calculation predicts that the $N = 32$ shell mirrors the evolution of the $N = 28$ shell but systematically lower by about 2 MeV. This reinforces the idea that similar mechanisms govern the evolution of both shells. However, as discussed in chapter 2, *ab initio* approaches are not the best tool to investigate the nature of specific effects.

Unlike the experimental data, the calculations predict that the peak of $N = 32$ shell effects happen in calcium ($Z = 20$) and not in scandium ($Z = 21$). It further motivates the need for new high-resolution mass measurements in the scandium chain.

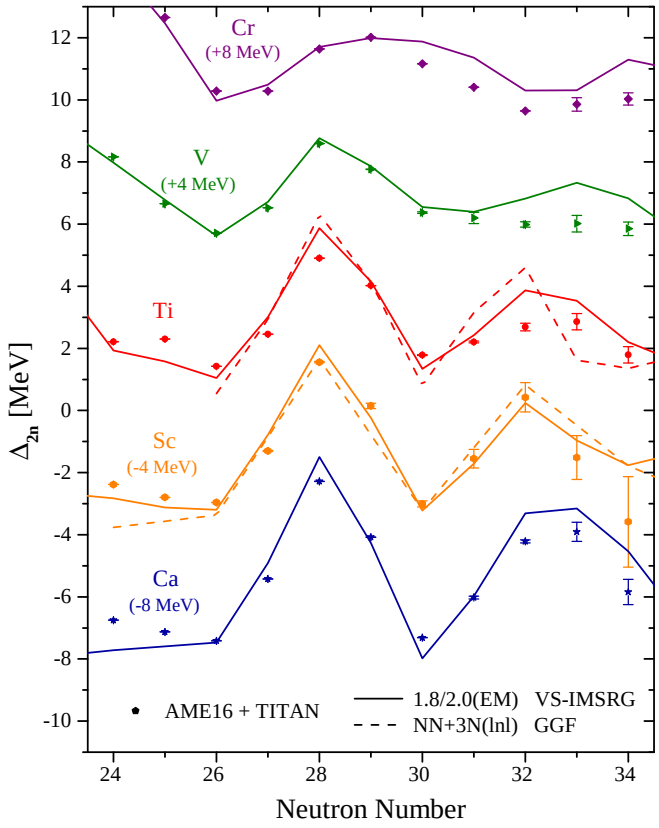

Figure 6.19: Results of *ab initio* calculations (lines) are compared to experimental values (points) of empirical neutron-shell gaps between K ($Z = 19$) and Cr ($Z = 24$) isotopic chains around $N = 28$ and $N = 32$. Experimental data combines measurements incorporated in AME16 and this TITAN experiment.

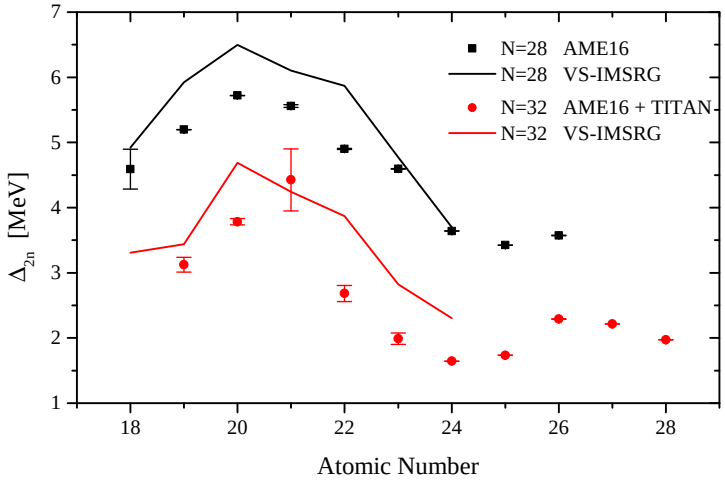

Figure 6.20: Evolution of empirical neutron-shell gaps across isotonic chains of $N = 28$ (black) and $N = 32$ (red), as calculated by the 1.8/2.0(EM) + VS-IMSRG combination (lines). Calculations are also compared with experimental data (points).

7 CONCLUSIONS AND OUTLOOK

In the last decades, we witnessed unprecedented progress in our understanding of the atomic nucleus. Novel high-sensitivity experimental techniques have opened up the pathway to inspect properties of very rare nuclei with high precision. Through them, surprising new phenomena were discovered, which challenge our nuclear theories. Also, for the first time, powerful computers enabled theories to describe complex atomic nuclei from fundamental principles, applying features of Quantum Chromodynamics to many-body quantum methods. These advances may finally trace the right route towards the long-sought understanding of nuclear matter. If successful they may also fill critical missing pieces in related fields, such as on the origin of chemical elements and the evolution of astrophysical objects.

These two fronts of research walk side-by-side, as advances in one guide advances in the other. The study presented at the core of this thesis is a state-of-the-art example of the interplay between experiment and theory in the field of nuclear structure. In this case, the emergence of shell effects at the non-canonical magic number $N = 32$ was investigated though precision mass measurements. Samples of neutron-rich titanium isotopes were produced by the ISAC facility through the ISOL method and ionized through the laser ionization technique. Vanadium isotopes were co-produced and were also present in the sample. The ions were transported to the TITAN's Penning trap and multiple-reflection time-of-flight mass spectrometers, where measurements were performed independently.

The atomic masses of $^{51-55}$Ti and $^{51-55}$V were successfully measured. The new measurements agree with the previous measurements in the literature and bring the structure of the nuclear mass landscape to the scale of a few tens of keV around $N = 32$. The results conclusively establish the existence of weak shell effects at $N = 32$ among titanium isotopes and confirm their absence among vanadium isotopes. It narrows down the evolution of this nuclear shell closure, mainly regarding its abrupt emergence. The $N = 32$ shell evolution outlined from inspecting mass observables agrees very well with conclusions drawn from other experimental approaches, such as from γ-spectroscopy (see fig. 1.7, for example).

The measurements were compared with the results of several *ab initio* nuclear theories. Overall, all presented theories perform well in this region, but the study reveals deficiencies in the description of the $N = 32$ shell. Specifically, the strength of shell effects are systematically overestimated, and they are wrongly predicted to start emerging in vanadium. This work provides fine information for the development of the next generation of nuclear *ab initio* techniques.

As demonstrated by this and other studies, the new magic number $N = 32$ is a fascinating phenomenon in nuclear structure and requires further experimental and theoretical exploration. As pointed out in our analysis, new mass measurements of scandium isotopes in the region are needed to better understand the peak strength of shell effects at $N = 32$. Moreover, the similarities between the evolution of the $N = 28$ and the $N = 32$ shells are remarkable and should be investigated theoretically, especially through shell model approaches.

Naturally, further investigation is required towards the low-Z boundary of $N = 32$ shell closure where data is most scarce. Trends from experimental data and results from theoretical models suggest the magicity of $N = 32$ should vanish in the region with $Z < 18$.

Similarly, shell effects emerging at $N = 34$ are receiving increasing attention from the scientific community [50, 200]. Shell model calculations predict similar mechanisms that drive the evolution of $N = 32$ and $N = 34$ shells. Meanwhile, recent experiments suggest that its effects start appearing at much lower Z than the $N = 32$, but become much stronger right in the argon chain [201].

Nevertheless, experiments pushing towards $N = 34$ and the low-Z boundary will probe increasingly rare isotopes. Consequently, techniques need to be able to overcome the challenges associated with them: shorter lifetimes, lower intensities, and more substantial contamination levels.

In face of those challenges, the results of the TITAN MR-ToF-MS for Ti and V provide an essential milestone on precision mass spectroscopy of rare isotopes. They highlight the scientific capabilities of this new type of spectrometer and illustrate how its sensitivity enables probing of much rarer species with competitive precision. Now successfully benchmarked against the "standard" mass measurement technique - Penning trap mass spectrometry - the TITAN MR-ToF-MS is an ideal candidate to probe outer regions of the nuclear chart for nuclear structure investigations.

In the near future, the TRIUMF Laboratory will commission its Advanced Rare Isotope Laboratory (ARIEL) [202] to expand its scientific capabilities beyond the ISAC production facility. It will diversify the radioisotope production through different target and driver beam combinations and deliver more exotic isotope species at high intensities to experiments. The MR-ToF-MS together with ongoing upgrades to the EBIT [203], the MPET (see appendix B) and the CPET [157] will leverage TITAN's capacity to perform experiments in the ARIEL era. They will place the TITAN facility in a prime position to push the precision boundary of the nuclear chart and answer the outstanding questions in nuclear structure.

BIBLIOGRAPHY

[1] D. Hanneke, S. Fogwell, and G. Gabrielse. New Measurement of the Electron Magnetic Moment and the Fine Structure Constant. *Phys. Rev. Lett.*, 100(12): 120801, mar 2008. ISSN 0031-9007. doi: 10.1103/PhysRevLett.100.120801. URL https://link.aps.org/doi/10.1103/PhysRevLett.100.120801.

[2] S. Sturm, F. Köhler, J. Zatorski, A. Wagner, Z. Harman, G. Werth, W. Quint, C. H. Keitel, and K. Blaum. High-precision measurement of the atomic mass of the electron. *Nature*, 506(7489):467–470, feb 2014. ISSN 0028-0836. doi: 10.1038/nature13026. URL http://www.nature.com/articles/nature13026.

[3] Edmund G. Myers. The teamwork of precision. *Nature*, 506(7489):440–441, feb 2014. ISSN 0028-0836. doi: 10.1038/nature13059. URL http://www.nature.com/articles/nature13059.

[4] R. A. Friesner. Ab initio quantum chemistry: Methodology and applications. *Proc. Natl. Acad. Sci.*, 102(19):6648–6653, may 2005. ISSN 0027-8424. doi: 10.1073/pnas.0408036102. URL http://www.nature.com/articles/s41570-018-0118http://www.pnas.org/cgi/doi/10.1073/pnas.0408036102.

[5] David C Clary. Quantum Dynamics of Chemical Reactions. *Science (80-.).*, 321(5890):789–791, 2008. ISSN 0036-8075. doi: 10.1126/science.1157718. URL http://science.sciencemag.org/content/321/5890/789.

[6] Michael Ruggenthaler, Nicolas Tancogne-Dejean, Johannes Flick, Heiko Appel, and Angel Rubio. From a quantum-electrodynamical light–matter description to novel spectroscopies. *Nat. Rev. Chem.*, 2(3):0118, mar 2018. ISSN 2397-3358. doi: 10.1038/s41570-018-0118. URL http://www.nature.com/articles/s41570-018-0118.

[7] Jordi José and Christian Iliadis. Nuclear astrophysics: the unfinished quest for the origin of the elements. *Reports Prog. Phys.*, 74(9):96901, 2011. URL http://stacks.iop.org/0034-4885/74/i=9/a=096901.

[8] Evgeny Epelbaum, Hermann Krebs, Timo A. Lähde, Dean Lee, and Ulf-G. Meißner. Structure and rotations of the hoyle state. *Phys. Rev. Lett.*, 109: 252501, Dec 2012. doi: 10.1103/PhysRevLett.109.252501. URL https://link.aps.org/doi/10.1103/PhysRevLett.109.252501.

[9] Stephen G. Benka. The hoyle state of carbon-12 unmasked. *Physics Today*, 2013. doi: 10.1063/pt.4.0057. URL https://doi.org/10.1063/pt.4.0057.

[10] J. C. Hardy and I. S. Towner. Superallowed $0^+ \to 0^+$ nuclear β decays: 2014 critical survey, with precise results for V_{ud} and ckm unitarity. *Phys. Rev. C*, 91: 025501, Feb 2015. doi: 10.1103/PhysRevC.91.025501. URL https://link.aps.org/doi/10.1103/PhysRevC.91.025501.

[11] E. Rutherford. The scattering of alpha and beta particles by matter and the structure of the atom. *Phil. Mag. Ser.6*, 21:669–688, 1911. doi: 10.1080/14786440508637080.

[12] J. J. Thomson. Bakerian Lecture: Rays of positive electricity. *Proc. R. Soc. London A Math. Phys. Eng. Sci.*, 89(607):1–20, 1913. ISSN 0950-1207. doi: 10.1098/rspa.1913.0057. URL http://rspa.royalsocietypublishing.org/content/89/607/1.

[13] E. Rutherford. Bakerian Lecture: Nuclear constitution of atoms. *Proc. R. Soc. London A Math. Phys. Eng. Sci.*, 97(686):374–400, 1920. ISSN 0950-1207. doi: 10.1098/rspa.1920.0040. URL http://rspa.royalsocietypublishing.org/content/97/686/374.

[14] J. Chadwick. The existence of a neutron. *Proc. R. Soc. London A Math. Phys. Eng. Sci.*, 136(830):692–708, 1932. ISSN 0950-1207. doi: 10.1098/rspa.1932.0112. URL http://rspa.royalsocietypublishing.org/content/136/830/692.

[15] D Iwanenko. The neutron hypothesis. 129:798–798, 01 1932. doi: 10.1038/129798d0.

[16] Hideki Yukawa. On the Interaction of Elementary Particles I. *Proc. Phys. Math. Soc. Jap.*, 17:48–57, 1935. doi: 10.1143/PTPS.1.1. [Prog. Theor. Phys. Suppl.1,1(1935)].

[17] C. M. G. Lattes, H. Muirhead, G. P. S. Occhialini, and C. F. Powell. PROCESSES INVOLVING CHARGED MESONS. *Nature*, 159:694–697, 1947. doi: 10.1038/159694a0. [,42(1947)].

[18] Roderick V Reid. Local phenomenological nucleon-nucleon potentials. *Ann. Phys. (N. Y).*, 50(3):411–448, 1968. ISSN 0003-4916. doi: https://doi.org/10.1016/0003-4916(68)90126-7. URL http://www.sciencedirect.com/science/article/pii/0003491668901267.

[19] J. L. Gammel and R. M. Thaler. Spin-orbit coupling in the proton-proton interaction. *Phys. Rev.*, 107:291–298, Jul 1957. doi: 10.1103/PhysRev.107.291. URL https://link.aps.org/doi/10.1103/PhysRev.107.291.

[20] J. L. Gammel and R. M. Thaler. Spin-orbit coupling in the neutron-proton interaction. *Phys. Rev.*, 107:1337–1340, Sep 1957. doi: 10.1103/PhysRev.107.1337. URL https://link.aps.org/doi/10.1103/PhysRev.107.1337.

[21] J. M. B. Kellogg, I. I. Rabi, N. F. Ramsey, and J. R. Zacharias. An electrical quadrupole moment of the deuteron. *Phys. Rev.*, 55:318–319, Feb 1939.

doi: 10.1103/PhysRev.55.318. URL https://link.aps.org/doi/10.1103/PhysRev.55.318.

[22] N. Kemmer and S. Chapman. The charge-dependence of nuclear forces. *Proceedings of the Cambridge Philosophical Society*, 34:354, 1938. doi: 10.1017/S0305004100020296.

[23] Gerald A. Miller, Allena K. Opper, and Edward J. Stephenson. Charge symmetry breaking and qcd. *Annual Review of Nuclear and Particle Science*, 56 (1):253–292, 2006. doi: 10.1146/annurev.nucl.56.080805.140446. URL https://doi.org/10.1146/annurev.nucl.56.080805.140446.

[24] E. D. Bloom, D. H. Coward, H. DeStaebler, J. Drees, G. Miller, L. W. Mo, R. E. Taylor, M. Breidenbach, J. I. Friedman, G. C. Hartmann, and H. W. Kendall. High-energy inelastic $e - p$ scattering at 6 and 10 degrees. *Phys. Rev. Lett.*, 23: 930–934, Oct 1969. doi: 10.1103/PhysRevLett.23.930. URL https://link.aps.org/doi/10.1103/PhysRevLett.23.930.

[25] M. Breidenbach, J. I. Friedman, H. W. Kendall, E. D. Bloom, D. H. Coward, H. DeStaebler, J. Drees, L. W. Mo, and R. E. Taylor. Observed behavior of highly inelastic electron-proton scattering. *Phys. Rev. Lett.*, 23:935–939, Oct 1969. doi: 10.1103/PhysRevLett.23.935. URL https://link.aps.org/doi/10.1103/PhysRevLett.23.935.

[26] M Gell-Mann. A schematic model of baryons and mesons. *Phys. Lett.*, 8(3):214–215, 1964. ISSN 0031-9163. doi: https://doi.org/10.1016/S0031-9163(64)92001-3. URL http://www.sciencedirect.com/science/article/pii/S0031916364920013.

[27] G Zweig. An SU_3 model for strong interaction symmetry and its breaking; Version 1. Technical Report CERN-TH-401, CERN, Geneva, Jan 1964. URL http://cds.cern.ch/record/352337.

[28] P Söding. On the discovery of the gluon. *Eur. Phys. J. H*, 35(1):3–28, jul 2010. ISSN 2102-6467. doi: 10.1140/epjh/e2010-00002-5. URL https://doi.org/10.1140/epjh/e2010-00002-5.

[29] Matthew D. Schwartz. *Quantum Field Theory and the Standard Model*. Cambridge University Press, 2014. ISBN 1107034736, 9781107034730. URL http://www.cambridge.org/us/academic/subjects/physics/theoretical-physics-and-mathematical-physics/quantum-field-theory-and-standard-model.

[30] H. Hergert, J. M. Yao, T. D. Morris, N. M. Parzuchowski, S. K. Bogner, and J. Engel. Nuclear Structure from the In-Medium Similarity Renormalization Group. *J. Phys. Conf. Ser.*, 1041(1):012007, jun 2018. ISSN 1742-6588. doi: 10.1088/1742-6596/1041/1/012007. URL http://stacks.iop.org/1742-6596/1041/i=1/a=012007?key=crossref.a38568cf679a9bdb959aff4d5873fb26.

[31] Mark Zastrow. Inner workings: In search for magic nuclei, theory catches up to experiments. *Proceedings of the National Academy of Sciences*, 114(20): 5060–5062, 2017. ISSN 0027-8424. doi: 10.1073/pnas.1703620114. URL https://www.pnas.org/content/114/20/5060.

[32] M Thoennessen. Reaching the limits of nuclear stability. *Reports on Progress in Physics*, 67(7):1187–1232, jun 2004. doi: 10.1088/0034-4885/67/7/r04. URL https://doi.org/10.1088%2F0034-4885%2F67%2F7%2Fr04.

[33] C F v. Weizsäcker. Zur Theorie der Kernmassen. *Zeitschrift für Phys.*, 96(7): 431–458, jul 1935. ISSN 0044-3328. doi: 10.1007/BF01337700. URL https://doi.org/10.1007/BF01337700.

[34] W.J. Huang, G. Audi, Meng Wang, F. G. Kondev, S. Naimi, and Xing Xu. The AME2016 atomic mass evaluation (I). Evaluation of input data; and adjustment procedures. *Chinese Phys. C*, 41(3):030002, 2017. ISSN 1674-1137. doi: 10.1088/1674-1137/41/3/030002. URL http://stacks.iop.org/1674-1137/41/i=3/a=030002?key=crossref.c5ac715502743b64b763cf8c555c73d2.

[35] I. Angeli and K.P. Marinova. Table of experimental nuclear ground state charge radii: An update. *At. Data Nucl. Data Tables*, 99(1):69–95, jan 2013. ISSN 0092-640X. doi: 10.1016/J.ADT.2011.12.006. URL https://www.sciencedirect.com/science/article/pii/S0092640X12000265.

[36] I. Bentley, Y. Colón Rodríguez, S. Cunningham, and A. Aprahamian. Shell structure from nuclear observables. *Phys. Rev. C*, 93(4):1–16, 2016. ISSN 24699993. doi: 10.1103/PhysRevC.93.044337.

[37] I Angeli and K P Marinova. Correlations of nuclear charge radii with other nuclear observables. *J. Phys. G Nucl. Part. Phys.*, 42(5): 055108, may 2015. ISSN 0954-3899. doi: 10.1088/0954-3899/42/5/055108. URL http://stacks.iop.org/0954-3899/42/i=5/a=055108?key=crossref.46317eb796fdbf30b253f66b4ae95e7c.

[38] Z.Y. Bao, H. Beer, F. Käppeler, F. Voss, K. Wisshak, and T. Rauscher. Neutron Cross Sections For Nucleosynthesis Studies. *At. Data Nucl. Data Tables*, 76(1):70–154, sep 2000. ISSN 0092-640X. doi: 10.1006/ADND.2000.0838. URL https://www-sciencedirect-com.ezproxy.library.ubc.ca/science/article/pii/S0092640X00908386.

[39] M.G. Mayer and J.H.D. Jensen. *Elementary Theory of Nuclear Shell Structure*. Structure of matter series. John Wiley & Sons, 1955. URL https://books.google.ca/books?id=9g9RAAAAMAAJ.

[40] Sonia Bacca. Structure models: From shell model to ab initio methods. *Eur. Phys. J. Plus*, 131(4):107, apr 2016. ISSN 2190-5444. doi: 10.1140/epjp/i2016-16107-6. URL http://link.springer.com/10.1140/epjp/i2016-16107-6.

[41] E. Caurier, G. Martínez-Pinedo, F. Nowacki, A. Poves, and A. P. Zuker. The shell model as a unified view of nuclear structure. *Rev. Mod. Phys.*, 77(2): 427–488, jun 2005. ISSN 0034-6861. doi: 10.1103/RevModPhys.77.427. URL https://link.aps.org/doi/10.1103/RevModPhys.77.427.

[42] Kenneth S Krane. *Introductory nuclear physics*. Wiley, New York, NY, 1988. URL https://cds.cern.ch/record/359790.

[43] D. Suzuki, H. Iwasaki, D. Beaumel, L. Nalpas, E. Pollacco, M. Assié, H. Baba, Y. Blumenfeld, N. De Séréville, A. Drouart, S. Franchoo, A. Gillibert, J. Guillot, F. Hammache, N. Keeley, V. Lapoux, F. Maréchal, S. Michimasa, X. Mougeot, I. Mukha, H. Okamura, H. Otsu, A. Ramus, P. Roussel-Chomaz, H. Sakurai, J.-A. Scarpaci, O. Sorlin, I. Stefan, and M. Takechi. Breakdown of the $z = 8$ shell closure in unbound ^{12}**O** and its mirror symmetry. *Phys. Rev. Lett.*, 103: 152503, Oct 2009. doi: 10.1103/PhysRevLett.103.152503. URL https://link.aps.org/doi/10.1103/PhysRevLett.103.152503.

[44] T. Motobayashi, Y. Ikeda, K. Ieki, M. Inoue, N. Iwasa, T. Kikuchi, M. Kurokawa, S. Moriya, S. Ogawa, H. Murakami, S. Shimoura, Y. Yanagisawa, T. Nakamura, Y. Watanabe, M. Ishihara, T. Teranishi, H. Okuno, and R.F. Casten. Large deformation of the very neutron-rich nucleus 32Mg from intermediate-energy Coulomb excitation. *Phys. Lett. B*, 346(1-2):9–14, mar 1995. ISSN 0370-2693. doi: 10.1016/0370-2693(95)00012-A. URL https://www-sciencedirect-com.ezproxy.library.ubc.ca/science/article/pii/037026939500012A.

[45] B. Bastin, S. Grévy, D. Sohler, O. Sorlin, Zs. Dombrádi, N. L. Achouri, J. C. Angélique, F. Azaiez, D. Baiborodin, R. Borcea, C. Bourgeois, A. Buta, A. Bürger, R. Chapman, J. C. Dalouzy, Z. Dlouhy, A. Drouard, Z. Elekes, S. Franchoo, S. Iacob, B. Laurent, M. Lazar, X. Liang, E. Liénard, J. Mrazek, L. Nalpas, F. Negoita, N. A. Orr, Y. Penionzhkevich, Zs. Podolyák, F. Pougheon, P. Roussel-Chomaz, M. G. Saint-Laurent, M. Stanoiu, I. Stefan, F. Nowacki, and A. Poves. Collapse of the N = 28 Shell Closure in 42Si. *Phys. Rev. Lett.*, 99(2):022503, jul 2007. ISSN 0031-9007. doi: 10.1103/PhysRevLett.99.022503. URL https://link.aps.org/doi/10.1103/PhysRevLett.99.022503.

[46] I. Dillmann, K.-L. Kratz, A. Wöhr, O. Arndt, B. A. Brown, P. Hoff, M. Hjorth-Jensen, U. Köster, A. N. Ostrowski, B. Pfeiffer, D. Seweryniak, J. Shergur, W. B. Walters, and W. B. Walters. N = 82 Shell Quenching of the Classical r -Process "Waiting-Point" Nucleus C d 130. *Phys. Rev. Lett.*, 91(16):162503, oct 2003. ISSN 0031-9007. doi: 10.1103/PhysRevLett.91.162503. URL https://link.aps.org/doi/10.1103/PhysRevLett.91.162503.

[47] J. Fridmann, I. Wiedenhöver, A. Gade, L. T. Baby, D. Bazin, B. A. Brown, C. M. Campbell, J. M. Cook, P. D. Cottle, E. Diffenderfer, D.-C. Dinca, T. Glas-

macher, P. G. Hansen, K. W. Kemper, J. L. Lecouey, W. F. Mueller, H. Olliver, E. Rodriguez-Vieitez, J. R. Terry, J. A. Tostevin, and K. Yoneda. 'Magic' nucleus 42Si. *Nature*, 435(7044):922–924, jun 2005. ISSN 0028-0836. doi: 10.1038/nature03619. URL http://www.nature.com/articles/nature03619.

[48] A. Ozawa, T. Kobayashi, T. Suzuki, K. Yoshida, and I. Tanihata. New Magic Number, N = 16 , near the Neutron Drip Line. *Phys. Rev. Lett.*, 84(24):5493–5495, jun 2000. ISSN 0031-9007. doi: 10.1103/PhysRevLett.84.5493. URL https://link.aps.org/doi/10.1103/PhysRevLett.84.5493.

[49] F Wienholtz, D Beck, K Blaum, Ch Borgmann, M Breitenfeldt, R B Cakirli, S George, F Herfurth, J D Holt, M Kowalska, S Kreim, D Lunney, V Manea, J Menéndez, D Neidherr, M Rosenbusch, L Schweikhard, A Schwenk, J Simonis, J Stanja, R N Wolf, and K Zuber. Masses of exotic calcium isotopes pin down nuclear forces. *Nature*, 498(7454):346–9, 2013. ISSN 1476-4687. doi: 10.1038/nature12226. URL http://www.ncbi.nlm.nih.gov/pubmed/23783629.

[50] D. Steppenbeck, S. Takeuchi, N. Aoi, P. Doornenbal, M. Matsushita, H. Wang, H. Baba, N. Fukuda, S. Go, M. Honma, J. Lee, K. Matsui, S. Michimasa, T. Motobayashi, D. Nishimura, T. Otsuka, H. Sakurai, Y. Shiga, P.-A. Söderström, T. Sumikama, H. Suzuki, R. Taniuchi, Y. Utsuno, J.J. Valiente-Dobón, and K. Yoneda. Evidence for a new nuclear 'magic number' from the level structure of 54 Ca. *Nature*, 502(7470):207–210, 2013. ISSN 1476-4687. doi: 10.1038/nature12522.

[51] R. Kanungo. Shell closures in the N and Z=40–60 region for neutron and proton-rich nuclei. *Phys. Lett. B*, 649(1):31–34, may 2007. ISSN 0370-2693. doi: 10.1016/J.PHYSLETB.2007.03.044. URL https://www-sciencedirect-com.ezproxy.library.ubc.ca/science/article/pii/S0370269307003930?via{%}3Dihub.

[52] F Tondeur. Self-consistent study of nuclei far from stability with the energy density method. 1981. URL https://cds.cern.ch/record/878069.

[53] A. Huck, G. Klotz, A. Knipper, C. Miehé, C. Richard-Serre, G. Walter, A. Poves, H. L. Ravn, and G. Marguier. Beta decay of the new isotopes ^{52}K, ^{52}Ca, and ^{52}Sc; a test of the shell model far from stability. *Phys. Rev. C*, 31:2226–2237, Jun 1985. doi: 10.1103/PhysRevC.31.2226. URL https://link.aps.org/doi/10.1103/PhysRevC.31.2226.

[54] ENSDF. Evaluated nuclear structure data file, 2018. Data extracted using the National Nuclear Data Center On-Line Data Service from the ENSDF database, file revised as of 20 Aug 2018.

[55] M. Rosenbusch, P. Ascher, D. Atanasov, C. Barbieri, D. Beck, K. Blaum, Ch. Borgmann, M. Breitenfeldt, R. B. Cakirli, A. Cipollone, S. George, F. Herfurth, M. Kowalska, S. Kreim, D. Lunney, V. Manea, P. Navrátil, D. Neidherr, L. Schweikhard, V. Somà, J. Stanja, F. Wienholtz, R. N. Wolf, and

K. Zuber. Probing the $n = 32$ shell closure below the magic proton number $z = 20$: Mass measurements of the exotic isotopes ^{52,53}K. *Phys. Rev. Lett.*, 114:202501, May 2015. doi: 10.1103/PhysRevLett.114.202501. URL https://link.aps.org/doi/10.1103/PhysRevLett.114.202501.

[56] A. T. Gallant, J. C. Bale, T. Brunner, U. Chowdhury, S. Ettenauer, A. Lennarz, D. Robertson, V. V. Simon, A. Chaudhuri, J. D. Holt, A. A. Kwiatkowski, E. Mané, J. Menéndez, B. E. Schultz, M. C. Simon, C. Andreoiu, P. Delheij, M. R. Pearson, H. Savajols, A. Schwenk, and J. Dilling. New precision mass measurements of neutron-rich calcium and potassium isotopes and three-nucleon forces. *Phys. Rev. Lett.*, 109(3):1–5, 2012. ISSN 00319007. doi: 10.1103/PhysRevLett.109.032506.

[57] Xing Xu, Meng Wang, Yu-Hu Zhang, Hu-Shan Xu, Peng Shuai, Xiao-Lin Tu, Yuri A. Litvinov, Xiao-Hong Zhou, Bao-Hua Sun, You-Jin Yuan, Jia-Wen Xia, Jian-Cheng Yang, Klaus Blaum, Rui-Jiu Chen, Xiang-Cheng Chen, Chao-Yi Fu, Zhuang Ge, Zheng-Guo Hu, Wen-Jia Huang, Da-Wei Liu, Yi-Hua Lam, Xin-Wen Ma, Rui-Shi Mao, T. Uesaka, Guo-Qing Xiao, Yuan-Ming Xing, T. Yamaguchi, Y. Yamaguchi, Qi Zeng, Xin-Liang Yan, Hong-Wei Zhao, Tie-Cheng Zhao, Wei Zhang, and Wen-Long Zhan. Direct mass measurements of neutron-rich 86Kr projectile fragments and the persistence of neutron magic number N=32 in Sc isotopes. *Chinese Phys. C*, 39(10):104001, 2015. ISSN 1674-1137. doi: 10.1088/1674-1137/39/10/104001. URL http://stacks.iop.org/1674-1137/39/i=10/a=104001?key=crossref.88e23e3c76af9204d6ec563fa6ef9922.

[58] A. Lapierre, M. Brodeur, T. Brunner, S. Ettenauer, P. Finlay, A. T. Gallant, V. V. Simon, P. Delheij, D. Lunney, R. Ringle, H. Savajols, and J. Dilling. Penning-trap mass measurements of the neutron-rich k and ca isotopes: Resurgence of the $n = 28$ shell strength. *Phys. Rev. C*, 85:024317, Feb 2012. doi: 10.1103/PhysRevC.85.024317. URL https://link.aps.org/doi/10.1103/PhysRevC.85.024317.

[59] R. F. Garcia Ruiz, M. L. Bissell, K. Blaum, A. Ekström, N. Frömmgen, G. Hagen, M. Hammen, K. Hebeler, J. D. Holt, G. R. Jansen, M. Kowalska, K. Kreim, W. Nazarewicz, R. Neugart, G. Neyens, W. Nörtershäuser, T. Papenbrock, J. Papuga, A. Schwenk, J. Simonis, K. A. Wendt, and D. T. Yordanov. Unexpectedly large charge radii of neutron-rich calcium isotopes. *Nat. Phys.*, advance on(February):8–13, 2016. ISSN 1745-2473. doi: 10.1038/nphys3645. URL http://dx.doi.org/10.1038/nphys3645.

[60] Takaharu Otsuka, Toshio Suzuki, Rintaro Fujimoto, Hubert Grawe, and Yoshinori Akaishi. Evolution of nuclear shells due to the tensor force. *Phys. Rev. Lett.*, 95:232502, Nov 2005. doi: 10.1103/PhysRevLett.95.232502. URL https://link.aps.org/doi/10.1103/PhysRevLett.95.232502.

[61] Takaharu Otsuka, Toshio Suzuki, Jason D. Holt, Achim Schwenk, and Yoshinori Akaishi. Three-body forces and the limit of oxygen isotopes. *Phys. Rev. Lett.*, 105:032501, Jul 2010. doi: 10.1103/PhysRevLett.105.032501. URL https://link.aps.org/doi/10.1103/PhysRevLett.105.032501.

[62] Takaharu Otsuka. Exotic nuclei and nuclear forces. *Physica Scripta*, T152: 014007, jan 2013. doi: 10.1088/0031-8949/2013/t152/014007. URL https://doi.org/10.1088%2F0031-8949%2F2013%2Ft152%2F014007.

[63] O. Sorlin and M. G. Porquet. Evolution of the N = 28 shell closure: A test bench for nuclear forces. *Phys. Scr.*, (T152), 2013. ISSN 00318949. doi: 10.1088/0031-8949/2013/T152/014003.

[64] S. N. Liddick, P. F. Mantica, R. Broda, B. A. Brown, M. P. Carpenter, A. D. Davies, B. Fornal, T. Glasmacher, D. E. Groh, M. Honma, M. Horoi, R. V. F. Janssens, T. Mizusaki, D. J. Morrissey, A. C. Morton, W. F. Mueller, T. Otsuka, J. Pavan, H. Schatz, A. Stolz, S. L. Tabor, B. E. Tomlin, and M. Wiedeking. Development of shell closures at $n = 32, 34$. i. β decay of neutron-rich sc isotopes. *Phys. Rev. C*, 70:064303, Dec 2004. doi: 10.1103/PhysRevC.70.064303. URL https://link.aps.org/doi/10.1103/PhysRevC.70.064303.

[65] T. D. Morris, J. Simonis, S. R. Stroberg, C. Stumpf, G. Hagen, J. D. Holt, G. R. Jansen, T. Papenbrock, R. Roth, and A. Schwenk. Structure of the lightest tin isotopes. *Phys. Rev. Lett.*, 120:152503, Apr 2018. doi: 10.1103/PhysRevLett.120.152503. URL https://link.aps.org/doi/10.1103/PhysRevLett.120.152503.

[66] Sven Binder, Joachim Langhammer, Angelo Calci, and Robert Roth. Ab initio path to heavy nuclei. *Phys. Lett. B*, 736:119–123, 2014. ISSN 0370-2693. doi: http://dx.doi.org/10.1016/j.physletb.2014.07.010. URL http://www.sciencedirect.com/science/article/pii/S0370269314004961.

[67] D. Lascar, R. Klawitter, C. Babcock, E. Leistenschneider, S. R. Stroberg, B. R. Barquest, A. Finlay, M. Foster, A. T. Gallant, P. Hunt, J. Kelly, B. Kootte, Y. Lan, S. F. Paul, M. L. Phan, M. P. Reiter, B. Schultz, D. Short, J. Simonis, C. Andreoiu, M. Brodeur, I. Dillmann, G. Gwinner, J. D. Holt, A. A. Kwiatkowski, K. G. Leach, and J. Dilling. Precision mass measurements of $^{125--127}$Cd isotopes and isomers approaching the $n = 82$ closed shell. *Phys. Rev. C*, 96:044323, Oct 2017. doi: 10.1103/PhysRevC.96.044323. URL https://link.aps.org/doi/10.1103/PhysRevC.96.044323.

[68] G. Hagen, A. Ekström, C. Forssén, G. R. Jansen, W. Nazarewicz, T. Papenbrock, K. A. Wendt, S. Bacca, N. Barnea, B. Carlsson, C. Drischler, K. Hebeler, M. Hjorth-Jensen, M. Miorelli, G. Orlandini, A. Schwenk, and J. Simonis. Neutron and weak-charge distributions of the 48Ca nucleus. *Nat. Phys.*, advance on(November), 2015. ISSN 1745-2473. doi: 10.1038/nphys3529. URL http://dx.doi.org/10.1038/nphys3529.

[69] J Dilling, R Baartman, P Bricault, M Brodeur, L Blomeley, F Buchinger, J Crawford, J R Crespo López-Urrutia, P Delheij, M Froese, G P Gwinner, Z Ke, J K P Lee, R B Moore, V Ryjkov, G Sikler, M Smith, J Ullrich, and J Vaz. Mass measurements on highly charged radioactive ions, a new approach to high precision with TITAN. *Int. J. Mass Spectrom.*, 251(2):198–203, 2006. ISSN 1387-3806. doi: http://dx.doi.org/10.1016/j.ijms.2006.01.044. URL http://www.sciencedirect.com/science/article/pii/S1387380606000777.

[70] N. Ishii, S. Aoki, and T. Hatsuda. Nuclear force from lattice qcd. *Phys. Rev. Lett.*, 99:022001, Jul 2007. doi: 10.1103/PhysRevLett.99.022001. URL https://link.aps.org/doi/10.1103/PhysRevLett.99.022001.

[71] G. Hagen, T. Papenbrock, D. J. Dean, and M. Hjorth-Jensen. Ab initio coupled-cluster approach to nuclear structure with modern nucleon-nucleon interactions. *Phys. Rev. C*, 82:034330, Sep 2010. doi: 10.1103/PhysRevC.82.034330. URL https://link.aps.org/doi/10.1103/PhysRevC.82.034330.

[72] Bruce R. Barrett, Petr Navrátil, and James P. Vary. Ab initio no core shell model, 2013. ISSN 01466410.

[73] Steven C. Pieper and R. B. Wiringa. Quantum Monte Carlo Calculations of Light Nuclei. *Annu. Rev. Nucl. Part. Sci.*, 51(1):53–90, 2001. doi: 10.1146/annurev.nucl.51.101701.132506. URL https://doi.org/10.1146/annurev.nucl.51.101701.132506.

[74] M Viviani, L E Marcucci, S Rosati, A Kievsky, and L Girlanda. Variational Calculation on A = 3 and 4 Nuclei with Non-Local Potentials. *Few-Body Syst.*, 39(3):159–176, sep 2006. ISSN 1432-5411. doi: 10.1007/s00601-006-0158-y. URL https://doi.org/10.1007/s00601-006-0158-y.

[75] S. Binder, A. Ekström, G. Hagen, T. Papenbrock, and K. A. Wendt. Effective field theory in the harmonic oscillator basis. *Phys. Rev. C*, 93:044332, Apr 2016. doi: 10.1103/PhysRevC.93.044332. URL https://link.aps.org/doi/10.1103/PhysRevC.93.044332.

[76] G Puddu. A new single-particle basis for nuclear many-body calculations. *J. Phys. G Nucl. Part. Phys.*, 44(10):105104, oct 2017. ISSN 0954-3899. doi: 10.1088/1361-6471/aa8234. URL http://stacks.iop.org/0954-3899/44/i=10/a=105104?key=crossref.9deb64206bda89e319299df32e3ce2cb.

[77] Alexander Tichai, Julius Müller, Klaus Vobig, and Robert Roth. Natural orbitals for ab initio no-core shell model calculations. *Phys. Rev. C*, 99:034321, Mar 2019. doi: 10.1103/PhysRevC.99.034321. URL https://link.aps.org/doi/10.1103/PhysRevC.99.034321.

[78] L. C. Chamon, D. Pereira, M. S. Hussein, M. A. Cândido Ribeiro, and D. Galetti. Nonlocal description of the nucleus-nucleus interaction. *Phys.*

Rev. Lett., 79:5218–5221, Dec 1997. doi: 10.1103/PhysRevLett.79.5218. URL https://link.aps.org/doi/10.1103/PhysRevLett.79.5218.

[79] R. B. Wiringa, V. G. J. Stoks, and R. Schiavilla. Accurate nucleon-nucleon potential with charge-independence breaking. *Phys. Rev. C*, 51:38–51, Jan 1995. doi: 10.1103/PhysRevC.51.38. URL https://link.aps.org/doi/10.1103/PhysRevC.51.38.

[80] Hans-Werner Hammer, Andreas Nogga, and Achim Schwenk. Colloquium: Three-body forces: From cold atoms to nuclei. *Rev. Mod. Phys.*, 85:197–217, Jan 2013. doi: 10.1103/RevModPhys.85.197. URL https://link.aps.org/doi/10.1103/RevModPhys.85.197.

[81] M J Savage. Nuclear physics from lattice QCD. *Prog. Part. Nucl. Phys.*, 67(2):140–152, 2012. ISSN 0146-6410. doi: https://doi.org/10.1016/j.ppnp.2011.12.008. URL http://www.sciencedirect.com/science/article/pii/S0146641011001256.

[82] Ruprecht Machleidt. Chiral Symmetry and the Nucleon-Nucleon Interaction. *Symmetry (Basel).*, 8(4):26, apr 2016. ISSN 2073-8994. doi: 10.3390/sym8040026. URL http://www.mdpi.com/2073-8994/8/4/26.

[83] S.K. Bogner, R.J. Furnstahl, and A. Schwenk. From low-momentum interactions to nuclear structure. *Progress in Particle and Nuclear Physics*, 65 (1):94 – 147, 2010. ISSN 0146-6410. doi: https://doi.org/10.1016/j.ppnp.2010.03.001. URL http://www.sciencedirect.com/science/article/pii/S0146641010000347.

[84] E. D. Jurgenson, P. Navrátil, and R. J. Furnstahl. Evolution of nuclear many-body forces with the similarity renormalization group. *Phys. Rev. Lett.*, 103:082501, Aug 2009. doi: 10.1103/PhysRevLett.103.082501. URL https://link.aps.org/doi/10.1103/PhysRevLett.103.082501.

[85] K. Hebeler, J. D. Holt, J. Menéndez, and A. Schwenk. Nuclear forces and their impact on neutron-rich nuclei and neutron-rich matter. *Ann. Rev. Nucl. Part. Sci.*, 65:457, 2015.

[86] K. Hebeler, S. K. Bogner, R. J. Furnstahl, A. Nogga, and A. Schwenk. Improved nuclear matter calculations from chiral low-momentum interactions. *Phys. Rev. C*, 83:031301, Mar 2011. doi: 10.1103/PhysRevC.83.031301. URL https://link.aps.org/doi/10.1103/PhysRevC.83.031301.

[87] J. Simonis, K. Hebeler, J. D. Holt, J. Menéndez, and A. Schwenk. Exploring *sd*-shell nuclei from two- and three-nucleon interactions with realistic saturation properties. *Phys. Rev. C*, 93(1):011302(R), 2016.

[88] J. Simonis, S. R. Stroberg, K. Hebeler, J. D. Holt, and A. Schwenk. Saturation with chiral interactions and consequences for finite nuclei. *Phys. Rev. C*, 96:014303, 2017.

[89] D. R. Entem and R. Machleidt. Accurate charge-dependent nucleon-nucleon potential at fourth order of chiral perturbation theory. *Phys. Rev. C*, 68:041001, Oct 2003. doi: 10.1103/PhysRevC.68.041001. URL https://link.aps.org/doi/10.1103/PhysRevC.68.041001.

[90] A. Ekström, G. R. Jansen, K. A. Wendt, G. Hagen, T. Papenbrock, B. D. Carlsson, C. Forssén, M. Hjorth-Jensen, P. Navrátil, and W. Nazarewicz. Accurate nuclear radii and binding energies from a chiral interaction. *Phys. Rev. C*, 91:051301, May 2015. doi: 10.1103/PhysRevC.91.051301. URL https://link.aps.org/doi/10.1103/PhysRevC.91.051301.

[91] Robert Roth, Sven Binder, Klaus Vobig, Angelo Calci, Joachim Langhammer, and Petr Navrátil. Medium-mass nuclei with normal-ordered chiral nn+3n interactions. *Phys. Rev. Lett.*, 109:052501, Jul 2012. doi: 10.1103/PhysRevLett.109.052501. URL https://link.aps.org/doi/10.1103/PhysRevLett.109.052501.

[92] H. Hergert, S. Binder, A. Calci, J. Langhammer, and R. Roth. Ab Initio Calculations of Even Oxygen Isotopes with Chiral Two-Plus-Three-Nucleon Interactions. *Phys. Rev. Lett.*, 110(24):242501, jun 2013. ISSN 0031-9007. doi: 10.1103/PhysRevLett.110.242501. URL http://link.aps.org/doi/10.1103/PhysRevLett.110.242501.

[93] H. Hergert, S. K. Bogner, T. D. Morris, S. Binder, A. Calci, J. Langhammer, and R. Roth. Ab initio multireference in-medium similarity renormalization group calculations of even calcium and nickel isotopes. *Phys. Rev. C*, 90(4):041302, oct 2014. ISSN 0556-2813. doi: 10.1103/PhysRevC.90.041302. URL http://link.aps.org/doi/10.1103/PhysRevC.90.041302.

[94] H. Hergert, S. K. Bogner, T. D. Morris, A. Schwenk, and K. Tsukiyama. The In-Medium Similarity Renormalization Group: A Novel Ab Initio Method for Nuclei. *Phys. Rep.*, 621:165, 2016.

[95] K. Tsukiyama, S. K. Bogner, and A. Schwenk. In-medium similarity renormalization group for open-shell nuclei. *Phys. Rev. C*, 85:061304(R), 2012.

[96] S. K. Bogner, H. Hergert, J. D. Holt, A. Schwenk, S. Binder, A. Calci, J. Langhammer, and R. Roth. Nonperturbative shell-model interactions from the in-medium similarity renormalization group. *Phys. Rev. Lett.*, 113:142501, 2014.

[97] S. R. Stroberg, H. Hergert, J. D. Holt, S. K. Bogner, and A. Schwenk. Ground and excited states of doubly open-shell nuclei from ab initio valence-space Hamiltonians. *Phys. Rev. C*, 93(5):051301(R), 2016.

[98] S. R. Stroberg, A. Calci, H. Hergert, J. D. Holt, S. K. Bogner, R. Roth, and A. Schwenk. Nucleus-dependent valence-space approach to nuclear structure. *Phys. Rev. Lett.*, 118:032502, 2017.

[99] A. Cipollone, C. Barbieri, and P. Navrátil. Isotopic chains around oxygen from evolved chiral two- and three-nucleon interactions. *Phys. Rev. Lett.*, 111: 062501, Aug 2013. doi: 10.1103/PhysRevLett.111.062501. URL https://link.aps.org/doi/10.1103/PhysRevLett.111.062501.

[100] V. Somà, A. Cipollone, C. Barbieri, P. Navrátil, and T. Duguet. Chiral two- and three-nucleon forces along medium-mass isotope chains. *Phys. Rev. C*, 89: 061301, Jun 2014. doi: 10.1103/PhysRevC.89.061301. URL https://link.aps.org/doi/10.1103/PhysRevC.89.061301.

[101] V. Somà, T. Duguet, and C. Barbieri. Ab initio self-consistent gorkov-greens function calculations of semimagic nuclei: Formalism at second order with a two-nucleon interaction. *Phys. Rev. C*, 84:064317, Dec 2011. doi: 10.1103/PhysRevC.84.064317. URL https://link.aps.org/doi/10.1103/PhysRevC.84.064317.

[102] V. Somà, C. Barbieri, and T. Duguet. Ab initio self-consistent gorkov-greens function calculations of semi-magic nuclei: Numerical implementation at second order with a two-nucleon interaction. *Phys. Rev. C*, 89:024323, Feb 2014. doi: 10.1103/PhysRevC.89.024323. URL https://link.aps.org/doi/10.1103/PhysRevC.89.024323.

[103] Carlo Barbieri and Arianna Carbone. *Self-Consistent Green's Function Approaches*, pages 571–644. Springer International Publishing, Cham, 2017. ISBN 978-3-319-53336-0. doi: 10.1007/978-3-319-53336-0_11. URL https://doi.org/10.1007/978-3-319-53336-0{_}11.

[104] M. S. Dewey, E. G. Kessler Jr., R. D. Deslattes, H. G. Börner, M. Jentschel, C. Doll, and P. Mutti. Precision measurement of the ^{29}Si, ^{33}S, and ^{36}Cl binding energies. *Phys. Rev. C*, 73:044303, Apr 2006. doi: 10.1103/PhysRevC.73.044303. URL https://link.aps.org/doi/10.1103/PhysRevC.73.044303.

[105] John L. Hall. Nobel lecture: Defining and measuring optical frequencies. *Rev. Mod. Phys.*, 78:1279–1295, Nov 2006. doi: 10.1103/RevModPhys.78.1279. URL https://link.aps.org/doi/10.1103/RevModPhys.78.1279.

[106] Theodor W. Hänsch. Nobel lecture: Passion for precision. *Rev. Mod. Phys.*, 78:1297–1309, Nov 2006. doi: 10.1103/RevModPhys.78.1297. URL https://link.aps.org/doi/10.1103/RevModPhys.78.1297.

[107] Jens Dilling, Klaus Blaum, Maxime Brodeur, and Sergey Eliseev. Penning-Trap Mass Measurements in Atomic and Nuclear Physics. *Annu. Rev. Nucl. Part. Sci.*, 68(1):45–74, 2018. doi: 10.1146/annurev-nucl-102711-094939. URL https://doi.org/10.1146/annurev-nucl-102711-094939.

[108] G Audi, F G Kondev, Meng Wang, W J Huang, and S Naimi. The NUBASE2016 evaluation of nuclear properties *. *Chinese Phys. C*, 41(3):30001,

2017. doi: 10.1088/1674-1137/41/3/030001. URL http://amdc.impcas.ac.cn/.

[109] H.G. Dehmelt. Hans g. dehmelt - biographical, 1990. URL https://www.nobelprize.org/prizes/physics/1989/dehmelt/biographical/.

[110] M Brodeur, V L Ryjkov, T Brunner, S Ettenauer, A T Gallant, V V Simon, M J Smith, A Lapierre, R Ringle, P Delheij, M Good, D Lunney, and J Dilling. Verifying the accuracy of the TITAN Penning-trap mass spectrometer. *Int. J. Mass Spectrom.*, 310:20–31, 2012. ISSN 1387-3806. doi: http://dx.doi.org/10.1016/j.ijms.2011.11.002. URL http://www.sciencedirect.com/science/article/pii/S1387380611004568.

[111] Klaus Blaum. High-accuracy mass spectrometry with stored ions. *Phys. Rep.*, 425(1):1–78, 2006. ISSN 0370-1573. doi: https://doi.org/10.1016/j.physrep.2005.10.011. URL http://www.sciencedirect.com/science/article/pii/S0370157305004643.

[112] Martin Kretzschmar. Theoretical investigations of different excitation modes for Penning trap mass spectrometry. *Int. J. Mass Spectrom.*, 349-350(1):227–239, 2013. ISSN 13873806. doi: 10.1016/j.ijms.2013.03.023.

[113] A.A. Kwiatkowski, G Bollen, M Redshaw, R Ringle, and S Schwarz. Isobaric beam purification for high precision Penning trap mass spectrometry of radioactive isotope beams with SWIFT. *Int. J. Mass Spectrom.*, pages 1–7, 2014. ISSN 13873806. doi: 10.1016/j.ijms.2014.09.016. URL http://linkinghub.elsevier.com/retrieve/pii/S1387380614004011.

[114] Alan G. Marshall and Tong Chen. 40 years of Fourier transform ion cyclotron resonance mass spectrometry. *Int. J. Mass Spectrom.*, 2015. ISSN 13873806. doi: 10.1016/j.ijms.2014.06.034.

[115] S. Eliseev, K. Blaum, M. Block, C. Droese, M. Goncharov, E. Minaya Ramirez, D. A. Nesterenko, Yu. N. Novikov, and L. Schweikhard. Phase-Imaging Ion-Cyclotron-Resonance Measurements for Short-Lived Nuclides. *Phys. Rev. Lett.*, 110(8):082501, 2013. ISSN 0031-9007. doi: 10.1103/PhysRevLett.110.082501. URL http://link.aps.org/doi/10.1103/PhysRevLett.110.082501.

[116] M. König, G. Bollen, H.-J. Kluge, T. Otto, and J. Szerypo. Quadrupole excitation of stored ion motion at the true cyclotron frequency. *Int. J. Mass Spectrom. Ion Process.*, 142(1-2):95–116, 1995. ISSN 01681176. doi: 10.1016/0168-1176(95)04146-C.

[117] R. Ringle, G. Bollen, A. Prinke, J. Savory, P. Schury, S. Schwarz, and T. Sun. A "Lorentz" steerer for ion injection into a Penning trap. *Int. J. Mass Spectrom.*, 263(1):38–44, 2007. ISSN 13873806. doi: 10.1016/j.ijms.2006.12.008.

[118] S George, K Blaum, F Herfurth, A Herlert, M Kretzschmar, S Nagy, S Schwarz, L Schweikhard, and C Yazidjian. The Ramsey method in high-precision mass spectrometry with Penning traps: Experimental results. *Int. J. Mass Spectrom.*, 264(2-3):110–121, 2007. ISSN 1387-3806. doi: 10.1016/j.ijms.2007.04.003. URL http://www.sciencedirect.com/science/article/pii/S1387380607001662.

[119] Martin Kretzschmar. The Ramsey method in high-precision mass spectrometry with Penning traps: Theoretical foundations. *Int. J. Mass Spectrom.*, 264 (2-3):122–145, 2007. ISSN 13873806. doi: 10.1016/j.ijms.2007.04.002.

[120] M. Smith, M. Brodeur, T. Brunner, S. Ettenauer, A. Lapierre, R. Ringle, V. L. Ryjkov, F. Ames, P. Bricault, G. W F Drake, P. Delheij, D. Lunney, F. Sarazin, and J. Dilling. First penning-trap mass measurement of the exotic halo nucleus Li11. *Phys. Rev. Lett.*, 2008. ISSN 00319007. doi: 10.1103/PhysRevLett.101.202501.

[121] Joseph E. Campana. Time-of-flight mass spectrometry: a historical overview. *Instrumentation Science & Technology*, 16(1):1–14, 1987. doi: 10.1080/10739148708543625. URL https://doi.org/10.1080/10739148708543625.

[122] H. Wollnik and M. Przewloka. Time-of-flight mass spectrometers with multiply reflected ion trajectories. *International Journal of Mass Spectrometry and Ion Processes*, 96(3):267 – 274, 1990. ISSN 0168-1176. doi: https://doi.org/10.1016/0168-1176(90)85127-N. URL http://www.sciencedirect.com/science/article/pii/016811769085127N.

[123] Wolfgang R Plaß, Timo Dickel, and Christoph Scheidenberger. Multiple-reflection time-of-flight mass spectrometry. *Int. J. Mass Spectrom.*, 349: 134–144, 2013. ISSN 1387-3806. doi: http://dx.doi.org/10.1016/j.ijms.2013.06.005. URL http://www.sciencedirect.com/science/article/pii/S138738061300239X.

[124] T Dickel, W R Plaß, A Becker, U Czok, H Geissel, E Haettner, C Jesch, W Kinsel, M Petrick, C Scheidenberger, A Simon, and M I Yavor. A high-performance multiple-reflection time-of-flight mass spectrometer and isobar separator for the research with exotic nuclei. *Nucl. Instruments Methods Phys. Res. Sect. A Accel. Spectrometers, Detect. Assoc. Equip.*, 777:172–188, 2015. ISSN 0168-9002. doi: http://dx.doi.org/10.1016/j.nima.2014.12.094. URL http://www.sciencedirect.com/science/article/pii/S0168900214015629.

[125] William H. Aberth, Rafael Schnitzer, and Ferdinand C. Engesser. Construction of an einzel lens capable of high voltage operation. *Rev. Sci. Instrum.*, 1974. ISSN 00346748. doi: 10.1063/1.1686484.

[126] Poul Dahl. *Introduction to Electron and Ion Optics*. Academic Press, 1973. ISBN 978-0-12-200650-0. doi: 10.1016/B978-0-12-200650-0.X5001-6. URL https://doi.org/10.1016/B978-0-12-200650-0.X5001-6.

[127] M. Diederich, H. Häffner, N. Hermanspahn, M. Immel, H.J. Kluge, R. Ley, R. Mann, W. Quint, S. Stahl, and G. Werth. Observing a single hydrogen-like ion in a penning trap at t = 4 k. *Hyperfine Interactions*, 115(1):185–192, Nov 1998. ISSN 1572-9540. doi: 10.1023/A:1012665109427. URL https://doi.org/10.1023/A:1012665109427.

[128] A Casares, A Kholomeev, and H Wollnik. Multipass time-of-flight mass spectrometers with high resolving powers. *Int. J. Mass Spectrom.*, 206(3):267–273, 2001. ISSN 1387-3806. doi: https://doi.org/10.1016/S1387-3806(00)00391-2. URL http://www.sciencedirect.com/science/article/pii/S1387380600003912.

[129] Mikhail I Yavor, Wolfgang R Plaß, Timo Dickel, Hans Geissel, and Christoph Scheidenberger. Ion-optical design of a high-performance multiple-reflection time-of-flight mass spectrometer and isobar separator. *Int. J. Mass Spectrom.*, 381(Supplement C):1–9, 2015. ISSN 1387-3806. doi: https://doi.org/10.1016/j.ijms.2015.01.002. URL http://www.sciencedirect.com/science/article/pii/S1387380615000202.

[130] Andrew Finlay. Integration of a multi reflection time of flight isobar separator into the titan experiment at triumf. M.sc. thesis, The University of British Columbia, Vancouver, 2017.

[131] Timo Dickel, Mikhail I Yavor, Johannes Lang, Wolfgang R Plaß, Wayne Lippert, Hans Geissel, and Christoph Scheidenberger. Dynamical time focus shift in multiple-reflection time-of-flight mass spectrometers. *Int. J. Mass Spectrom.*, 412:1–7, 2017. ISSN 1387-3806. doi: http://dx.doi.org/10.1016/j.ijms.2016.11.005. URL http://www.sciencedirect.com/science/article/pii/S1387380616302664.

[132] Samuel Ayet San Andrés, Christine Hornung, Jens Ebert, Wolfgang R. Plaß, Timo Dickel, Hans Geissel, Christoph Scheidenberger, Julian Bergmann, Florian Greiner, Emma Haettner, Christian Jesch, Wayne Lippert, Israel Mardor, Ivan Miskun, Zygmunt Patyk, Stephane Pietri, Alexander Pihktelev, Sivaji Purushothaman, Moritz P. Reiter, Ann-Kathrin Rink, Helmut Weick, Mikhail I. Yavor, Soumya Bagchi, Volha Charviakova, Paul Constantin, Marcel Diwisch, Andrew Finlay, Satbir Kaur, Ronja Knöbel, Johannes Lang, Bo Mei, Iain D. Moore, Jan-Hendrik Otto, Ilkka Pohjalainen, Andrej Prochazka, Christophe Rappold, Maya Takechi, Yoshiki K. Tanaka, John S. Winfield, and Xiaodong Xu. High-resolution, accurate multiple-reflection time-of-flight mass spectrometry for short-lived, exotic nuclei of a few events in their ground and low-lying isomeric states. *Phys. Rev. C*, 99:064313, Jun 2019. doi: 10.1103/PhysRevC.99.064313. URL https://link.aps.org/doi/10.1103/PhysRevC.99.064313.

[133] Paul Fischer, Stefan Knauer, Gerrit Marx, and Lutz Schweikhard. Non-isobaric time-of-flight correction for isobar resolving in MR-ToF mass spec-

trometry. *Int. J. Mass Spectrom.*, 432:44–51, 2018. ISSN 1387-3806. doi: https://doi.org/10.1016/j.ijms.2018.07.004. URL http://www.sciencedirect.com/science/article/pii/S1387380618301507.

[134] Y Toker, N Altstein, O Aviv, M L Rappaport, O Heber, D Schwalm, D Strasser, and D Zajfman. The kick-out mass selection technique for ions stored in an electrostatic ion beam trap. *Journal of Instrumentation*, 4(09):P09001–P09001, sep 2009. doi: 10.1088/1748-0221/4/09/p09001. URL https://doi.org/10.1088%2F1748-0221%2F4%2F09%2Fp09001.

[135] Christian Will. Titan's multiple-reflection time-of-flight mass spectrometer and isobar separator - characterization and first experiments. B.sc. thesis, Justus Liebig University, Gießen, 2017.

[136] C Scheidenberger, F Attallah, A Casares, U Czok, A Dodonov, S A Eliseev, H Geissel, M Hausmann, A Kholomeev, V Kozlovski, Yu. A Litvinov, M Maier, G Münzenberg, N Nankov, Yu. N Novikov, T Radon, J Stadlmann, H Weick, M Weidenmüller, H Wollnik, and Z Zhou. A New Concept for Time-of-Flight Mass Spectrometry with Slowed-down Short-Lived Isotopes. In David Lunney, Georges Audi, and H.-Jürgen Kluge, editors, *At. Phys. Accel. Mass Spectrom.*, pages 531–534, Dordrecht, 2001. Springer Netherlands. ISBN 978-94-015-1270-1.

[137] P. Chauveau, P. Delahaye, G. De France, S. El Abir, J. Lory, Y. Merrer, M. Rosenbusch, L. Schweikhard, and R.N. Wolf. Pilgrim, a multi-reflection time-of-flight mass spectrometer for spiral2-s3 at ganil. *Nuclear Instruments and Methods in Physics Research Section B: Beam Interactions with Materials and Atoms*, 376:211 – 215, 2016. ISSN 0168-583X. doi: https://doi.org/10.1016/j.nimb.2016.01.025. URL http://www.sciencedirect.com/science/article/pii/S0168583X16000732. Proceedings of the XVIIth International Conference on Electromagnetic Isotope Separators and Related Topics (EMIS2015), Grand Rapids, MI, U.S.A., 11-15 May 2015.

[138] M.P. Reiter, F. Ames, C. Andreoiu, S. Ayet San Andrés, C. Babcock, B.R. Barquest, J. Bergmann, J. Bollig, T. Brunner, T. Dickel, J. Dilling, I. Dillmann, E. Dunling, A. Finlay, G. Gwinner, L. Graham, C. Hornung, B. Kootte, R. Klawitter, P. Kunz, Y. Lan, D. Lascar, J. Lassen, E. Leistenschneider, R. Li, J.E. McKay, M. Mostamand, S.F. Paul, W.R. Plaß, C. Scheidenberger, B.E. Schultz, R. Steinbrügge, A. Teigelhoefer, R. Thompson, M.E. Wieser, C. Will, and A.A. Kwiatkowski. Improved beam diagnostics and optimization at isac via titan's mr-tof-ms. *Nuclear Instruments and Methods in Physics Research Section B: Beam Interactions with Materials and Atoms*, 2019. ISSN 0168-583X. doi: https://doi.org/10.1016/j.nimb.2019.04.034. URL http://www.sciencedirect.com/science/article/pii/S0168583X19302186.

[139] G C Ball, G Hackman, and R Krücken. The TRIUMF-ISAC facility: two decades of discovery with rare isotope beams. *Phys. Scr.*, 91(9):93002, 2016. URL http://stacks.iop.org/1402-4896/91/i=9/a=093002.

[140] Y Blumenfeld, T Nilsson, and P Van Duppen. Facilities and methods for radioactive ion beam production. *Phys. Scr.*, 2013(T152):14023, 2013. URL http://stacks.iop.org/1402-4896/2013/i=T152/a=014023.

[141] M. Brodeur. *First direct mass measurement of the two and four neutron halos 6He and 8He using the TITAN Penning trap mass spectrometer*. PhD thesis, The University of British Columbia, Vancouver, 2010.

[142] TRIUMF. Isac yield database, 2018. URL http://isys01.triumf.ca/search/yield/data.

[143] Pierre G. Bricault. Thick target for high-power isol facilities. *Nuclear Instruments and Methods in Physics Research Section B: Beam Interactions with Materials and Atoms*, 376:3 – 7, 2016. ISSN 0168-583X. doi: https://doi.org/10.1016/j.nimb.2016.03.024. URL http://www.sciencedirect.com/science/article/pii/S0168583X16002275. Proceedings of the XVIIth International Conference on Electromagnetic Isotope Separators and Related Topics (EMIS2015), Grand Rapids, MI, U.S.A., 11-15 May 2015.

[144] A. Gottberg. Target materials for exotic ISOL beams. *Nucl. Instruments Methods Phys. Res. Sect. B Beam Interact. with Mater. Atoms*, 376:8–15, 2016. ISSN 0168583X. doi: 10.1016/j.nimb.2016.01.020. URL http://dx.doi.org/10.1016/j.nimb.2016.01.020.

[145] U. Köster, P. Carbonez, A. Dorsival, J. Dvorak, R. Eichler, S. Fernandes, H. Frånberg, J. Neuhausen, Z. Novackova, R. Wilfinger, and A. Yakushev. (im-)possible isol beams. *The European Physical Journal Special Topics*, 150(1):285–291, Nov 2007. ISSN 1951-6401. doi: 10.1140/epjst/e2007-00326-1. URL https://doi.org/10.1140/epjst/e2007-00326-1.

[146] Sebastian Raeder, Henning Heggen, Jens Lassen, Friedhelm Ames, Daryl Bishop, Pierre Bricault, Peter Kunz, Anders Mjøs, and Andrea Teigelhöfer. An ion guide laser ion source for isobar-suppressed rare isotope beams. *Rev. Sci. Instrum.*, 85(3):33309, 2014. doi: 10.1063/1.4868496. URL https://doi.org/10.1063/1.4868496.

[147] M. Turek, A. Droździel, K. Pyszniak, D. Maczka, and B. Słowiński. Simulations of ionization in a hot cavity surface ion source. *Review of Scientific Instruments*, 83(2):023303, 2012. doi: 10.1063/1.3685247. URL https://doi.org/10.1063/1.3685247.

[148] B A Marsh. Resonance ionization laser ion sources for on-line isotope separators. *Rev. Sci. Instrum.*, 85(2):02B923, 2014. doi: 10.1063/1.4858015. URL https://doi.org/10.1063/1.4858015.

[149] J Lassen, P Bricault, M Dombsky, J P Lavoie, M Gillner, T Gottwald, F Hellbusch, A Teigelhöfer, A Voss, and K D A Wendt. Laser Ion Source Operation at the TRIUMF Radioactive Ion Beam Facility. *AIP Conf. Proc.*, 1104(1):9–15, 2009. doi: 10.1063/1.3115616. URL http://aip.scitation.org/doi/abs/10.1063/1.3115616.

[150] Takahide Takamatsu, Hideki Tomita, Yujin Furuta, Takaaki Takatsuka, Yoshitaka Adachi, Takuma Noto, Volker Sonnenschein, Tobias Kron, Klaus Wendt, Tetsuo Iguchi, Tetsu Sonoda, and Michiharu Wada. *Development of High Resolution Resonance Ionization Spectroscopy on Titanium Using Injection-Locked Ti:Sapphire Laser System*. 2015. doi: 10.7566/JPSCP.6.030142. URL http://journals.jps.jp/doi/abs/10.7566/JPSCP.6.030142.

[151] Pierre Bricault, Richard Baartman, Marik Dombsky, Andrew Hurst, Clive Mark, Guy Stanford, and Paul Schmor. TRIUMF-ISAC target station and mass separator commissioning. *Nucl. Phys. A*, 701(1):49–53, 2002. ISSN 03759474. doi: 10.1016/S0375-9474(01)01546-9.

[152] A A Kwiatkowski, T D Macdonald, C Andreoiu, J C Bale, T Brunner, A Chaudhuri, U Chowdhury, S Ettenauer, A T Gallant, A Grossheim, A Lennarz, E Mané, M R Pearson, B E Schultz, M C Simon, V V Simon, and J Dilling. Precision mass measurements at TITAN with radioactive ions. *Nucl. Instruments Methods Phys. Res. Sect. B Beam Interact. with Mater. Atoms*, 317:517–521, 2013. ISSN 0168-583X. doi: https://doi.org/10.1016/j.nimb.2013.05.087. URL http://www.sciencedirect.com/science/article/pii/S0168583X13007064.

[153] V. L. Ryjkov, M. Brodeur, T. Brunner, M. Smith, R. Ringle, A. Lapierre, F. Ames, P. Bricault, M. Dombsky, P. Delheij, D. Lunney, M. R. Pearson, and J. Dilling. Direct mass measurement of the four-neutron halo nuclide ^{8}He. *Phys. Rev. Lett.*, 101:012501, Jul 2008. doi: 10.1103/PhysRevLett.101.012501. URL https://link.aps.org/doi/10.1103/PhysRevLett.101.012501.

[154] T Brunner, M J Smith, M Brodeur, S Ettenauer, A T Gallant, V V Simon, A Chaudhuri, A Lapierre, E Mané, R Ringle, M C Simon, J A Vaz, P Delheij, M Good, M R Pearson, and J Dilling. TITAN's digital RFQ ion beam cooler and buncher, operation and performance. *Nucl. Instruments Methods Phys. Res. Sect. A Accel. Spectrometers, Detect. Assoc. Equip.*, 676:32–43, 2012. ISSN 0168-9002. doi: http://dx.doi.org/10.1016/j.nima.2012.02.004. URL http://www.sciencedirect.com/science/article/pii/S0168900212001398.

[155] A. Lapierre, M. Brodeur, T. Brunner, S. Ettenauer, A. T. Gallant, V. Simon, M. Good, M. W. Froese, J. R. Crespo Lpez-Urrutia, P. Delheij, S. Epp, R. Ringle, S. Schwarz, J. Ullrich, and J. Dilling. The TITAN EBIT charge breeder for mass measurements on highly charged short-lived isotopes - First online operation. *Nucl. Instruments Methods Phys. Res. Sect. A Accel. Spectrometers, Detect. Assoc. Equip.*, 624(1):54–64, 2010. ISSN 01689002. doi: 10.1016/j.nima.2010.09.030.

[156] S. Ettenauer, M. C. Simon, A. T. Gallant, T. Brunner, U. Chowdhury, V. V. Simon, M. Brodeur, A. Chaudhuri, E. Mané, C. Andreoiu, G. Audi, J. R Crespo López-Urrutia, P. Delheij, G. Gwinner, A. Lapierre, D. Lunney, M. R. Pearson, R. Ringle, J. Ullrich, and J. Dilling. First Use of high charge states for mass measurements of short-lived nuclides in a penning trap. *Phys. Rev. Lett.*, 107 (27):1–5, 2011. ISSN 00319007. doi: 10.1103/PhysRevLett.107.272501.

[157] V V Simon, P Delheij, J Dilling, Z Ke, W Shi, and G Gwinner. Cooling of short-lived, radioactive, highly charged ions with the TITAN cooler Penning trap. *Hyperfine Interact.*, 199(1):151–159, jul 2011. ISSN 1572-9540. doi: 10.1007/s10751-011-0309-5. URL https://doi.org/10.1007/s10751-011-0309-5.

[158] M. Brodeur, T. Brunner, C. Champagne, S. Ettenauer, M. Smith, A. Lapierre, R. Ringle, V. L. Ryjkov, G. Audi, P. Delheij, D. Lunney, and J. Dilling. New mass measurement of ^{6}Li and ppb-level systematic studies of the penning trap mass spectrometer titan. *Phys. Rev. C*, 80:044318, Oct 2009. doi: 10.1103/PhysRevC.80.044318. URL https://link.aps.org/doi/10.1103/PhysRevC.80.044318.

[159] Joseph Ladislas Wiza. Microchannel plate detectors. *Nuclear Instruments and Methods*, 162(1–3):587 – 601, 1979. ISSN 0029-554X. doi: http://dx.doi.org/10.1016/0029-554X(79)90734-1. URL http://www.sciencedirect.com/science/article/pii/0029554X79907341.

[160] Christian Jesch, Timo Dickel, Wolfgang R Plaß, Devin Short, Samuel Ayet San Andres, Jens Dilling, Hans Geissel, Florian Greiner, Johannes Lang, Kyle G Leach, Wayne Lippert, Christoph Scheidenberger, and Mikhail I Yavor. The MR-TOF-MS isobar separator for the TITAN facility at TRIUMF. *Hyperfine Interact.*, 235(1):97–106, nov 2015. ISSN 1572-9540. doi: 10.1007/s10751-015-1184-2. URL https://doi.org/10.1007/s10751-015-1184-2.

[161] Wolfgang R Plaß, Timo Dickel, Ulrich Czok, Hans Geissel, Martin Petrick, Katrin Reinheimer, Christoph Scheidenberger, and Mikhail I.Yavor. Isobar separation by time-of-flight mass spectrometry for low-energy radioactive ion beam facilities. *Nucl. Instruments Methods Phys. Res. Sect. B Beam Interact. with Mater. Atoms*, 266(19):4560–4564, 2008. ISSN 0168-583X. doi: http://dx.doi.org/10.1016/j.nimb.2008.05.079. URL http://www.sciencedirect.com/science/article/pii/S0168583X08007763.

[162] Devin Short. Nuclear isobar separation for penning trap mass measurements at triumf. M.sc. thesis, Simon Fraser University, Burnaby, 2018.

[163] Wolfgang R Plaß, Timo Dickel, Samuel Ayet San Andres, Jens Ebert, Florian Greiner, Christine Hornung, Christian Jesch, Johannes Lang, Wayne Lippert, Tamas Majoros, Devin Short, Hans Geissel, Emma Haettner, Moritz P Reiter, Ann-Kathrin Rink, Christoph Scheidenberger, and Mikhail I Yavor. High-performance multiple-reflection time-of-flight mass spectrometers for

research with exotic nuclei and for analytical mass spectrometry. *Physica Scripta*, T166:014069, nov 2015. doi: 10.1088/0031-8949/2015/t166/014069. URL https://doi.org/10.1088%2F0031-8949%2F2015%2Ft166%2F014069.

[164] E. Leistenschneider, M. P. Reiter, S. Ayet San Andrés, B. Kootte, J. D. Holt, P. Navrátil, C. Babcock, C. Barbieri, B. R. Barquest, J. Bergmann, J. Bollig, T. Brunner, E. Dunling, A. Finlay, H. Geissel, L. Graham, F. Greiner, H. Hergert, C. Hornung, C. Jesch, R. Klawitter, Y. Lan, D. Lascar, K. G. Leach, W. Lippert, J. E. McKay, S. F. Paul, A. Schwenk, D. Short, J. Simonis, V. Somà, R. Steinbrügge, S. R. Stroberg, R. Thompson, M. E. Wieser, C. Will, M. Yavor, C. Andreoiu, T. Dickel, I. Dillmann, G. Gwinner, W. R. Plaß, C. Scheidenberger, A. A. Kwiatkowski, and J. Dilling. Dawning of the $n = 32$ shell closure seen through precision mass measurements of neutron-rich titanium isotopes. *Phys. Rev. Lett.*, 120:062503, Feb 2018. doi: 10.1103/PhysRevLett.120.062503. URL https://link.aps.org/doi/10.1103/PhysRevLett.120.062503.

[165] P. Schury, M. Wada, Y. Ito, F. Arai, S. Naimi, T. Sonoda, H. Wollnik, V.A. Shchepunov, C. Smorra, and C. Yuan. A high-resolution multi-reflection time-of-flight mass spectrograph for precision mass measurements at riken/slowri. *Nuclear Instruments and Methods in Physics Research Section B: Beam Interactions with Materials and Atoms*, 335:39 – 53, 2014. ISSN 0168-583X. doi: https://doi.org/10.1016/j.nimb.2014.05.016. URL http://www.sciencedirect.com/science/article/pii/S0168583X1400559X.

[166] Christine Hornung. *High-Resolution Experiments with the Multiple-Reflection Time-Of-Flight Mass Spectrometer at the Fragment Separator FRS*. PhD thesis, Justus-Liebig-Universität, Otto-Behaghel-Str. 8, 35394 Gießen, 2018. URL http://geb.uni-giessen.de/geb/volltexte/2018/13908.

[167] John Wolberg. *Data Analysis Using the Method of Least Squares*. Springer-Verlag, 2006. doi: 10.1007/3-540-31720-1. URL https://doi.org/10.1007/3-540-31720-1.

[168] G C Rodrigues, P Indelicato, J P Santos, P Patté, and F Parente. Systematic calculation of total atomic energies of ground state configurations. *At. Data Nucl. Data Tables*, 86(2):117–233, 2004. ISSN 0092-640X. doi: https://doi.org/10.1016/j.adt.2003.11.005. URL http://www.sciencedirect.com/science/article/pii/S0092640X03000846.

[169] G. Bollen, H.-J. Kluge, M. König, T. Otto, G. Savard, H. Stolzenberg, R. B. Moore, G. Rouleau, G. Audi, and ISOLDE Collaboration. Resolution of nuclear ground and isomeric states by a penning trap mass spectrometer. *Phys. Rev. C*, 46:R2140–R2143, Dec 1992. doi: 10.1103/PhysRevC.46.R2140. URL https://link.aps.org/doi/10.1103/PhysRevC.46.R2140.

[170] G Bollen, R B Moore, G Savard, and H Stolzenberg. The accuracy of heavy-ion mass measurements using time of flight-ion cyclotron resonance in a Penning

trap. *J. Appl. Phys.*, 68(9):4355–4374, 1990. doi: 10.1063/1.346185. URL https://doi.org/10.1063/1.346185.

[171] A. T. Gallant, M. Brodeur, T. Brunner, U. Chowdhury, S. Ettenauer, V. V. Simon, E. Mané, M. C. Simon, C. Andreoiu, P. Delheij, G. Gwinner, M. R. Pearson, R. Ringle, and J. Dilling. Highly charged ions in Penning traps: A new tool for resolving low-lying isomeric states. *Phys. Rev. C*, 85(4):044311, 2012. ISSN 0556-2813. doi: 10.1103/PhysRevC.85.044311. URL http://link.aps.org/doi/10.1103/PhysRevC.85.044311.

[172] C. Babcock, R. Klawitter, E. Leistenschneider, D. Lascar, B. R. Barquest, A. Finlay, M. Foster, A. T. Gallant, P. Hunt, B. Kootte, Y. Lan, S. F. Paul, M. L. Phan, M. P. Reiter, B. Schultz, D. Short, C. Andreoiu, M. Brodeur, I. Dillmann, G. Gwinner, A. A. Kwiatkowski, K. G. Leach, and J. Dilling. Mass measurements of neutron-rich indium isotopes toward the $n = 82$ shell closure. *Phys. Rev. C*, 97:024312, Feb 2018. doi: 10.1103/PhysRevC.97.024312. URL https://link.aps.org/doi/10.1103/PhysRevC.97.024312.

[173] M. E. Bunker and J. W. Starner. Decay of ti^{51} and cr^{51}. *Phys. Rev.*, 97:1272–1275, Mar 1955. doi: 10.1103/PhysRev.97.1272. URL https://link.aps.org/doi/10.1103/PhysRev.97.1272.

[174] T. Mayer-Kuckuk and H. Daniel. Der zerfall von ti^{51}. *Z.Naturforsch.*, 10a:168, 1955.

[175] P. D. Barnes, J. R. Comfort, C. K. Bockelman, Ole Hansen, and A. Sperduto. Inelastic deuteron scattering and (d, p) reactions from isotopes of titanium. iv. $ti^{48}(d, p)ti^{49}$. *Phys. Rev.*, 159:920–926, Jul 1967. doi: 10.1103/PhysRev.159.920. URL https://link.aps.org/doi/10.1103/PhysRev.159.920.

[176] P. L. Jolivette, J. D. Goss, J. A. Bieszk, R. D. Hichwa, and C. P. Browne. Charged particle q-value measurements in the iron region. *Phys. Rev. C*, 13:439–439, Jan 1976. doi: 10.1103/PhysRevC.13.439. URL https://link.aps.org/doi/10.1103/PhysRevC.13.439.

[177] S E Arnell, R Hardell, A Hasselgren, C-G Mattsson, and Ö Skeppstedt. Thermal neutron capture in50ti and64ni. *Physica Scripta*, 4(3):89–94, sep 1971. doi: 10.1088/0031-8949/4/3/001. URL https://doi.org/10.1088%2F0031-8949%2F4%2F3%2F001.

[178] H. Morinaga, K. Miyano, K. Fujikawa, R. Chiba, K. Ebisawa, and N. Kawai. A new activity 52ti. *Physics Letters B*, 25(1):22 – 23, 1967. ISSN 0370-2693. doi: https://doi.org/10.1016/0370-2693(67)90063-9. URL http://www.sciencedirect.com/science/article/pii/0370269367900639.

[179] D.C. Williams, J.D. Knight, and W.T. Leland. The (t, p) and (t,) reactions on 48ca and 50ti. *Physics Letters*, 22(2):162 – 164, 1966. ISSN 0031-9163. doi: https:

//doi.org/10.1016/0031-9163(66)90559-2. URL http://www.sciencedirect.com/science/article/pii/0031916366905592.

[180] R. F. Casten, E. R. Flynn, Ole Hansen, and T. J. Mulligan. Strong $l = 0(t, p)$ transitions in the even isotopes of ti, cr, and fe. *Phys. Rev. C*, 4:130–137, Jul 1971. doi: 10.1103/PhysRevC.4.130. URL https://link.aps.org/doi/10.1103/PhysRevC.4.130.

[181] L. A. Parks, C. N. Davids, and R. C. Pardo. β decay and mass of the new neutron-rich isotope ^{53}Ti. *Phys. Rev. C*, 15:730–739, Feb 1977. doi: 10.1103/PhysRevC.15.730. URL https://link.aps.org/doi/10.1103/PhysRevC.15.730.

[182] T. Dörfler, W.-D. Schmidt-Ott, T. Hild, T. Mehren, W. Böhmer, P. Möller, B. Pfeiffer, T. Rauscher, K.-L. Kratz, O. Sorlin, V. Borrel, S. Grévy, D. Guillemaud-Mueller, A. C. Mueller, F. Pougheon, R. Anne, M. Lewitowicz, A. Ostrowsky, M. Robinson, and M. G. Saint-Laurent. Neutron-rich isotopes $^{54-57}$Ti. *Phys. Rev. C*, 54:2894–2903, Dec 1996. doi: 10.1103/PhysRevC.54.2894. URL https://link.aps.org/doi/10.1103/PhysRevC.54.2894.

[183] X. L. Tu, X. G. Zhou, D. J. Vieira, J. M. Wouters, Z. Y. Zhou, H. L. Seifert, and V. G. Lind. Direct mass measurements of the neutron-rich isotopes of chlorine through iron. *Zeitschrift für Physik A Atomic Nuclei*, 337(4):361–366, Dec 1990. ISSN 0939-7922. doi: 10.1007/BF01294971. URL https://doi.org/10.1007/BF01294971.

[184] H L Seifert, J M Wouters, D J Vieira, H Wollnik, X. G. Zhou, X L Tu, Z Yo Zhou, and G W Butler. Mass measurement of neutron-rich isotopes from 51Ca to 72Ni. *Zeitschrift fur Phys. A Hadron. Nucl.*, 349(1):25–32, mar 1994. ISSN 0939-7922. doi: 10.1007/BF01296329. URL http://link.springer.com/10.1007/BF01296329.

[185] Y. Bai, D. J. Vieira, H. L. Seifert, and J. M. Wouters. Mass measurement in the fp-shell using the tofi spectrometer. *AIP Conference Proceedings*, 455(1):90–93, 1998. doi: 10.1063/1.57312. URL https://aip.scitation.org/doi/abs/10.1063/1.57312.

[186] R. M. E. B. Kandegedara, G. Bollen, M. Eibach, N. D. Gamage, K. Gulyuz, C. Izzo, M. Redshaw, R. Ringle, R. Sandler, and A. A. Valverde. β-decay q values among the $a = 50$ ti-v-cr isobaric triplet and atomic masses of ^{46,47,49,50}Ti,^{50,51} V, and $^{50,52--54}$Cr. *Phys. Rev. C*, 96:044321, Oct 2017. doi: 10.1103/PhysRevC.96.044321. URL https://link.aps.org/doi/10.1103/PhysRevC.96.044321.

[187] A.W. Schardt and B. Dropesky. In *Bulletin of the American Physical Society*, volume 1, page 162, 1956.

[188] S. Hinds, H. Marchant, and R. Middleton. The 51v(t, p) 53v reaction. *Physics Letters B*, 24(1):34 – 37, 1967. ISSN 0370-2693. doi: https://doi.org/10.1016/0370-2693(67)90331-0. URL http://www.sciencedirect.com/science/article/pii/0370269367903310.

[189] C.P. Browne et al. In *Annual Report - University of Notre Dame*, volume 1, 1979.

[190] T.E. Ward, P.H. Pile, and P.K. Kuroda. Decay of 54v. *Nuclear Physics A*, 148(1):225 – 235, 1970. ISSN 0375-9474. doi: https://doi.org/10.1016/0375-9474(70)90620-2. URL http://www.sciencedirect.com/science/article/pii/0375947470906202.

[191] E. R. Flynn, J. W. Sunier, and F. Ajzenberg-Selove. States of ^{54}V and ^{58}Mn. *Phys. Rev. C*, 15:879–882, Mar 1977. doi: 10.1103/PhysRevC.15.879. URL https://link.aps.org/doi/10.1103/PhysRevC.15.879.

[192] A. M. Nathan, D. E. Alburger, J. W. Olness, and E. K. Warburton. Beta decay of $^{54-55}$V and the mass of ^{55}V. *Phys. Rev. C*, 16:1566–1575, Oct 1977. doi: 10.1103/PhysRevC.16.1566. URL https://link.aps.org/doi/10.1103/PhysRevC.16.1566.

[193] M. P. Reiter, S. Ayet San Andrés, E. Dunling, B. Kootte, E. Leistenschneider, C. Andreoiu, C. Babcock, B. R. Barquest, J. Bollig, T. Brunner, I. Dillmann, A. Finlay, G. Gwinner, L. Graham, J. D. Holt, C. Hornung, C. Jesch, R. Klawitter, Y. Lan, D. Lascar, J. E. McKay, S. F. Paul, R. Steinbrügge, R. Thompson, J. L. Tracy, M. E. Wieser, C. Will, T. Dickel, W. R. Plaß, C. Scheidenberger, A. A. Kwiatkowski, and J. Dilling. Quenching of the $n = 32$ neutron shell closure studied via precision mass measurements of neutron-rich vanadium isotopes. *Phys. Rev. C*, 98:024310, Aug 2018. doi: 10.1103/PhysRevC.98.024310. URL https://link.aps.org/doi/10.1103/PhysRevC.98.024310.

[194] R. B. Cakirli, R. F. Casten, and K. Blaum. Correlations of experimental isotope shifts with spectroscopic and mass observables. *Phys. Rev. C*, 82:061306, Dec 2010. doi: 10.1103/PhysRevC.82.061306. URL https://link.aps.org/doi/10.1103/PhysRevC.82.061306.

[195] M. Mougeot, D. Atanasov, K. Blaum, K. Chrysalidis, T. Day Goodacre, D. Fedorov, V. Fedosseev, S. George, F. Herfurth, J. D. Holt, D. Lunney, V. Manea, B. Marsh, D. Neidherr, M. Rosenbusch, S. Rothe, L. Schweikhard, A. Schwenk, C. Seiffert, J. Simonis, S. R. Stroberg, A. Welker, F. Wienholtz, R. N. Wolf, and K. Zuber. Precision mass measurements of $^{58--63}$Cr: Nuclear collectivity towards the $n = 40$ island of inversion. *Phys. Rev. Lett.*, 120:232501, Jun 2018. doi: 10.1103/PhysRevLett.120.232501. URL https://link.aps.org/doi/10.1103/PhysRevLett.120.232501.

[196] Evgeny Epelbaum, Hans-Werner Hammer, and Ulf-G. Meißner. Modern Theory of Nuclear Forces. *Rev. Mod. Phys.*, 81:1773, 2009.

[197] R. Machleidt and D. R. Entem. Chiral effective field theory and nuclear forces. *Phys. Rep.*, 503:1, 2011.

[198] X. Xu, M. Wang, K. Blaum, J. D. Holt, Yu. A. Litvinov, A. Schwenk, J. Simonis, S. R. Stroberg, Y. H. Zhang, H. S. Xu, P. Shuai, X. L. Tu, X. H. Zhou, F. R. Xu, G. Audi, R. J. Chen, X. C. Chen, C. Y. Fu, Z. Ge, W. J. Huang, S. Litvinov, D. W. Liu, Y. H. Lam, X. W. Ma, R. S. Mao, A. Ozawa, B. H. Sun, Y. Sun, T. Uesaka, G. Q. Xiao, Y. M. Xing, T. Yamaguchi, Y. Yamaguchi, X. L. Yan, Q. Zeng, H. W. Zhao, T. C. Zhao, W. Zhang, and W. L. Zhan. Masses of neutron-rich $^{52–54}$Sc and ^{54,56}Ti nuclides: The $n = 32$ subshell closure in scandium. *Phys. Rev. C*, 99:064303, Jun 2019. doi: 10.1103/PhysRevC.99.064303. URL https://link.aps.org/doi/10.1103/PhysRevC.99.064303.

[199] T. Duguet, V. Somà, S. Lecluse, C. Barbieri, and P. Navrátil. Ab initio. *Phys. Rev. C*, 95:034319, Mar 2017. doi: 10.1103/PhysRevC.95.034319. URL https://link.aps.org/doi/10.1103/PhysRevC.95.034319.

[200] D. Steppenbeck, S. Takeuchi, N. Aoi, P. Doornenbal, M. Matsushita, H. Wang, Y. Utsuno, H. Baba, S. Go, J. Lee, K. Matsui, S. Michimasa, T. Motobayashi, D. Nishimura, T. Otsuka, H. Sakurai, Y. Shiga, N. Shimizu, P. A. Söderström, T. Sumikama, R. Taniuchi, J. J. Valiente-Dobón, and K. Yoneda. Low-Lying Structure of Ar 50 and the N=32 Subshell Closure. *Phys. Rev. Lett.*, 114(25): 1–6, 2015. ISSN 10797114. doi: 10.1103/PhysRevLett.114.252501.

[201] H. N. Liu, A. Obertelli, P. Doornenbal, C. A. Bertulani, G. Hagen, J. D. Holt, G. R. Jansen, T. D. Morris, A. Schwenk, R. Stroberg, N. Achouri, H. Baba, F. Browne, D. Calvet, F. Château, S. Chen, N. Chiga, A. Corsi, M. L. Cortés, A. Delbart, J.-M. Gheller, A. Giganon, A. Gillibert, C. Hilaire, T. Isobe, T. Kobayashi, Y. Kubota, V. Lapoux, T. Motobayashi, I. Murray, H. Otsu, V. Panin, N. Paul, W. Rodriguez, H. Sakurai, M. Sasano, D. Steppenbeck, L. Stuhl, Y. L. Sun, Y. Togano, T. Uesaka, K. Wimmer, K. Yoneda, O. Aktas, T. Aumann, L. X. Chung, F. Flavigny, S. Franchoo, I. Gašparić, R.-B. Gerst, J. Gibelin, K. I. Hahn, D. Kim, T. Koiwai, Y. Kondo, P. Koseoglou, J. Lee, C. Lehr, B. D. Linh, T. Lokotko, M. MacCormick, K. Moschner, T. Nakamura, S. Y. Park, D. Rossi, E. Sahin, D. Sohler, P.-A. Söderström, S. Takeuchi, H. Törnqvist, V. Vaquero, V. Wagner, S. Wang, V. Werner, X. Xu, H. Yamada, D. Yan, Z. Yang, M. Yasuda, and L. Zanetti. How robust is the $n = 34$ subshell closure? first spectroscopy of ^{52}Ar. *Phys. Rev. Lett.*, 122:072502, Feb 2019. doi: 10.1103/PhysRevLett.122.072502. URL https://link.aps.org/doi/10.1103/PhysRevLett.122.072502.

[202] J Dilling, R Krücken, and L Merminga. *ARIEL overview*, pages 253–262. Springer Netherlands, Dordrecht, 2014. ISBN 978-94-007-7963-1. doi: 10.1007/978-94-007-7963-1_30. URL https://doi.org/10.1007/978-94-007-7963-1{_}30.

[203] K. Leach, M. Foster, I. Dillmann, C. Babcock, M. Good, A.A. Kwiatkowski, A. Lennarz, J. Dilling, E. Leistenschneider, R. Klawitter, C. Andreoiu, T. Brunner, and D. Frekers. Decay Spectroscopy of Highly Charged Radioactive Ions with TITAN at TRIUMF. In *Proceedings of the 26th International Nuclear Physics Conference (INPC2016)*. PROCEEDINGS of SCIENCE, 2017. doi: 10.22323/1.281.0097. URL https://pos.sissa.it/281/097/.

[204] A Herlert, D Beck, K Blaum, F Carrel, P Delahaye, S George, C Guénaut, F Herfurth, A Kellerbauer, H-J Kluge, D Lunney, M Mukherjee, L Schweikhard, and C Yazidjian. Mass spectrometry of atomic ions produced by in-trap decay of short-lived nuclides. *New J. Phys.*, 7(1):44, 2005. URL http://stacks.iop.org/1367-2630/7/i=1/a=044.

[205] A. Herlert, S. van Gorp, D. Beck, K. Blaum, M. Breitenfeldt, R. B. Cakirli, S. George, U. Hager, F. Herfurth, A. Kellerbauer, D. Lunney, R. Savreux, L. Schweikhard, and C. Yazidjian. Recoil-ion trapping for precision mass measurements. *Eur. Phys. J. A*, 48(7):97, 2012. ISSN 1434601X. doi: 10.1140/epja/i2012-12097-2.

[206] J de Walle, V Bildstein, N Bree, J Cederkäll, P Delahaye, J Diriken, A Ekström, V N Fedosseev, R Gernhäuser, A Gustafsson, A Herlert, M Huyse, O Ivanov, T Kröll, R Krücken, B Marsh, N Partronis, P Van Duppen, D Voulot, N Warr, F Wenander, K Wimmer, and S M Lenzi. In-trap decay of 61Mn and Coulomb excitation of 61Mn/61Fe. *Eur. Phys. J. A*, 42 (3):401, jun 2009. ISSN 1434-601X. doi: 10.1140/epja/i2009-10814-6. URL https://doi.org/10.1140/epja/i2009-10814-6.

[207] L P Gaffney, J de Walle, B Bastin, V Bildstein, A Blazhev, N Bree, J Cederkäll, I Darby, H De Witte, D DiJulio, J Diriken, V N Fedosseev, Ch. Fransen, R Gernhäuser, A Gustafsson, H Hess, M Huyse, N Kesteloot, Th. Kröll, R Lutter, B A Marsh, P Reiter, M Seidlitz, P Van Duppen, D Voulot, N Warr, F Wenander, K Wimmer, and K Wrzosek-Lipska. Low-energy Coulomb excitation of 62Fe and 62Mn following in-beam decay of 62Mn. *Eur. Phys. J. A*, 51 (10):136, oct 2015. ISSN 1434-601X. doi: 10.1140/epja/i2015-15136-6. URL https://doi.org/10.1140/epja/i2015-15136-6.

[208] F. Currell and G. Fussmann. Physics of electron beam ion traps and sources. *IEEE Trans. Plasma Sci.*, 33(6):1763– 1777, 2005. ISSN 0093-3813. doi: 10.1109/TPS.2005.860072. URL http://ieeexplore.ieee.org.ezproxy.library.wisc.edu/ielx5/27/33110/01556668.pdf?tp={&}arnumber=1556668{&}isnumber=33110.

[209] G. Zschornacka, M. Schmidt, and A. Thorn. Electron Beam Ion Sources. (arXiv:1410.8014):165–201. 37 p, Oct 2014. URL http://cds.cern.ch/record/1965922. Comments: 37 pages, contribution to the CAS-CERN Accelerator School: Ion Sources, Senec, Slovakia, 29 May - 8 June 2012, edited by R. Bailey.

[210] F Wenander. Charge breeding of radioactive ions with EBIS and EBIT. *J. Instrum.*, 5(10):C10004, 2010. URL http://stacks.iop.org/1748-0221/5/i=10/a=C10004.

[211] D Frekers, M C Simon, C Andreoiu, J C Bale, M Brodeur, T Brunner, A Chaudhuri, U Chowdhury, J R Crespo López-Urrutia, P Delheij, H Ejiri, S Ettenauer, A T Gallant, V Gavrin, A Grossheim, M N Harakeh, F Jang, A A Kwiatkowski, J Lassen, A Lennarz, M Luichtl, T Ma, T D Macdonald, E Mané, D Robertson, B E Schultz, V V Simon, A Teigelhöfer, and J Dilling. Penning-trap Q-value determination of the Ga71(ν,e)Ge71 reaction using threshold charge breeding of on-line produced isotopes. *Phys. Lett. B*, 722(4):233–237, 2013. ISSN 0370-2693. doi: https://doi.org/10.1016/j.physletb.2013.04.019. URL http://www.sciencedirect.com/science/article/pii/S0370269313002980.

[212] B. Olaizola, H. Mach, L. M. Fraile, J. Benito, M. J.G. Borge, R. Boutami, P. A. Butler, Z. Dlouhy, H. O.U. Fynbo, P. Hoff, S. Hyldegaard, H. B. Jeppesen, A. Jokinen, C. Jollet, A. Korgul, U. Köster, Th Kröll, W. Kurcewicz, F. Marechal, J. Mrazek, T. Nilsson, W. A. Płóciennik, E. Ruchowska, R. Schuber, W. Schwerdtfeger, M. Sewtz, G. S. Simpson, M. Stanoiu, O. Tengblad, P. G. Thirolf, and D. T. Yordanov. High-sensitivity study of levels in Al 30 following β decay of Mg 30. *Phys. Rev. C*, 94(5):054318, 2016. ISSN 24699993. doi: 10.1103/PhysRevC.94.054318. URL https://link.aps.org/doi/10.1103/PhysRevC.94.054318.

[213] D. E. Alburger and D. R. Goosman. Decay schemes of ^{30}Al, ^{30}P, and ^{20}O. *Phys. Rev. C*, 9:2236–2242, Jun 1974. doi: 10.1103/PhysRevC.9.2236. URL https://link.aps.org/doi/10.1103/PhysRevC.9.2236.

[214] V Yu. Kozlov, M Beck, F Ames, D Beck, S Coeck, P Delahaye, B Delauré, V V Golovko, A Lindroth, I S Kraev, T Phalet, N Severijns, and S Versyck. Physics and present status of the WITCH experiment. *Phys. At. Nucl.*, 67(6): 1112–1118, jun 2004. ISSN 1562-692X. doi: 10.1134/1.1772445. URL https://doi.org/10.1134/1.1772445.

[215] Sam Coeck. *Search for non Standard Model Physics in nuclear Beta-decay with the WITCH experiment*. PhD thesis, Leuven U., 2007. URL http://inspirehep.net/record/1231332/files/phd_sam.pdf.

[216] Peter Kunz, Corina Andreoiu, Pierre Bricault, Marik Dombsky, Jens Lassen, Andrea Teigelhöfer, Henning Heggen, and Fiona Wong. Nuclear and in-source laser spectroscopy with the ISAC yield station. *Rev. Sci. Instrum.*, 85 (5):53305, 2014. doi: 10.1063/1.4878718. URL https://doi.org/10.1063/1.4878718.

[217] A Lennarz, A Grossheim, K. G. Leach, M Alanssari, T Brunner, A Chaudhuri, U Chowdhury, J. R. Crespo López-Urrutia, A. T. Gallant, M Holl, A. A. Kwiatkowski, J Lassen, T. D. Macdonald, B. E. Schultz, S Seeraji, M. C. Simon,

C Andreoiu, J Dilling, and D Frekers. In-Trap Spectroscopy of Charge-Bred Radioactive Ions. *Phys. Rev. Lett.*, 113(8):082502, 2014. ISSN 0031-9007. doi: 10.1103/PhysRevLett.113.082502. URL http://link.aps.org/doi/10.1103/PhysRevLett.113.082502.

[218] K. G. Leach, A. Grossheim, A. Lennarz, T. Brunner, J. R. Crespo L??pez-Urrutia, A. T. Gallant, M. Good, R. Klawitter, A. A. Kwiatkowski, T. Ma, T. D. Macdonald, S. Seeraji, M. C. Simon, C. Andreoiu, J. Dilling, and D. Frekers. The TITAN in-trap decay spectroscopy facility at TRIUMF. *Nucl. Instruments Methods Phys. Res. Sect. A Accel. Spectrometers, Detect. Assoc. Equip.*, 780:91–99, 2015. ISSN 01689002. doi: 10.1016/j.nima.2014.12.118.

[219] T Brunner, A R Mueller, K O'Sullivan, M C Simon, M Kossick, S Ettenauer, A T Gallant, E Mané, D Bishop, M Good, G Gratta, and J Dilling. A large Bradbury Nielsen ion gate with flexible wire spacing based on photo-etched stainless steel grids and its characterization applying symmetric and asymmetric potentials. *Int. J. Mass Spectrom.*, 309:97–103, 2012. ISSN 1387-3806. doi: https://doi.org/10.1016/j.ijms.2011.09.004. URL http://www.sciencedirect.com/science/article/pii/S1387380611003770.

[220] A. Mutschler et al. A proton density bubble in the doubly magic ^{34}Si nucleus. *Nature Phys.*, 13:152–156, 2017. doi: 10.1038/nphys3916,10.1038/NPHYS3916.

[221] Jennifer A. Shusterman, Nicholas D. Scielzo, Keenan J. Thomas, Eric B. Norman, Suzanne E. Lapi, C. Shaun Loveless, Nickie J. Peters, J. David Robertson, Dawn A. Shaughnessy, and Anton P. Tonchev. The surprisingly large neutron capture cross-section of 88zr. *Nature*, 565(7739):328–330, 2019. ISSN 1476-4687. doi: 10.1038/s41586-018-0838-z. URL https://doi.org/10.1038/s41586-018-0838-z.

[222] A. A. Kwiatkowski, C. Andreoiu, J. C. Bale, A. Chaudhuri, U. Chowdhury, S. Malbrunot-Ettenauer, A. T. Gallant, A. Grossheim, G. Gwinner, A. Lennarz, T. D. Macdonald, T. J. M. Rauch, B. E. Schultz, S. Seeraji, M. C. Simon, V. V. Simon, D. Lunney, A. Poves, and J. Dilling. Observation of a crossover of S_{2n} in the island of inversion from precision mass spectrometry. *Phys. Rev. C*, 92:061301, Dec 2015. doi: 10.1103/PhysRevC.92.061301. URL https://link.aps.org/doi/10.1103/PhysRevC.92.061301.

[223] R. Lica, F. Rotaru, M. J. G. Borge, S. Grévy, F. Negoiţă, A. Poves, O. Sorlin, A. N. Andreyev, R. Borcea, C. Costache, H. De Witte, L. M. Fraile, P. T. Greenlees, M. Huyse, A. Ionescu, S. Kisyov, J. Konki, I. Lazarus, M. Madurga, N. Mărginean, R. Mărginean, C. Mihai, R. E. Mihai, A. Negret, R. D. Page, J. Pakarinen, S. Pascu, V. Pucknell, P. Rahkila, E. Rapisarda, A. Şerban, C. O. Sotty, L. Stan, M. Stănoiu, O. Tengblad, A. Turturică, P. Van Duppen, R. Wadsworth, and N. Warr. Identification of the crossing point at $n = 21$ between normal and intruder configurations. *Phys. Rev. C*, 95:021301, Feb

2017. doi: 10.1103/PhysRevC.95.021301. URL https://link.aps.org/doi/10.1103/PhysRevC.95.021301.

[224] F. Rotaru, F. Negoita, S. Grévy, J. Mrazek, S. Lukyanov, F. Nowacki, A. Poves, O. Sorlin, C. Borcea, R. Borcea, A. Buta, L. Cáceres, S. Calinescu, R. Chevrier, Zs. Dombrádi, J. M. Daugas, D. Lebhertz, Y. Penionzhkevich, C. Petrone, D. Sohler, M. Stanoiu, and J. C. Thomas. Unveiling the intruder deformed 0_2^+ state in ^{34}Si. *Phys. Rev. Lett.*, 109:092503, Aug 2012. doi: 10.1103/PhysRevLett.109.092503. URL https://link.aps.org/doi/10.1103/PhysRevLett.109.092503.

[225] S. Malbrunot-Ettenauer, T. Brunner, U. Chowdhury, A. T. Gallant, V. V. Simon, M. Brodeur, A. Chaudhuri, E. Mané, M. C. Simon, C. Andreoiu, G. Audi, J. R. Crespo López-Urrutia, P. Delheij, G. Gwinner, A. Lapierre, D. Lunney, M. R. Pearson, R. Ringle, J. Ullrich, and J. Dilling. Penning trap mass measurements utilizing highly charged ions as a path to benchmark isospin-symmetry breaking corrections in ^{74}Rb. *Phys. Rev. C*, 91:045504, Apr 2015. doi: 10.1103/PhysRevC.91.045504. URL https://link.aps.org/doi/10.1103/PhysRevC.91.045504.

[226] Erich Leistenschneider, A A Kwiatkowski, and J Dilling. Vacuum requirements for Penning trap mass spectrometry with highly charged ions. *Nucl. Instruments Methods Phys. Res. Sect. B Beam Interact. with Mater. Atoms*, 2019. ISSN 0168-583X. doi: https://doi.org/10.1016/j.nimb.2019.03.047. URL http://www.sciencedirect.com/science/article/pii/S0168583X19301673.

[227] S. George, K. Blaum, M. Block, M. Breitenfeldt, M. Dworschak, F. Herfurth, A. Herlert, M. Kowalska, M. Kretzschmar, E. Minaya Ramirez, D. Neidherr, S. Schwarz, and L. Schweikhard. Damping effects in Penning trap mass spectrometry. *Int. J. Mass Spectrom.*, 299(2-3):102–112, 2011. ISSN 13873806. doi: 10.1016/j.ijms.2010.09.030. URL http://www.sciencedirect.com/science/article/pii/S1387380610003635.

[228] Martin Knudsen. The kinetic theory of gases; some modern aspects., 1950.

[229] R Feres and G Yablonsky. Knudsen's cosine law and random billiards. *Chem. Eng. Sci.*, 59(7):1541–1556, 2004. ISSN 00092509. doi: 10.1016/j.ces.2004.01.016. URL http://www.sciencedirect.com/science/article/B6TFK-4C04V14-1/2/fa0dfb4810da4e3ba01190a25800a275.

[230] Alfred Muller and Erhard Salzborn. Scaling of cross sections for multiple electron transfer to highly charged ions colliding with atoms and molecules. *Physics Letters A*, 62(6):391 – 394, 1977. ISSN 0375-9601. doi: https://doi.org/10.1016/0375-9601(77)90672-7. URL http://www.sciencedirect.com/science/article/pii/0375960177906727.

[231] Peter J Linstrom and William G Mallard. The NIST Chemistry WebBook: A Chemical Data Resource on the Internet. *J. Chem. Eng. Data*, 46(5):1059–1063, 2001. doi: 10.1021/je000236i. URL https://doi.org/10.1021/je000236i.

[232] C Carlberg, T Fritioff, G Douysset, and R Schuch. SMILETRAP - A Penning trap facility for precision mass measurements using highly charged ions. *Nucl. Instruments Methods Phys. Res.*, 487:618–651, 2002. ISSN 01689002. doi: 10.1016/S0168-9002(01)02178-7.

[233] Stanford Research Systems Inc. *Models RGA100, RGA200, and RGA300 Residual Gas Analyzer - Operating Manual and Programming Reference*. Stanford Research Systems Inc., Sunnyvale, California, 2009. URL http://www.thinkSRS.com.

[234] S. Ettenauer. *First Mass Measurements of Highly Charged, Short-lived Nuclides in a Penning Trap and the Mass of 74Rb*. PhD thesis, The University of British Columbia, Vancouver, 2012.

[235] C Day. Basics and Applications of Cryopumps. *Cern Accel. Sch. Proc. 'Vacuum Accel.*, pages 241–274, 2006. doi: 10.5170/CERN-2007-003.241.

[236] Ronald G. Ross Jr. Chapter 6: Refrigeration systems for achieving cryogenic temperatures. In Yoseph Bar-Cohen, editor, *Low Temperature Materials and Mechanisms*, chapter 6, pages 109–181. CRC Press, Boca Raton, 2016. URL https://doi.org/10.1201/9781315371962.

[237] Christian Day. The use of active carbons as cryosorbent. *Colloids Surfaces A Physicochem. Eng. Asp.*, 187-188:187–206, 2001. ISSN 09277757. doi: 10.1016/S0927-7757(01)00630-6.

[238] Chr. Day, A. Antipenkov, M. Dremel, H. Haas, V. Hauer, A. Mack, D.K. Murdoch, and M. Wykes. R&D and design for the cryogenic and mechanical vacuum pumping systems of ITER. *Vacuum*, 81(6):738–747, 2007. ISSN 0042207X. doi: 10.1016/j.vacuum.2005.11.050. URL http://www.sciencedirect.com/science/article/pii/S0042207X05003945.

[239] P Duthil. Material Properties at Low Temperature. (arXiv:1501.07100. arXiv:1501.07100):77–95. 18 p, Jan 2015. doi: 10.5170/CERN-2014-005.77. URL http://cds.cern.ch/record/1973682. Comments: 18 pages, contribution to the CAS-CERN Accelerator School: Superconductivity for Accelerators, Erice, Italy, 24 April - 4 May 2013, edited by R. Bailey.

[240] Kouji Mimura, Yukio Ishikawa, Minoru Isshiki, and Masanori Kato. Precise Purity-Evaluation of High-Purity Copper by Residual Resistivity Ratio. *Mater. Trans. JIM*, 38(8):714–718, 1997. doi: 10.2320/matertrans1989.38.714.

[241] David Meeker. *Finite Element Method Magnetics - Version 4.2 User's Manual*. FEMM, 2015. URL http://www.femm.info.

[242] Geoff Nunes and Dinsie Williams. Thermal contraction of ultrahigh vacuum materials for scanning probe microscopy from 300 to 4 k. *Journal of Vacuum Science Technology B: Microelectronics and Nanometer Structures*, 13:1063 – 1065, 06 1995. doi: 10.1116/1.587905.

[243] Lowell S. Brown and Gerald Gabrielse. Geonium theory: Physics of a single electron or ion in a Penning trap. *Rev. Mod. Phys.*, 58(1):233–311, jan 1986. ISSN 0034-6861. doi: 10.1103/RevModPhys.58.233. URL http://link.aps.org/doi/10.1103/RevModPhys.58.233.

[244] M Harlander, M Brownnutt, W Hänsel, and R Blatt. Trapped-ion probing of light-induced charging effects on dielectrics. *New J. Phys.*, 12(9):93035, sep 2010. doi: 10.1088/1367-2630/12/9/093035. URL https://doi.org/10.1088{%}2F1367-2630{%}2F12{%}2F9{%}2F093035.

[245] D. Yosifov and M. Good. Triumf uhv cleaning and assembling procedures. TRIUMF Design Notes, 2012.

APPENDICES

In the following appendices, I describe a few of my contributions to further leverage the experimental capabilities of the TITAN facility, and that may allow future extensions of the work presented at the core of this thesis. In appendix A, I describe a novel technique to enable experimental investigation of some radioactive species that the ISAC facility cannot provide directly. In appendix B, I give an overview of the cryogenic upgrade of the MPET mass spectrometer.

A DECAY AND RECAPTURE ION TRAPPING

Access to exotic radioactive nuclei enables a broad range of scientific investigations from fundamental to applied sciences. The improvement of their production techniques, focusing on quality, intensity, purity, efficiency, and selectivity, has been a highly active area of research [140]. The ISOL method of production of radionuclides, employed at ISAC, is known for producing high-quality and high-intensity RIBs. However, as explained in section 4.1, chemical and physical processes that influence the extraction of species of interest from the production target (such as ionization potential and volatility) limit the availability of certain beams [140, 144]. Consequently, ion beams of refractory metals and reactive elements, such as iron and boron, are challenging to produce.

One way to circumvent these limitations is the Decay and Recapture Ion Trapping (DRIT) technique. It allows the production of particular beams that the RIB facility is unable to provide directly but can provide a parent species. It consists of storing a cloud of the parent ion in an ion trap for a time comparable to its half-life or longer. Then, a cloud of the ion of interest can be created if the trapping potential is deep enough to recapture the recoiling particles. It permits the creation of beams of not only refractory and reactive elements, in the case of ISOL facilities, but also of isomeric beams if a suitable parent is available.

The technique was first employed at CERN-ISOLDE for the creation of ^{37}Ar [204] and $^{61-63}$Fe [205] ions for mass spectrometry experiments. In both cases, parent ions were stored in a buffer-gas-filled Penning trap, which reportedly re-trapped about 50% of recoils. Two other experiments [206, 207] performed in the same facility employed Electron Beam Ion Traps (EBIT) [208, 209] as storage device. Evidence from these experiments suggests that EBITs have high re-trapping efficiencies and are ideal storing devices for this technique.

Here, we further explore the use of such ion traps and report the in-EBIT production of ^{30}Al from a parent beam of ^{30}Mg, performed for the first time at TITAN. We characterized the evolution of the trapped contents and adjusted operating parameters to optimize the creation of daughter beam. The ^{30}Al ions were extracted and delivered to MPET, where its mass was successfully measured.

In the following section, we discuss the technique in detail and the advantages and challenges regarding using an EBIT as the storage device. In section A.2, we present a simple model to describe the evolution of stored radioactive contents in EBIT, applied to the proof-of-principle experiment herein. In section A.3, we describe our apparatus and of the experimental procedures employed. In section A.4,

we present the results of the systematic investigations on the creation of the daughter beam using EBIT. In section A.5, we demonstrate the production of daughter beam through unambiguous identification using the mass spectrometer and describe the subsequent mass measurements performed. We conclude with possible applications of the technique.

A.1 In-EBIT DRIT

Conceptually, the DRIT technique is simple. If a suitable parent species is available, it is stored for the timescale of its half-life and its daughter is recaptured. The key question to the success of this method lies in the confinement capabilities of the trap: first, can the cloud be stored for such a period? Second, how many of the decay daughters will be retained in the trapping volume? These questions are central to selecting the most suitable trapping setup and, more indirectly, potential candidate species.

Ion traps, such as Penning or Paul traps, typically create potential wells of a few eV to a few hundreds of eV deep. The three-body β-decay, for example, generates a recoil energy spectrum that can span a few hundreds of eV. Therefore, β-decay products can be recaptured in typical ion traps. In contrast, α-decays may produce recoils up to a few hundreds of keV, which makes their recapture challenging. Here, we focus on the recapture of weak decay products only.

EBITs have storing capabilities that typically outperform other ion traps [208, 209]. They have an electrode structure that provides axial ion confinement overlapped with a strong magnetic field that provides radial confinement. EBITs also have a dense electron beam passing through the trapping region (see figure A.1), which ionizes ions through electron impact. For this reason, they are widely used to provide charge-bred beams for experiments or post-acceleration [210]. The electron beam also deepens confinement: as the ion's charge state increases, it experiences a deeper trapping potential in all directions. Consequently, the recoil energy has less effect on re-trapping efficiency. Furthermore, highly charged ions (HCI) remain charged after decay, whereas singly charged ions (SCI) may be neutralized in gas-filled traps or by β^+-decays [204]. Therefore, EBITs offer a nearly ideal environment to re-trap decay products.

However, the use of EBITs poses particular challenges that must also be considered: (a) Electron-impact ionization generates a distribution of charge states. If the generated beam is transported out of the trap, only the fraction in a charge state of choice will be used, typically around 20% [210, 211]. (b) The electron beam also ionizes residual gases that are present in the trapping volume, which may contaminate the beam. Last (c), EBITs may be "hot" environments due to complex thermodynamical processes, such as heating of the ion cloud by the electron beam and heat exchange by ion-ion collisions. A large thermal input to the ion of interest may "boil" them out of the trap and reduce the efficiency of the technique.

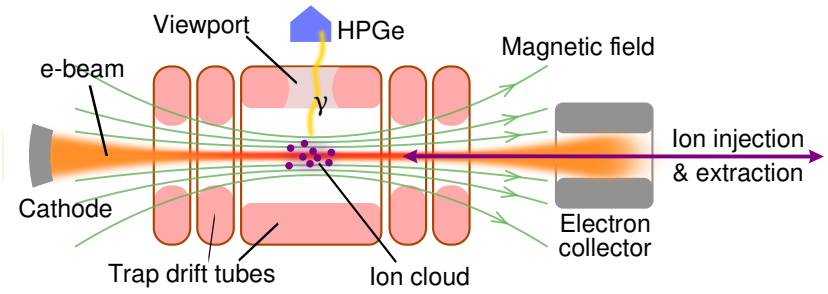

Figure A.1: Schematic overview of the TITAN EBIT. Trapping of ions is achieved axially by an electrostatic potential and radially by both a magnetic field and an intense electron beam passing through the trapping region.

Therefore, EBIT operating parameters must be carefully tuned in order to balance re-trapping efficiency, charge breeding, ion-cloud thermodynamics, and other physical processes that influence the final quality of the created beam. In the next section, the evolution of stored radioactive contents in EBIT is described using a simple model, which illustrates some of these challenges and provides a clearer picture of the variables that play a relevant role in the technique.

A.2 Simulations of Daughter Beam Creation

To understand the daughter beam creation and its confinement, we simulated the in-trap decay of a cloud of a parent ion in the TITAN EBIT, including population evolution and a simple EBIT thermodynamical model. ^{30}Mg was chosen as a suitable parent to explore as a proof-of-principle case, both from its decay properties and from its experimental availability.

The decay chain of $^{30}\text{Mg} \rightarrow {}^{30}\text{Al} \rightarrow {}^{30}\text{Si}$ provides representative examples of typical β^- decays. First, the half-lives of ^{30}Mg and ^{30}Al, respectively 0.335(10) s [212] and 3.62(6) s [213], allow us to probe two different timescales of interest, each one order of magnitude apart. Second the Q_β values of the decays (both above 6 MeV) are higher than average [54], allowing for a higher recoil energy contribution. Their decay schemes are also complex, with many intermediate γ de-excitation steps, but are well understood [212, 213]. Moreover, $^{30}\text{Mg}^+$ can be provided to TITAN as a pure beam by the ISAC facility. Hence, this decay chain allows a robust proof-of-principle experiment to explore the DRIT technique at TITAN.

In a Monte Carlo approach, particles in an initially pure $^{30}\text{Mg}^{q+}$ cloud, where q is the charge state of the ion, were randomly assigned a starting energy following a Maxwell-Boltzmann distribution. Particles were evolved in time (t, iterated by time step Δt) and were subject to three physical processes described below: Spitzer heating, radioactive decay, and trap escape. A flow diagram of the employed algorithm is shown in figure A.2.

Spitzer heating [208]: Trapped ions constantly gain energy from collisions with the intense electron beam. This is known to be a dominant process in EBIT thermodynamics and, if no active cooling mechanism is employed, ions will eventually gain enough energy to escape the trap barriers. The energy input per particle from Spitzer heating is proportional to q^2 and was calculated by the prescription outlined in ref. [208], assuming a perfect overlap between the electron beam and the ion cloud.

Radioactive decay: The population change from decay was modeled through simple decay laws, while the heating contribution from recoiling energy required consideration of the three-body nature of β-decay. We followed the same kinematic procedure outlined in detail in ref. [205] to calculate the recoil energy distributions. The calculation included not only the β-decay itself but also the intermediate de-excitation through γ-emission and all possible known decay branches. The β-decays schemes of ^{30}Mg and ^{30}Al are well described in refs. [212] and [213], respectively. These are almost pure Gamow-Teller transitions, for which the spectral shape of recoil energy distribution is well known [214, 215]. In the case of γ-emission, there are no long-lived isomeric states in the cases studied; therefore, we assumed that all de-excitations occur instantaneously. The final recoiling energy distributions are shown in fig. A.3. The Q_β-value of the decay of ^{30}Al (8561 keV) is higher than that of the ^{30}Mg (6990 keV). However, the average recoil energy gained by the daughter is higher in the ^{30}Mg decay (355 eV) than in the ^{30}Al decay (214 eV). The ^{30}Al decay mainly decays to much higher excited states of ^{30}Si, thus in some cases photon emission can revert the orientation of the recoiling momentum gained in the β-decay.

Trap escape: The escape of ions from the trap was incorporated at the end of every time step by removing particles from the simulation if their energy exceeded the trapping potential barriers. The escape also cools the trapped ion cloud through evaporative cooling. It was assumed that ion losses occur predominantly through axial potential barriers, as prescribed in [208].

For simplicity, other typical EBIT processes [208] such as radiative recombination, charge exchange, ionization heating, and effects from ion-ion interaction were neglected. The simulation also did not include the whole charge breeding dynamics, and the population was assumed to be in the $+11$ charge state through the whole calculation. The choice of charge state was guided by an EBIT charge-state evolution calculation (such as in [208]) that showed that the ion cloud should be predominantly in charge states between $+10$ to $+12$ for the timescales of the half-lives of the radioactive species. In section A.4.2, we verified this assumption experimentally.

All the parameters needed for the calculation are also displayed in fig. A.2. The trap parameters were chosen according to the characteristics of the TITAN EBIT. The chosen electron beam energy was twice the threshold energy to completely ionize Mg ions (1.962 keV [168]). Most parameters are typically well known or easily calculable, making this approach almost clear of free parameters. However,

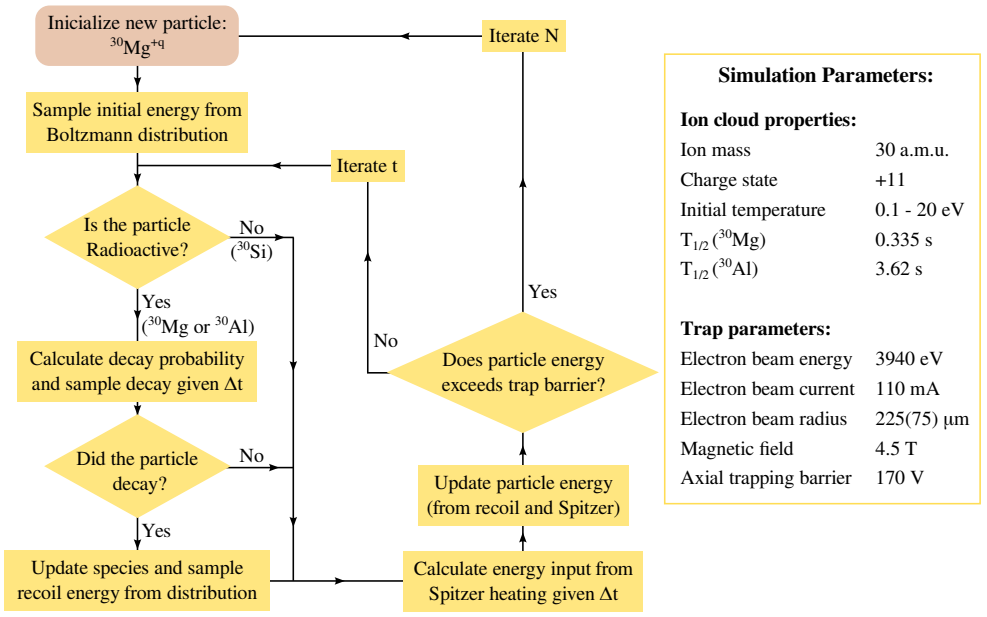

Figure A.2: A simplified flow diagram of the Monte Carlo algorithm to calculate daughter beam creation and its confinement in the TITAN EBIT. Only three physical processes are included: Spitzer heating [208], radioactive decay and trap escape. The relevant parameters on these processes are described in the table. Nuclear properties were taken from [212, 213], and typical TITAN EBIT operating parameters were chosen.

the radius of the electron beam of the TITAN EBIT is known to be between 150 and 300 μm, which does not sufficiently constrain the calculation of Spitzer heating rate [208]. This uncertainty was accounted for in the calculation by running the algorithm with different values of electron beam radius inside the range.

Results of the simulation are displayed in figure A.4. The total population, defined as the sum of populations of ^{30}Mg, ^{30}Al and ^{30}Si, remained constant until about $t \approx 2.0$ s, when it sharply decreased. According to these results, created ^{30}Al dominates the population after $\approx$ 300 ms or roughly $T_{1/2}(^{30}\mathrm{Mg})$, but the population of ^{30}Si could not become dominant before the cloud vanished from the trap ($2\,\mathrm{s} < T_{1/2}(^{30}\mathrm{Al})$).

The same calculation was performed without any additional recoiling energy in order to understand the contribution of decay energy input to ion losses. The total storing time was prolonged by only 20%. This result indicates that the recoiling energy contributes little to the losses mechanisms in an EBIT as a storage device and that losses from Spitzer heating dominate. This finding contrasts with observations of DRIT in Penning traps [204, 205], where ion losses were attributed to recoil energy exceeding trap barriers.

The results of these simulations were confirmed by an experiment at the TITAN facility, described in the next section.

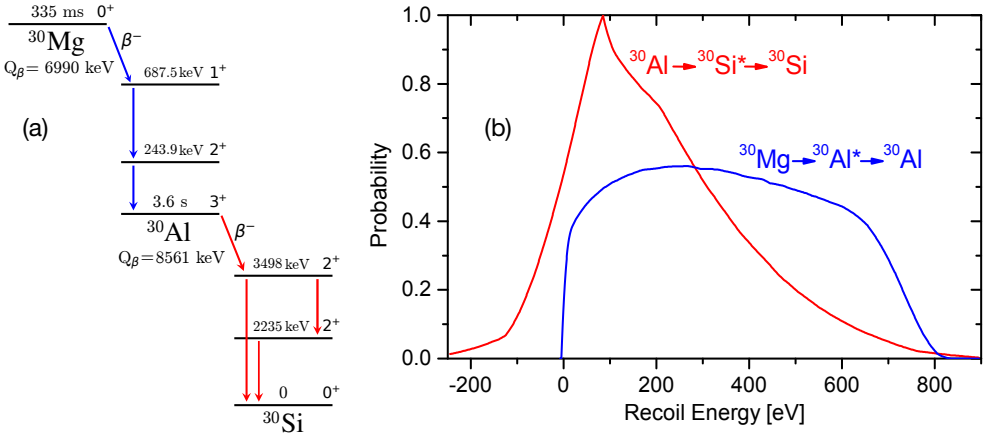

Figure A.3: (a) The decay scheme of the ^{30}Mg $\rightarrow$ ^{30}Al $\rightarrow$ ^{30}Si chain [212, 213] shows the energy levels and major transitions (arrows). (b) The recoiling energy distributions following the β-decays and γ de-excitations of ^{30}Mg and ^{30}Al in the center-of-mass reference frame. Negative energies refer to a final recoil momentum direction opposite to that initially gained in the β-decay, meaning an antiparallel and higher-energetic γ-recoil.

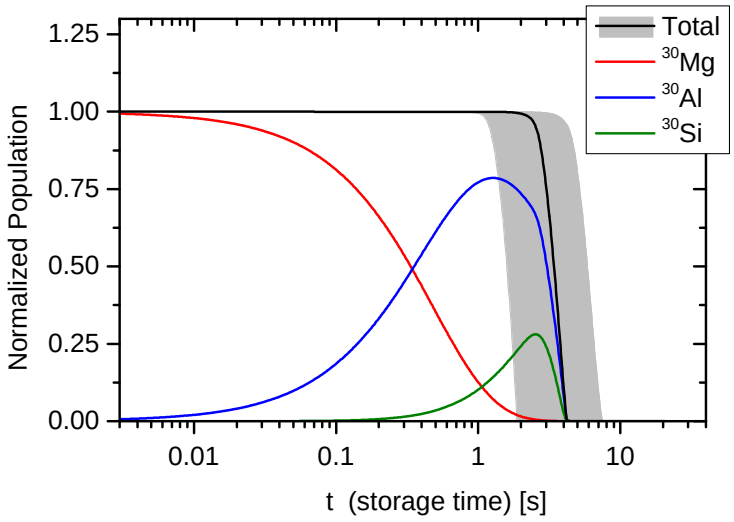

Figure A.4: Simulated population evolution of radioactive ions trapped in EBIT. Total population (black curve - normalized to initial) is shown alongside its constituents: ^{30}Mg (red), ^{30}Al (blue) and ^{30}Si (green) populations. The grey band represent the uncertainty of the total population evolution due to electron beam radius.

A.3 Experiment Overview

In the experimental procedure described herein, we investigated RIB population evolution inside EBIT, tracked ion losses, and unambiguously identified the daughter species after storage. In addition, we performed an experiment with the created beam outside the EBIT to substantiate the technique.

The RIB was produced at ISAC by impinging a 480 MeV proton beam onto a low-power uranium-carbide target. Magnesium isotopes were selectively ionized using TRILIS [149] (see sec. 4.1). The beam was extracted, separated by ISAC's mass separator [151], and sent initially to ISAC's Yield Station [216] for a composition measurement, which revealed a purity of $\geq$99.4(1)% of $^{30}Mg^{+}$.

The $^{30}Mg^{+}$ beam was then delivered to the TITAN facility, presented in sec. 4.2 (see fig. 4.3). The beam was accumulated in the TITAN RFQ and sent in bunches to the EBIT [155], where DRIT was performed.

The TITAN EBIT is designed to provide charge-bred ions for mass measurements with MPET [156] and to perform in-trap decay spectroscopy [217, 218]. In this experiment, its trapping and electron beam parameters were identical to those listed in figure A.2. For mass spectrometry, as beams are extracted from the EBIT and sent towards MPET, they pass through a Bradbury-Nielsen Gate (BNG) [219], which selects the bunched beam by its time-of-flight and thus mass-to-charge ratio (m/q). Additionally, an MCP detector can be moved into the beamline before the MPET, about 10 meters downstream of EBIT. It yields a time-of-flight spectrum that allows the m/q identification of the constituents of the beam extracted from the EBIT.

A.4 Population Evolution

In this section, we describe the systematic studies of the evolution of the trapped radioactive ion cloud over a range of storage time. To ensure a constant amount of RIB was employed every cycle, the RFQ accumulated RIB for 100 ms. Then the beam was sent to the EBIT, where the storage time was varied between $t = 15$ ms and 8 s, covering one order of magnitude above and below the half-life of ^{30}Mg. After the storage, the composition of the ion cloud was inspected by extracting it onto the MCP detector.

The time-of-flight spectrum allowed m/q identification of each species as well as their count rates. A typical time-of-flight spectrum can be seen in fig. A.5 (top panel), where the average spectra of measurements with $t \geq 100$ ms is shown. As ionized residual gases could have the same m/q as the RIB, spectra were measured with and without the injection of RIB into EBIT under identical conditions. The subtracted spectrum contains only the RIB species, and an example can be seen in fig. A.5 (bottom panel). The spectra obtained at each storage time were analyzed with a multiple-peak fitting routine, through which the count rate for each peak could be

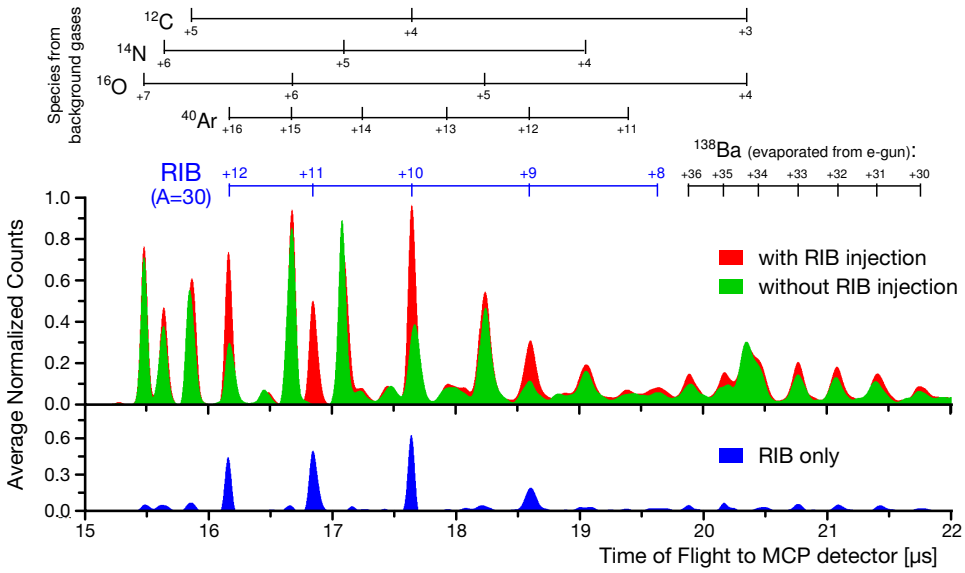

Figure A.5: Spectra of time-of-flight measurements between EBIT and the MCP (top panel), which allow m/q identification of trapped species. Spectra were obtained with (top, red) and without (top, green) RIB injection into EBIT. RIB peaks can be identified by subtracting the two spectra (bottom, blue). RIB charge states between $+9$ and $+12$ of $A = 30$ beam can be clearly identified. Other identified species are also marked for reference. The shown spectra are averaged among all measurements with $t \geq 0.1$ s.

determined, including from overlapping peaks. With these data, we monitored the evolution of both the charge state distribution and the absolute population of RIB.

A.4.1 Optimal Storage Time for DRIT

We verified if the ion cloud could be stored as long as needed to create a sample of ^{30}Al or ^{30}Si through DRIT. At each storage time, we analyzed the total count rate of RIB by summing the counts of all RIB peaks present on the spectrum. The result is shown in figure A.6.

The count rate was nearly constant and independent of t up to $t = 2.0$ s, much longer than $T_{1/2}(^{30}\text{Mg})$. This suggests a high re-trapping efficiency of the decay daughters, especially at $t \gtrsim 300$ ms $\approx T_{1/2}(^{30}\text{Mg})$. After $t \approx 2$ s, the RIB count rate dropped. This is shorter than $T_{1/2}(^{30}\text{Al})$, thus the creation of a ^{30}Si beam may not be feasible.

The simulated evolution of the total RIB population (sec. A.2, fig. A.4) is overlaid on the data in figure A.6 and agrees well with it. This result substantiates the simple EBIT thermodynamical model and confirms Spitzer heating as the dominant source of ion losses.

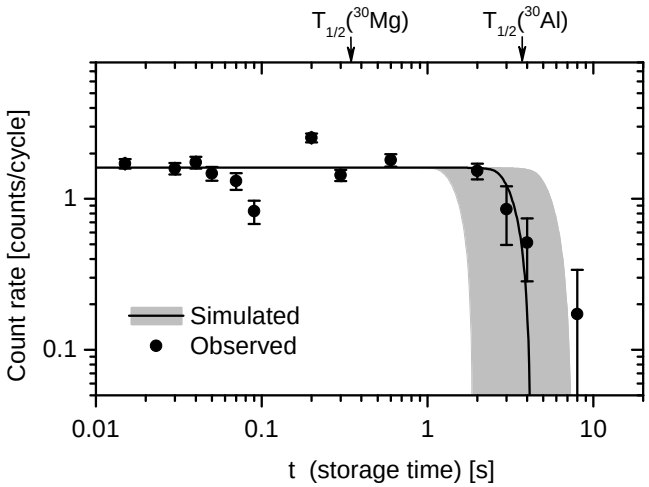

Figure A.6: Integrated RIB count rates on the MCP as a function of storage time, obtained from the spectral analysis of time-of-flight data. The simulated RIB population evolution from sec. A.2 is shown normalized to the measured count rate data.

A.4.2 Charge State Evolution

In EBITs, the storing time governs the charge state distribution of the ion cloud and; thus, it influences confinement and Spitzer heating. It also influences how much background gas gets ionized, which might contaminate the produced beam. Furthermore, if the beam were used outside the EBIT, it needs to match the subsequent device's acceptance. Therefore, the storing time and the desired charge state must be chosen to balance the quality of the created beam and the amount of daughter species it contains.

To maximize the production of daughter beam, optimize its purity, and minimize decay losses for its mass measurement, we analyzed the time-of-flight data looking for charge state evolution of the stored RIB. In fig. A.5, the RIB peaks corresponding to $q = +9$ to $+12$ can be seen, as well as the series of peaks of typical background gas species ($^{12}C^{q+}$, $^{14}N^{q+}$, $^{16}O^{q+}$ and $^{40}Ar^{q+}$) and of $^{138}Ba^{q+}$ originating from evaporated material from the electron source cathode.

The relative populations of each of the RIB charge states are shown in figure A.7 as function of storage time. During the analyzed storage time interval, the RIB cloud evolved from charge state $q = +5$ to $+12$.

The charge state $q = +11$ dominates the RIB population for $t \gtrapprox 300$ ms, which confirms the charge state chosen to perform the simulations in sec. A.2. It is also clear from fig. A.5 that the $q = +11$ RIB peak is the most separated charge state from any background species. Thus it was the best choice to be employed for further study outside of the EBIT.

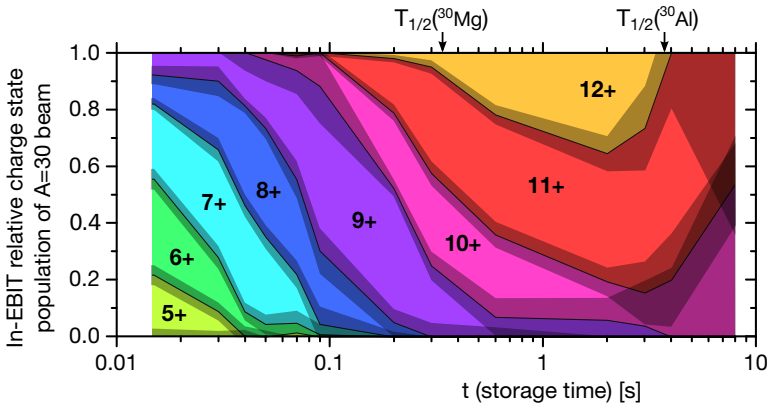

Figure A.7: Evolution of charge state population of $A = 30$ beam in EBIT as a function of storage time. Relative populations are stacked by charge state. Darkened regions are the error of the higher charge-state population. The increase in uncertainties after 3 s is due to the drop in RIB count rate and to overlap with intense background peaks.

A.5 Identification of Daughter Beam through PTMS

Although the systematic measurements performed with EBIT reveal strong evidence of in-trap decay and creation of daughter beam, it still did not provide definitive proof that the daughter species was present in the beam extracted from the EBIT. The time-of-flight to the MCP cannot resolve isobars. For this reason, the identification of the daughter beam was performed with the MPET high-precision mass spectrometer, which also served as a demonstrative experiment.

High-precision mass spectrometry provided unambiguous identification of each species. The mass precision required to resolve $^{30}Al^{+q}$ from $^{30}Mg^{+q}$ (in the same charge state) is $3 \cdot 10^{-4}$ [34], which is well within MPET's capabilities [110].

In the first identification measurement, the RIB was stored in EBIT for $t = 50$ ms, which is much shorter than the half-life of ^{30}Mg ($T_{1/2} = 335(10)$ ms). The BNG selected the $+8$ charge state of RIB, which was the most populated (see Fig. A.7). The selected beam was loaded to the MPET, where a search for $^{30}Mg^{8+}$, $^{30}Al^{8+}$ and $^{30}Si^{8+}$ was done. The analysis revealed the presence of $^{30}Mg^{8+}$, but no detectable amount of $^{30}Al^{8+}$ or $^{30}Si^{8+}$ was found in the beam.

Likewise, the RIB was stored in EBIT for $t = 300$ ms, close to ^{30}Mg half-life, which mostly populated the $+11$ charge state. This time, $^{30}Al^{11+}$ was successfully identified in the MPET, confirming the production of a daughter beam in EBIT. Figure A.8 shows a sample ToF-ICR resonance of $^{30}Al^{11+}$ acquired. Once again, ^{30}Si was not observed. However, measurements with a longer storing time at EBIT, which could enable the creation of ^{30}Si, were not attempted.

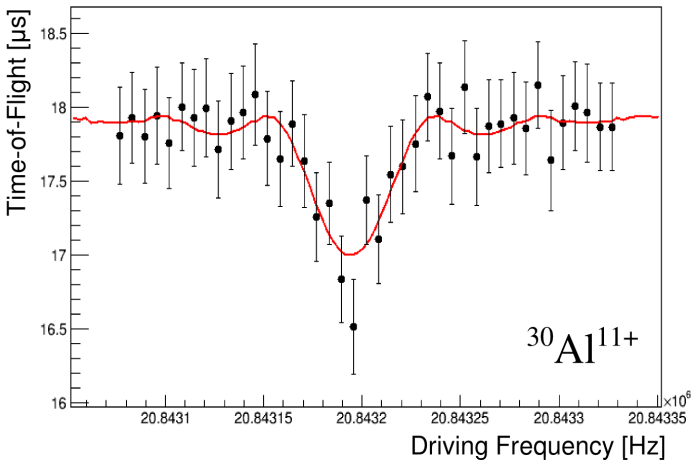

Figure A.8: A typical ToF-ICR resonance of $^{30}Al^{11+}$ measured with MPET. The beam used was created by storing the parent beam for $t = 300$ ms in the EBIT. The red curve is an analytical fit to the data.

A.5.1 Demonstrative Experiment

The last goal of this proof-of-principle experimental campaign was to use the beam created through DRIT in an experiment outside the storage device. High-precision mass measurements using MPET are susceptible to the incoming beam quality. A successful precision mass spectrometry measurement reveals that the beams produced using the technique meet high-quality criteria.

High-precision mass measurements of $^{30}Al^{11+}$ and $^{30}Mg^{8+}$ were performed. The measurement and analysis procedure followed the same as described in section 5.2. However, differently than the measurements described in the core of this thesis, PTMS measurements employing HCI may have a non-negligible contribution from the binding energy (B_e) of the electrons removed from the atomic form of the ion of interest [67]. The ratio (R_ν, see eq. 3.6) between their cyclotron frequencies (ν_c) of the ion of interest and the reference ion is updated to include the electron binding energies:

$$R_\nu = \frac{\nu_{c,ref}}{\nu_c} = \frac{(m_a - q\,m_e + B_e)\;q_{ref}}{(m_{a,ref} - q_{ref}\,m_e + B_{e,ref})\;q} \quad , \tag{A.1}$$

where m_e is the mass of the electron, m_a is the atomic mass and q is the charge state of the ion. The subscript ref refers to the calibrant ion, otherwise it refers to the ion of interest. In the case of this experiment, $^{16}O^{6+}$ ($B_e = 0.43$ keV) was used as a reference for $^{30}Al^{11+}$ ($B_e = 2.22$ keV), while $^{39}K^{10+}$ ($B_e = 1.28$ keV) was used for $^{30}Mg^{8+}$ ($B_e = 1.03$ keV). Atomic masses of the reference ions were taken from [34], while electron binding energies were taken from [168].

The results of the mass measurements performed are shown in table A.1. Our values agree with the Atomic Mass Evaluation of 2016 [34] and provide a modest improvement on their precision.

Table A.1: Atomic masses of ^{30}Al and ^{30}Mg, given as mass excesses. Values presented in this work are compared to [34]. The weighted average of the measured frequency ratios between the ion of interest and of reference are also given.

Ion of interest	Reference	R_ν	Atomic mass excess [keV]	
			This work	Literature
$^{30}Al^{11+}$	$^{16}O^{6+}$	1.022476354(95)	−15863.5(2.6)	−15864.8(2.9)
$^{30}Mg^{8+}$	$^{39}K^{10+}$	0.962122910(48)	−8880.9(1.4)	−8883.8(3.4)

A.6 Conclusions and Applications

We successfully demonstrated the Decay and Recapture Ion Trapping technique using the EBIT at TITAN facility. A cloud of $^{30}Mg^{q+}$ ions was stored in the EBIT, and the creation of a $^{30}Al^{q+}$ daughter beam was identified through Penning trap mass spectrometry. The extraction for mass measurement in the Penning trap also demonstrated the capability of DRIT to produce beams compatible with subsequent experiments.

We performed EBIT simulations to understand losses mechanisms related to re-trapping efficiency. Simulated results agree with the observations made in the experiment and indicate that Spitzer heating is the primary source of observed losses, and not the recoil energy from β-decay. Our results are in line with findings of other experiments performed using DRIT with EBITs as storage media [206, 207], which indicated high re-trapping efficiency of decay products. However, they contrast with those performed in Penning traps [204, 205], which suggest a significant influence of the recoil energy in the observed efficiencies.

EBITs are reliable storage devices for DRIT. They have demonstrated superior confinement capabilities, higher charge-space limit, and larger recapture efficiencies than other ion traps. Moreover, Spitzer heating depends on operating parameters that can be tuned for specific experiments. Since EBITs are regularly employed in RIB facilities to provide charge-bred beams for experiments and post-acceleration, this technique has the potential to become a regular tool to increase beam availability.

DRIT can allow access to non-ISOL beams at ISOL facilities. For example, ^{34}Si [220] and ^{88}Zr [221], nuclides that were the object of particular interest in recent years, could be produced from ^{34}Al and ^{88}Y. Using the parameters of this experiment only, over 50 new nuclides could be available at ISAC facility using DRIT. These are shown in fig. A.9 together with the currently available RIB yields [142]. The technique also can give direct access to certain nuclear isomers. The long-lived

isomeric 1^+ state of ^{34}Al, for instance, has been an object of curiosity [222, 223, 224] and is preferentially and cleanly populated only through a ^{34}Mg parent beam.

In some cases, better beam properties could be achieved through DRIT even for available beams. A clear example is the measurement of the Q-value of the superallowed β decay ^{74}Rb $\rightarrow$ ^{74}Kr [156, 225]. Noble gases produced in ISOL facilities suffer from high levels of contamination co-produced in the ion sources. In contrast, pure alkali beams are commonly available. The ^{74}Kr beam can be more cleanly produced through the decay of ^{74}Rb.

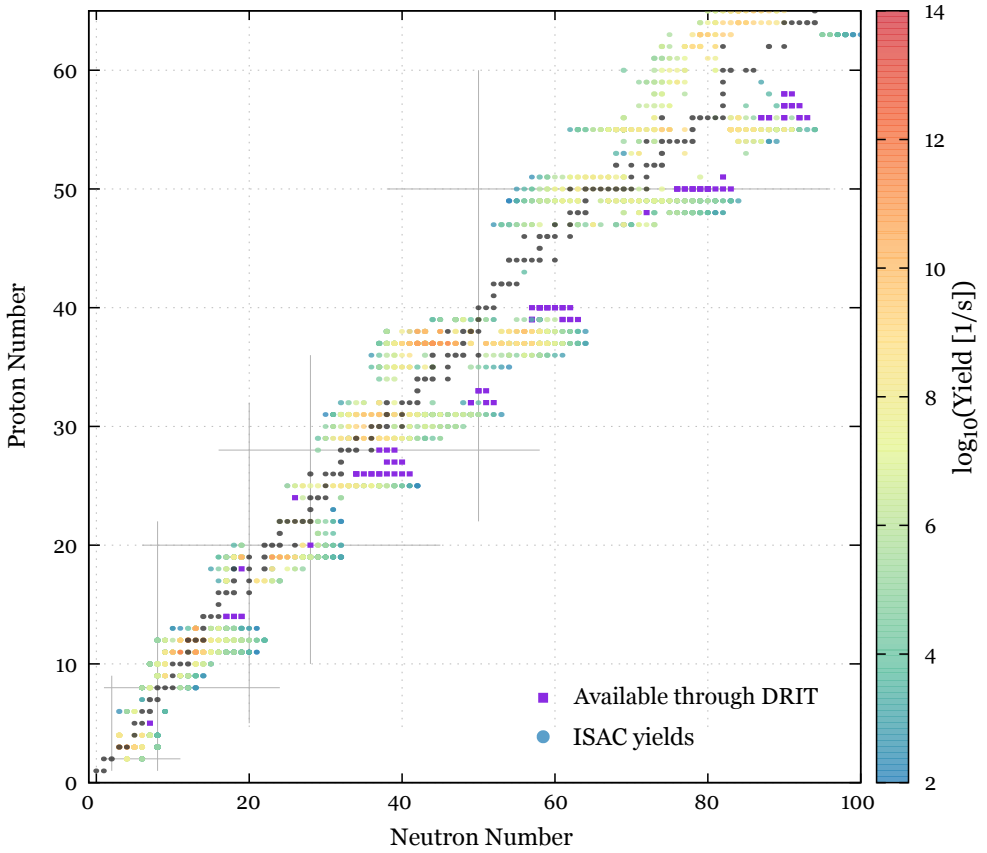

Figure A.9: Current yields of radioactive ion beams available at the ISAC facility at TRIUMF [142]; purple nuclides are accessible through DRIT. These were selected based on the availability of a suitable parent with a minimum yield of 50 pps, maximum half-life of 2 s and $Q_\beta < 15$ MeV. Courtesy of R. Klawitter.

B THE CRYOGENIC UPGRADE TO THE TITAN MPET

The mass Measurement Penning Trap (MPET) at TITAN has been successfully performing precision mass measurements of radioactive nuclei for over a decade. As detailed in sec. 4.2.2, it is designed to probe masses of ions living as short as 10 ms, reaching relative mass precision in the $10^{-7} - 10^{-9}$ range. A powerful way to boost this precision and its resolving power is to charge breed the inspected ion [156, 171], as can be seen by the dependence with the charge state q in the cyclotron frequency (eq. 3.5). At TITAN charge breeding is achieved through electron impact ionization in the EBIT, as illustrated in appendix A.

The advantage of employing highly charged ions (HCI) in PTMS is illustrated in the top panel of figure B.1. It shows a typical ToF-ICR measurement (see sec. 3.2) performed at the MPET. The spectrum shows the presence of two close-lying species: $^{130}Cs^{+12}$ and $^{130}Ba^{+12}$, whose mass difference is in the order of 3 parts in a million [34]. Using HCI, in this case, boosted the resolution and enabled the mass separation of the isobar pair in a measurement of only 100 ms.

HCIs are widely used in nuclear and atomic sciences, but experimental investigations with them are challenging. They interact more strongly with neutral molecules than singly charged ions (SCI), thus keeping their charge states for long measurement times requires more stringent criteria for vacuum conditions. In PTMS, increasing charge state or measurement time also raises the probability that the ion interacts with residual gas species in the trap. Ion-gas viscous interactions are known to create damping artifacts on ToF-ICR measurements using SCI [227]. When using HCI, charge-exchange reactions, such as

$$X^{+q} + N_2 \longrightarrow X^{+(q-i)} + N_2^{+i} \quad ,$$

become dominant.

Such electron recombination reactions can have very detrimental effects on the quality of ToF-ICR resonances. One example is shown in the bottom panel of figure B.1. Charge exchange events ionize background gas particles, which have very different m/q than the sampled ion. Such ions will appear in very different positions in the time-of-flight spectrum. Meanwhile, the charge exchanged ions slightly increase their m/q, leaving the measured cyclotron frequency range but still appearing as a background in a similar time-of-flight range as the undisturbed ions of interest. Furthermore, the simultaneous trapping of the produced contaminant ion will affect the ion motion of the ion of interest that could result in a systematic shift of the measured cyclotron frequency.

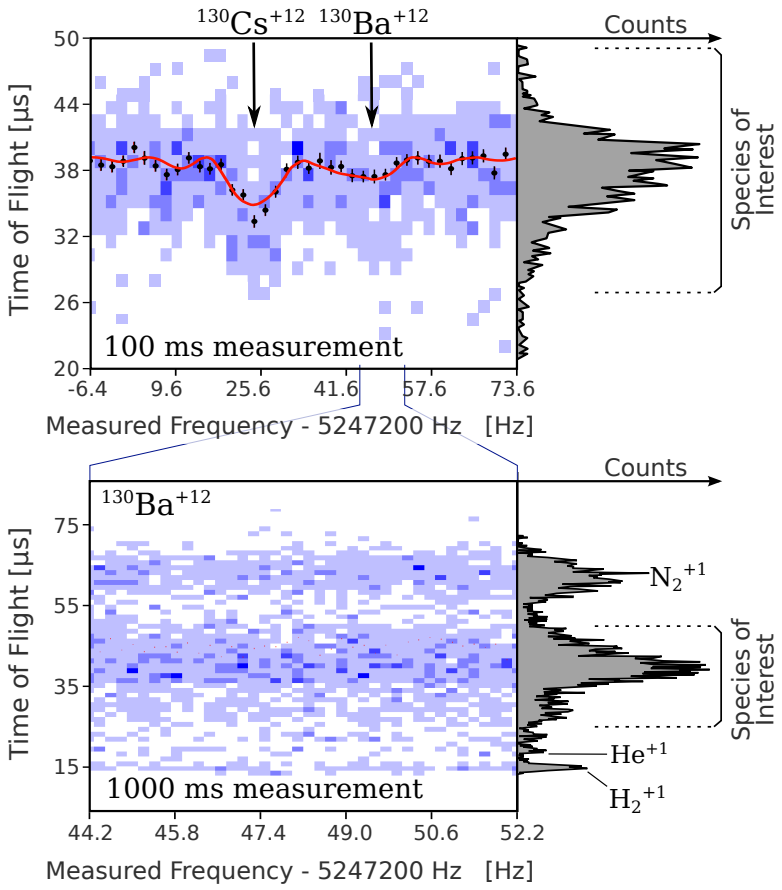

Figure B.1: A comparison of ToF-ICR resonances taken at different measurement times illustrates the degradation of measurement quality due to ion-gas interactions. On top, the measurement done in 100 ms shows the presence of two species: $^{130}Cs^{+12}$ and $^{130}Ba^{+12}$ (bi-dimensional histogram events is in blue and average time-of-flights in black, red curve is an analytical fit [116]). On bottom, the same species are measured for 1 s, centered on $^{130}Ba^{+12}$, but the resonance pattern can no longer be seen. Also the presence of additional species is now seen in the time-of-flight spectrum (grey histogram), and are compatible with ionized N_2^+, H_2^+ and He^+. First published in [226].

Recently, the TITAN EBIT was upgraded to enable access to bare, H-like or He-like configurations of species up to $Z = 70$ [203]. With higher charge states available, the demand for better vacuum in the MPET increases. In section B.1, we estimate the required vacuum in order to take full advantage of EBIT's improved performance. In section B.2, we evaluate the pressure levels in the MPET, which revealed that substantial improvements to its vacuum system were required. We carried out vacuum simulations, discussed in section B.3, to explore the impact of potential modifications to the vacuum system. Finally, in section B.4, the concept of the upgraded system is presented.

B.1 Vacuum Requirements for PTMS of HCI

The maximum pressure in the experimental setup is bound to the maximum tolerable level of ion-gas interactions during a measurement. In order to understand the factors that play a role in such interactions, we model the ion as a particle traveling through a region filled with a gas of constant density. We assume the background gas is in the Knudsen's regime (molecular flow) [228, 229] and thus can be approximated by an ideal gas of temperature T and pressure P.

The ion travels a distance s through the background gas and has an interaction cross section σ with the residual gas particles. The expected number of interactions η between the ion and residual gas particles is given by the number of particles present in the "interaction volume" σs:

$$\eta = \sigma \, s \, \frac{P}{k_B \, T} \quad , \tag{B.1}$$

where k_B is the Boltzmann's constant[27]. We use this equation to relate an expected number of interaction events to the corresponding pressure in the trap volume. Next, we discuss how s and σ were calculated in the context of ToF-ICR measurements of HCI, subject to charge-exchange interactions.

The path length (s) of the ion motion inside a Penning trap grows with q/m of the ion and with measurement time (t_{RF}). Here, we estimated it from the equations of motion of the ion during a ToF-ICR measurement, as formulated in [116]. It can be approximated by the length covered by an ion through a conversion from a pure magnetron motion (of angular frequency ω_- and initial radius r_0) to a pure reduced cyclotron motion (of angular frequency ω_+) by a quadrupole radiofrequency excitation:

$$s(t_{RF}) \approx r_0 \int_0^{t_{RF}} \sqrt{\omega_+^2 \sin^2\left(\frac{\pi}{2}\frac{t}{t_{RF}}\right) + \omega_-^2 \cos^2\left(\frac{\pi}{2}\frac{t}{t_{RF}}\right) + 2\sin\left(\frac{\pi}{2}\frac{t}{t_{RF}}\right)\cos\left(\frac{\pi}{2}\frac{t}{t_{RF}}\right)\cos[(\omega_+ - \omega_-)t]}\, dt \quad .$$

Examples of path lengths for a few ions are shown in figure B.2. As can be seen, it can easily surpass a kilometer in a typical measurement procedure.

Cross-section data for charge-exchange processes are scarce. An estimate for one electron transfer can be obtained through a simple scaling rule obtained by Müller and Salzborn [230]:

$$\sigma_{q \to q-1} = C \, q^{\alpha} \, E_0^{-\beta} \quad [\mathrm{cm}^2] \, , \tag{B.2}$$

where E_0 is the first ionization potential (in eV) of the neutral gas molecule. At TITAN, a residual gas analysis revealed that the background gas is mainly composed by nearly equal amounts of N_2 and H_2 (see discussion in the next section), both with $E_0 \approx 15.5$ eV [231]. The empirical parameters are $C = 1.43(76) \cdot 10^{-12}$,

27 Note that this equation is only valid if the kinetic energy of the ion is much greater than the background gas particles' $k_B T$ ($\sim$ tens of meV). The energy of the ion motion in a typical ToF-ICR measurement is on the order of tens of eV, so this condition is easily satisfied.

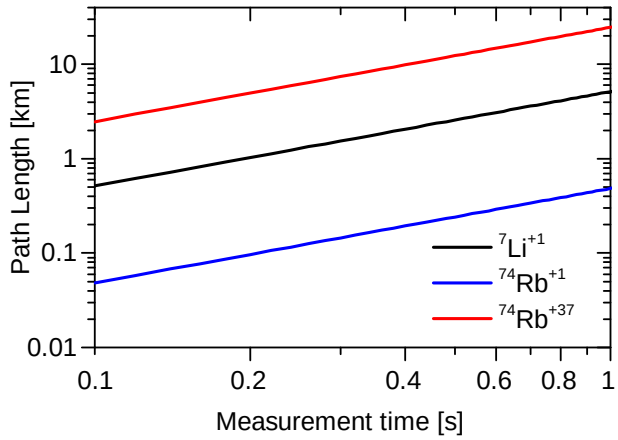

Figure B.2: Calculated path length of the motion of a few ions during a ToF-ICR measurement procedure in MPET, as a function of the measurement time. First published in [226].

$\alpha = 1.17(9)$ and $\beta = 2.76(19)$ [230]. The charge-exchange cross section is typically on the order of 10^{-14} cm^2 (or 10^{10} b) for $q \geqslant 10$, about an order of magnitude larger than cross section of ion-gas collisions (see fig. B.3). Multiple-electron transfers were not considered.

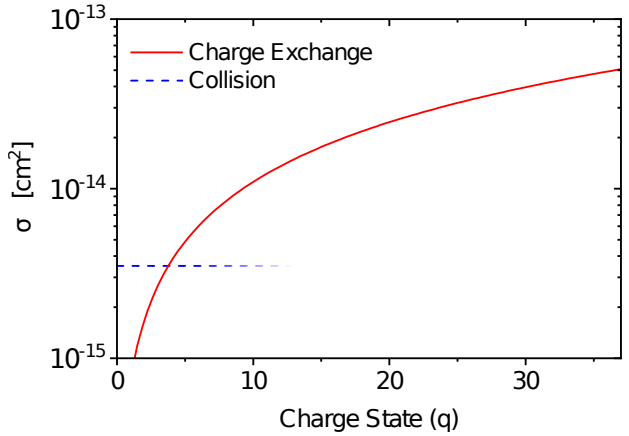

Figure B.3: Calculated interaction cross sections between Rb^{+q} ion and N_2 neutral molecule. The cross section for charge exchange process (red) was calculated through eq. B.2 and has a dependence with the charge state q. The collision cross section (blue) was calculated from the radii of the molecule and the singly charged Rb^+ ion (taken from [231]) and therefore it does not have the appropriate charge dependence built in.

Finally, in order to have an undisturbed measurement, we chose $\eta < 0.1$, which corresponds to less than 10% of ions experiencing any interaction with the residual gas during a measurement. The maximum pressure required to achieve such conditions can be calculated through inverting eq. B.1. In figure B.4, this pressure is calculated for ToF-ICR measurements of the superallowed β-emitter $^{74}Rb^{+37}$, fully ionized ($m/q = 2$).

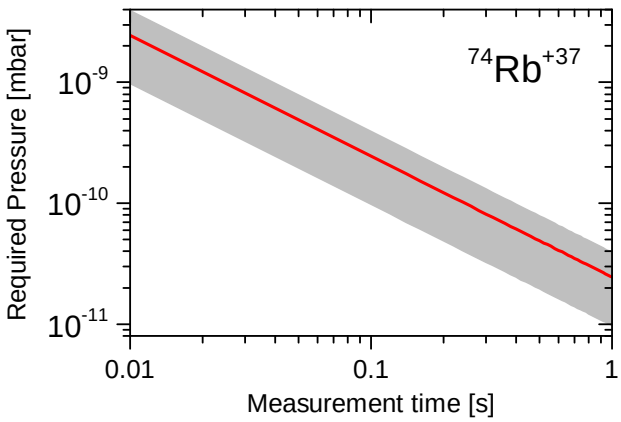

Figure B.4: Maximum background N_2 gas pressure required for $\eta < 0.1$ calculated for a ToF-ICR measurement of $^{74}Rb^{+37}$, as a function of measurement time. The gray band represents the error inherent to the model of eq. B.2 [230]. First published in [226].

The results of this analysis for many different HCI at charges higher than +20 reveal that longer measurements ($t_{RF} > 100$ ms) require pressures at least in the 10^{-11} mbar range. To benchmark our method, we verified that such requirement levels were satisfied at the SMILETRAP mass spectrometer [232], which was used to perform ToF-ICR of stable HCI up to 1 s. Next, we evaluate the pressure levels at the MPET mass spectrometer at TITAN and discuss its agreement with the established criteria.

B.2 HCI as Vacuum Probes and the Pressure at MPET

At TITAN, two ionization vacuum gauges measure the pressure at the ends of MPET's superconducting magnet, both yielding $\sim 10^{-10}$ mbar. Such pressure values are higher than desired, given the analysis presented in the previous section. However, the gas pumping conductance from the inner volume of the Penning trap is very restricted. Thus, the pressure levels are expected to be higher than where the gauges are installed. Yet, in order to address appropriate solutions to improve the vacuum at MPET, it is imperative that we measure the pressure inside the trap.

The inner volume of a precision Penning trap is a tightly enclosed space that restricts the placement of any vacuum gauge. Therefore, we resorted to indirect ways to determine the pressure of residual gases by observing charge exchange reactions with the sampled ions. ToF-ICR measurements of $^{133}Cs^{+13}$ ions were performed at several measurement times, ranging from 25 ms to 100 ms. First, we determined the ratio of ^{133}Cs ions that underwent charge-exchange during each

measurement. The η was estimated by the ratio between the number of charge-exchange events (N_{cx}) and the number of ^{133}Cs ions (N_{ion}):

$$\eta = \frac{N_{cx}}{N_{ion}} \quad . \tag{B.3}$$

N_{ion} is determined by the number of counts inside the time-of-flight window that contains the species of interest (see, for example, the ranges marked in the histograms of figure B.1). Similarly, N_{cx} can be determined from the number of counts outside the same range, which should correspond to ionized background gases counts. In figure B.5 the measured η values are presented for all inspected measurement times. The expected linear trend from eq. B.1 is clearly followed.

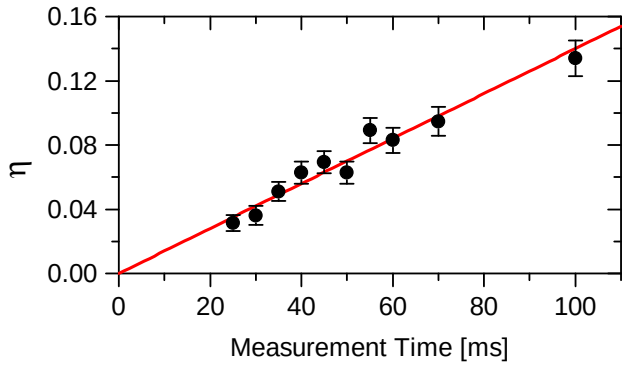

Figure B.5: Measured ratio of $^{133}Cs^{+13}$ ions that went through charge exchange, as a function of the measurement time. The red line is a linear fit to the data. First published in [226].

Using the data in figure B.5 and equation B.1, the pressure in MPET was estimated to be $8(5) \cdot 10^{-9}$ mbar. By comparing this number to the calculated required pressures presented in section B.1, it is immediate that the quality of the vacuum in MPET is not good enough for long measurements of HCI with $q > +20$. In the situation presented in figure B.4, for example, the Penning trap requires a vacuum upgrade of about two orders of magnitude to be able to perform a mass measurement of $^{74}Rb^{+37}$ of a few hundreds of milliseconds long.

Besides the magnitude of the pressure levels in the trap, it is also important to know the composition of the residual gas. Therefore, a Residual Gas Analyzer (RGA) was installed in the beamline near MPET. This device works by ionizing the residual gas particles and sending the ionized particles through a mass filter (further details can be found at [233]). The generated mass spectrum is shown in figure B.6. The analysis revealed the presence mostly of ions of mass 2 u and 28 u, assumed to be from ionized H_2^+ and N_2^+ or CO molecules. Their presence is also seen in the charge-exchange products shown in the bottom panel of figure B.1. Smaller amounts of water and carbon dioxide were also seen, but no meaningful amount of He gas was detected.

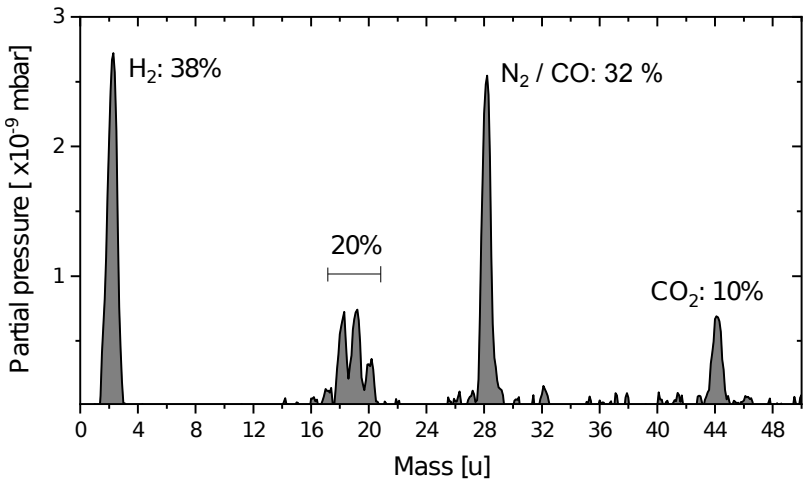

Figure B.6: RGA analysis of the vacuum in the beamline near MPET, taken with a RGA200 module from Stanford Research Systems [233].

B.3 Vacuum Simulations

The need for improvements in the vacuum system of MPET had already been identified in the early experiments employing HCI [156, 225]. Past attempts include "baking" of the system (degassing using high temperatures) [234] and the addition of new vacuum pumps. However, the analysis presented in the previous sections revealed the need for more profound upgrades.

Possible upgrades were studied through computer simulations of the MPET vacuum system. The procedure had two phases. The first consisted of creating a model of the vacuum profile in the present system. It had to accurately reproduce the pressure in the three different locations of the system where measurements exist: inside the Penning trap (by the method described in sec. B.2), and by two ionization gauges placed near the two ends of the superconducting magnet. The second phase consisted in exploring potential modifications to the vacuum system to verify which can produce the required pressure in the trap.

B.3.1 Monte-Carlo Algorithm

The developed algorithm followed a Monte-Carlo approach. It simulated the transport of residual gas particles through the vacuum system to analyze how they could be more efficiently pumped out and where density pockets could be formed.

Outgassing from the internal surfaces was considered the only source of particles, and the system was considered to be in the molecular flow regime. In the molecular flow, the gas particles are non-interacting and behave as in an ideal gas. Therefore, the simulation is only adequate to describe the steady-state and cannot model pumping speeds or any gas flow dynamics happening in the transient phase.

First, a geometrical model of the vacuum system was constructed, including vacuum chambers, pumps, and objects like electrodes and support structures (also considering their materials and respective outgassing rates). Then, particles were generated and transported through the system following the prescription below:

1. **Outgassing events:** a new particle is initiated at a random point of the surface of a random object inside the system. The likelihood of an "outgassing event" happening at a given object is regulated by the outgassing rates of the object's material. The event happens at a random instant (t) between $t = 0$ and $t = t_{end}$ (see item 5 below). The particle is assumed to be of N_2 molecule, but minimal variation was seen in the results by using other particles.
2. **Release from surface:** the particle is emitted from the surface of the object. The emission angle with respect to the surface follows Knudsen's Cosine Law [228, 229], while the particle's velocity (v) follows a Boltzmann distribution with the temperature of the surface (~ 300 K).
3. **Transport through the system:** the particle travels through the vacuum system in fixed distance steps (Δs). The time is iterated in the appropriate time step $\Delta t = \Delta s/v$. The advantage of fixing the Δs instead of Δt is the better control over the spatial resolution of the generated density profile, which must be much smaller than the geometrical features of the objects in the system. In this case, $\Delta s = 0.1$ mm.
4. **Interaction with objects:** the particle may hit an object as it is transported through the system. If it reaches an ordinary object, it is instantly re-emitted following the prescription of item 2. If it reaches a pump, it is removed from the simulation. Pumps are assumed to be ideal, with no backflow to the system.
5. **Density snapshot:** if the particle survives in the system until the time t_{end} is reached, its position is registered in the density profile. The density profile is a snapshot of the particle distribution inside the system taken at the instant t_{end}. To ensure it reflects an equilibrium condition, t_{end} must be much longer than the average lifetime of particles inside the system, and the particles need to be introduced into the system at random times during the inspected period. An analysis of the average lifetime of particles in the system is shown in figure B.7. It reveals that $t_{end} = 0.1$ s fits the criteria.

The procedure described is depicted in the flow diagram of figure B.8. After a sufficiently large amount (N, usually on the order of 10^6) of iterated particles, the generated particle density distribution at the end of the simulation was transformed into a pressure distribution following procedures described in the next section.

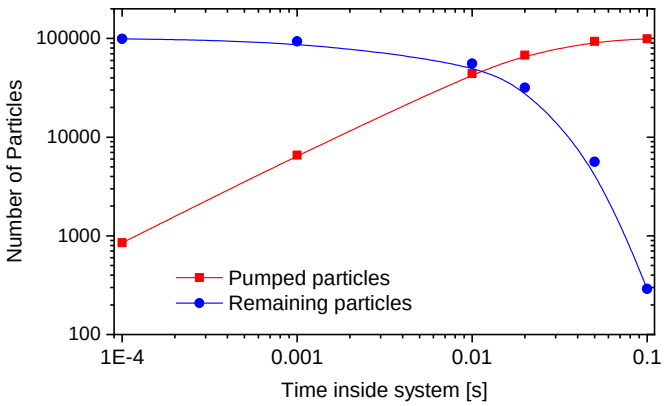

Figure B.7: Survival time of simulated particles in the vacuum system. Almost all particles are expected to be pumped out after 0.1 s of their release in the system.

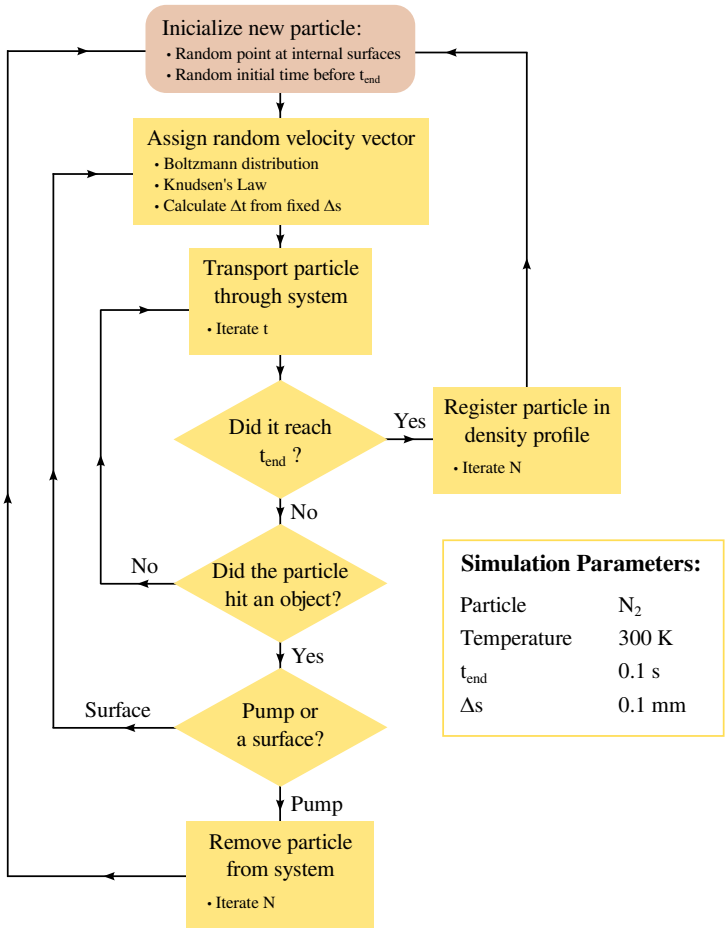

Figure B.8: A simplified flow diagram of the Monte-Carlo algorithm employed to simulate the vacuum in the MPET system.

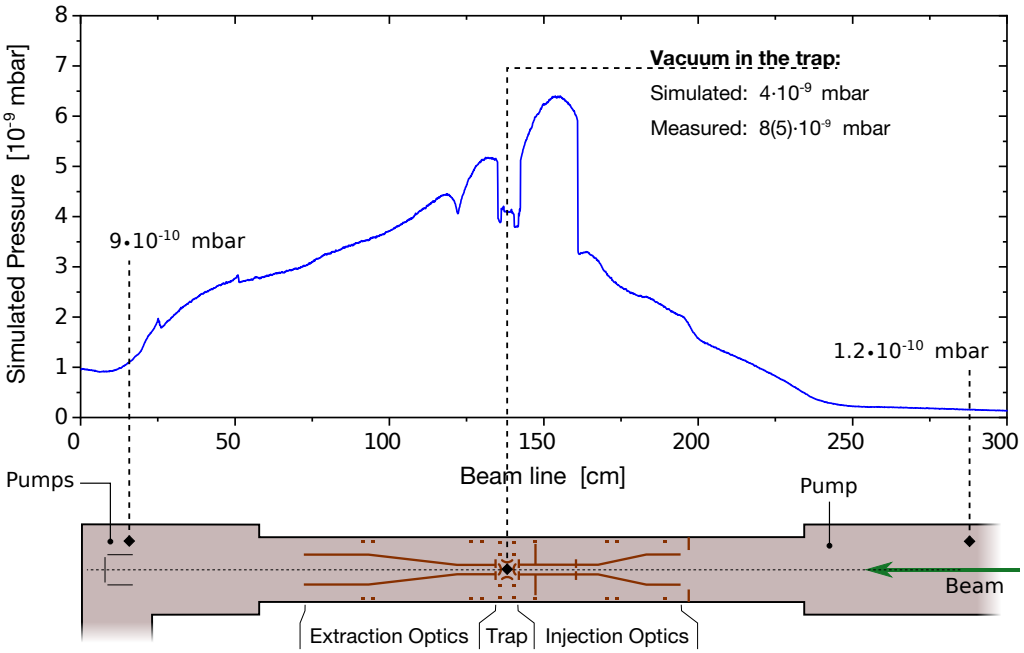

Figure B.9: Simulated pressure along the ion transport axis in the MPET beamline. In the bottom is shown a schematic representation of the elements in the beamline for reference. Points where pressure measurements were taken, either by gauges or by indirect techniques (sec. B.2), are marked with black diamonds.

B.3.2 Results: Current System

Simulations using the geometry of the current system were performed. Since the simulated density distribution is generated in arbitrary units, it was normalized to fit the ionization gauge measurements in the real system. Outgassing rates of the different materials were varied within an order of magnitude to achieve the best agreement with the ionization gauge measurements.

The resulting simulated pressure profile of the current MPET system is shown in figure B.9. It shows the average pressure along a cylindrical volume of 5 mm radius along the beam axis, where the ion transport path is expected to be contained. The simulated pressure in the trap and in the ionization gauges are compatible with the measured pressures in the same locations.

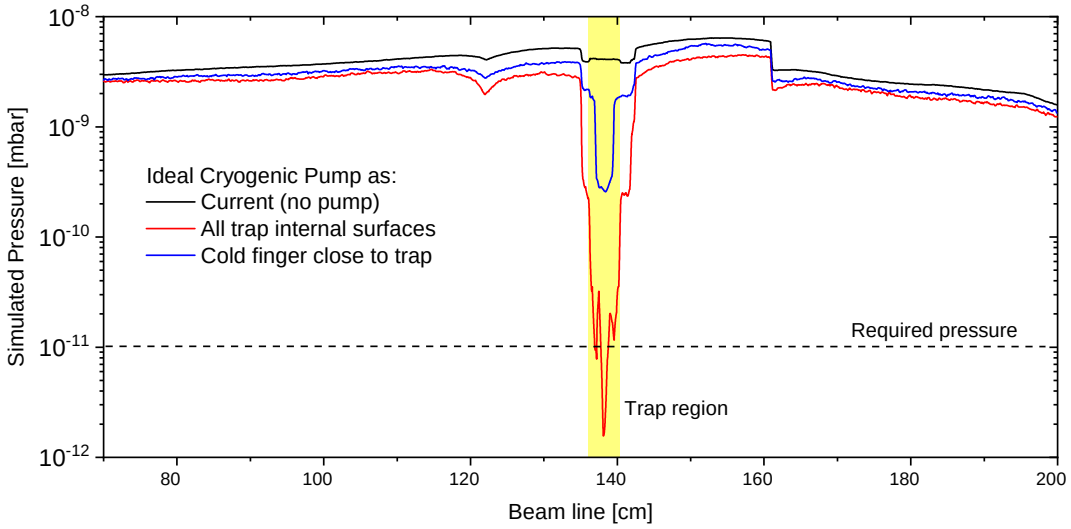

Figure B.10: Simulated pressure along the ion transport axis in the MPET beamline, with the addition of ideal cryopumps: a cold finger near the trap (blue) and all trap electrodes acting as cryopumps (red). The black curve is the simulated pressure with no modifications (as in fig. B.9). The trap region is marked by the yellow shaded area and the dashed line marks the required pressure in the trap.

B.3.3 Results: Upgraded System

With the simulation framework successfully benchmarked, it was used to study potential upgrades to the vacuum system. The goal was to reach a pressure on the order of 10^{-11} mbar in the trap volume. The modeled system included modifications that ranged from the addition of new vacuum pumps, the use of materials with lower outgassing rates and geometrical changes to the objects (for example, increasing diameters of apertures to improve gas flow). The generated density distributions were converted into realistic pressure distributions using the same normalization factor obtained in the simulations of the current system.

Most of the explored modifications produced minimal improvements. Only one class was able to produce the desired vacuum levels in the trap: the ones that included cryopumps in the trap region. Cryopumps were simulated as objects that acted as ideal pumps. Particles that hit them would not be reflected back to the system. Figure B.10 shows the simulated pressure profile generated by a few of the studied modifications including cryopumps.

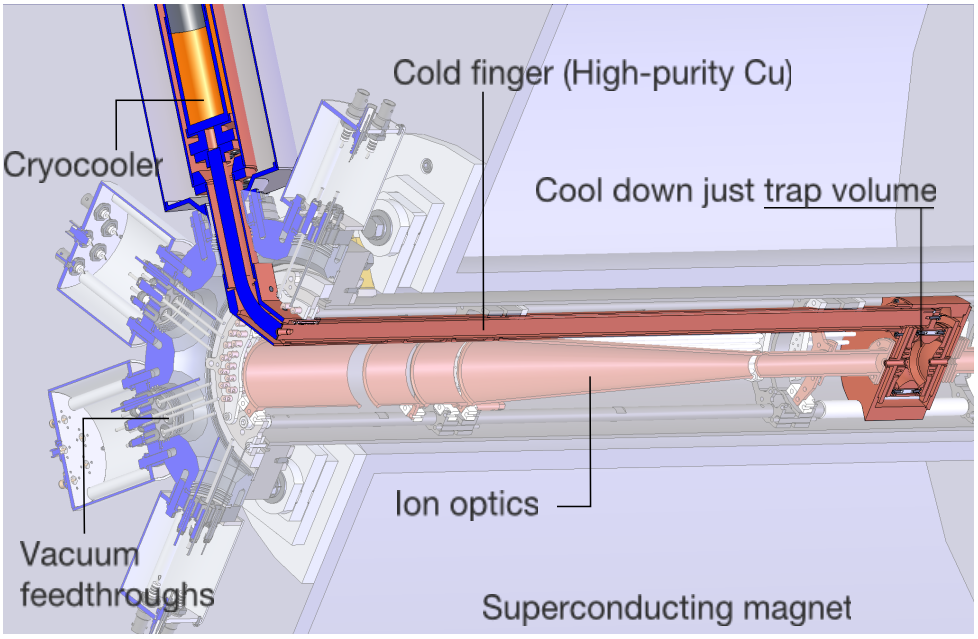

Figure B.11: Model of the CryoMPET upgrade highlights its main components: a cryogenic Penning trap is coupled to a two-stage cryocooler by a high-purity Cu finger. The remaining of the system is kept at room temperature.

B.4 The Cryogenic Measurement Penning Trap

The vacuum simulations detailed in the previous section suggested that a solution based on cryopumping can successfully bring the pressure levels in the MPET down to the required levels for PTMS of HCI. This result led to the development of the Cryogenic Measurement Penning Trap (CryoMPET): the upgrade system to MPET which incorporated a cryopump into the Penning trap.

The goal was to address a cryopumping solution to MPET that minimized changes to the current setup, enabled cryogenic operation for extended periods, and could be integrated into the system within its restrictive spatial limitations. In the designed system a new Penning trap, kept at cryogenic temperatures, has capabilities of cryopumping the residual gas in its interior. The trap is coupled to an external cryocooler by a high-purity Cu finger. A thermal shield encloses the cold pieces, and the remaining of the system is kept at room temperature. A model of the upgraded system is shown in figure B.11. The concept, the design, and the construction of CryoMPET are detailed in the next sections.

B.4.1 Concept of Cryopumping

CryoMPET's vacuum pumping mechanism is based on cryopumping. Background gas particles are removed from the volume of the trap by adhering to cold surfaces through weak intermolecular bonds. Particles are not removed from the system,

but they are removed from the region where they could interact with ions during a mass measurement. A review article on cryopumping can be found in [235].

The trap is essentially a cold enclosed volume with apertures for ion injection and extraction. The cold surfaces of the trap are required to remove from the volume the room-temperature gas particles that enter the trap through the apertures. To achieve that, two cryopumping mechanisms are employed in the CryoMPET: *cryosorption*, targeting light and weakly interacting gasses such as He or H_2, and *cryocondensation*, targeting heavier gasses. The concept of these mechanisms is explained in the following in the context of the upgraded system.

Cryocondensation

Condensation is the most elementary form of cryopumping. It consists of the solidification of the gas molecules onto the cold surface. The achievable pressure is determined by the saturation pressure of the gas at the temperature of the cold surface, which is shown in figure B.12 for a few common gases. As can be seen, the saturation pressure decreases very rapidly as the system is cooled down. This is where lies the strength of this type of pumping: a small decrease in temperature can lead to orders of magnitude better vacuum quality.

The saturation curve is defined in the thermodynamic equilibrium of the solid-gas phase at the given temperature. It means that at this pressure, the flux of particles leaving the surface is equal to the flux of particles sticking to the surface; therefore it has zero net pumping. Moreover, the particle adhesion occurs when the particle is at near thermal equilibrium with the surface. With warm gas entering the trap through the apertures, its particles will require to bounce in the internal surfaces a few times before adhesion. For these reasons, it is recommended to design the temperature of the system to achieve two orders of magnitude lower saturation pressure than required [235].

In CryoMPET, the background gas composition is expected to be similar to what was measured in the MPET (see fig. B.6). Then, according to figure B.12, a temperature below 20 K should be sufficient to pump most gases, targeting specially N_2. However, efficient pumping of light gases such as He and H_2 is hardly done through cryocondensation.

Cryosorption

The cryopumping of gases of difficult condensation is typically done with the use of cryosorbents. They are made of high porosity materials that can have a large surface area. As the gas particles enter the pores and reach the inner surfaces, the irregular geometry constricts particle motion, and the particles remain confined in the material [235, 237].

Cryosorbents can pump large amounts of gas and considerably reduce the pressure of the system. However, they saturate after some time, and their effect becomes negligible. Therefore, a regeneration procedure that includes the warming of the system must be incorporated into the routine operation. In addition, the design of

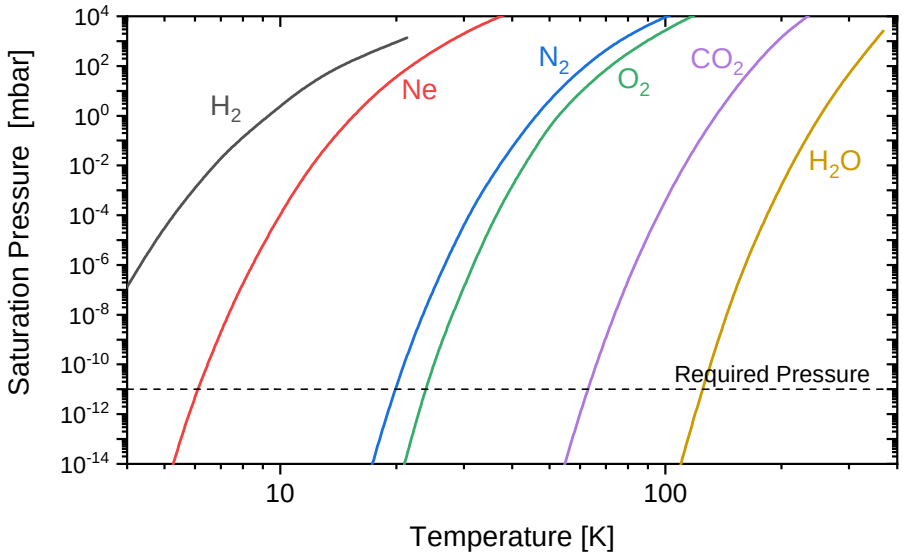

Figure B.12: Saturation pressure curves of several common gases, with data from [236]. CryoMPET's required pressure is marked by the dashed line.

the system must ensure that the sorbents are not directly exposed to the inflow of gas particles. Otherwise, the material may quickly saturate with gases that are easy to condense.

Cryosorption is less dependent on the temperature than condensation and more dependent on other factors like chemical properties and construction geometry. Nevertheless, it is still advisable to keep the temperature as low as possible. Typical temperatures employed in cryosorption are around 10 K or lower.

At CryoMPET, the cryosorbent of choice was the OLC AW 12X40 coconut-based activated charcoal from Calgon Carbon. This product is the equivalent as the one employed in the vacuum system of the International Thermonuclear Experimental Reactor (ITER) [237, 238], whose performance was extensively tested against many other products in the market.

Feasibility

Although the concept is feasible according to the simulations with ideal cryopumps, a simple model can provide a more analytical look into the involved factors. CryoMPET can be modeled as an enclosed volume of internal temperature T_{trap} and internal pressure P_{trap}. Two apertures (for ion injection and extraction) connect its interior to the exterior environment, whose gas is at pressure P_{out} at room temperature T_{out}. The apertures can be modeled as cylindrical pipes (like the tube electrodes at MPET, see sec. 4.2.2) of diameter D_{tube} and length L_{tube}. Figure B.13 shows a schematic illustration of this model.

To achieve equilibrium, the flux of gas particles to the interior of the trap (Q_{in}) must be equal to the flux of cryopumped particles (Q_{out}) to the internal surfaces.

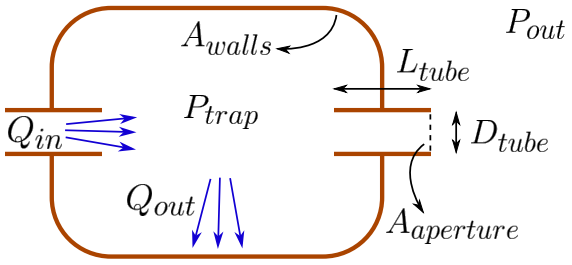

Figure B.13: Schematic illustration of the variables involved in the concept of CryoMPET's pumping by cryosorption.

The flux Q_{in} can be modeled as the flux through the two tubes in molecular flow, considering $P_{out} \gg P_{trap}$:

$$Q_{in} = 2\,\frac{\pi\, D_{tube}^3}{3\, L_{tube}}\, P_{out} \sqrt{\frac{k_B T_{out}}{2\pi\, m}} \quad , \tag{B.4}$$

where k_B is the Boltzmann constant and m is the mass of the background gas molecule.

If the design temperature is below 20 K, most gases are pumped by condensation in the tubes or inner surfaces of the trap. Therefore their vapor pressure becomes a negligible contribution to the P_{trap}. Then, the pumped flux Q_{out} can be modeled as pure cryosorption [235]:

$$Q_{out} = A_{walls}\, P_{trap} \sqrt{\frac{k_B T_{trap}}{2\pi\, m}}\; \alpha(T_{trap}, \text{gas}, \text{surf.}) \quad , \tag{B.5}$$

where A_{walls} is the internal surface area available for cryosorption and α is called the "sticking" coefficient, which is the probability of a gas particle adhere to the surface of the sorbent upon impinging into it. It greatly depends on the specific combination of gas, sorbent material and temperature.

Imposing the equilibrium condition $Q_{in} = Q_{out}$, we have that

$$\frac{P_{out}}{P_{trap}} = \left(\frac{3}{8}\,\frac{L_{tube}}{D_{tube}}\,\frac{A_{walls}}{A_{aperture}}\right) \sqrt{\frac{T_{out}}{T_{trap}}}\; \alpha(T_{trap}, \text{gas}, \text{surf.}) \quad , \tag{B.6}$$

where $A_{aperture} = \pi D_{tube}^2/4$ is the area of the apertures of the trap. The geometry-dependent factor (in between brackets) is on the order of 300 using the MPET trap design. However, A_{walls} can be greatly increased by the use of cryosorbents, which have a large surface area due to their porosity. The sticking coefficient has a mild variation with temperature. For H_2 pumping by the ITER-type charcoal, $\alpha = 0.6$ at 5 K and $\alpha = 0.3$ at 12 K [238].

According to the analysis presented in sections B.1 and B.2, it is desirable that $P_{out}/P_{trap} \approx 500$. Given the variables in equation B.6, considering the use of ITER-type cryosorbents and trap temperature on the order of < 20 K, the desired pressure in the trap is achievable.

B.4.2 Design Considerations

The overall design concept of CryoMPET is displayed in figure B.11 and presented in the beginning of this section. Next, the choices and considerations that were incorporated into the design to enable the cryopumping concept are described.

General design

Material selection: in general, the materials and components employed in CryoMPET have to be non-magnetic to not disturb the homogeneity of the magnetic field in the trap, have low outgassing rates for better vacuum properties, have known performance at cryogenic temperatures, and withstand temperatures up to 120° C for baking of the system and regeneration of cryosorbents.

Cryocooler: we opt for a cryogen-free approach for cooling. Since a typical MPET experiment requires continuous operation for many weeks, including tuning and preparation, a liquid helium cryostat would require high maintenance costs as it consumes about a liter of the cryogen per hour. With a closed-cycle cryocooler, the system can run continuously with minimal human interference or consumption of expensive goods[28]. The employed cryocooler in CryoMPET is the DE-215S model from Advanced Research Systems Corporation. It has two stages, with zero heat load the first stage can reach down to 20 K, while the second stage can reach 2.5 K. A critical disadvantage of using a cryocooler is that the cold tip lies about half a meter away from the trap and requires a very efficient thermal transport solution.

Trap Temperature and Coupling to Cryocooler: the trap is thermally coupled to the second stage of the cryocooler by a rod of solid high-purity copper (also denoted by *cold finger*). The rod is anchored to the ring electrode, which is thermally coupled to the other electrodes of the trap. Given the limited space in the setup, the finger diameter was limited to only 12.7 mm. Therefore, we resort to special materials in order to have efficient thermal coupling.

Some materials have an exceptionally high thermal conductivity at cryogenic temperatures [239]. It is related to the Residual Resistive Ratio (RRR) grading, which is the ratio between the electrical resistance of the material at room temperature and 4.2 K. In metals, the RRR grading is mostly governed by its purity and crystalline structure [240].

The copper rod was fabricated by Luvata Special Products and had a purity of 99.99995% and RRR $\approx$ 2000. The expected thermal conductivity is on the order of 10^4 W/(m·K) at $\sim$ 10 K. A Finite Elements Method analysis [241] revealed that the trap temperature can reach 8 K using a Cu rod of $RRR = 1000$, considering the specifications of the cryocooler and heat input only from thermal radiation. This result does not consider heat input from conduction from the planned points of contact (see below). The trap electrodes were made from 99.9995% pure Cu of RRR $\approx$ 1080 produced by the same company.

28 The employed model requires regular maintenance after 10,000 hours of operation

Thermal Shield: the cold system containing the trap and cold finger was enclosed by a thermal shield to limit the exposure of the cold surfaces to the room temperature environment. The shield was attached to the first stage (20 K) of the cryocooler and was polished for high reflectance. Given the surface area of the shield, it could receive up to 3 W from thermal radiation depending on the quality of the polishing. The shield pieces were made of Oxygen-Free Electronic Copper (OFE Cu, alloy C10100).

Thermal contacts: good thermal coupling between different pieces is essential to have the necessary heat conduction and thus to reach the desired temperatures. In most cases, the pieces are screwed or clamped together with a layer of a vacuum-friendly grease in between. In many other cases, good thermal coupling is desired, but also electrical insulation is required. It is the case of the connections between trap electrodes and between the trap and the cold finger. The coupling of these parts is then mediated by a custom piece made of sapphire, which has a high thermal conductivity at cryogenic temperatures.

Fixture and interface: minimal contact must exist between warm and cold structures to avoid heat conduction to the trap. However, they need to be integrated with each other for appropriate positioning and alignment. In the original MPET design, all ion optics elements and the trap were held in place by a support structure made of three parallel titanium rods. In the CryoMPET design, the same triple rod structure is maintained, but ceramic sleeves of low thermal conductivity cover two of the rods. The shield assembly, which also holds the trap in its interior, is held by gravity on these two covered rods touching only a few support points (see fig. B.14). The same idea is reproduced to hold the trap inside its shield. A pair of ceramic rods run across the inside of the thermal shield structure; the trap assembly rests on the two rods at two support points each, without touching the shield assembly.

Thermal contraction: besides minimizing heat conduction, another advantage of having the trap lying on the ceramic rods is that it can slide freely along them without losing alignment as the system cools down. The cold finger, which is about 70 cm in length, is expected to contract about 2.2 mm from its original size at room temperature [242]. This was incorporated into the design: the trap sits at the point of maximum homogeneity of the magnetic field when cold.

Instrumentation: two pairs of high precision thermal sensors (model DT-670B-SD from Lakeshore) and resistive heaters were incorporated into the cryogenic system. The heaters will aid in the regeneration cycles, and the sensors will monitor the temperature of the system. One instrumentation pair was placed at the tip of the cryocooler while the other was installed at one of the trap electrodes. The heater was placed as near as possible to the sensor for most accurate readings during regeneration.

Safety: gas leaks in cryogenic vacuum systems can become a relevant safety issue. If the leaked gases liquefy and accumulate, they may quickly expand when the system is warmed up. Therefore a burst disk was installed at the vacuum system to generate relief in case of overpressurization. Besides, an interlocking system was added to the system; if the pressure inside the vacuum chamber exceeds 5 mbar, it will automatically turn the cryocooler off.

Trap design

The design of the cryogenic Penning trap followed the design of the precursor trap, adapted to the needs of the new setup. Further modifications unrelated to the cryogenic upgrade were included to improve its overall performance. The design choices are described in the following. A schematic representation of CryoMPET construction is shown in figure B.14.

Trap dimensions: the trap hyperbolic shape was slightly modified from the original MPET version to better agree with the optimal configuration identified in [243]. The characteristic dimensions of the new trap are shown in table B.1. The outer structure of the electrodes was also designed to be massive and bulkier than previously to facilitate thermal conduction.

Table B.1: Characteristic dimensions of the CryoMPET, according to eq. 3.7.

r_0	13.670 mm
z_0	11.785 mm
d_0	10.778 mm

Gold plating: copper easily oxides when exposed to air, potentially forming insulating patches on the surface of the electrode. These patches may charge and disturb the transport of ions crossing its vicinities [244] and can be very detrimental for the correct shaping of the trap potential. A common solution is to plate the piece with an inert metal, such as gold. All CryoMPET trap electrodes received gold plating (type I, grade A, 7.5 μm thick) with a thin underlayer of silver acting as a diffusion barrier[29].

Electrodes for RF: in the original MPET design the RF signal for ion motion excitation was applied to the guard electrodes, which were appropriately segmented. However, their smaller size and longer distance to the ions compared to the central ring electrode resulted in a lower RF power delivered to the ions. Consequently, the implementation of broadband RF techniques such as described in [113] was challenging. In CryoMPET, the guard electrodes are solid, and the RF excitations are delivered by the central ring electrode, which is segmented accordingly. This modification is expected to increase the RF power delivered to the ions by a factor 10. A picture of the new segmented ring electrode (disassembled) is shown in picture 3.4.

29 A more appropriate diffusion barrier for gold is nickel; however, its use in the Penning trap is undesirable due to its magnetic properties.

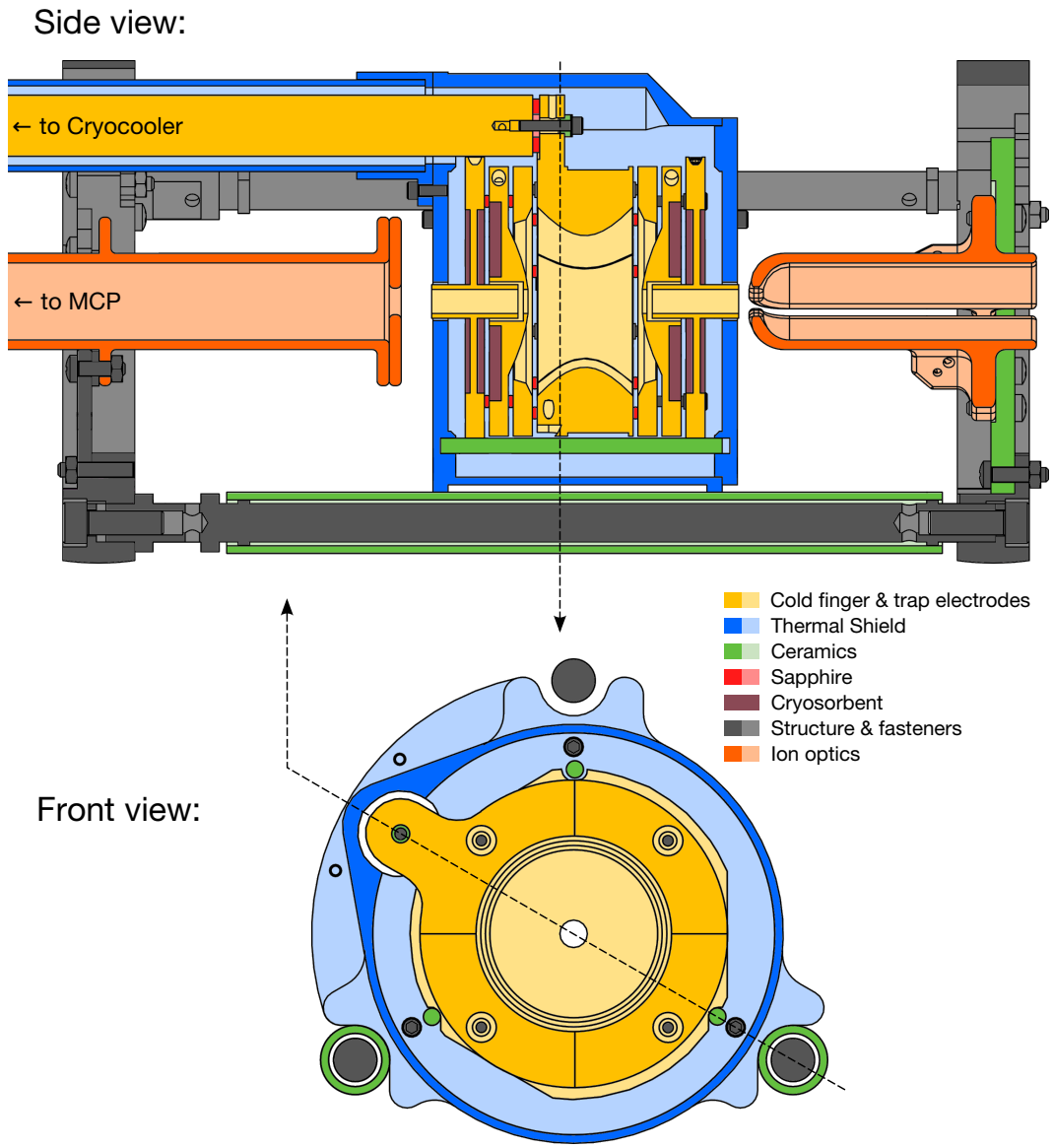

Figure B.14: Schematic illustration of the CryoMPET trap construction and its surrounding structures.

Tube electrodes: their lengths were extended out to shape the injection and extraction potential beyond the shield. In addition, they received a 1 mm increment in diameter from the original MPET design, which is expected to increase the ion extraction efficiency.

Guard electrodes: two solid ring pieces form the guard electrodes and their shape was slightly modified from the previous design. Instead of a flat surface, they are formed by two angled surfaces to avoid Knudsen re-emission towards the center of the trap.

Wiring: both the trap and the shield have built-in connector assemblies. Wires from the room temperature system are connected to the shield external connectors. In the interior of the shield, cryogenic thin wires leave the connectors and are wrapped onto thermal anchoring poles. From there, the cryogenic wires are attached to the trap connectors.

Cryosorbents: the activated charcoal granules were applied to six surfaces in the electrode structure that are not relevant to the shaping of the trapping potential: the back of the endcap electrodes and the two sides of the supporting structure of the tube electrodes. The granules were applied one by one on a layer of about 1 mm thick of the MCT $3715-2SE$ adhesive from MicroCoat Technologies. After the application, the pieces were baked at 150° C for an hour at a vacuum oven for curing of the adhesive.

B.4.3 Construction

MPET was removed from the TITAN beamline in December 2017 for the upgrade. The pieces from the CryoMPET were machined at the specialized machine shop at TRIUMF laboratory. Every component went through a rigorous UHV cleaning procedure [245], and the assembly occurred in the Winter of $2018-2019$. The system was installed back to the TITAN facility in March 2019 and is now under commissioning. Figures B.15, B.16 and B.17 shows pictures of the CryoMPET assemblies.

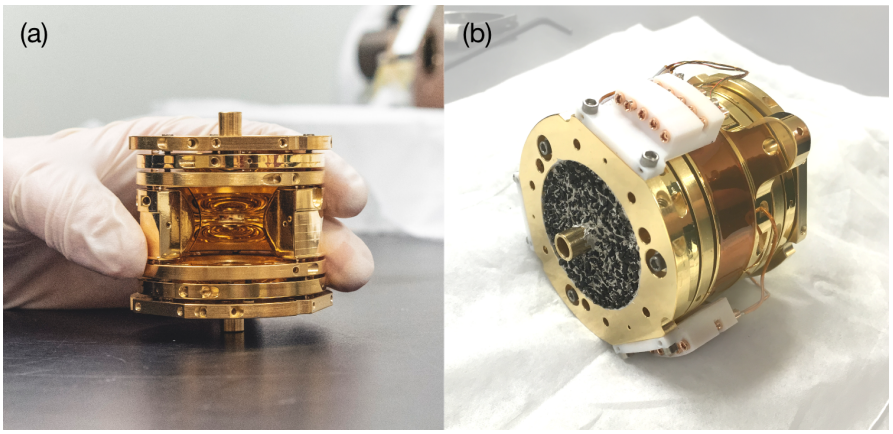

Figure B.15: Pictures of the assembled electrode structure of the cryogenic Penning trap: *(a)* without one segment of the central ring electrode showing its interior, courtesy of Stuart Shepherd; *(b)* fully assembled with cryosorbent, wires, connectors and instrumentation.

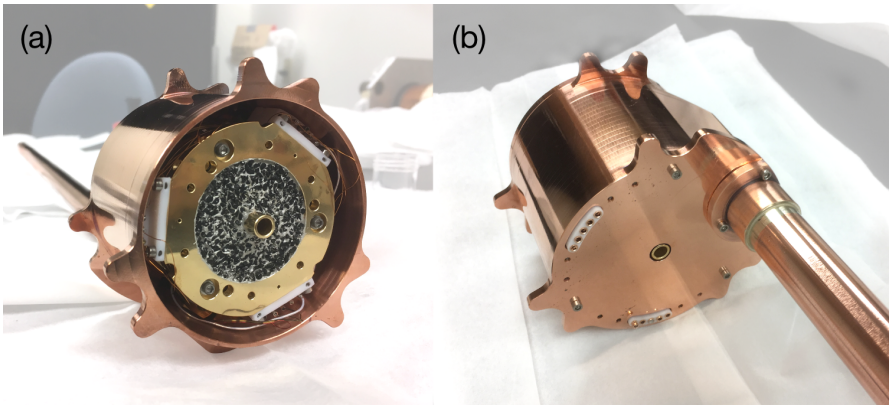

Figure B.16: Pictures of the trap and shield assemblies: *(a)* with open shield viewed from ion injection side, showing the trap; *(b)* closed shield viewed from the ion extraction side.

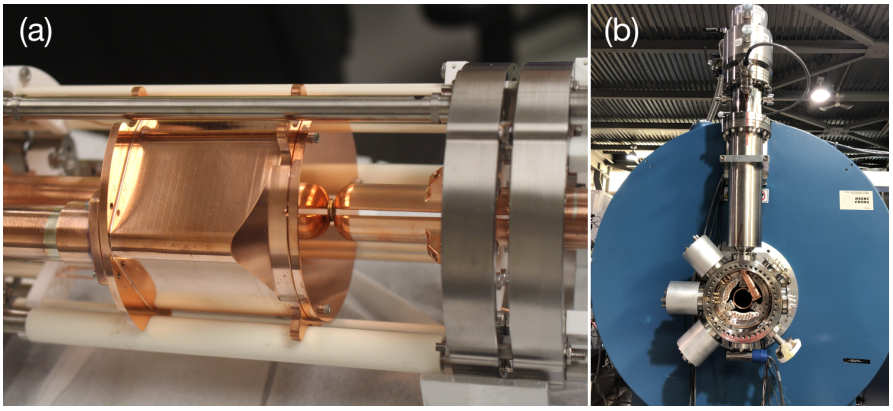

Figure B.17: *(a)* picture of the trap assembly in the together with structural elements and ion optics; *(b)* CryoMPET system installed at the superconducting magnet, the cryocooler and part of the shield around the cold finger are visible.